

# Cells, biomaterials, and biophysical stimuli for bone, cartilage, and muscle regeneration

**Edited by**

Lorenzo Fassina, Nora Bloise, Livia Visai, Murugan Ramalingam and Gabriella Cusella

**Published in**

Frontiers in Bioengineering and Biotechnology



## FRONTIERS EBOOK COPYRIGHT STATEMENT

The copyright in the text of individual articles in this ebook is the property of their respective authors or their respective institutions or funders. The copyright in graphics and images within each article may be subject to copyright of other parties. In both cases this is subject to a license granted to Frontiers.

The compilation of articles constituting this ebook is the property of Frontiers.

Each article within this ebook, and the ebook itself, are published under the most recent version of the Creative Commons CC-BY licence. The version current at the date of publication of this ebook is CC-BY 4.0. If the CC-BY licence is updated, the licence granted by Frontiers is automatically updated to the new version.

When exercising any right under the CC-BY licence, Frontiers must be attributed as the original publisher of the article or ebook, as applicable.

Authors have the responsibility of ensuring that any graphics or other materials which are the property of others may be included in the CC-BY licence, but this should be checked before relying on the CC-BY licence to reproduce those materials. Any copyright notices relating to those materials must be complied with.

Copyright and source acknowledgement notices may not be removed and must be displayed in any copy, derivative work or partial copy which includes the elements in question.

All copyright, and all rights therein, are protected by national and international copyright laws. The above represents a summary only. For further information please read Frontiers' Conditions for Website Use and Copyright Statement, and the applicable CC-BY licence.

ISSN 1664-8714  
ISBN 978-2-8325-2247-9  
DOI 10.3389/978-2-8325-2247-9

## About Frontiers

Frontiers is more than just an open access publisher of scholarly articles: it is a pioneering approach to the world of academia, radically improving the way scholarly research is managed. The grand vision of Frontiers is a world where all people have an equal opportunity to seek, share and generate knowledge. Frontiers provides immediate and permanent online open access to all its publications, but this alone is not enough to realize our grand goals.

## Frontiers journal series

The Frontiers journal series is a multi-tier and interdisciplinary set of open-access, online journals, promising a paradigm shift from the current review, selection and dissemination processes in academic publishing. All Frontiers journals are driven by researchers for researchers; therefore, they constitute a service to the scholarly community. At the same time, the *Frontiers journal series* operates on a revolutionary invention, the tiered publishing system, initially addressing specific communities of scholars, and gradually climbing up to broader public understanding, thus serving the interests of the lay society, too.

## Dedication to quality

Each Frontiers article is a landmark of the highest quality, thanks to genuinely collaborative interactions between authors and review editors, who include some of the world's best academicians. Research must be certified by peers before entering a stream of knowledge that may eventually reach the public - and shape society; therefore, Frontiers only applies the most rigorous and unbiased reviews. Frontiers revolutionizes research publishing by freely delivering the most outstanding research, evaluated with no bias from both the academic and social point of view. By applying the most advanced information technologies, Frontiers is catapulting scholarly publishing into a new generation.

## What are Frontiers Research Topics?

Frontiers Research Topics are very popular trademarks of the *Frontiers journals series*: they are collections of at least ten articles, all centered on a particular subject. With their unique mix of varied contributions from Original Research to Review Articles, Frontiers Research Topics unify the most influential researchers, the latest key findings and historical advances in a hot research area.

Find out more on how to host your own Frontiers Research Topic or contribute to one as an author by contacting the Frontiers editorial office: [frontiersin.org/about/contact](https://frontiersin.org/about/contact)



# Cells, biomaterials, and biophysical stimuli for bone, cartilage, and muscle regeneration

## Topic editors

Lorenzo Fassina — University of Pavia, Italy  
Nora Bloise — University of Pavia, Italy  
Livia Visai — University of Pavia, Italy  
Murugan Ramalingam — VIT University, India  
Gabiella Cusella — University of Pavia, Italy

## Citation

Fassina, L., Bloise, N., Visai, L., Ramalingam, M., Cusella, G., eds. (2023). *Cells, biomaterials, and biophysical stimuli for bone, cartilage, and muscle regeneration*. Lausanne: Frontiers Media SA. doi: 10.3389/978-2-8325-2247-9

## Table of contents

- 04 **Editorial: Cells, biomaterials, and biophysical stimuli for bone, cartilage, and muscle regeneration**  
Lorenzo Fassina, Nora Bloise, Murugan Ramalingam, Maria Gabriella Cusella De Angelis and Livia Visai
- 06 **Effects of Channels and Micropores in Honeycomb Scaffolds on the Reconstruction of Segmental Bone Defects**  
Keigo Shibahara, Koichiro Hayashi, Yasuharu Nakashima and Kunio Ishikawa
- 21 **Enhancing Myoblast Fusion and Myotube Diameter in Human 3D Skeletal Muscle Constructs by Electromagnetic Stimulation**  
Lisanne Terrie, Margherita Burattini, Sandra Van Vlierberghe, Lorenzo Fassina and Lieven Thorrez
- 31 **Identification of Small-Molecule Inhibitors for Osteosarcoma Targeted Therapy: Synchronizing *In Silico*, *In Vitro*, and *In Vivo* Analyses**  
Juan Liu, Qi Yao, Yu Peng, Zhihong Dong, Lu Tang, Xiaoyu Su, Lishuang Liu, Cheng Chen, Murugan Ramalingam and Lijia Cheng
- 44 **Physical and Chemical Properties, Biosafety Evaluation, and Effects of Nano Natural Deer Bone Meal on Bone Marrow Mesenchymal Stem Cells**  
Yongbo Li, Zhe Tan, Jixiang Zhang, Junhan Mu and Han Wu
- 61 **Microporous structures on mineralized collagen mediate osteogenesis by modulating the osteo-immune response of macrophages**  
Jun Li, Xin Luo, Zhao-Yong Lv, Hui-Fen Qiang, Cai-Yao Hou, Kun Liu, Chun-Xiu Meng, Yu-Jue Zhang, Feng-Zhen Liu and Bin Zhang
- 75 **Ultrasound and laser-promoted dual-gas nano-generator for combined photothermal and immune tumor therapy**  
XinYu Li, Yong Gao, XinZheng Liu, XiaoQian Hu, YunMeng Li, JunXi Sun, PingYu Wang, Hongkai Wu, HaeWon Kim, Murugan Ramalingam, ShuYang Xie and RanRan Wang
- 93 **Efficient co-isolation of microvascular endothelial cells and satellite cell-derived myoblasts from human skeletal muscle**  
Rebecca Wüst, Lisanne Terrie, Thomas Müntefering, Tobias Ruck and Lieven Thorrez
- 108 **Pulsed electromagnetic fields as a promising therapy for glucocorticoid-induced osteoporosis**  
Tianxiao Zhang, Zhiliang Zhao and Tiantian Wang
- 117 **Osteochondrogenesis by TGF- $\beta$ 3, BMP-2 and noggin growth factor combinations in an *ex vivo* muscle tissue model: Temporal function changes affecting tissue morphogenesis**  
Heng Liu, Peter E. Müller, Attila Aszódi and Roland M. Klar



## OPEN ACCESS

EDITED AND REVIEWED BY  
Hasan Uludag,  
University of Alberta, Canada

## \*CORRESPONDENCE

Lorenzo Fassina,  
✉ lorenzo.fassina@unipv.it  
Nora Bloise,  
✉ nora.bloise@unipv.it  
Murugan Ramalingam,  
✉ rmurug2000@gmail.com  
Maria Gabriella Cusella De Angelis,  
✉ cusella@unipv.it  
Livia Visai,  
✉ livia.visai@unipv.it

RECEIVED 04 April 2023

ACCEPTED 05 April 2023

PUBLISHED 11 April 2023

## CITATION

Fassina L, Bloise N, Ramalingam M,  
Cusella De Angelis MG and Visai L (2023),  
Editorial: Cells, biomaterials, and  
biophysical stimuli for bone, cartilage,  
and muscle regeneration.  
*Front. Bioeng. Biotechnol.* 11:1200368.  
doi: 10.3389/fbioe.2023.1200368

## COPYRIGHT

© 2023 Fassina, Bloise, Ramalingam,  
Cusella De Angelis and Visai. This is an  
open-access article distributed under the  
terms of the [Creative Commons  
Attribution License \(CC BY\)](#). The use,  
distribution or reproduction in other  
forums is permitted, provided the original  
author(s) and the copyright owner(s) are  
credited and that the original publication  
in this journal is cited, in accordance with  
accepted academic practice. No use,  
distribution or reproduction is permitted  
which does not comply with these terms.

# Editorial: Cells, biomaterials, and biophysical stimuli for bone, cartilage, and muscle regeneration

Lorenzo Fassina<sup>1\*</sup>, Nora Bloise<sup>2,3\*</sup>, Murugan Ramalingam<sup>4,5,6,7,8,9\*</sup>,  
Maria Gabriella Cusella De Angelis<sup>10\*</sup> and Livia Visai<sup>2,3\*</sup>

<sup>1</sup>Department of Electrical, Computer and Biomedical Engineering, Centre for Health Technologies (CHT), University of Pavia, Pavia, Italy, <sup>2</sup>Department of Molecular Medicine, Centre for Health Technologies (CHT), INSTM UdR of Pavia, University of Pavia, Pavia, Italy, <sup>3</sup>Medicina Clinica-Specialistica, UOR5 Laboratorio di Nanotecnologie, ICS Maugeri, IRCCS, Pavia, Italy, <sup>4</sup>School of Basic Medical Sciences, Chengdu University, Chengdu, China, <sup>5</sup>Institute of Tissue Regeneration Engineering, Dankook University, Cheonan, Republic of Korea, <sup>6</sup>Department of Nanobiomedical Science, BK21 NBM Global Research Center for Regenerative Medicine, Dankook University, Cheonan, Republic of Korea, <sup>7</sup>Mechanobiology Dental Medicine Research Center, Dankook University, Cheonan, Republic of Korea, <sup>8</sup>UCL Eastman-Korea Dental Medicine Innovation Centre, Dankook University, Cheonan, Republic of Korea, <sup>9</sup>Department of Metallurgical and Materials Engineering, Atilim University, Ankara, Türkiye, <sup>10</sup>Department of Public Health, Experimental and Forensic Medicine, Human Anatomy Unit, University of Pavia, Pavia, Italy

## KEYWORDS

tissue engineering, biomaterials, physical stimuli, bone regeneration, cartilage regeneration, muscle regeneration

## Editorial on the Research Topic:

Cells, biomaterials, and biophysical stimuli for bone, cartilage, and muscle regeneration

Over the last few years, a variety of Tissue Engineering strategies have been developed to improve the regeneration of bone, cartilage, and skeletal muscle. Numerous studies have proven that physical factors (e.g., external forces, electromagnetic waves, electric fields, ultrasounds, lasers, fluid flow shear stresses, mechanical vibrations, mechanical deformations, and biomaterials' features), as well as biochemical factors, may induce cells to reprogram their functions and dynamically adapt to the microenvironment conditions. In this context, many efforts are dedicated to engineer the biomaterial scaffolds, the physical stimuli, and the biochemical cues to whom the mammalian cells respond in terms of proliferation, differentiation, and production of extracellular matrix.

Effective regeneration of bone, cartilage, and skeletal muscle defects often presents significant challenges, particularly in patients with decreased tissue regeneration ability due to extensive trauma, diseases, or aging.

To this regard, in the present Research Topic, 55 Authors from all over the world decided to publish their outstanding and promising results.

It is well known that the reconstruction of critical-sized segmental bone defects is a key challenge in orthopedics. Shibahara et al. fabricated various types of carbonate apatite honeycomb scaffolds to deal with critical-sized segmental bone. The authors showed that the scaffolds with a larger channel volume promoted bone ingrowth compared to that with a larger micropore volume, whereas scaffolds with a larger volume of the micropores rather than the channels promoted the scaffold resorption by osteoclasts and the bone formation; in

other words, the channels affected bone ingrowth in the early stage and, subsequently, micropores affected scaffold resorption and bone formation. The findings of this study provide direction for designing the pore structure of scaffolds for bone regeneration.

The geometrical features of the regeneration scaffolds are, actually, of great importance, but also the growth factors applied during the healing time are equally significant. To this regard, Liu et al. investigated whether multiple growth factors applied to muscle tissue *in vitro*, such as TGF- $\beta$ 3, BMP-2 and Noggin, can lead to tissue morphogenesis with a specific osteochondrogenic nature. In particular, they revealed a synergistic effect between TGF- $\beta$ 3 and Noggin that positively influenced the tissue morphogenesis; in addition, Noggin was observed to upregulate BMP-2 and osteocalcin at a specific time of culture in the presence of TGF- $\beta$ 3, suggesting that signals change their functions throughout the process of new tissue formation.

The origin of the scaffold material is also crucial. For example, various commercial scaffolds are manufactured using a source of bovine bone or porcine bone. Li et al. showed that deer bone powder has important osteogenic effects; in particular, nano-deer bone meal can be used as a potential osteoinductive active nanomaterial to enhance bone tissue engineering scaffolds.

A new hot theme in bone tissue engineering is the assessment of the properties of biomaterials on regulating the macrophage polarization in order to stimulate the tissue regeneration. In this context, Li et al. fabricated mineralized collagen scaffolds with different microporous structures mediating the osteo-immunomodulation; in particular, the regeneration was characterized by increased expression of some osteogenic markers such as alkaline phosphatase, type-I collagen, and osteocalcin.

Besides the features of the biomaterial scaffolds, the physical tensile integrity around the cells can lead the regeneration process. To this regard, Terrie et al. developed an innovative method for skeletal muscle tissue engineering via a dynamic tissue culture system, where the stimulus is a pulsed electromagnetic field. In particular, in 2D experiments, an enhanced myogenesis was observed, as evidenced by an increased myotube diameter and fusion index; in addition, 3D bioartificial muscles were subjected to an electromagnetic stimulus for varying exposure times: once the myotubes were formed, the pulsed electromagnetic wave caused significantly higher myotube diameter, fusion index, and increased myosin heavy chain 1 expression. This research shows the potential of electromagnetic stimulation for enhancing myotube formation both in 2D and 3D, warranting its further consideration in dynamic culturing techniques.

The vascularization of tissue-engineered constructs remains a key challenge in the field of skeletal muscle tissue engineering. A strategy for vascularizing muscle organoids relies on *de novo* assembly of undifferentiated endothelial cells into capillaries. Wüst et al. built a pioneering method to use muscle-specific endothelial cells in order to study the pre-vascularization in skeletal muscle tissue engineering, since the endothelial cells display a tissue-specific phenotype. In particular, they describe a detailed protocol for the co-isolation of human skeletal muscle endothelial cells and satellite cell-derived myoblasts. The isolation of the two cell types is crucial for further studies to elucidate cell

crosstalk in health and disease. Furthermore, the use of muscle-specific endothelial cells allows a shift towards engineering more functional tissue, with downstream applications including drug screening and regenerative medicine.

The electromagnetic waves are also very useful in therapy (e.g., to deal with delayed bone fracture healing and bone non-unions). In their review, Zhang et al. propose that pulsed electromagnetic fields may be considered a potential and side-effect-free therapy for glucocorticoid-induced osteoporosis.

Another bone disease is the osteosarcoma which is the most common primary bone cancer in children and adolescents and the third most common in adults. The research of Liu et al. aimed to explore a new approach for the treatment of osteosarcoma by combining biomaterials with next-generation small molecule-based targeted therapy. In particular, after tumor resection in mice, the combination of tumor cell inhibitor ZINC150338698 and collagen-thermosensitive hydrogel-calcium phosphate composites could repair the bone defects with no foreign body reaction or new tumor growth.

A potential new cancer treatment is shown by Li et al. They report an ultrasound and laser-promoted dual-gas nano-generator, where calcium carbonate-polydopamine-manganese oxide nanoparticles are source of calcium ions, manganese ions, carbon dioxide, and oxygen. In particular, calcium and manganese ions act as adjuvants for an immune response, whereas the cancer cell membrane is broken by the burst of gas bubbles under ultrasound stimulation and the photothermal properties of polydopamine also contribute to the immunogenic cell death. The generation of oxygen alleviates the tumor hypoxia and thus reduces hypoxia-induced heat resistance and immunosuppressive effects, thereby improving the therapeutic efficacy.

In conclusion, we believe that these papers can provide help and reference in Tissue Engineering research and practical scenarios.

## Author contributions

All authors listed have made a substantial, direct, and intellectual contribution to the work and approved it for publication.

## Conflict of interest

The authors declare that the research was conducted in the absence of any commercial or financial relationships that could be construed as a potential conflict of interest.

## Publisher's note

All claims expressed in this article are solely those of the authors and do not necessarily represent those of their affiliated organizations, or those of the publisher, the editors and the reviewers. Any product that may be evaluated in this article, or claim that may be made by its manufacturer, is not guaranteed or endorsed by the publisher.





# Effects of Channels and Micropores in Honeycomb Scaffolds on the Reconstruction of Segmental Bone Defects

Keigo Shibahara<sup>1,2</sup>, Koichiro Hayashi<sup>1\*</sup>, Yasuharu Nakashima<sup>2</sup> and Kunio Ishikawa<sup>1</sup>

<sup>1</sup>Department of Biomaterials Faculty of Dental Science, Kyushu University, Fukuoka, Japan, <sup>2</sup>Department of Orthopedic Surgery, Graduate School of Medical Sciences, Kyushu University, Fukuoka, Japan

## OPEN ACCESS

### Edited by:

Lorenzo Fassina,  
University of Pavia, Italy

### Reviewed by:

Cecilia Persson,  
Uppsala University, Sweden  
Dietmar W. Werner Hutmacher,  
Queensland University of Technology,  
Australia

### \*Correspondence:

Koichiro Hayashi  
khayashi@dent.kyushu-u.ac.jp

### Specialty section:

This article was submitted to  
Biomaterials,  
a section of the journal  
Frontiers in Bioengineering and  
Biotechnology

**Received:** 30 November 2021

**Accepted:** 01 February 2022

**Published:** 18 March 2022

### Citation:

Shibahara K, Hayashi K, Nakashima Y  
and Ishikawa K (2022) Effects of  
Channels and Micropores in  
Honeycomb Scaffolds on the  
Reconstruction of Segmental  
Bone Defects.  
Front. Bioeng. Biotechnol. 10:825831.  
doi: 10.3389/fbioe.2022.825831

The reconstruction of critical-sized segmental bone defects is a key challenge in orthopedics because of its intractability despite technological advancements. To overcome this challenge, scaffolds that promote rapid bone ingrowth and subsequent bone replacement are necessary. In this study, we fabricated three types of carbonate apatite honeycomb (HC) scaffolds with uniaxial channels bridging the stumps of a host bone. These HC scaffolds possessed different channel and micropore volumes. The HC scaffolds were implanted into the defects of rabbit ulnar shafts to evaluate the effects of channels and micropores on bone reconstruction. Four weeks postoperatively, the HC scaffolds with a larger channel volume promoted bone ingrowth compared to that with a larger micropore volume. In contrast, 12 weeks postoperatively, the HC scaffolds with a larger volume of the micropores rather than the channels promoted the scaffold resorption by osteoclasts and bone formation. Thus, the channels affected bone ingrowth in the early stage, and micropores affected scaffold resorption and bone formation in the middle stage. Furthermore, 12 weeks postoperatively, the HC scaffolds with large volumes of both channels and micropores formed a significantly larger amount of new bone than that attained using HC scaffolds with either large volume of channels or micropores, thereby bridging the host bone stumps. The findings of this study provide guidance for designing the pore structure of scaffolds.

**Keywords:** honeycomb, scaffold, pore architecture, carbonate apatite, bone reconstruction

## INTRODUCTION

Despite technological advancements, segmental bone defects (SBDs) are intractable, and their suitable treatment scheme remains to be established (Bezstarosti et al., 2021; Norris et al., 2021). Frequent failure of SBD treatment may lead to functional disorders or amputations (Lasanianos et al., 2010; Mauffrey et al., 2015). In addition, the presence of SBDs leads to the loss of bone continuity, which increases risk of nonunion and renders the treatment difficult (Lasanianos et al., 2010; Mauffrey et al., 2015; Bezstarosti et al., 2021; Norris et al., 2021). Notably, critical-sized SBDs disrupt the bone orientation, resulting in a high rate of nonunion (Petersen et al., 2018). To achieve favorable outcomes in SBD treatments, a promising approach is to implant osteoconductive scaffolds that connect the stumps of the host bones and allow the penetration of various cells engaged in bone regeneration into the SBDs (Feng et al., 2012; Tanaka et al., 2017; Petersen et al., 2018).

Considering the aforementioned approach, we have been developing osteoconductive bioceramic honeycomb (HC) scaffolds with numerous channels directionally penetrating the scaffold (Hayashi et al., 2019a, 2019b, 2020b, 2020c, 2021c, 2021d, 2021e, 2022; Hayashi and Ishikawa 2020a, 2021a, 2021b; Sakemi et al., 2021; Shibahara et al., 2021). We confirmed that the presence of uniaxial channels in the HC scaffolds could promote bone ingrowth from the stumps of the host bone in SBD treatments (Sakemi et al., 2021; Shibahara et al., 2021). The HC scaffolds could realize adhesion to the bone and bone ingrowth as early or earlier than various three-dimensional porous scaffolds, and even combined three-dimensional porous scaffolds and mesenchymal stem cells (MSCs) (Zhou et al., 2010; Alluri et al., 2019). Other researchers also reported scaffolds that connected the stumps of the host bones without osteogenic growth factors, such as hydrogen-mineral composite (Patel et al., 2020), polylactide-coglycolide/tricalcium phosphate composite (Yu et al., 2018), and porous magnesium alloy (Wang et al., 2020). The ideal scaffold must be replaced with a new bone, while the scaffold parts corresponding to the bone marrow regions are resorbed (Zhang et al., 2020). However, previously developed HC scaffold did not achieve these requirements (Shibahara et al., 2021).

To surpass the efficacy of previous HC scaffolds and satisfy these requirements, an effective approach is to control the chemical composition and pore structure of the HC scaffold, which can crucially affect its osteoconductivity and resorption. In terms of the chemical composition, carbonate apatite (CAP) is resorbed by the osteoclasts at a similar pace as that of new bone formation and can thus be replaced with new bone (Doi et al., 1998; Zhang et al., 2021). In contrast, hydroxyapatite (HAP) is not resorbed and beta-tricalcium phosphate ( $\beta$ -TCP) is resorbed prior to new bone formation (Ishikawa et al., 2018; Hayashi et al., 2019b, 2020b). Considering the above properties of these calcium phosphate materials, CAP is desirable for the chemical composition of HC scaffolds in SBD reconstruction.

Existing studies on intrabony defect reconstruction and vertical bone augmentation demonstrated that HC scaffolds having channels with an aperture size of 190–300  $\mu\text{m}$  can realize the ingrowth of bone and blood vessels more effectively than those with aperture sizes of 100–190 and 300–630  $\mu\text{m}$  (Hayashi et al., 2020c, 2021d, 2021e, 2022; Hayashi and Ishikawa 2021a). Furthermore, the micropores affect osteoclastogenesis and the subsequent resorption of scaffolds by osteoclasts and new bone formation (Hayashi et al., 2019a; Hayashi and Ishikawa, 2020a). The scaffolds with both channels and micropores can exert osteoinduction and osteoconduction, and can shorten the bone reconstruction period (Woodard et al., 2007; Polak et al., 2011; Pei et al., 2017; Hayashi et al., 2020b). Thus, HC scaffolds with channels and micropores of suitable sizes are expected to exert superior efficacy for critical-sized SBD reconstruction.

Previously, researchers reported that three-dimensional scaffolds with optimized multiscale pores successfully reconstructed critical-sized SBDs in combination with osteogenic growth factors (Tang et al., 2016; Liu et al., 2019; Niu et al., 2019). However, these scaffolds were unable to

reconstruct the critical-sized SBDs in the absence of osteogenic growth factors (Tang et al., 2016; Liu et al., 2019; Niu et al., 2019). This issue might be attributed to the focus on pore size only, while the importance of pore volume has been overlooked. Thus, the effects of pore volume on the SBD reconstruction efficacy remain unknown.

In this study, we investigated the efficacy of critical-sized SBD reconstruction using CAP HC scaffolds with different volume proportions of the channels and micropores to clarify the interrelation between these properties. Furthermore, we evaluated the SBD reconstruction efficacy of CAP HC scaffolds with suitable channel and micropore volumes.

## MATERIALS AND METHODS

### Preparation of CAP HC Scaffolds

CAP HC scaffolds were fabricated by extrusion molding as described in our previous work (Hayashi and Ishikawa 2021a). In detail, a mixture of  $\text{CaCO}_3$  (Sakai Chemical Industry Co., Ltd., Osaka, Japan) and organic binder (Nagamine Manufacturing Co., Ltd., Kagawa, Japan) was extruded through the HC dies of a uniaxial extruder (Universe Co., Ltd., Saga, Japan). The organics in the HC green bodies were removed by sintering at 600–650°C in a  $\text{CO}_2$  atmosphere. Subsequently,  $\text{CaCO}_3$  HC blocks were obtained. The  $\text{CaCO}_3$  HC blocks were immersed in 1 mol/L  $\text{Na}_2\text{HPO}_4$  (Fujifilm Wako Pure Chemical Co., Ltd., Osaka, Japan) at 80°C for 7 days. The chemical composition of the HC blocks was modified by transforming  $\text{CaCO}_3$  to CAP through dissolution–precipitation reactions to maintain the HC architecture. The prepared CAP HC blocks were washed at least five times with distilled water and shaped into cuboids (height, width, and length of 6, 3, and 10 mm, respectively) using computer-aided design and manufacturing tools (monoFab SPM-20, Roland DG, Shizuoka, Japan). Hereafter, the CAP HC scaffolds with a large channel volume and small micropore volume; small channel volume and large micropore volume; and large channel and micropore volumes are labeled c-HC, m-HC, and cm-HC, respectively.

### Characterizations of the CAP HC Scaffolds

The macro-/microstructures of the CAP HC scaffolds were examined through computer tomography imaging ( $\mu$ -CT; Skyscan 1076, Bruker Co., Ltd., MA, United States) and scanning electron microscopy (S3400N, Hitachi High-Technologies Corporation, Tokyo, Japan). The crystal structure of the  $\text{CaCO}_3$  blocks and CAP HC scaffolds were determined through X-ray diffraction (XRD) analysis. The XRD patterns were recorded on a diffractometer (D8 Advance, Bruker AXS GmbH, Karlsruhe, Germany) with Cu K $\alpha$  radiation of 40 kV and 40 mA. The chemical composition of the  $\text{CaCO}_3$  blocks and CAP HC scaffolds was examined through Fourier transform infrared spectroscopy (FTIR). The FTIR spectra were recorded on a spectrometer (FT/IR-6200; JASCO, Tokyo, Japan) using the KBr disk method. The standard XRD patterns and FTIR spectrum of HAP powder (HAP-100, Taihei Chemical Industries, Co., Ltd., Nara, Japan) were derived. Moreover,

carbon–hydrogen–nitrogen (CHN) analysis (MT-6, Yanako Analytical Instruments, Kyoto, Japan) was performed to measure the carbonate content in the CAP HC scaffolds. The average carbonate contents were calculated from the results of three samples for each scaffold type. Mercury injection porosimetry (AutoPore 9420, Shimadzu Corporation, Kyoto, Japan) was performed to determine the size distribution and volume of open pores in the CAP HC scaffolds. The theoretical density of hydroxyapatite ( $3.16 \text{ g/cm}^3$ ) was used to calculate the porosities of CAP because the chemical composition of CAP varies based on the amount of  $\text{CO}_3$  (Gibson and Bonfield 2001). In this analysis, eight samples for each scaffold type were tested. Furthermore, the compressive strength of the CAP HC scaffolds was measured as the mechanical strength using a universal testing machine (Autograph AGS-J, Shimadzu, Kyoto, Japan) installed with a load cell with the maximum capacity of 5,000 N. The samples were compressed parallel to the channel at a crosshead speed of 1 mm/min, and the value when sample fracture occurred was recorded. The mechanical strength test was performed using eight samples for each scaffold type.

## Animal Surgery

The animal experiments in this study were approved by the Animal Care and Use Committee of Kyushu University (Approval no. A21-010-0). Rabbits aged 18 weeks and weighing 2.9–3.4 kg have been used for SBD models (Okada et al., 1999; Kokubo et al., 2003; Suga et al., 2004). Ulnar or radial SBD models were used in this study owing to their low management cost (Horner et al., 2010). Previously reported SBD models of 10–20 mm ulna until 12 weeks postoperatively were considered critical-sized (Shibahara et al., 2021). Thus, in this study, a 10-mm-length SBD model of the rabbit ulna was selected to evaluate the SBD reconstruction efficacy of HC scaffolds over a short observation period (**Supplementary Figure S1**).

The rabbits were bred in the animal center of Kyushu University. The animal experiments were conducted according to the procedure used in our previous report (Shibahara et al., 2021). General anesthesia was performed by intramuscular injection of ketamine (30 mg/kg, Daiichi Sankyo Co., Ltd, Tokyo, Japan) and xylazine (5.0 mg/kg, Elanco Japan, Co., Ltd, Tokyo, Japan). After shaving and disinfecting the region of interest with 10% povidone iodine (Meiji Seika Pharma Co., Ltd., Tokyo, Japan), local anesthesia with lidocaine (2%, 6.0 mg/kg, Dentsply Sirona Co., Ltd., Tokyo) was provided through subcutaneous injection into the forearm. The skin on the lateral forearm was incised with a blade (Akiyama Medical MFG. Co., Ltd., Tokyo, Japan) to expose the ulna. The midshaft of the ulna was osteotomized along the side of a 10-mm-long guide block with a bone saw (sagittal blade; Zimmer Biomet Co., Ltd., Tokyo, Japan) to generate critical-sized SBDs (length of 10 mm) in the ulna (Shibahara et al., 2021). The periosteum and interosseous membrane were removed together with 10-mm-long bone fragment (Shibahara et al., 2021). Despite this procedure, bones are formed on the opposite bone by the periosteal reaction, and the generated bones are likely to elicit the bone formation in the defect (Bodde et al., 2008). In previous studies (Elbackly et al., 2015), GORE-TEX® was placed between

the radius and the ulna to prevent the migration of cells from the radius and to eliminate the effect of periosteal reaction. Based on this report by Elbackly et al., in our study, a 10-mm-long cell-shielding membrane composed of polyethylene terephthalate was placed between the radius and the ulna to eliminate the effects of periosteal reaction from the radial side (Shibahara et al., 2021). The ulna was fixed using a nonlocking stainless-steel plate with a thickness of 0.6 mm. The scaffold was implanted in the bone defect and fixed to the plate with a 4-0 silk surgical suture (MANI Co., Ltd., Tochigi, Japan). The abovementioned procedures were implemented on both forearms, and the scaffold type (c-HC, m-HC, and cm-HC) inserted was randomly selected. Finally, the fasciae and skin were sutured with a 4-0 nylon surgical suture (MANI Co., Ltd.). To prevent wound infection, gentamicin (4 mg/kg, Takata Pharma Co., Ltd., Saitama, Japan) was injected intraperitoneally. The surgical site was again disinfected with 10% povidone iodine (Meiji Seika Pharma Co., Ltd.). The forearms were not immobilized after surgery, and the rabbits were allowed to move freely in their cages. Four weeks and 12 weeks postoperatively, the rabbits were euthanized with an anesthetic overdose, and both forearms were harvested ( $n = 4$  per group).

## Radiographic Evaluation

After sacrifice, the reconstruction images of the specimens were checked by radiographs (HA-60, HITEX Co., Ltd., Osaka, Japan). The bone formation at the osteotomized region and scaffold resorption were evaluated from the radiographs.

## μ-CT Evaluation

After removing the nonlocking stainless-steel plates and screws, the specimens were scanned through μ-CT (Skyscan 1076; Bruker Co., Ltd., MA, United States). The images were reconstructed using the NRecon software (Skyscan). The reconstructed images were evaluated based on their grayscale intensity. In the two-dimensional μ-CT image, threshold ranges were selected for the HC scaffold and bones to create segmentation images, respectively. Subsequently, the obtained segmentation images were compared with the original image to check whether they reflected their morphology (Bouxsein et al., 2010). The μ-CT images were observed to examine the long axis of the scaffolds 4 and 12 weeks postoperatively. The relevant values were calculated using **Eqs 1–4**.

$$\text{BV/TV (\%)} = \frac{\text{(volume of new bone in the scaffold)}}{\text{(total volume of the bone defect)}} \times 100 \quad (1)$$

$$\text{BV/CMV (\%)} = \frac{\text{(volume of new bone in the scaffold)}}{\text{(total volume of channels and micropores)}} \times 100 \quad (2)$$

$$\text{SV/TV (\%)} = \frac{\text{(volume of the scaffold)}}{\text{(total volume of the bone defect)}} \times 100 \quad (3)$$

$$\begin{aligned} \text{The volume percentage of remaining scaffolds (\%)} \\ = \frac{\text{(volume of the scaffold)}}{\text{(volume of the scaffold before implantation)}} \times 100 \quad (4) \end{aligned}$$

## Histological evaluation

Hematoxylin-eosin (HE)-stained tissue sections were prepared for histological evaluation. The long-axis images were evaluated

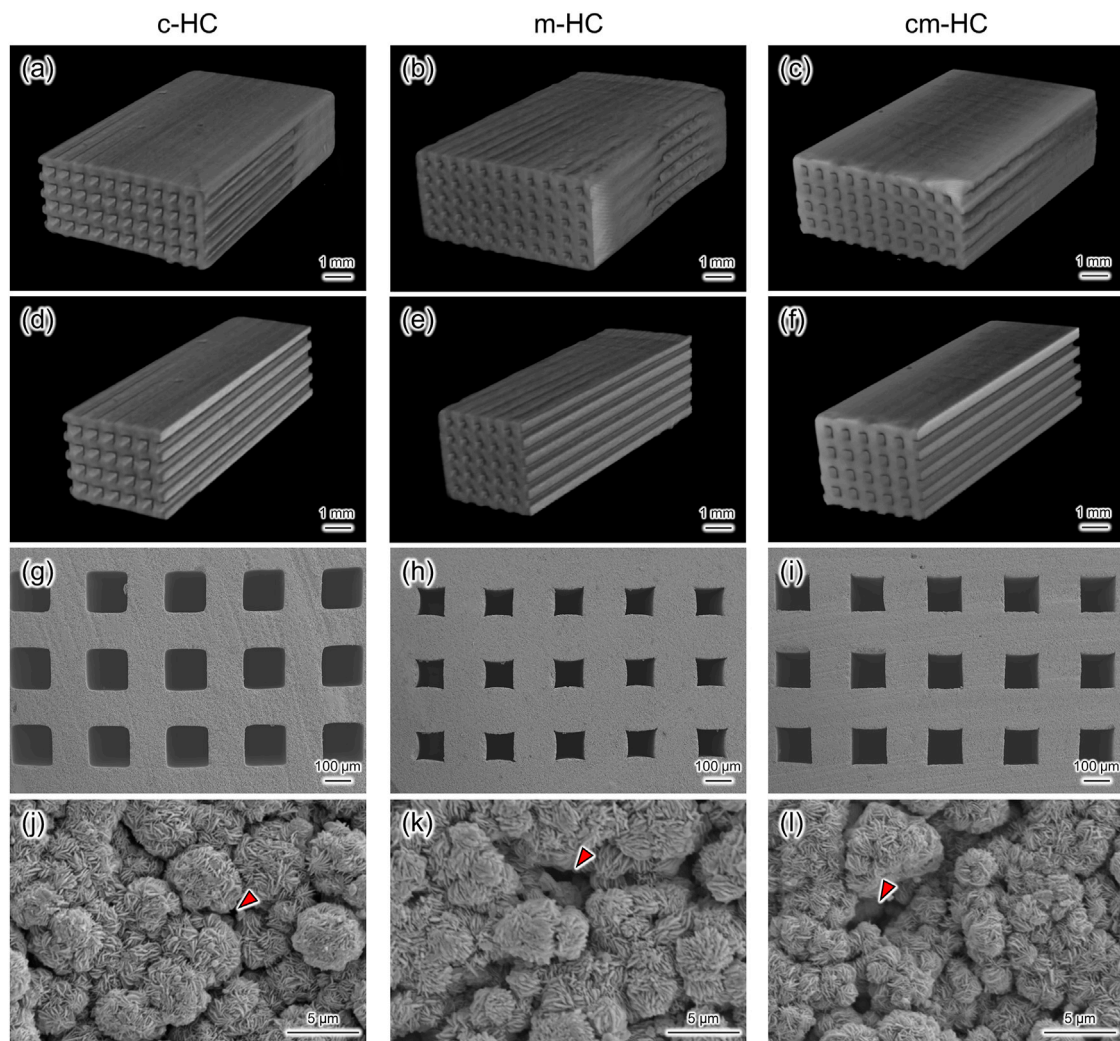


**FIGURE 1 |** Three-dimensional  $\mu$ -CT images of (A) c-HC, (B) m-HC, and (C) cm-HC. (D–F) Cross-sectional images of (A–C), respectively. SEM images in the channel aperture region of (G) c-HC, (H) m-HC, and (I) cm-HC at low magnification. SEM images in the struts region of (J) c-HC, (K) m-HC, and (L) cm-HC at high magnification. Red arrowheads show the micropores formed in the struts of CAP HC scaffolds.

considering a single cross-section along the ulnar shaft. The areas of the bones and blood vessels and the number of osteoclasts were estimated from the HE-stained tissue sections using a BZ-X digital analyzer (Keyence Corporation, Osaka, Japan). The multinucleated cells on the scaffold or bone were determined to be osteoclasts (Araújo et al. 2015). The relevant values were calculated using Eqs 5–8:

$$\text{BA/TA (\%)} = \frac{\text{(total area of bones formed in the defect)}}{\text{(total defect area)}} \times 100 \quad (5)$$

$$\text{BA/CMA (\%)} = \frac{\text{(total area of bones formed in the defect)}}{\text{(total area of channels and micropores)}} \times 100 \quad (6)$$

$$\text{BVA/TA (\%)} = \frac{\text{(area of the blood vessels)}}{\text{(total defect area)}} \times 100 \quad (7)$$

$$\begin{aligned} \text{Number of osteoclasts (cells/mm}^2\text{)} \\ = \text{(number of osteoclasts)} / \text{(total defect area)} \quad (8) \end{aligned}$$

## Statistical Analysis

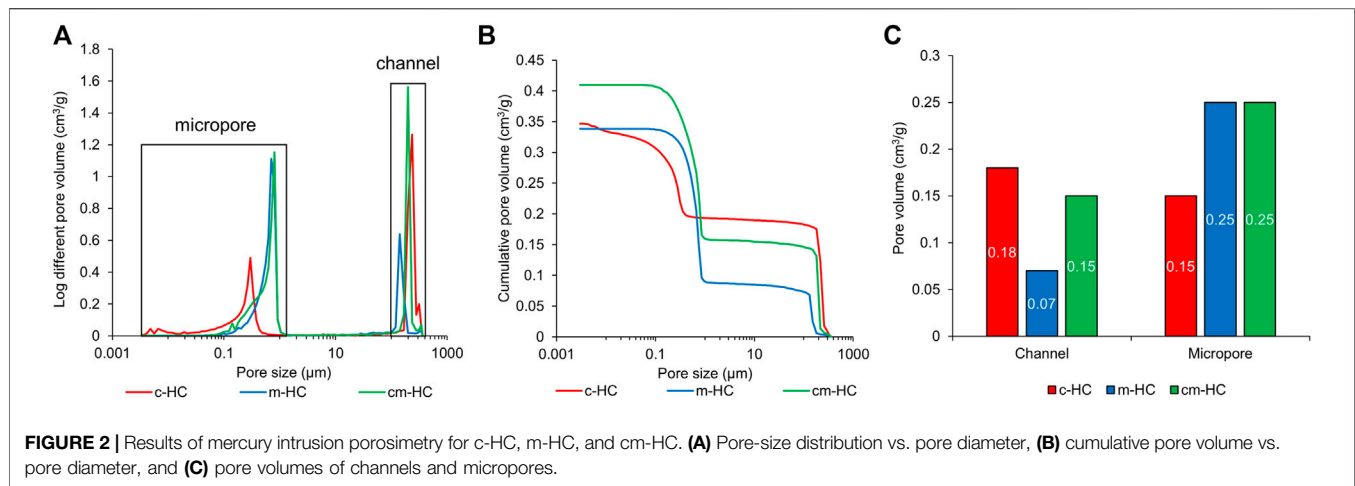
Statistical analysis was performed through a one-way analysis of variance followed by Tukey's test.  $p$ -value < 0.05 was considered statistically significant.

## RESULTS

### Physicochemical, Structural, and Mechanical Properties of CAP HC Scaffolds

In the XRD patterns, there were no  $\text{CaCO}_3$  (calcite) diffractions observed, whereas diffractions corresponding to apatite crystals were detected in all scaffolds (Supplementary Figure S2A). According to the FTIR spectra, the doublet carbonate bands were detected in the  $\nu_3$  regions of all scaffolds (Supplementary Figure S2B). Although the FTIR spectrum of



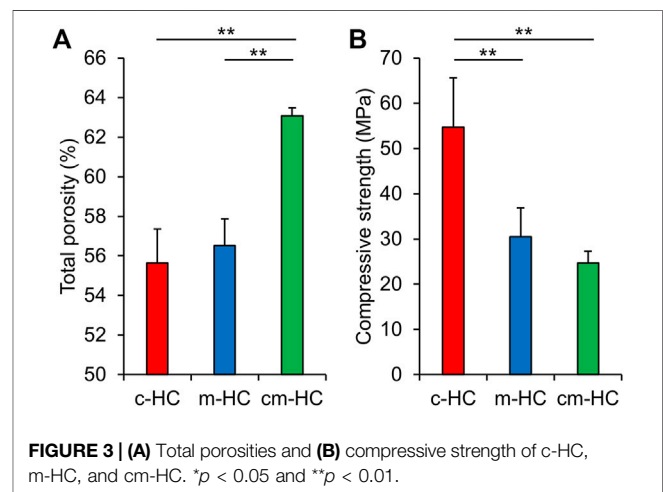


HAP presented a hydroxyl band at  $630\text{ cm}^{-1}$ , the FTIR spectrum of the CAP HC scaffolds did not exhibit this band (**Supplementary Figure S2B**). These results indicated that the chemical compositions of all scaffolds were AB-type CAP (Fleet et al., 2004). The CHN analysis highlighted that all scaffolds had a carbonate content of 13.0–14.8%, indicating their similar chemical compositions.

Uniformly sized channels uniaxially penetrated the scaffolds (**Figures 1A–I**). The channel aperture sizes of c-HC, m-HC, and cm-HC were  $292.2 \pm 4.7$ ,  $194.1 \pm 6.8$ , and  $259.1 \pm 2.8\text{ }\mu\text{m}$ , respectively. In particular, the channel aperture sizes were suitable for the ingrowth of bone and blood vessels ( $190\text{--}300\text{ }\mu\text{m}$ ) (Hayashi et al., 2020c, 2021d; Hayashi and Ishikawa 2021a). The sizes of the struts of c-HC, m-HC, and cm-HC were  $256.8 \pm 5.1$ ,  $320.7 \pm 6.0$ , and  $278.2 \pm 4.0\text{ }\mu\text{m}$ , respectively. Micropores were formed in the struts of all scaffolds (**Figures 1J–L**).

The pore volume and distribution were measured through mercury intrusion porosimetry. All scaffolds possessed pores of sizes greater than  $100\text{ }\mu\text{m}$  and less than  $1\text{ }\mu\text{m}$ , corresponding to the channels and micropores, respectively (**Figure 2A**). The channel volumes in c-HC, m-HC, and cm-HC were 0.18, 0.07, and  $0.15\text{ cm}^3/\text{g}$ , respectively (**Figures 2B,C**). The micropore volumes in c-HC, m-HC, and cm-HC were 0.15, 0.25, and  $0.25\text{ cm}^3/\text{g}$ , respectively (**Figures 2B,C**). Thus, the combined volume of the channels and micropores in c-HC ( $0.33\text{ cm}^3/\text{g}$ ) was nearly equal to that in m-HC ( $0.32\text{ cm}^3/\text{g}$ ), although the volume ratio between the channels and micropores was different. The combined volume of the channels and micropores in cm-HC was 25% larger than those in c-HC and m-HC.

The porosities of c-HC, m-HC, and cm-HC were  $55.7 \pm 1.7\%$ ,  $56.5 \pm 1.3\%$ , and  $63.1 \pm 0.5\%$ , respectively (**Figure 3A**). Thus, the porosity of c-HC was nearly equal to that of m-HC, whereas the porosity of cm-HC was significantly higher than those of c-HC and m-HC ( $p < 0.01$ ), consistent with the results of the mercury intrusion porosimetry. The compressive strength values for c-HC, m-HC, and cm-HC were  $54.7 \pm 10.9$ ,  $30.4 \pm 6.4$ , and  $24.7 \pm 2.6\text{ MPa}$ , respectively (**Figure 3B**). All scaffolds possessed a higher compressive strength than those of the scaffolds used for clinical treatment (Tanaka et al., 2008, 2018; Onodera et al.,



2014). Furthermore, the compressive strength of c-HC was significantly higher than those of m-HC and cm-HC ( $p < 0.01$ ), whereas those of m-HC and cm-HC were comparable. This finding indicated that the compressive strength was highly influenced by the presence of micropores in the struts than the channels.

## Radiographic Evaluation

Four weeks postoperatively, the proximal gap between the scaffold and the host bone was filled with new bones in c-HC and cm-HC, whereas both proximal and distal gaps were not observed in m-HC (**Figures 4A–C**). Twelve weeks postoperatively, both gaps were filled with new bones in all groups (**Figures 4D–F**). The intensity in c-HC did not vary visibly from four to 12 weeks postoperatively (**Figures 4A,D**), whereas that in m-HC and cm-HC decreased at 12 weeks postoperatively (**Figures 4B,C,E,F**), suggesting that m-HC and cm-HC were partially resorbed during 8 weeks. Four weeks and 12 weeks postoperatively, newly formed bones on the radius neither made contact with HC scaffolds nor got into the defects, indicating that scaffolds were not affected by the bones on the radius (**Figures 4A–F**).

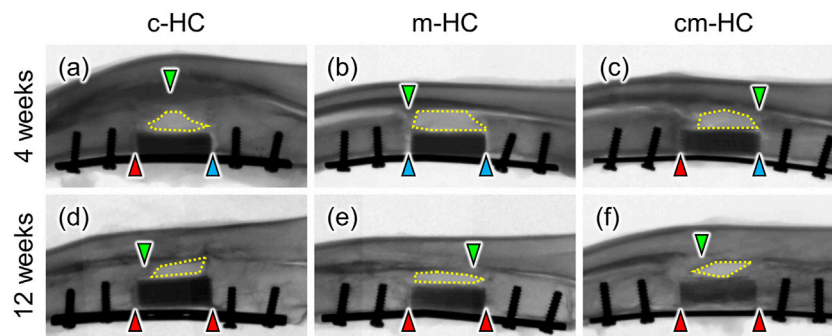


**FIGURE 4** | Typical radiographic images of **(A)** c-HC, **(B)** m-HC, and **(C)** cm-HC groups 4 weeks postoperatively and **(D)** c-HC, **(E)** m-HC, and **(F)** cm-HC groups 12 weeks postoperatively. The red arrowheads indicate osseointegration between the scaffold and host bones. The blue arrowheads indicate gaps between the scaffold and host bones. The green arrowheads indicate bone formation on the radius. The regions enclosed by yellow dotted lines are gaps between scaffolds and the radius. The left and right sides of the radiographs are the proximal ulna and the distal ulna, respectively.

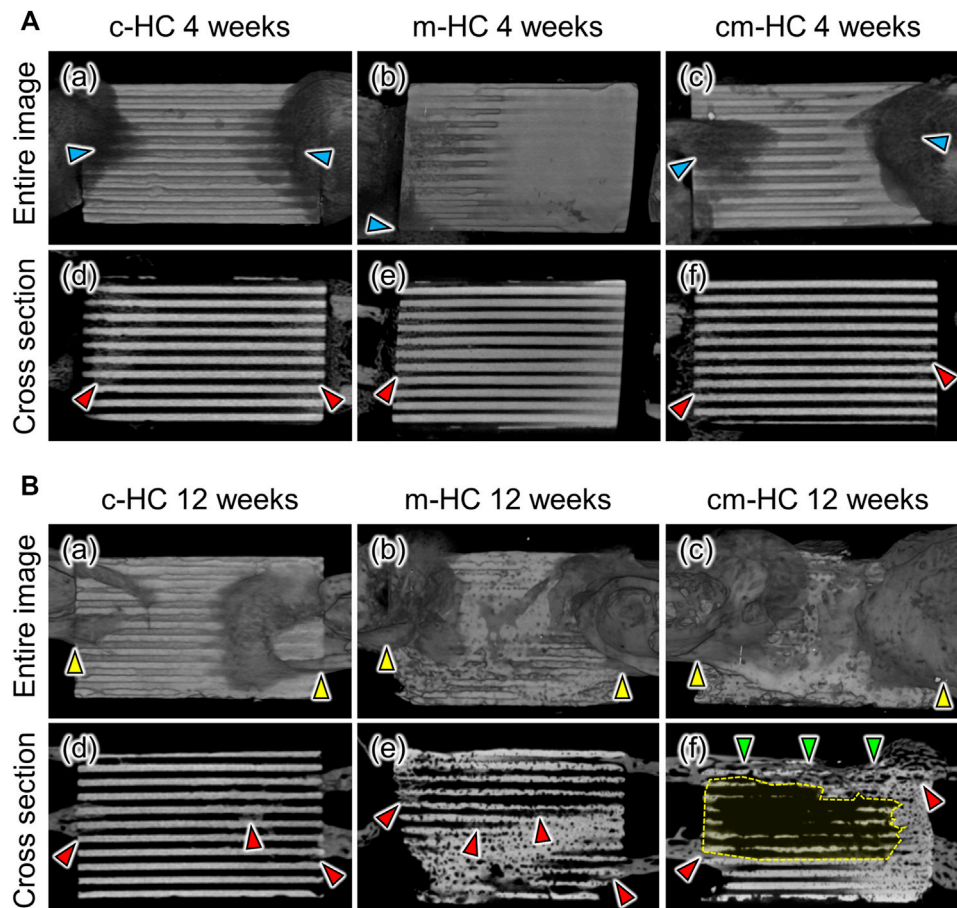
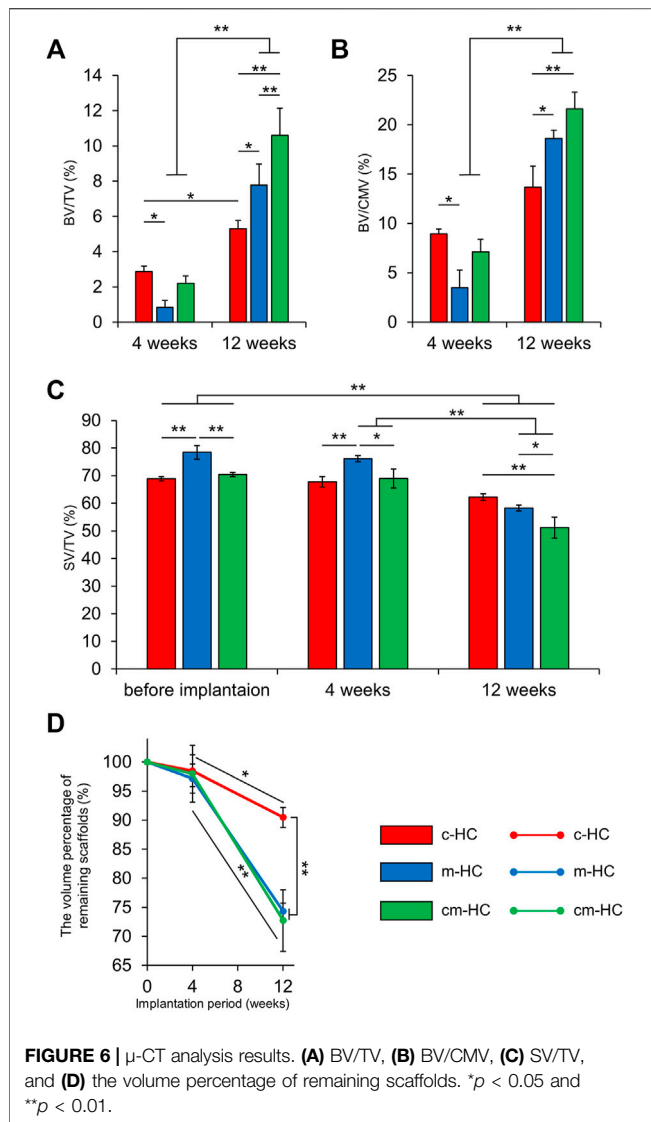


**FIGURE 5** | Typical  $\mu$ CT images of **(A,D)** c-HC, **(B,E)** m-HC, and **(C,F)** cm-HC groups **(A)** at 4 weeks postoperatively and **(B)** at 12 weeks postoperatively. The red, blue, yellow, and green arrowheads indicate new bone formation, bony calluses formed around the edge of scaffolds, osseointegration between the scaffold and host bones, and bony bridging in the defect, respectively. The regions enclosed by yellow dotted lines show that most of the channels were resorbed and began to be replaced by bone marrow.



## $\mu$ -CT Evaluation

Four weeks postoperatively, bony calluses were formed around the scaffolds (Figure 5Aa–c), and new bone tissues emerged in the regions between the stump of the host bone and the scaffold (Figure 5Ad–f). Notably, there was a significant formation of bony calluses and new bones for c-HC (Figure 5Aa,d). Clear scaffold resorption was not visualized, and the HC structure was maintained in all scaffolds.

Twelve weeks postoperatively, osseointegration was achieved in all groups (Figure 5Ba–c). In particular, new bone formation remarkably covered both edges of cm-HC (Figure 5Bc). In the case of c-HC, although the struts were slightly resorbed, the HC structure was maintained (Figure 5Bd). New bone was also partially formed within the channels. In the case of m-HC, the struts were resorbed and became thinner than those at 4 weeks (Figure 5Be). New bone was widely formed in the interior of the scaffold. In the case of cm-HC, the new bones formed on the surface and inside the scaffold in the regions corresponding to

the bone substance and consequently connected the separated host bones (Figure 5Bf). Furthermore, in the region corresponding to the bone marrow, the scaffold was extensively resorbed (Figure 5Bf). Thus, cm-HC was replaced with tissues similar to the actual bone in the SBD (Figure 5Bf).

BV/TV (%), BV/CMV (%), SV/TV, and the volume percentage of the remaining scaffolds (%) were calculated by analyzing the  $\mu$ -CT images (Figures 6A–D). The BV/TV values for c-HC, m-HC, and cm-HC were  $2.9 \pm 0.3\%$ ,  $0.8 \pm 0.4\%$ , and  $2.2 \pm 0.4\%$  4 weeks postoperatively, and  $5.3 \pm 0.5\%$ ,  $7.8 \pm 1.2\%$ , and  $10.6 \pm 1.5\%$  12 weeks postoperatively, respectively (Figure 6A). The BV/CMV values for c-HC, m-HC, and cm-HC were  $8.9 \pm 0.5\%$ ,  $3.5 \pm 1.8\%$ , and  $7.1 \pm 1.3\%$  4 weeks postoperatively and  $13.7 \pm 2.1\%$ ,  $18.6 \pm 0.8\%$ , and  $21.6 \pm 1.7\%$  12 weeks postoperatively, respectively (Figure 6B). SV/TV for c-HC, m-HC, and cm-HC were  $68.8 \pm 0.8\%$ ,  $78.4 \pm 2.5\%$ , and  $70.4 \pm 0.8\%$  before implantation,  $67.8 \pm 1.9\%$ ,  $76.2 \pm 1.1\%$ , and  $68.9 \pm 3.5\%$  4 weeks postoperatively, and  $62.2 \pm 1.2\%$ ,  $58.3 \pm 1.1\%$ , and  $51.2 \pm 3.7\%$  12 weeks postoperatively, respectively (Figure 6C). The volume percentages of the remaining scaffolds for c-HC, m-HC, and cm-HC were  $98.5 \pm 2.7\%$ ,  $97.2 \pm 2.5\%$ , and  $98.0 \pm 4.9\%$  4 weeks postoperatively and  $90.5 \pm 1.7\%$ ,  $74.3 \pm 1.4\%$ , and  $72.7 \pm 5.3\%$  12 weeks postoperatively, respectively (Figure 6D).

At 4 weeks postoperatively, the bone volume percentage in the c-HC group was higher than that in the m-HC group. There was no difference in the percentage of the scaffold resorption in all groups. At 12 weeks postoperatively, c-HC had the lowest percentage of scaffold resorption. The BV/CMV in c-HC showed no significant increase in 8 weeks, indicating the delayed bone formation relative to the scaffold resorption in the middle stage. Therefore, channels had a significant impact on early bone formation and poor impact on medium-term bone formation. The m-HC and cm-HC scaffolds showed significant increments of bone formation from four to 12 weeks postoperatively despite the significant scaffold resorption, indicating that the volume of the bones increased more than that of the scaffold resorption.

The findings indicated that the effect of the channels on bone formation was higher than that of the micropores 4 weeks postoperatively. The differences in the volumes of the channels and micropores did not affect the scaffold resorption. Twelve weeks postoperatively, the effect of the micropores on both scaffold resorption and bone formation was more notable than that of the channels.

## Histological Evaluations

Four weeks postoperatively, pronounced resorption of the scaffold was not observed for any scaffolds (Figures 7A–C), consistent with the  $\mu$ -CT image findings. New bones formed on the strut surfaces and blood vessels were formed within channels contacting the host bone (Figures 7D–F). However, in the regions where the scaffolds did not contact the host bone, fibrous tissues were formed within channels (Figures 7G–I). In all groups, osteoclasts were present on the scaffold struts (Figures 7J–L).



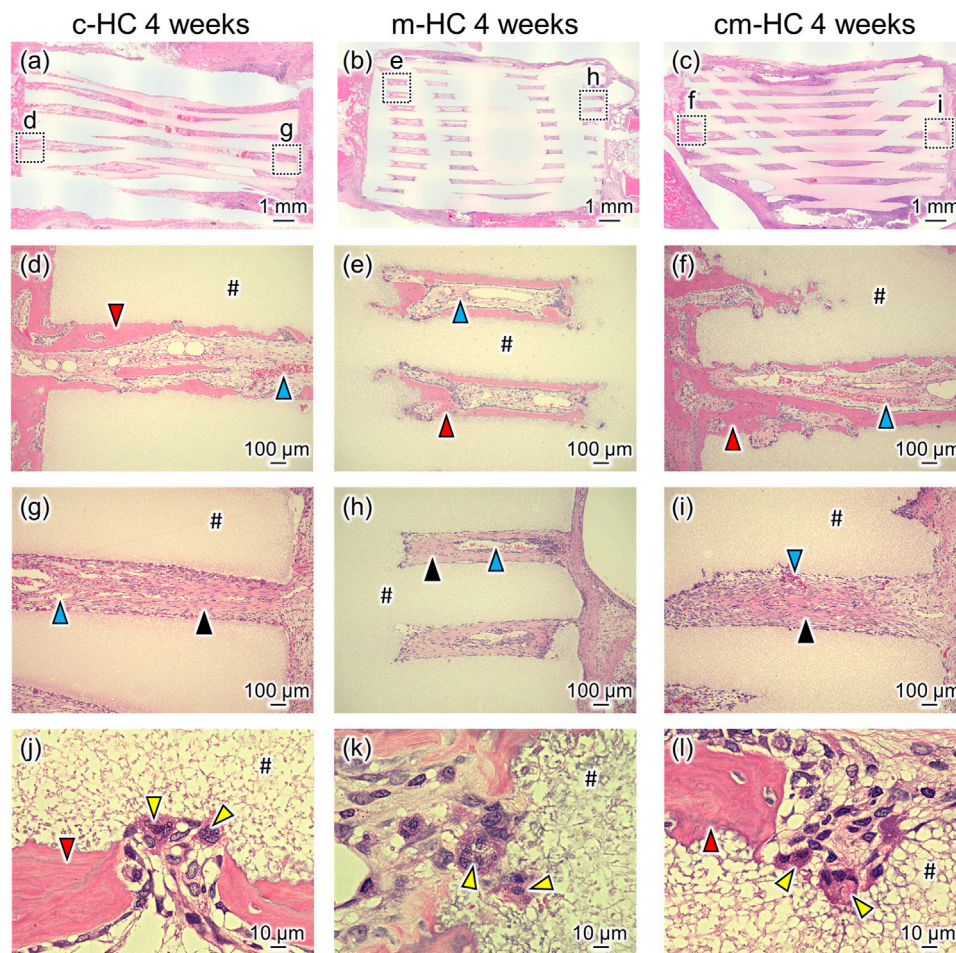


**FIGURE 7 |** Typical HE-stained images (A) c-HC, (B) m-HC, and (C) cm-HC groups 4 weeks postoperatively. Postoperatively, (D,G), (E,H), and (F,I) correspond to the low-magnification images of the region enclosed by dotted lines in (A–C), respectively; (J–L) are the high-magnification images of (D–F), respectively. The red, blue, yellow, and black arrowheads indicate mature bone inside the channel, blood vessel, osteoclast, and fibrous tissue, respectively. “#” indicates the material.

Twelve weeks postoperatively, m-HC and cm-HC were more extensively resorbed than c-HC (Figures 8A–C). In the case of c-HC, new bones were formed within the channels along the strut surface, whereas fibrous tissue was still observed within some channels at the aperture region (Figures 8D,G). In the case of m-HC, new bones were formed both on the strut surfaces and in the resorption lacunae formed in the struts (Figures 8E,H). However, as with c-HC, fibrous tissue was also observed within some channels at the aperture region (Figure 8H). The struts in cm-HC were more extensively replaced with new bones than those in m-HC. Few fibrous tissues were observed within channels at the aperture region (Figures 8F,I). Notably, bony bridging was observed between the host bones, and the scaffold corresponding to ulnar bone marrow was filled with bone marrow (Figure 8C and Supplementary Figure S3), suggesting bone remodeling in cm-HC. In terms of vascularization in the scaffold, well-developed blood vessels were observed in the edge region of the scaffolds, whereas in the central region of the scaffolds, thin blood vessels were observed within some channels at 4 weeks postoperatively

(Supplementary Figure S4A). Twelve weeks postoperatively, well-developed blood vessels were observed in both scaffold edge and central regions, notably in the cm-HC (Supplementary Figure S4B). In all scaffolds, osteoclasts were present on the strut surfaces (Figures 8J–L).

BA/TA, BA/CMA, BVA/TA, and the number of osteoclasts were calculated from the histological observations of the c-HC, m-HC, and cm-HC groups (Figures 9A–D). The BA/TA values for the c-HC, m-HC, and cm-HC groups were  $2.5 \pm 0.5\%$ ,  $0.6 \pm 0.8\%$ , and  $1.8 \pm 0.2\%$  4 weeks postoperatively; and  $5.6 \pm 2.0\%$ ,  $8.2 \pm 1.2\%$ , and  $12.4 \pm 4.5\%$  12 weeks postoperatively, respectively (Figure 9A). The BA/CMA values for the c-HC, m-HC, and cm-HC groups were  $8.8 \pm 2.4\%$ ,  $2.1 \pm 2.7\%$ , and  $5.6 \pm 0.8\%$  4 weeks postoperatively; and  $14.1 \pm 5.0\%$ ,  $19.5 \pm 3.1\%$ , and  $26.2 \pm 8.3\%$  12 weeks postoperatively, respectively (Figure 9B). BVA/TA for the c-HC, m-HC, and cm-HC groups were  $1.2 \pm 0.3\%$ ,  $1.2 \pm 0.1\%$ , and  $1.3 \pm 0.4\%$  4 weeks postoperatively; and  $4.9 \pm 0.7\%$ ,  $4.6 \pm 1.2\%$ , and  $7.6 \pm 0.9\%$  12 weeks postoperatively, respectively (Figure 9C). The numbers of osteoclasts for the c-HC, m-HC, and cm-HC groups were  $5.0 \pm 2.1$ ,  $4.5 \pm 2.3$ , and  $4.7 \pm 1.9$  cells/



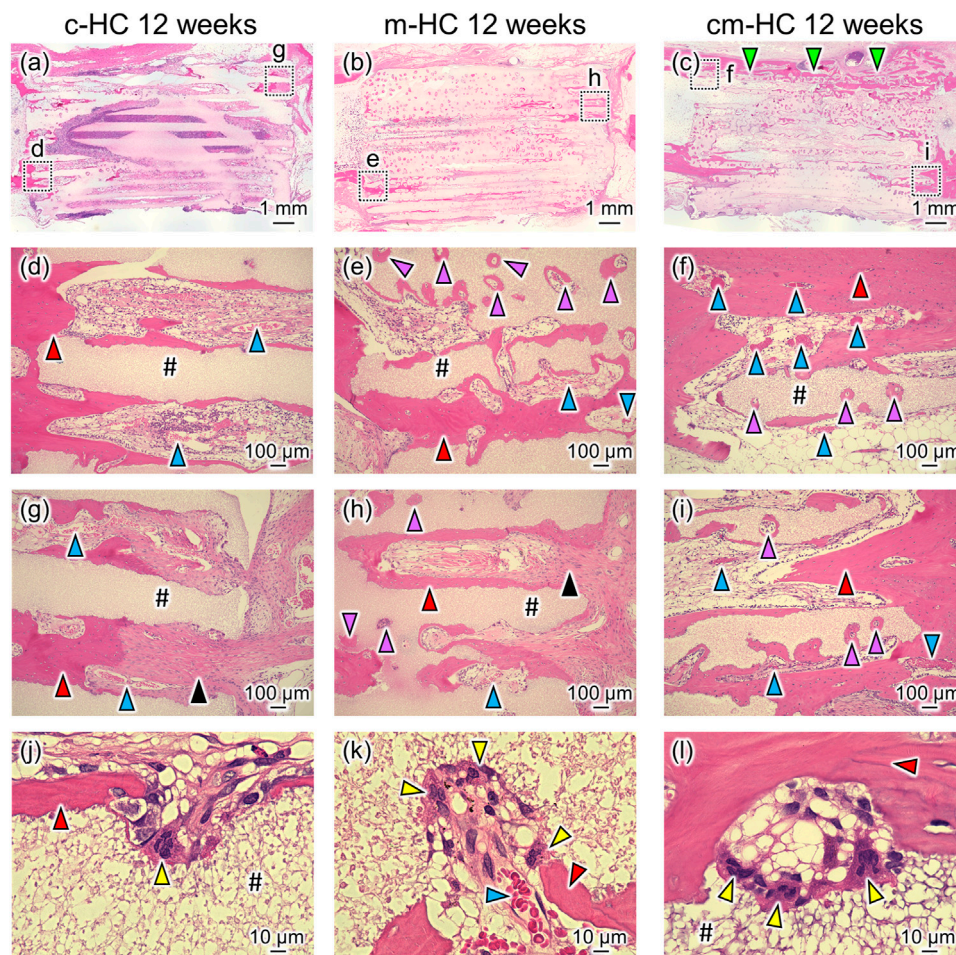


**FIGURE 8 |** Typical HE-stained images (A) c-HC, (B) m-HC, and (C) cm-HC groups 12 weeks postoperatively. Postoperatively, (D,G), (E,H), and (F,I) correspond to the low-magnification images of the region enclosed by dotted lines in (A–C), respectively; (J–L) are the high-magnification images of (D–F), respectively. The red, purple, blue, yellow, and black arrowheads indicate mature bone within the channel, mature bone in the resorption lacunae formed in the struts, blood vessel, osteoclast, and fibrous tissue, respectively; “#” indicates the material. The green arrowhead indicates the bony bridging in the defect.

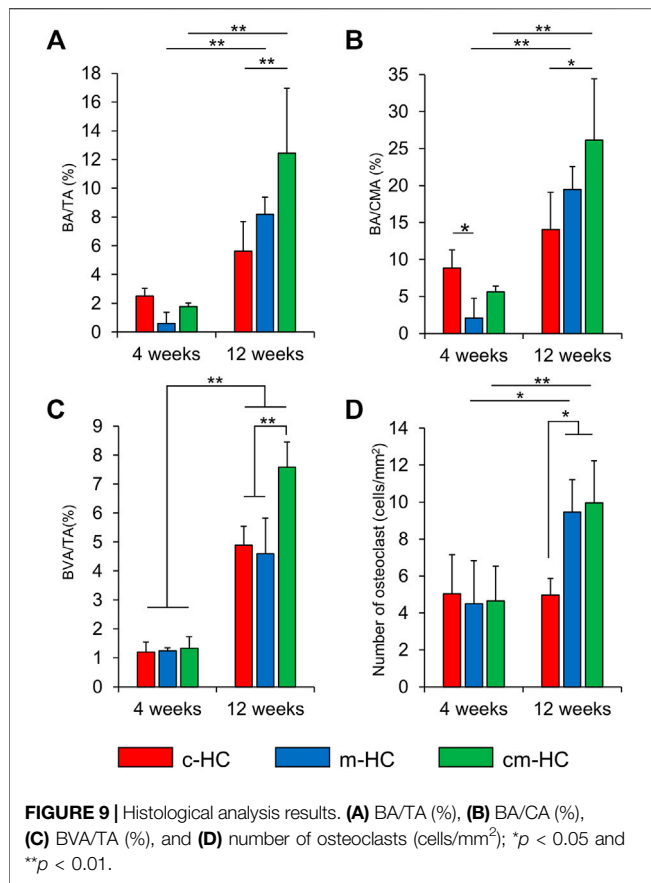
mm<sup>2</sup> 4 weeks postoperatively; and  $5.0 \pm 1.0$ ,  $9.5 \pm 1.8$ , and  $10.0 \pm 2.3$  cells/mm<sup>2</sup> 12 weeks postoperatively, respectively (Figure 9D).

Four weeks postoperatively, the bone area percentage in the channels and micropores of c-HC was significantly larger than that of m-HC ( $p < 0.05$ ), although there was no significant difference observed in the bone area percentage between c-HC and cm-HC. For all groups, the bone area percentages increased in 8 weeks. The increments in the m-HC and cm-HC groups were larger than that in the c-HC group. These results for the bone formation were highly consistent with that obtained from the  $\mu$ -CT analysis. The semiquantification of the vascularization indicated that the area of blood vessels increased in all groups from 4 weeks and 12 weeks postoperatively, and the increase in cm-HC at 12 weeks postoperatively was the highest among all the groups (Figure 9C). The numbers of osteoclasts were equal for all groups after 4 weeks. Twelve weeks postoperatively, the numbers of osteoclasts in the m-HC and cm-HC groups were significantly larger than those at 4 weeks; the same phenomenon was not observed for the c-HC group. The abovementioned *in vivo* results

demonstrated that the channels promoted the bone ingrowth in the early stage, and the micropores promoted the scaffold resorption, bone formation, and replacement of the HC scaffolds with new bone in the medium term.

## DISCUSSION

The obtained findings demonstrated that the channels promoted bone ingrowth in the early stage, and the micropores promoted the scaffold resorption by osteoclasts, bone formation, and replacement of scaffolds with new bone in the medium term. Thus, the influence of the channels and micropores was different at different time points in the SBD reconstruction. In addition, when the scaffolds had both suitable channel and micropore volumes, they were successfully replaced with new bone. The roles of the channels and micropores in the HC scaffold for the biological responses in SBD reconstruction are discussed in detail below.



For the channel effects, we previously reported the ability of CAP HC scaffolds to reconstruct SBD with a channel aperture size of 146  $\mu\text{m}$ , a channel volume of 0.16  $\text{cm}^3/\text{g}$ , and a micropore volume of 0.17  $\text{cm}^3/\text{g}$  using the same animal experiment as that in this study (Hayashi and Ishikawa 2021a; Shibahara et al., 2021). Thus, the channel aperture size of the CAP HC scaffolds used in our previous study was half that of c-HC in the present study, whereas these two HC scaffolds had nearly equal channel and micropore volumes. Importantly, the amount of the new bone was equal for these two HC scaffolds. The above results demonstrated that bone ingrowth in the early stage was affected by the channel volume rather than the channel size, when the channel size was suitable for promoting the bone ingrowth into the scaffold ( $>100 \mu\text{m}$ ) (Karageorgiou and Kaplan 2005; Perez and Mestres 2016; Bobbert and Zadpoor 2017; Abbasi et al., 2020).

For the effects of the micropores on the biological responses in SBD reconstruction, the size of the micropores used in this study was less than 1  $\mu\text{m}$ . Although micropores less than 1  $\mu\text{m}$  did not directly promote bone ingrowth in the early stage, they promoted osteoclastogenesis followed by osteoclast–osteoblast interactions (Cappariello et al., 2014; Bohner et al., 2017; Hayashi et al., 2019a; Hayashi and Ishikawa 2020a; Kim et al., 2020). Osteoclastogenesis requires longer time than bone ingrowth into the scaffold *via* channels. This can be attributed to the micropore effects for SBD reconstruction in the middle stage.

Finally, we discuss the effects of the combined channels and micropores on the biological responses in SBD reconstruction. This study demonstrated that CAP HC scaffold with suitable volumes of channels and micropores exhibited superior osteoconductivity and scaffold replacement ability with new bones and bone marrow compared to scaffolds with suitable volume of either channels or micropores. In the case of cm-HC, most of the fibrous tissues within channels at the aperture region were replaced with new bones during 8 weeks. Meanwhile, in the case of c-HC and m-HC, fibrous tissues were still observed within some channels at the aperture region at 12 weeks postoperatively, suggesting that c-HC and m-HC did not achieve biomechanically stable states in SBDs owing to their low osteoconductivities, and bone remodeling did not start yet. Therefore, scaffolds with insufficient volume of channels or micropores are likely to delay the initiation of bone remodeling in SBDs. Zhang et al. (2017) reported the reconstruction of 10-mm-long SBDs in a rabbit radius using hollow-pipe-packed silicate and  $\beta$ -TCP scaffolds with channels having an aperture size of 500  $\mu\text{m}$ . Although the new bone areas in these hollow-pipe-packed scaffolds at 12 weeks postoperatively were comparable to that in cm-HC in the present study, there were inadequate remnants of the hollow-pipe-packed scaffolds, and they were not replaced with the new bone (Zhang et al., 2017). This phenomenon likely occurred because of the overlooked importance of the micropores. Furthermore, the area of blood vessels in the CAP HC scaffold with suitable volumes of channels and micropores was the highest at 12 weeks postoperatively. Vascularization is a crucial finding because it can contribute to bone remodeling (Lafage-Proust et al., 2015). One of the reasons for the progression of bone remodeling in cm-HC was inferred to be the favorable vascularization in the scaffold. Although this study was unable to reveal whether channels or micropores had a greater impact on scaffold vascularization, the results in this study suggested that lack of volume for either channels or micropores might cause delayed vascularization in HC scaffolds, subsequently delaying bone remodeling. In detail, the above findings highlighted the roles of the channels and micropores, which indicated that the control of both channels and micropores is necessary to achieve scaffold replacement with new bones and bone marrow.

Although the present study did not focus on the channel shape, several researchers reported their effects on bone formation. Particularly, there have been several reports that a rectangular pore shape provides an intermediate effect on bone formation among various shapes, suggesting its unsuitability (VanBael et al., 2012; Entezari et al., 2019). VanBael et al. (2012) investigated the effect of three types of Ti6Al4V scaffolds with different pore shapes (triangular, rectangular, and hexagonal) on the proliferation and differentiation of human periosteum-derived cell cultures (hPDCs). They demonstrated the highest alkaline phosphatase (ALP) activity in the Ti6Al4V scaffolds with triangle pores, whereas those with rectangular and hexagonal pores were comparable. In addition, the amount of pore occlusion with hPDCs in the hexagonal pores was larger than that in other pore shapes, thereby decreasing the open space for cell distribution in hexagonal pores. Furthermore,

Entezari et al. (2019) reported that strontium–Hardystonite–Gahnite scaffolds with quatrefoil-shaped channels provided a larger bone volume in the bone defect of rabbit calvaria and higher effective stiffness after implantation in the defect than those with rectangular channels. The abovementioned findings suggest that the bone formation ability of rectangular channels is presumed to be equal or superior to those of hexagonal channels, and inferior to those of triangle and quatrefoil-shaped channels.

The present study revealed that the mechanical strength of HC scaffolds depended on the micropore volume rather than the channel volume. Owing to the presence of micropores in the struts of HC scaffolds, the increase in the micropore volume decreased the strut robustness (Cordell et al., 2009; Ali et al., 2017). Furthermore, in HC scaffolds, the channels and struts were arranged parallel to one another; thereby, the struts were not separated by the channels and completely continuous. Owing to these reasons, even though the pore volume ( $\sim 0.3 \text{ cm}^3/\text{g}$ ) and porosity ( $\sim 56\%$ ) in c-HC and m-HC were approximately equal, c-HC possessed higher mechanical strength than m-HC. Nevertheless, if the channels and struts were not arranged in parallel, the influence of the channels on the compressive strength was considerably high. In fact, even though the scaffold channels are unidirectional, the scaffold had a low compressive strength when the channels and struts were not parallel. For example, the compressive strengths of the unidirectional porous HAp and  $\beta$ -TCP scaffolds were 14 and 8 MPa, respectively, because the struts were discontinuous and separated (Makihara et al., 2018; Kumagai et al., 2019). Thus, owing to the HC structure, the HC scaffolds in this study minimally suppressed the strength reduction by increasing the channel volume. Consequently, the influence of the micropore volume was proportionally high.

Several researchers have attempted to reconstruct SBDs using MSCs or bone morphogenesis proteins (BMPs) in combination with scaffolds (Rathbone et al., 2014; Akilbekova et al., 2018). Rathbone et al. (2014) combined 3D porous hydroxyapatite scaffolds and MSCs for reconstructing 10-mm-long SBDs of the rabbit radius. Despite being combined with MSCs, the SBDs were not reconstructed, although the scaffolds with MSCs corresponded to a higher rate of bone healing compared to those without MSCs 2 weeks postoperatively. Akilbekova et al. (2018) used heparin-conjugated fibrin hydrogel scaffolds with BMPs for the reconstruction of 10-mm-long SBDs in the rabbit radius. The sole scaffold could not heal the defect. In contrast, the combined scaffolds and BMPs could connect the stumps of the host bone 12 weeks postoperatively. Thus, MSCs and BMPs have minimal and significant effect on bone regeneration, respectively. Notably, the use of MSCs and BMPs increases the treatment cost and involves concerns regarding safety, such as carcinogenesis and immune responses (Lukomska et al., 2019; Ramly et al., 2019). Furthermore, in existing studies on combined scaffolds and MSCs or BMPs, a cell-shielding membrane was not placed between the radius and the ulna (Rathbone et al., 2014; Akilbekova et al., 2018). In previous studies that achieved the formation of new bone connecting the stumps of the host bone in 10-mm-long SBDs, the efficacy of scaffolds was evaluated without using a cell-

shielding membrane (Zhang et al., 2017; Chu et al., 2018; Tovar et al., 2018). In these cases, as new bone was formed from the radius (Bodde et al., 2008), new bone formation merely from the ulna might not be evaluated precisely. In this study, we placed the cell-shielding membrane to accurately evaluate the bone formation from the ulna, which rendered bone reconstruction more challenging than that without a cell-shielding membrane (Elbackly et al., 2015; Shibahara et al., 2021). Despite the more challenging evaluation environment, cm-HC in this study achieved the reconstruction of SBDs. Thus, the optimization of the channels and micropores can promote the efficacy of SBD reconstruction than the combined use of MSCs or BMPs. These findings can facilitate the development of scaffolds with a high ability of reconstructing SBDs without sacrificing cost and safety.

As a scaffold with similar HC structure, Osteopore® (Osteopore International Pte Ltd.), which is composed of polycaprolactone (PCL) and TCP (PCL:TCP = 80 wt%:20 wt%) and fabricated by three-dimensional printing, is well known (Rai et al., 2005, 2007; Bae et al., 2011; Lim et al., 2011; Holzapfel et al., 2019; Kobbe et al., 2020; Henkel et al., 2021). Researchers have attempted to reconstruct critical-sized SBDs using Osteopore® (Rai et al., 2005, 2007; Bae et al., 2011; Lim et al., 2011; Holzapfel et al., 2019; Kobbe et al., 2020; Henkel et al., 2021). Osteopore® combined with platelet-rich plasma (PRP) or BMPs or autografts successfully connected the stumps of the host bone with the new bone in animal studies and clinical trials (Rai et al., 2007; Bae et al., 2011; Lim et al., 2011; Holzapfel et al., 2019; Kobbe et al., 2020; Henkel et al., 2021). However, when Osteopore® alone was implanted in a critical-sized SBD, the stumps of the host were not fully connected during 12 weeks postoperatively (Rai et al., 2007; Bae et al., 2011). The results can be attributed to the absence of osteoconductivity of PCL, which was the main component of the composite HC scaffolds, resulting in the inflammatory response in the body (Xiao et al., 2012; Hasan et al., 2018). CAP has superior biocompatibility, osteoconductivity, and bioresorbability among several calcium phosphates (Ishikawa et al., 2018; Hayashi et al., 2019b, 2020b), and does not elicit any inflammatory response during resorption. Furthermore, Osteopore® was also burdened by the limitations of the mechanical strength. In detail, the compressive strength of Osteopore® was approximately 6.4 MPa (Rai et al., 2007; Bae et al., 2011; Lim et al., 2011), whereas that of CAP HC scaffolds in this study was at least 22 MPa. In general, the compressive strengths of the scaffolds fabricated by 3D printing are lower than those by extrusion molding (Hayashi et al., 2021c). Therefore, in terms of mechanical strength, CAP HC scaffolds are expected to be more advantageous than Osteopore®.

Although CAP HC scaffolds are promising for critical-size SBD reconstruction, there are several limitations in this study. First, this study did not evaluate the biomechanical strengths of the bones reconstructed by the CAP HC scaffolds. However, all CAP HC scaffolds used in this study did not crack until 12 weeks postoperatively, suggesting their sufficient biomechanical strengths required for SBD treatment. Second, the volume of bone newly formed in HC scaffolds was still low at 12 weeks postoperatively. However, the scaffolds occupied more than half of the defects in any observation period (Figure 6C).



Consequently, the volume of tissues within the scaffold was less than half the volume of defects even if the scaffold was fully filled with regenerated tissues. In addition, the HC scaffolds did not fully cover the stumps of host bones (**Supplementary Figure S5**). In this environment, the average bone volume in the cm-HC was 10.6% at 12 weeks postoperatively. The volume percentage of the ulnar cortical bone in the diaphysis of the ulna is  $35.2 \pm 2.7\%$  (**Supplementary Figure S6**). Therefore, cm-HC reconstructed approximately 30% of the ulna at 12 weeks postoperatively. We would like to clarify that HC scaffolds might be further replaced by bones in a long observation period in our future research. Third, the results of this study were obtained from experiments using small animals, i.e., rabbits, which may not perfectly correspond to the results obtained by preclinical experiments using large animals, such as sheep and pigs. As the bones of a large animal have higher similarity to human bones than those of small animals (Reichert et al., 2009; McGovern et al., 2018), experiments using large animals are preferred for preclinical experiments. Nevertheless, previous studies using Osteopore® demonstrated that the experimental results of small animal models can infer findings for large animal models (Rai et al., 2007; Bae et al., 2011; Lim et al., 2011; Henkel et al., 2021). Nonetheless, Osteopore® alone could not reconstruct critical-sized SBDs regardless of the animal size or species, i.e., rat, rabbit, or pig (Rai et al., 2007; Bae et al., 2011; Lim et al., 2011). To achieve reconstruction, the combination of Osteopore® and PRP or BMPs or autografts was necessary (Rai et al., 2007; Bae et al., 2011; Lim et al., 2011; Henkel et al., 2021). Although the results of experiments using small animals are not entirely consistent with those of experiments using large animals, they are useful for predicting the benefits of the scaffold. In our present study, CAP HC scaffolds with suitable volumes of the channels and micropores achieved the formation of new bone connecting the stumps of the host bone in critical-sized SBDs in the rabbit ulna. This result suggests the applicability of the CAP HC scaffolds for the reconstruction of critical-sized SBDs in large animals. To verify this inference, the efficacy of CAP HC scaffolds for the reconstruction of critical-sized SBDs in large animals will be evaluated in future research.

## CONCLUSION

In this study, three types of HC scaffolds were fabricated using extrusion molding. HC scaffolds with a larger volume of the channels than that of the micropores promoted bone ingrowth in the early stage (4 weeks postoperatively). Meanwhile, HC scaffolds with a larger volume of the micropores than that of the channels promoted scaffold resorption by osteoclasts, bone

formation, and replacement of scaffolds with new bone in the medium term (12 weeks postoperatively). Thus, channels and micropores exerted different effects at different time points in SBD reconstruction. In addition, HC scaffolds with large volumes of both channels and micropores achieved replacement with new bone. The presented findings can help clarify the effect of channels and micropores, and their combination on SBD reconstruction, thereby facilitating the development of scaffolds with superior abilities.

## DATA AVAILABILITY STATEMENT

The original contributions presented in the study are included in the article/**Supplementary Material**, further inquiries can be directed to the corresponding author.

## ETHICS STATEMENT

The animal study was reviewed and approved by Animal Care and Use Committee of Kyushu University (Approval no. A21-010-0).

## AUTHOR CONTRIBUTIONS

KS performed the experiments, collected raw data, analyzed the data, prepared the figures for the manuscript, and wrote the initial draft. KH conceived and supervised the project and reviewed and edited the manuscript. YN and KI managed the project. All authors have read and agreed to the published version of the manuscript.

## FUNDING

This study was supported, in part, by the Japan Agency for Medical Research and Development (AMED) under grant nos. JP20lm0203123h, JP21im0502004h, and JP21he0422005j and by the Japan Society for the Promotion of Science (JSPS) under grant no. JP19K22970.

## SUPPLEMENTARY MATERIAL

The Supplementary Material for this article can be found online at: <https://www.frontiersin.org/articles/10.3389/fbioe.2022.825831/full#supplementary-material>

## REFERENCES

- Abbasi, N., Hamlet, S., Love, R. M., and Nguyen, N.-T. (2020). Porous Scaffolds for Bone Regeneration. *J. Sci. Adv. Mater. Devices* 5, 1–9. doi:10.1016/j.jsam.2020.01.007
- Akilbekova, D., Ogay, V., Yakupov, T., Sarsenova, M., Umbayev, B., Nurakhmetov, A., et al. (2018). Brillouin Spectroscopy and Radiography for Assessment of

- Viscoelastic and Regenerative Properties of Mammalian Bones. *J. Biomed. Opt.* 23, 1. doi:10.1117/1.jbo.23.9.097004
- Ali, M. S., Mohamed Ariff, A. H., Jaafar, C. N. A., Tahir, S. M., Mazlan, N., Maori, K. A., et al. (2017). *Factors Affecting the Porosity and Mechanical Properties of Porous Ceramic Composite Materials*. Elsevier. doi:10.1016/b978-0-12-803581-8.10131-6
- Alluri, R., Song, X., Bougioukli, S., Pannell, W., Vakhshori, V., Sugiyama, O., et al. (2019). Regional Gene Therapy with 3D Printed Scaffolds to Heal Critical Sized



- Bone Defects in a Rat Model. *J. Biomed. Mater. Res.* 107, 2174–2182. doi:10.1002/jbm.a.36727
- Araújo, A. S., Fernandes, A. B. N., Maciel, J. V. B., Netto, J. d. N. S., and Bolognese, A. M. (2015). New Methodology for Evaluating Osteoclastic Activity Induced by Orthodontic Load. *J. Appl. Oral Sci.* 23, 19–25. doi:10.1590/1678-775720140351
- Bae, J.-H., Song, H.-R., Kim, H.-J., Lim, H.-C., Park, J.-H., Liu, Y., et al. (2011). Discontinuous Release of Bone Morphogenetic Protein-2 Loaded within Interconnected Pores of Honeycomb-like Polycaprolactone Scaffold Promotes Bone Healing in a Large Bone Defect of Rabbit Ulna. *Tissue Eng. A* 17, 2389–2397. doi:10.1089/ten.tea.2011.0032
- Bezstarosti, H., Metsemakers, W. J., van Lieshout, E. M. M., Voskamp, L. W., Kortram, K., McNally, M. A., et al. (2021). Management of Critical-Sized Bone Defects in the Treatment of Fracture-Related Infection: a Systematic Review and Pooled Analysis. *Arch. Orthop. Trauma Surg.* 141, 1215–1230. doi:10.1007/s00402-020-03525-0
- Bobbert, F. S. L., and Zadpoor, A. A. (2017). Effects of Bone Substitute Architecture and Surface Properties on Cell Response, Angiogenesis, and Structure of New Bone. *J. Mater. Chem. B* 5, 6175–6192. doi:10.1039/c7tb00741h
- Bodde, E. W. H., Spauwen, P. H. M., Mikos, A. G., and Jansen, J. A. (2008). Closing Capacity of Segmental Radius Defects in Rabbits. *J. Biomed. Mater. Res.* 85A, 206–217. doi:10.1002/jbm.a.31549
- Bohner, M., Baroud, G., Bernstein, A., Döbelin, N., Galea, L., Hesse, B., et al. (2017). Characterization and Distribution of Mechanically Competent Mineralized Tissue in Micropores of  $\beta$ -tricalcium Phosphate Bone Substitutes. *Mater. Today* 20, 106–115. doi:10.1016/j.mattod.2017.02.002
- Boussein, M. L., Boyd, S. K., Christiansen, B. A., Guldberg, R. E., Jepsen, K. J., and Müller, R. (2010). Guidelines for Assessment of Bone Microstructure in Rodents Using Micro-computed Tomography. *J. Bone Miner. Res.* 25, 1468–1486. doi:10.1002/jbmr.141
- Cappariello, A., Maurizi, A., Veeriah, V., and Teti, A. (2014). The Great Beauty of the Osteoclast. *Arch. Biochem. Biophys.* 558, 70–78. doi:10.1016/j.abb.2014.06.017
- Chu, L., Jiang, G., Hu, X.-L., James, T. D., He, X.-P., Li, Y., et al. (2018). Osteogenesis, Vascularization and Osseointegration of a Bioactive Multiphase Macroporous Scaffold in the Treatment of Large Bone Defects. *J. Mater. Chem. B* 6, 4197–4204. doi:10.1039/c8tb00766g
- Cordell, J. M., Vogl, M. L., and Wagoner Johnson, A. J. (2009). The Influence of Micropore Size on the Mechanical Properties of Bulk Hydroxyapatite and Hydroxyapatite Scaffolds. *J. Mech. Behav. Biomed. Mater.* 2, 560–570. doi:10.1016/j.jmbbm.2009.01.009
- Doi, Y., Shibutani, T., Moriwaki, Y., Kajimoto, T., and Iwayama, Y. (1998). Sintered Carbonate Apatites as Bioresorbable Bone Substitutes. *J. Biomed. Mater. Res.* 39, 603–610. doi:10.1002/(sici)1097-4636(19980315)39:4<603aid-jbm15>3.0.co;2-7
- El Backly, R. M., Chiapale, D., Muraglia, A., Tromba, G., Ottonello, C., Santolini, F., et al. (2015). A Modified Rabbit Ulna Defect Model for Evaluating Periosteal Substitutes in Bone Engineering: A Pilot Study. *Front. Bioeng. Biotechnol.* 2, 1–8. doi:10.3389/fbioe.2014.00080
- Entezari, A., Roohani, I., Li, G., Dunstan, C. R., Rognon, P., Li, Q., et al. (2019). Architectural Design of 3D Printed Scaffolds Controls the Volume and Functionality of Newly Formed Bone. *Adv. Healthc. Mater.* 8, 1801353. doi:10.1002/adhm.201801353
- Feng, Y.-F., Wang, L., Li, X., Ma, Z.-S., Zhang, Y., Zhang, Z.-Y., et al. (2012). Influence of Architecture of  $\beta$ -Tricalcium Phosphate Scaffolds on Biological Performance in Repairing Segmental Bone Defects. *PLoS ONE* 7, e49955. doi:10.1371/journal.pone.0049955
- Fleet, M. E., Liu, X., and King, P. L. (2004). Accommodation of the Carbonate Ion in Apatite: An FTIR and X-ray Structure Study of Crystals Synthesized at 2–4 GPa. *Am. Mineral.* 89, 1422–1432. doi:10.2138/am-2004-1009
- Gibson, I. R., and Bonfield, W. (2001). Novel Synthesis and Characterization of an AB-type Carbonate-Substituted Hydroxyapatite. *J. Biomed. Mater. Res.* 59, 697–708. doi:10.1002/jbm.10044
- Hasan, A., Byambaa, B., Morshed, M., Cheikh, M. I., Shakoore, R. A., Mustafy, T., et al. (2018). Advances in Osteobiologic Materials for Bone Substitutes. *J. Tissue Eng. Regen. Med.* 12, 1448–1468. doi:10.1002/term.2677
- Hayashi, K., and Ishikawa, K. (2020a). Effects of Nanopores on the Mechanical Strength, Osteoclastogenesis, and Osteogenesis in Honeycomb Scaffolds. *J. Mater. Chem. B* 8, 8536–8545. doi:10.1039/d0tb01498b
- Hayashi, K., and Ishikawa, K. (2021b). Honeycomb Scaffolds Capable of Ectopic Osteogenesis: Histological Evaluation of Osteoinduction Mechanism. *Nano Select* 3, 60–77. doi:10.1002/nano.202000283
- Hayashi, K., and Ishikawa, K. (2021a). Honeycomb Scaffolds Fabricated Using Extrusion Molding and the Sphere-Packing Theory for Bone Regeneration. *ACS Appl. Bio Mater.* 4, 721–730. doi:10.1021/acsabm.0c01279
- Hayashi, K., Kato, N., Kato, M., and Ishikawa, K. (2021c). Impacts of Channel Direction on Bone Tissue Engineering in 3D-Printed Carbonate Apatite Scaffolds. *Mater. Des.* 204, 109686. doi:10.1016/j.matdes.2021.109686
- Hayashi, K., Kishida, R., Tsuchiya, A., and Ishikawa, K. (2019a). Carbonate Apatite Micro-Honeycombed Blocks Generate Bone Marrow-Like Tissues as Well as Bone. *Adv. Biosys.* 3, 1900140. doi:10.1002/adbi.201900140
- Hayashi, K., Kishida, R., Tsuchiya, A., and Ishikawa, K. (2020b). Granular Honeycombs Composed of Carbonate Apatite, Hydroxyapatite, and  $\beta$ -Tricalcium Phosphate as Bone Graft Substitutes: Effects of Composition on Bone Formation and Maturation. *ACS Appl. Bio Mater.* 3, 1787–1795. doi:10.1021/acsabm.0c00060
- Hayashi, K., Kishida, R., Tsuchiya, A., and Ishikawa, K. (2019b). Honeycomb Blocks Composed of Carbonate Apatite,  $\beta$ -tricalcium Phosphate, and Hydroxyapatite for Bone Regeneration: Effects of Composition on Biological Responses. *Mater. Today Bio* 4, 100031. doi:10.1016/j.mtbio.2019.100031
- Hayashi, K., Munar, M. L., and Ishikawa, K. (2020c). Effects of Macropore Size in Carbonate Apatite Honeycomb Scaffolds on Bone Regeneration. *Mater. Sci. Eng. C* 111, 110848. doi:10.1016/j.msec.2020.110848
- Hayashi, K., Shimabukuro, M., and Ishikawa, K. (2022). Antibacterial Honeycomb Scaffolds for Achieving Infection Prevention and Bone Regeneration. *ACS Appl. Mater. Inter.* 14, 3762–3772. doi:10.1021/acsami.1c20204
- Hayashi, K., Shimabukuro, M., Kishida, R., Tsuchiya, A., and Ishikawa, K. (2021d). Honeycomb Scaffolds Capable of Achieving Barrier Membrane-free Guided Bone Regeneration. *Mater. Adv.* 2, 7638–7649. doi:10.1039/d1ma00698c
- Hayashi, K., Shimabukuro, M., Kishida, R., Tsuchiya, A., and Ishikawa, K. (2022e). Structurally Optimized Honeycomb Scaffolds with Outstanding Ability for Vertical Bone Augmentation. *J. Adv. Res.* 2 (in press).doi:10.1016/j.jare.2021.12.010
- Henkel, J., Medeiros Savi, F., Berner, A., Fountain, S., Saifzadeh, S., Steck, R., et al. (2021). Scaffold-guided Bone Regeneration in Large Volume Tibial Segmental Defects. *Bone* 153, 116163. doi:10.1016/j.bone.2021.116163
- Holzappel, B., Gilbert, F., Prodinger, P. M., Raab, P., Knebel, C., Wille, M.-L., et al. (2019). 3D-printed, Patient-specific Scaffolds for Regenerative Therapy of Osseous Defects of Long Bone: Successfully Bridging the gap between Basic Research and Clinical Application. *GMS Ger. Med. Sci.* 1, 22–25. doi:10.3205/19dkou552
- Horner, E. A., Kirkham, J., Wood, D., Curran, S., Smith, M., Thomson, B., et al. (2010). Long Bone Defect Models for Tissue Engineering Applications: Criteria for Choice. *Tissue Eng. B: Rev.* 16, 263–271. doi:10.1089/ten.TEB.2009.0224
- Ishikawa, K., Miyamoto, Y., Tsuchiya, A., Hayashi, K., Tsuru, K., and Ohe, G. (2018). Physical and Histological Comparison of Hydroxyapatite, Carbonate Apatite, and  $\beta$ -Tricalcium Phosphate Bone Substitutes. *Materials* 11, 1993. doi:10.3390/ma11101993
- Karageorgiou, V., and Kaplan, D. (2005). Porosity of 3D Biomaterial Scaffolds and Osteogenesis. *Biomaterials* 26, 5474–5491. doi:10.1016/j.biomaterials.2005.02.002
- Kim, J.-M., Lin, C., Stavre, Z., Greenblatt, M. B., and Shim, J.-H. (2020). Osteoblast-Osteoclast Communication and Bone Homeostasis. *Cells* 9, 2073. doi:10.3390/cells9092073
- Kobbe, P., Laubach, M., Hutmacher, D. W., Alabdulrahman, H., Sellei, R. M., and Hildebrand, F. (2020). Convergence of Scaffold-Guided Bone Regeneration and RIA Bone Grafting for the Treatment of a Critical-Sized Bone Defect of the Femoral Shaft. *Eur. J. Med. Res.* 25, 70. doi:10.1186/s40001-020-00471-w
- Kokubo, S., Fujimoto, R., Yokota, S., Fukushima, S., Nozaki, K., Takahashi, K., et al. (2003). Bone Regeneration by Recombinant Human Bone Morphogenetic Protein-2 and a Novel Biodegradable Carrier in a Rabbit Ulnar Defect Model. *Biomaterials* 24, 1643–1651. doi:10.1016/S0142-9612(02)00551-3
- Kumagai, H., Makihara, T., Funayama, T., Sato, K., Noguchi, H., Abe, T., et al. (2019). Angiogenesis and New Bone Formation in Novel Unidirectional Porous Beta-Tricalcium Phosphate: a Histological Study. *J. Artif. Organs* 22, 294–299. doi:10.1007/s10047-019-01120-8

- Lafage-Proust, M.-H., Roche, B., Langer, M., Cleret, D., Vanden Bossche, A., Olivier, T., et al. (2015). Assessment of Bone Vascularization and its Role in Bone Remodeling. *Bonekey Rep.* 4, 662. doi:10.1038/bonekey.2015.29
- Lasanianos, N. G., Kanakaris, N. K., and Giannoudis, P. v. (2010). Current Management of Long Bone Large Segmental Defects. *Orthopaedics and Trauma* 24, 149–163. doi:10.1016/j.mporth.2009.10.003
- Lim, H.-C., Bae, J.-H., Song, H.-R., Teoh, S. H., Kim, H.-K., and Kum, D.-H. (2011). High Tibial Osteotomy Using Polycaprolactone-Tricalcium Phosphate Polymer Wedge in a Micro Pig Model. *The J. Bone Jt. Surg. Br. volume* 93-B, 120–125. doi:10.1302/0301-620X.93B1.24767
- Liu, Y., Yang, S., Cao, L., Zhang, X., Wang, J., and Liu, C. (2020). Facilitated Vascularization and Enhanced Bone Regeneration by Manipulation Hierarchical Pore Structure of Scaffolds. *Mater. Sci. Eng. C* 110, 110622. doi:10.1016/j.msec.2019.110622
- Lukomska, B., Stanaszek, L., Zuba-Surma, E., Legosz, P., Sarzynska, S., and Drela, K. (2019). Challenges and Controversies in Human Mesenchymal Stem Cell Therapy. *Stem Cell Int.* 2019, 1–10. doi:10.1155/2019/9628536
- Makihara, T., Sakane, M., Noguchi, H., Tsukanishi, T., Suetsugu, Y., and Yamazaki, M. (2018). Formation of Osteon-like Structures in Unidirectional Porous Hydroxyapatite Substitute. *J. Biomed. Mater. Res.* 106, 2665–2672. doi:10.1002/jbm.b.34083
- Mauffrey, C., Barlow, B. T., and Smith, W. (2015). Management of Segmental Bone Defects. *J. Am. Acad. Orthopaedic Surgeons* 23, 143–153. doi:10.5435/JAAOS-D-14-00018
- McGovern, J. A., Griffin, M., and Hutmacher, D. W. (2018). Animal Models for Bone Tissue Engineering and Modelling Disease. *Dis. Model. Mech.* 11, dmm033084. doi:10.1242/dmm.033084
- Niu, H., Ma, Y., Wu, G., Duan, B., Wang, Y., Yuan, Y., et al. (2019). Multicellularity-interweaved Bone Regeneration of BMP-2-Loaded Scaffold with Orchestrated Kinetics of Resorption and Osteogenesis. *Biomaterials* 216, 119216. doi:10.1016/j.biomaterials.2019.05.027
- Norris, B. L., Vanderkarr, M., Sparks, C., Chitnis, A. S., Ray, B., and Holy, C. E. (2021). Treatments, Cost and Healthcare Utilization of Patients with Segmental Bone Defects. *Injury* 52, 2935–2940. doi:10.1016/j.injury.2021.01.016
- Okada, Y., Kawanabe, K., Fujita, H., Nishio, K., and Nakamura, T. (1999). Repair of Segmental Bone Defects Using Bioactive Bone Cement: Comparison with PMMA Bone Cement. *J. Biomed. Mater. Res.* 47, 353–359. doi:10.1002/(sici)1097-4636(19991205)47:3<353aid-jbm9>3.0.co;2-p
- Onodera, J., Kondo, E., Omizu, N., Ueda, D., Yagi, T., and Yasuda, K. (2014). Beta-tricalcium Phosphate Shows superior Absorption Rate and Osteoconductivity Compared to Hydroxyapatite in Open-Wedge High Tibial Osteotomy. *Knee Surg. Sports Traumatol. Arthrosc.* 22, 2763–2770. doi:10.1007/s00167-013-2681-y
- Patel, A., Zaky, S. H., Li, H., Schoedel, K., Almarza, A. J., Sfeir, C., et al. (2020). Bottom-Up Self-Assembled Hydrogel-Mineral Composites Regenerate Rabbit Ulna Defect without Added Growth Factors. *ACS Appl. Bio Mater.* 3, 5652–5663. doi:10.1021/acsabm.0c00371
- Pei, X., Ma, L., Zhang, B., Sun, J., Sun, Y., Fan, Y., et al. (2017). Creating Hierarchical Porosity Hydroxyapatite Scaffolds with Osteoinduction by Three-Dimensional Printing and Microwave Sintering. *Biofabrication* 9, 045008–045024. doi:10.1088/1758-5090/aa90ed
- Perez, R. A., and Mestres, G. (2016). Role of Pore Size and Morphology in Musculo-Skeletal Tissue Regeneration. *Mater. Sci. Eng. C* 61, 922–939. doi:10.1016/j.msec.2015.12.087
- Petersen, A., Princ, A., Korus, G., Ellinghaus, A., Leemhuis, H., Herrera, A., et al. (2018). A Biomaterial with a Channel-like Pore Architecture Induces Endochondral Healing of Bone Defects. *Nat. Commun.* 9, 4430. doi:10.1038/s41467-018-06504-7
- Polak, S. J., Levensgood, S. K. L., Wheeler, M. B., Maki, A. J., Clark, S. G., and Johnson, A. J. W. (2011). Analysis of the Roles of Microporosity and BMP-2 on Multiple Measures of Bone Regeneration and Healing in Calcium Phosphate Scaffolds. *Acta Biomater.* 7, 1760–1771. doi:10.1016/j.actbio.2010.12.030
- Rai, B., Oest, M. E., Dupont, K. M., Ho, K. H., Teoh, S. H., and Guldberg, R. E. (2007). Combination of Platelet-Rich Plasma with Polycaprolactone-Tricalcium Phosphate Scaffolds for Segmental Bone Defect Repair. *J. Biomed. Mater. Res.* 81A, 888–899. doi:10.1002/jbm.a.31142
- Rai, B., Teoh, S. H., Hutmacher, D. W., Cao, T., and Ho, K. H. (2005). Novel PCL-Based Honeycomb Scaffolds as Drug Delivery Systems for rhBMP-2. *Biomaterials* 26, 3739–3748. doi:10.1016/j.biomaterials.2004.09.052
- Ramly, E. P., Alfonso, A. R., Kantar, R. S., Wang, M. M., Siso, J. R. D., Ibrahim, A., et al. (2019). Safety and Efficacy of Recombinant Human Bone Morphogenetic Protein-2 (rhBMP-2) in Craniofacial Surgery. *Plast. Reconstr. Surg. Glob. Open* 7, e2347–9. doi:10.1097/GOX.0000000000002347
- Rathbone, C. R., Guda, T., Singleton, B. M., Oh, D. S., Appleford, M. R., Ong, J. L., et al. (2014). Effect of Cell-Seeded Hydroxyapatite Scaffolds on Rabbit Radius Bone Regeneration. *J. Biomed. Mater. Res.* 102, 1458–1466. doi:10.1002/jbm.a.34834
- Reichert, J. C., Saifzadeh, S., Wullschlegel, M. E., Epari, D. R., Schütz, M. A., Duda, G. N., et al. (2009). The challenge of Establishing Preclinical Models for Segmental Bone Defect Research. *Biomaterials* 30, 2149–2163. doi:10.1016/j.biomaterials.2008.12.050
- Sakemi, Y., Hayashi, K., Tsuchiya, A., Nakashima, Y., and Ishikawa, K. (2021). Reconstruction of Critical-size Segmental Defects in Rat Femurs Using Carbonate Apatite Honeycomb Scaffolds. *J. Biomed. Mater. Res.* 109, 1613–1622. doi:10.1002/jbm.a.37157
- Shibahara, K., Hayashi, K., Nakashima, Y., and Ishikawa, K. (2021). Honeycomb Scaffold-Guided Bone Reconstruction of Critical-Sized Defects in Rabbit Ulnar Shafts. *ACS Appl. Bio Mater.* 4, 6821–6831. doi:10.1021/acsabm.1c00533
- Suga, K., Saitoh, M., Kokubo, S., Nozaki, K., Fukushima, S., Yasuda, S., et al. (2004). Synergism between Interleukin-11 and Bone Morphogenetic Protein-2 in the Healing of Segmental Bone Defects in a Rabbit Model. *J. Interferon Cytokine Res.* 24, 343–349. doi:10.1089/107999004323142204
- Tanaka, M., Haniyu, H., Kamanaka, T., Takizawa, T., Sobajima, A., Yoshida, K., et al. (2017). Physico-chemical, In Vitro, and In Vivo Evaluation of a 3D Unidirectional Porous Hydroxyapatite Scaffold for Bone Regeneration. *Materials* 10, 33–13. doi:10.3390/ma10010033
- Tanaka, N., Nakanishi, K., Fujimoto, Y., Sasaki, H., Kamei, N., Hamasaki, T., et al. (2008). Expansive Laminoplasty for Cervical Myelopathy with Interconnected Porous Calcium Hydroxyapatite Ceramic Spacers. *J. Spinal Disord. Tech.* 21, 547–552. doi:10.1097/BSD.0b013e31815c85bd
- Tanaka, N., Nakanishi, K., Kamei, N., Nakamae, T., Kotaka, S., Fujimoto, Y., et al. (2018). Novel Hybrid Hydroxyapatite Spacers Ensure Sufficient Bone Bonding in Cervical Laminoplasty. *Asian Spine J.* 12, 1078–1084. doi:10.31616/asj.2018.12.6.1078
- Tang, W., Lin, D., Yu, Y., Niu, H., Guo, H., Yuan, Y., et al. (2016). Bioinspired Trimodal Macro/micro/nano-Porous Scaffolds Loading rhBMP-2 for Complete Regeneration of Critical Size Bone Defect. *Acta Biomater.* 32, 309–323. doi:10.1016/j.actbio.2015.12.006
- Tovar, N., Witek, L., Atria, P., Sobieraj, M., Bowers, M., Lopez, C. D., et al. (2018). Form and Functional Repair of Long Bone Using 3D-printed Bioactive Scaffolds. *J. Tissue Eng. Regen. Med.* 12, 1986–1999. doi:10.1002/term.2733
- Van, Bael, S., Chai, Y. C., Truscetto, S., Moesen, M., Kerckhofs, G., VanOosterwyck, H., et al. (2012). The Effect of Pore Geometry on the In Vitro Biological Behavior of Human Periosteum-Derived Cells Seeded on Selective Laser-Melted Ti6Al4V Bone Scaffolds. *Acta Biomater.* 8, 2824–2834. doi:10.1016/j.actbio.2012.04.001
- Wang, W., Jia, G., Wang, Q., Huang, H., Li, X., Zeng, H., et al. (2020). The In Vitro and In Vivo Biological Effects and Osteogenic Activity of Novel Biodegradable Porous Mg alloy Scaffolds. *Mater. Des.* 189, 108514. doi:10.1016/j.matdes.2020.108514
- Woodard, J. R., Hildore, A. J., Lan, S. K., Park, C. J., Morgan, A. W., Eurell, J. A. C., et al. (2007). The Mechanical Properties and Osteoconductivity of Hydroxyapatite Bone Scaffolds with Multi-Scale Porosity. *Biomaterials* 28, 45–54. doi:10.1016/j.biomaterials.2006.08.021
- Xiao, L., Wang, B., Yang, G., and Gauthier, M. (2012). Poly(Lactic Acid)-Based Biomaterials: Synthesis, Modification and Applications. *Biomed. Sci. Eng. Tech.* 1, 1. doi:10.5772/23927
- Yu, W., Li, R., Long, J., Chen, P., Hou, A., Li, L., et al. (2019). Use of a Three-Dimensional Printed Poly(lactide-Coglycolide)/tricalcium Phosphate Composite Scaffold Incorporating Magnesium Powder to Enhance Bone

- Defect Repair in Rabbits. *J. Orthopaedic Translation* 16, 62–70. doi:10.1016/j.jot.2018.07.007
- Zhang, M., Matinlinna, J. P., Tsoi, J. K. H., Liu, W., Cui, X., Lu, W. W., et al. (2020). Recent Developments in Biomaterials for Long-Bone Segmental Defect Reconstruction: A Narrative Overview. *J. Orthopaedic Translation* 22, 26–33. doi:10.1016/j.jot.2019.09.005
- Zhang, W., Feng, C., Yang, G., Li, G., Ding, X., Wang, S., et al. (2017). 3D-printed Scaffolds with Synergistic Effect of Hollow-Pipe Structure and Bioactive Ions for Vascularized Bone Regeneration. *Biomaterials* 135, 85–95. doi:10.1016/j.biomaterials.2017.05.005
- Zhang, X., Atsuta, I., Narimatsu, I., Ueda, N., Takahashi, R., Egashira, Y., et al. (2021). Replacement Process of Carbonate Apatite by Alveolar Bone in a Rat Extraction Socket. *Materials* 14, 4457. doi:10.3390/ma14164457
- Zhou, J., Lin, H., Fang, T., Li, X., Dai, W., Uemura, T., et al. (2010). The Repair of Large Segmental Bone Defects in the Rabbit with Vascularized Tissue Engineered Bone. *Biomaterials* 31, 1171–1179. doi:10.1016/j.biomaterials.2009.10.043

**Conflict of Interest:** The authors declare that the research was conducted in the absence of any commercial or financial relationships that could be construed as a potential conflict of interest.

**Publisher's Note:** All claims expressed in this article are solely those of the authors and do not necessarily represent those of their affiliated organizations, or those of the publisher, the editors, and the reviewers. Any product that may be evaluated in this article, or claim that may be made by its manufacturer, is not guaranteed or endorsed by the publisher.

Copyright © 2022 Shibahara, Hayashi, Nakashima and Ishikawa. This is an open-access article distributed under the terms of the Creative Commons Attribution License (CC BY). The use, distribution or reproduction in other forums is permitted, provided the original author(s) and the copyright owner(s) are credited and that the original publication in this journal is cited, in accordance with accepted academic practice. No use, distribution or reproduction is permitted which does not comply with these terms.





# Enhancing Myoblast Fusion and Myotube Diameter in Human 3D Skeletal Muscle Constructs by Electromagnetic Stimulation

Lisanne Terrie<sup>1†</sup>, Margherita Burattini<sup>1,2†</sup>, Sandra Van Vlierberghe<sup>3</sup>, Lorenzo Fassina<sup>4</sup> and Lieven Thorrez<sup>1\*</sup>

## OPEN ACCESS

### Edited by:

Malcolm Xing,  
University of Manitoba, Canada

### Reviewed by:

Darren Player,  
University College London,  
United Kingdom  
David Lee Mack,  
University of Washington,  
United States

### \*Correspondence:

Lieven Thorrez  
lieven.thorrez@kuleuven.be

<sup>†</sup>These authors have contributed  
equally to this work and share first  
authorship

### Specialty section:

This article was submitted to  
Biomaterials,  
a section of the journal  
Frontiers in Bioengineering and  
Biotechnology

**Received:** 08 March 2022

**Accepted:** 06 June 2022

**Published:** 22 June 2022

### Citation:

Terrie L, Burattini M, Van Vlierberghe S,  
Fassina L and Thorrez L (2022)  
Enhancing Myoblast Fusion and  
Myotube Diameter in Human 3D  
Skeletal Muscle Constructs by  
Electromagnetic Stimulation.  
Front. Bioeng. Biotechnol. 10:892287.  
doi: 10.3389/fbioe.2022.892287

<sup>1</sup>Tissue Engineering Lab, Dep. Development and Regeneration, KU Leuven Kulak, Kortrijk, Belgium, <sup>2</sup>Dept. of Surgical Sciences, Dentistry and Maternity, University of Verona, Verona, Italy, <sup>3</sup>Polymer Chemistry & Biomaterials Group, Centre of Macromolecular Chemistry, Dep. of Organic and Macromolecular Chemistry, Ghent University, Ghent, Belgium, <sup>4</sup>Dept. of Electrical, Computer and Biomedical Engineering, University of Pavia, Pavia, Italy

Skeletal muscle tissue engineering (SMTE) aims at the *in vitro* generation of 3D skeletal muscle engineered constructs which mimic the native muscle structure and function. Although native skeletal muscle is a highly dynamic tissue, most research approaches still focus on static cell culture methods, while research on stimulation protocols indicates a positive effect, especially on myogenesis. A more mature muscle construct may be needed especially for the potential applications for regenerative medicine purposes, disease or drug disposition models. Most efforts towards dynamic cell or tissue culture methods have been geared towards mechanical or electrical stimulation or a combination of those. In the context of dynamic methods, pulsed electromagnetic field (PEMF) stimulation has been extensively used in bone tissue engineering, but the impact of PEMF on skeletal muscle development is poorly explored. Here, we evaluated the effects of PEMF stimulation on human skeletal muscle cells both in 2D and 3D experiments. First, PEMF was applied on 2D cultures of human myoblasts during differentiation. In 2D, enhanced myogenesis was observed, as evidenced by an increased myotube diameter and fusion index. Second, 2D results were translated towards 3D bioartificial muscles (BAMs). BAMs were subjected to PEMF for varying exposure times, where a 2-h daily stimulation was found to be effective in enhancing 3D myotube formation. Third, applying this protocol for the entire 16-days culture period was compared to a stimulation starting at day 8, once the myotubes were formed. The latter was found to result in significantly higher myotube diameter, fusion index, and increased myosin heavy chain 1 expression. This work shows the potential of electromagnetic stimulation for enhancing myotube formation both in 2D and 3D, warranting its further consideration in dynamic culturing techniques.

**Keywords:** tissue engineering, skeletal muscle, pulsed electromagnetic field, biophysical stimuli, bioartificial muscle, myotube, human myoblast

## INTRODUCTION

Skeletal muscle has a complex yet extremely functional organization. Its contractile function is exerted by aligned myofibers, formed by the fusion of single-nucleated myoblasts, resulting in multinucleated myotubes. Quiescent multipotent stem cells, satellite cells (SCs), located between the basement membrane of the muscle fibers and the sarcolemma (Powell et al., 2002) guarantee the muscle regeneration, when small injuries occur. Consequently, a long-term goal of skeletal muscle tissue engineering (SMTE) is to replicate the structure and function of native skeletal muscle *in vitro* and, to obtain functional constructs. Such an *in vitro* model can enhance research focused on skeletal muscle development and regeneration both in the healthy or diseased states (Vigodarzere and Mantero, 2014; Maffioletti et al., 2018; Khodabukus, 2021). Many approaches for SMTE still focus on static cell culture methods. However, skeletal muscle tissue is highly dynamic, changing its size and power output in response to activity. For this reason, physiological activity is seen as an imperative step to replicate native skeletal muscle structure and function.

This physiological activity can be mimicked *in vitro* through mechanical stimulation or electrical stimulation or the combination of the two (Somers et al., 2017; Maleiner et al., 2018). Several studies have shown how mimicking this physiological activity can advance engineered skeletal muscle. For instance, mechanical loading of 3D cultured C2C12 cells was found to induce significant hypertrophy of the myotubes and augmented maximal force production (Aguilar-Agon et al., 2019). Similarly, repetitive stretch/relaxation cycles were found to increase mean myofiber diameter and myofiber area fraction (%) when applied to 3D cultured human myoblasts (Powell et al., 2002). However, mechanical stimulation does not necessarily stimulate myotube development. For example, stretch was found to negatively influence the maturation of both C2C12 and murine muscle progenitor cells in a 2D and 3D environment (Boonen et al., 2010).

While mechanical stimulation can thus lead to different outcomes, the usage of electrical stimulation in SMTE has led to more consistent improvements in myotube development. Electrical stimulation aims to recapitulate the function of muscle stimulation by fast and slow motor neurons and was found to induce a fast-to-slow shift in engineered muscle when using a stimulation frequency of 10 Hz and an active time of 60% (Khodabukus et al., 2015). An intermittent electrical stimulation at 10 Hz for one week was also found to induce myotube hypertrophy and decrease fatigue resistance and increase force generation (Khodabukus et al., 2019). However, many parameters, such as the period of stimulation and starting point, are not commonly defined and vary among groups. Additionally, results derived from cell lines such as C2C12 are not necessarily translated to primary muscle progenitor cells (Langelaan et al., 2010). In the aforementioned work, 3D constructs engineered with primary progenitor cells were more susceptible to electrical stimuli and showed an overall higher level of maturation than C2C12 constructs.

While mechanical and electrical stimuli have been explored for advancing tissue-engineered skeletal muscle constructs, the use of

pulsed electromagnetic field (PEMF) stimulation for SMTE appears to be still unexplored. Nevertheless, the potential of PEMF for tissue engineering has been shown in other fields, especially for osteogenesis and chondrogenesis (Varani et al., 2021). Indeed, PEMF has been demonstrated to promote osteogenesis in nonunion fractures, partly by regulating mesenchymal stem cell (MSC) or osteoblast activity.

Similarly, PEMF stimulation of periodontal ligament stem cells increased the osteogenic potential of the cells (Wang et al., 2017). Moreover, prolonged exposure to PEMF of MSCs isolated from the human umbilical cord was found to enhance the tenogenic potential (Marmotti et al., 2019). In addition, PEMF-based devices are currently sold in the context of muscle pain relief. Still, only a few papers have described the influence of PEMF stimulation on skeletal muscle of patients (Kim et al., 2012; Jeon et al., 2015). Given the scarce evidence of these devices *in vivo* and the lack of studies using these for SMTE, the rationale of this study is to evaluate the value of PEMF stimulation for SMTE by applying PEMF stimulation on both 2D cultured myoblasts and subsequently 3D tissue-engineered skeletal muscle constructs.

## MATERIALS AND METHODS

### Cell Culture

Human skeletal muscle cells were isolated from a fresh human muscle tissue biopsy, obtained from the Human Body Donation programme of KU Leuven as described previously (Gholobova et al., 2019). The donor provided written consent and ethical committee approval was obtained (NH019-2020-04-02). After isolation, the myoblasts were expanded in gelatin-coated culture flasks with growth medium consisting of DMEM Glutamax (DMEM, Gibco, #41966029), 1% Ultrosol solution (Pall Corporation, #15950-017), 10% fetal bovine serum (FBS, Biowest, #S1400-500) and 50 µg/ml gentamicin (Life Technologies, #15750060). Differentiation medium was composed of DMEM Glutamax, 10 ng/ml hEGF (Peprotech, #AF10015), 10 µg/ml insulin (Sigma, #I9278), 50 µg/ml bovine serum albumin (BSA, Sigma, #A2153) and 50 µg/ml gentamicin (Sigma, #15750037) and was used to promote formation of multinucleated myotubes once the cultures reached 80% confluency. 2D cell culture experiments were performed in gelatin-coated 24-well plates using 50,000 cells per well. Cells were subsequently cultured for 2 days in growth medium. Next, the medium was switched to fusion medium to induce myotube formation for 5 days.

### Human Biopsy Characterization: Immunocytochemistry

To determine the percentage of myoblasts, isolated muscle cells were cultured in growth medium in 24-well dishes (5000 cells/well) for 2–3 days until 60–70% confluency. Fixation was performed in a 1:1 methanol–acetone mix at –20°C for 10 min. Next, fixed cells were blocked and permeabilized in blocking buffer containing 1x phosphate buffer saline (PBS), 1% BSA and 0.2% Triton X-100 (Sigma, #X100). Subsequently, cells were incubated overnight at 4°C with a monoclonal mouse antibody against desmin (Sigma, #D1033, 1:200 in blocking buffer). Cells were labelled with a polyclonal rabbit

anti-mouse secondary antibody (Alexa Fluor 488, Invitrogen, #A11059) for 30 min in the dark and subsequently incubated with 4',6-diamidino-2-phenylindole (DAPI, 0.1  $\mu\text{g}/\text{ml}$  in PBS, Life Technologies) for 1 h. To determine the fusion index, cells were cultured to 80% confluency in growth medium in 12-well dishes (50,000 cells/well), and then switched to differentiation medium for 4 days to induce fusion into myotubes. Next, myotubes were fixed using 4% formaldehyde, freshly prepared from paraformaldehyde (PFA, Merck, #1040031000) solution weight/volume (w/v), at room temperature (RT) for 10 min followed by methanol fixation at  $-20^{\circ}\text{C}$  for 10 min. Next, fixed myotubes were blocked and permeabilized in blocking buffer containing 1x phosphate buffer saline (PBS), 1% BSA and 0.2% Triton X-100 (Sigma, #X100). Subsequently, cells were incubated overnight at  $4^{\circ}\text{C}$  with a monoclonal mouse antibody against tropomyosin (Sigma, T9283, 1:100 in blocking buffer). Myotubes were labelled with a polyclonal rabbit anti-mouse secondary antibody (Alexa Fluor 488, Invitrogen, #A11059) for 30 min in the dark and subsequently incubated with 4',6-diamidino-2-phenylindole (DAPI, 0.1  $\mu\text{g}/\text{ml}$  in PBS, Life Technologies) for 1 h. Images were acquired with Zeiss Zen software by an AxioCam ICc 1 camera mounted on a Zeiss Axiovert 10 microscope. The percentage of myoblasts in a muscle cell population was defined as the ratio of desmin-positive cells to the total amount of cells (identified by the DAPI-stained nuclei). Fusion index was defined as the ratio of tropomyosin-positive cells to the total amount of myoblasts in the population.

### 3D Bio Artificial Muscles

Tissue engineering of the bioartificial muscles (BAMs) was described in detail in previous work (Gholobova et al., 2015; Gholobova et al., 2018; Thorrez et al., 2018; Gholobova et al., 2019; Gholobova et al., 2020). Briefly, myogenic cells were isolated, cultured, and harvested as described. After cell expansion, for each BAM, 2 million cells were mixed with 500  $\mu\text{l}$  of human thrombin (4 U/mL, Stago, #HT1002a). To create the 3D constructs, the cell-thrombin mixture was added to 500  $\mu\text{l}$  of fibrinogen (2 mg/mL, Merck Chemicals, #341576) into 25-mm silicone molds containing two metal pins spaced 20 mm, serving as attachment points. Following a 2-h incubation at  $37^{\circ}\text{C}$  during which the fibrin solidified, BAMs were cultured for the first 2 days in growth medium supplemented with the fibrinolysis inhibitors aprotinin (92.5  $\mu\text{g}/\text{ml}$ , Carl Roth, #A1624) and tranexamic acid (400  $\mu\text{M}$ , Sigma, #857653). The medium was switched to differentiation medium with fibrinolysis inhibitors (92.5  $\mu\text{g}/\text{ml}$  aprotinin and 400  $\mu\text{M}$  tranexamic acid) from day 3 until day 8 to induce myoblast fusion. After day 8, BAMs were cultured further in growth medium containing fibrinolysis inhibitors until the end of the experiment. The cell culture medium was refreshed every two days.

### Immunohistology of BAMs

For longitudinal analysis of myotube organization, BAMs were washed with PBS and then fixed using 4% PFA solution (w/v) in PBS for 1 h. BAMs were pinned on Styrofoam to preserve their original shape while fixing. Before staining, constructs were additionally fixed in  $-20^{\circ}\text{C}$  methanol for 10 min. Fixed constructs were blocked and permeabilized in blocking buffer containing 1x phosphate buffer saline (PBS), 1% BSA and 0.2% Triton X-100 (Sigma, #X100). Subsequently, BAMs were

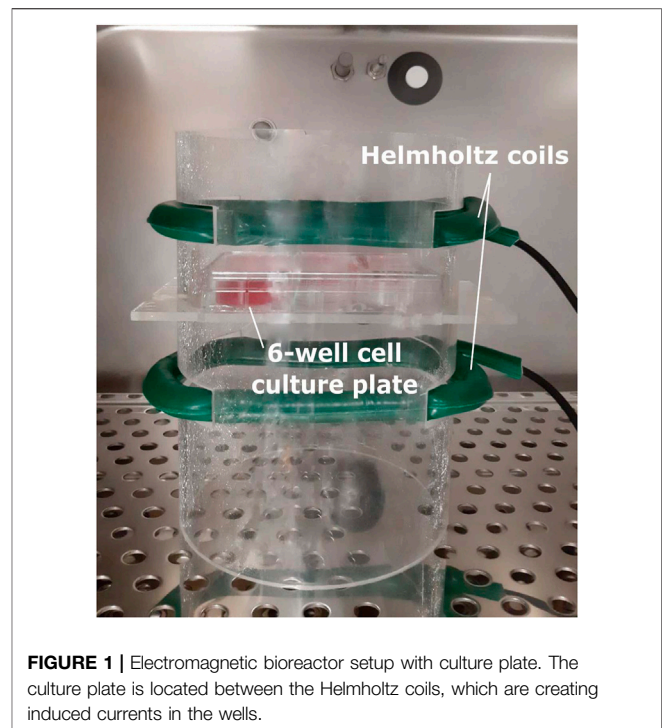


**FIGURE 1 |** Electromagnetic bioreactor setup with culture plate. The culture plate is located between the Helmholtz coils, which are creating induced currents in the wells.

incubated overnight at  $4^{\circ}\text{C}$  with a monoclonal mouse antibody against tropomyosin (Sigma, #T9283, 1:100 in blocking buffer). After extensive washing with PBS, BAMs were incubated with polyclonal rabbit anti-mouse antibody (Alexa Fluor 488, Invitrogen, #A11059, 1:200 or Alexa Fluor 633, Invitrogen, #21,063, 1:200) for 3 h in the dark followed by incubation with DAPI (Life Technologies, 0.1  $\mu\text{g}/\text{ml}$  in PBS) for 1 h. BAMs were stored in PBS in the dark until visualized. Images of tropomyosin in 3D BAMs were acquired with Zeiss Zen software by confocal microscopy (Zeiss LSM710) with PlanApoChromat 25x/0.8, WD 0.57 mm objective.

For cross-sectional analysis of myotube organization, BAMs were washed with PBS and submerged in optimal cutting temperature compound (OCT) (VWR, #25608-930) and frozen in liquid  $\text{N}_2$ -cooled isopentane. Frozen cross-sections (5  $\mu\text{m}$ ) were made using a cryostat (Leica CM 1950) and collected on Superfrost Ultra Plus slides (VWR, #631-9483). Sections were placed at room temperature for 5 min followed by washing in PBS to remove OCT. Next, sections were fixed with 4% PFA for 10 min at room temperature. After washing with PBS, sections were permeabilized for 25 min using 1x PBS, 1% BSA and 0.2% Triton X-100. Subsequently, samples were incubated overnight in a moist chamber with rabbit polyclonal anti-laminin (Sigma, #L9393, 1:400 in blocking buffer). Following washing with PBS, sections were incubated for 45 min with a donkey anti-rabbit IgG secondary antibody (Alexa Fluor 488; #A21206; 1:1000 in PBS) in the dark. Lastly, after washing with PBS, slides were mounted with prolong gold antifade mounting medium with DAPI (Thermo Fisher; #P36935). Slides were imaged with an AxioCam ICc 1 camera mounted on a Zeiss Axiovert 10 microscope and images were acquired and stored with Zeiss

**TABLE 1** | List of the primers used for RT-qPCR analysis.

Gene	Orientation	Primer Sequence (5'-3')	Amplicon Size (bp)
MYH1	Forward	GGG AGA CCT AAA ATT GGC TCA A	106
	Reverse	TTG CAG ACC GCT CAT TTC AAA	
MYH3	Forward	CTT GTG GGC GGA GGT CTG G	119
	Reverse	AGC TAT GCC GAA CAC TTC CAT	
MYH8	Forward	ACA TTA CTG GCT GGC TGG AC	143
	Reverse	ACC TTT CTT CGC GCT GCT AT	
<i>Reference genes</i>			
GAPDH	Forward	TCA AGA AGG TGG TGA AGC AGG	168
	Reverse	ACC AGG AAA TGA GCT TGA CAA A	
HSP90AB1	Forward	AGA AAT TGC CCA ACT CAT GTC C	75
	Reverse	ATC AAC TCC CGA AGG AAA ATC TC	
RPL13A	Forward	CCT GGA GGA GAA GAG GAA AGA GA	126
	Reverse	TTG AGG ACC TCT GTG TAT TTG TCA A	

Zen software. Images were further processed using Fiji ImageJ (version 1.53f51) to determine the cross-sectional diameter of the myotubes. For each biological replicate ( $n = 3$ ), 6 sections were quantified of which 5 pictures were taken for each section.

## Electromagnetic Bioreactor

The electromagnetic bioreactor and its settings were extensively described in previous work (Fassina et al., 2006; Osera et al., 2011; Ceccarelli et al., 2013; Mognaschi et al., 2014). Briefly, it includes a carrying windowed tube of polymethylmethacrylate, in which a culture well plate can be positioned, as represented in **Figure 1**. Two solenoids (i.e., Helmholtz coils) complete the stimulator, producing a perpendicular magnetic field with respect to the plane of the well plate and inducing a parallel electric field in the wells. In particular, the stimulated cells are 5 cm away from each solenoid plane, and the coils are powered by a Biostim SPT pulse generator (IGEA Medical, Carpi, Italy). Given the position of the solenoids and the characteristics of the pulse generator, the electromagnetic stimulation has the following parameters: intensity of the magnetic field equal to  $2 \pm 0.2$  mT, amplitude of the induced electric tension equal to  $5 \pm 1$  mV, signal frequency of  $75 \pm 2$  Hz, and pulse duration of 1.3 ms. The electromagnetic bioreactor was placed into a standard cell culture incubator at 37°C and exposed to 5% CO<sub>2</sub>.

A more detailed description and analysis of the field distribution and induced current magnitude is provided in Mognaschi et al. (2014). Briefly, the time-varying magnetic induction (with a frequency of 75 Hz) generated a concentric distribution of induced electric currents with a corresponding induced distribution of radial mechanical forces. In other words, stimulated cells are subjected to mechanical vibration at the same frequency as the PEMF. Moreover, the vibration force applied reaches the pN magnitude, which is comparable to the force applied for studying cellular mechanics as reported in Diz-Muñoz et al. (Diz-Muñoz et al., 2010).

## Gene Expression Analysis

To assess differences in the developmental stage of the myotubes, RT-qPCR was performed on the different myosin heavy chain isoforms (MYH1, MYH3, MYH8). We used RPL13A, GAPDH and HSP90AB1 as reference genes.

Primers were designed using NCBI/Prime-Blast and verified for an efficiency >90% by a serial dilution analysis. Sequences of the primers are reported in **Table 1**. As described previously (Gholobova et al., 2020), BAMs were washed in PBS, transferred in freshly prepared lysis buffer (from PureLink™ RNA Mini Kit, Ambion #12183020) containing 1%  $\beta$ -mercaptoethanol (Gibco, #31350010) and homogenized on ice using a tip sonicator until the solution appears homogenous ( $3 \times 15$  s) (MSE Soniprep Tip Sonicator). After centrifugation (5 min, 3000 g), total RNA was extracted from the supernatant with an RNA extraction kit (PureLink™ RNA Mini Kit). RNA quality was evaluated by the A260/A280 ratio as measured with a Nanodrop spectrophotometer (NP80, Westburg). Two  $\mu$ g total RNA was reverse transcribed with the cDNA SuperMix (Quantabio, #95 048-100) in a total reaction volume of 20  $\mu$ l using the PCR System 9700 (Applied Biosystems) according to the manufacturer's instructions. For RT-qPCR, the Perfecta Sybr Green SuperMix (Quantabio, #95 054-500) was used. Reaction mixes were prepared in 10  $\mu$ l volumes, containing 0.2  $\mu$ l of the cDNA, according to the manufacturer's instructions. RTqPCR was performed on a LightCycler® 480 (Roche) with a hold stage of 2 min at 50°C followed by 2 min at 95°C. Next, 40 cycles of 15 s denaturation at 95°C and 45 s of primer annealing and extension at 60°C were used. All conditions were assessed in experimental replicates ( $n = 3-6$ ) and each replicate was tested with technical triplicates by RT-qPCR. Threshold cycles were determined and used to calculate the expression fold changes within experimental conditions using the Pfaffl method.

## Statistics

Statistical analysis was performed using GraphPad Prism software (version 8.0.2). Normality tests (Shapiro-Wilk) were performed on data before performing ANOVA tests. Unless described otherwise, non-parametric Kruskal-Wallis tests with Dunn's post-tests were used when comparing the three culture conditions. For multiple comparisons, the mean rank of the stimulated conditions was compared only with the static culture. Biological triplicates were used, and at least 3



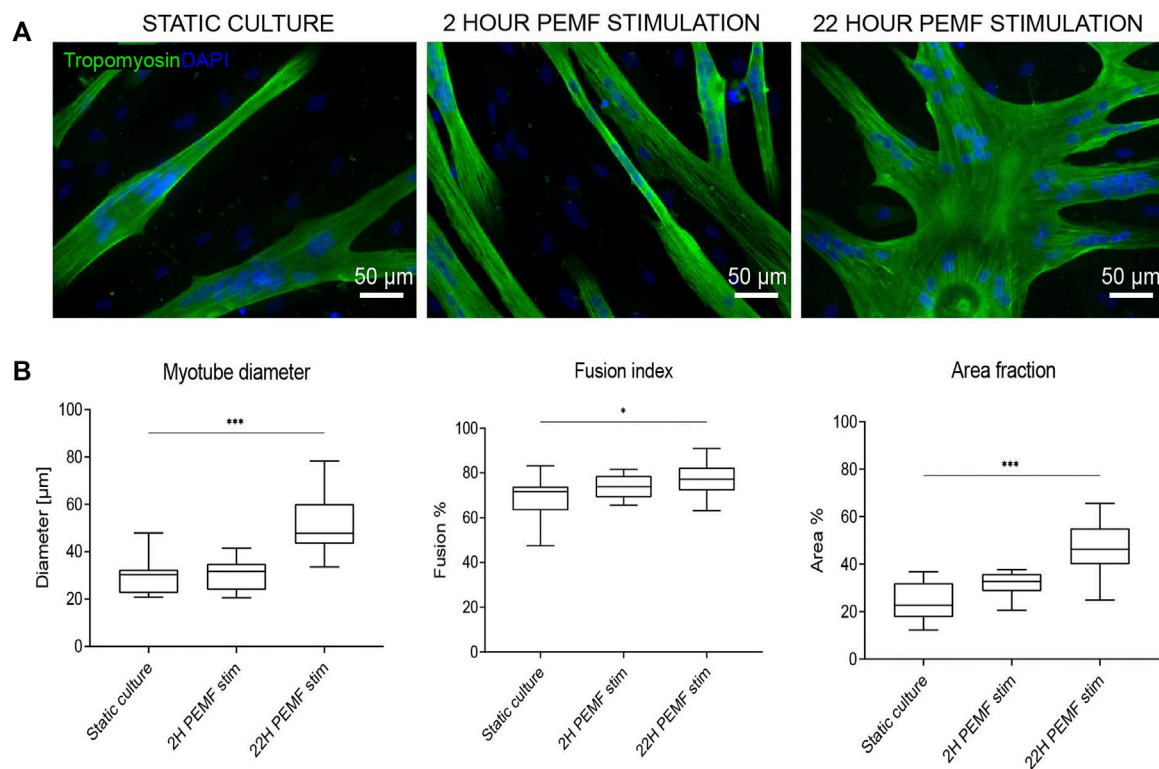


**FIGURE 2 | (A)** Tropomyosin staining of 2D samples after no, 2 h per day or 22 h per day PEMF stimulation for 4 days. Blue: nuclei stained with DAPI; green: myotubes stained for tropomyosin. Scale bars: 50  $\mu\text{m}$ . **(B)** Quantification from the tropomyosin staining images via Fiji software, diameter (left), fusion index (middle) and area fraction (% of surface covered by cells) (right) (\* $p < 0.05$ , \*\* $p < 0.01$ , \*\*\* $p < 0.001$ ) ( $n = 3$  experimental replicates, for each 5 random images were analysed).

measurements were taken for each parameter reported. In the text, all data are reported as mean  $\pm$  standard deviation and significance levels are indicated with \* $p < 0.05$ , \*\* $p < 0.01$ , and \*\*\* $p < 0.001$ . Boxplot graphs show the data as the median with 5 and 95% percentiles.

## RESULTS

### Determining the Effect of PEMF Stimulation on 2D Cultured Human Myoblasts During Myotube Formation

First, to determine whether the pulsed electromagnetic field stimulation can induce an enhanced formation of multinucleated myotubes, the primary human myoblasts seeded onto 24-well plates were stimulated for either 2 h or 22 h per day using the bioreactor setup as shown in **Figure 1**. These two different exposure times were applied starting at 24 h post cell seeding to allow for cell adhesion. Stimulation was maintained for 4 days of which 1 day in growth medium and 3 days in differentiation medium. After this period, myotube formation was assessed by quantification of the percentage of the surface occupied by tropomyosin positive myotubes. Representative images are shown in **Figure 2A**. Cultures stimulated for 22 h per day showed an overall significant

increase in myotube formation ( $46 \pm 10\%$ ) compared to statically cultured cells ( $24 \pm 8\%$ ) as shown in **Figure 2B**. In addition, myotubes stimulated for 22 h were found to have a significant increase in diameter ( $51 \pm 12 \mu\text{m}$ ) compared to statically cultured myotubes ( $30 \pm 7 \mu\text{m}$ ). The fusion index was determined to estimate the fusion capacity of the cultured myoblasts within the different stimulation conditions. The fusion index was found to be slightly increased in the 22 h per day stimulation condition ( $77 \pm 7\%$ ) compared to statically cultured myotubes ( $69 \pm 9\%$ ) (**Figures 2A,B**).

### Optimal Duration of PEMF Stimulation During Myotube Formation in BioArtificial Muscles

Since cellular behaviour is known to be different in a 3D environment versus monolayers on a plastic dish, we evaluated the impact of the previously applied PEMF stimulus durations on human muscle cell differentiation in a 3D culture format. Thus, human myoblasts were embedded within a fibrin hydrogel and cast in a custom silicone mold containing two attachment sites. The cells self-organize in the longitudinal direction due to cell-induced contraction of the hydrogel, resulting in a compact cylindrical-shaped 3D tissue by the end of the differentiation phase on day 8. Stimulation was carried out daily up to 16 days of the culture period, starting 24 h after casting. The samples were cultured for 3 days in the growth medium,

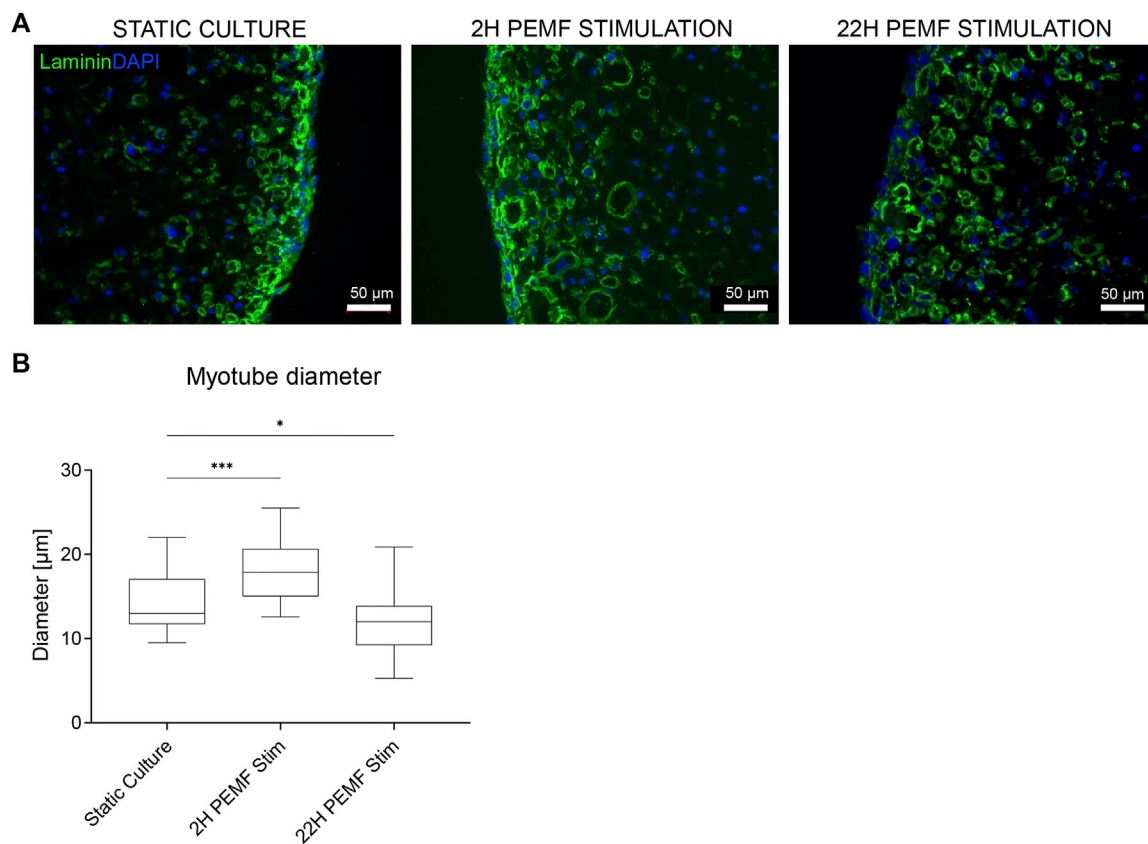


**FIGURE 3 | (A)** Laminin staining of the 3D samples. Blue: nuclei stained with DAPI; green: myotubes stained for laminin. Scale bars: 50  $\mu$ m. **(B)** Myotube width quantifications from the laminin staining images via Fiji software. ( $n = 6$  BAMs, for each 3 images quantified,  $***p < 0.001$ ). The boxplot represents the median, 5 and 95% percentiles.

5 days in fusion medium and finally again 8 days in growth medium. Two hours of stimulation per day was effective in enhancing myotube cross-sectional diameter ( $18 \pm 4 \mu\text{m}$ ,  $n = 6$ ), compared to the static culture ( $15 \pm 4 \mu\text{m}$ ,  $n = 6$ ) (Figures 3A,B). On the other hand, differently in the 2D condition, the 22 h of stimulation/day resulted in a slight, but a nonsignificant reduction of myotube diameter ( $12 \pm 3 \mu\text{m}$ ,  $n = 6$  vs.  $15 \pm 4 \mu\text{m}$ ,  $n = 6$ ) (Figures 3A,B).

### Determination of Optimal Time Window for PEMF Stimulation During 3D Myotube Formation

In previous experiments, stimulation was started early during the formation of myotubes, overlapping with the time window when cells still actively fuse. We next investigated whether this was a good starting point for applying the PEMF stimulation protocol on BAM constructs, or whether it would be preferential to allow cell fusion before the PEMF stimulation. Therefore, we compared static controls with two other groups where the stimulation was applied from day 1 until day 16 or from day 8 until day 16 (coinciding with switching back to a high serum growth medium). Overall, myotube formation was found to be improved with a

significantly higher number of myoblasts fusing into myotubes for both stimulation conditions compared to the control or static culture (Figures 4A,B). More specifically, statically cultured 3D constructs had a fusion index of  $28 \pm 4\%$ , while 3D constructs stimulated from day 1 until day 16 had a fusion index of  $51 \pm 11\%$  and stimulating from day 8 until day 16 further improved the fusion index to  $66 \pm 18\%$ . Myotube diameter increased as well when stimulation was applied between day 8 and 16 of culture ( $25 \pm 15 \mu\text{m}$ ,  $n = 3$ ) and was found to be significantly higher compared to static culture ( $18 \pm 9 \mu\text{m}$ ,  $n = 2$ ) but not significantly different from stimulation applied from day 1 onwards ( $23 \pm 14 \mu\text{m}$ ,  $n = 3$ ). When checking the area fraction per image taken up by myotubes, an increasing trend for the stimulated conditions, but with no significant difference, was found. RT-qPCR was performed to assess possible differences in myosin heavy chain isoform expression. We quantified *MYH1* (adult fast IId), *MYH3* (embryonic) and *MYH8* (perinatal), determining which differentiation stage is enhanced. As shown in Figure 5, samples stimulated during the differentiation phase (stimulation applied from day 8 until day 16) show an increased *MYH1* expression (relative to the average of the reference genes) ( $1.8 \pm 0.5$ ,  $n = 6$ ) when compared to the

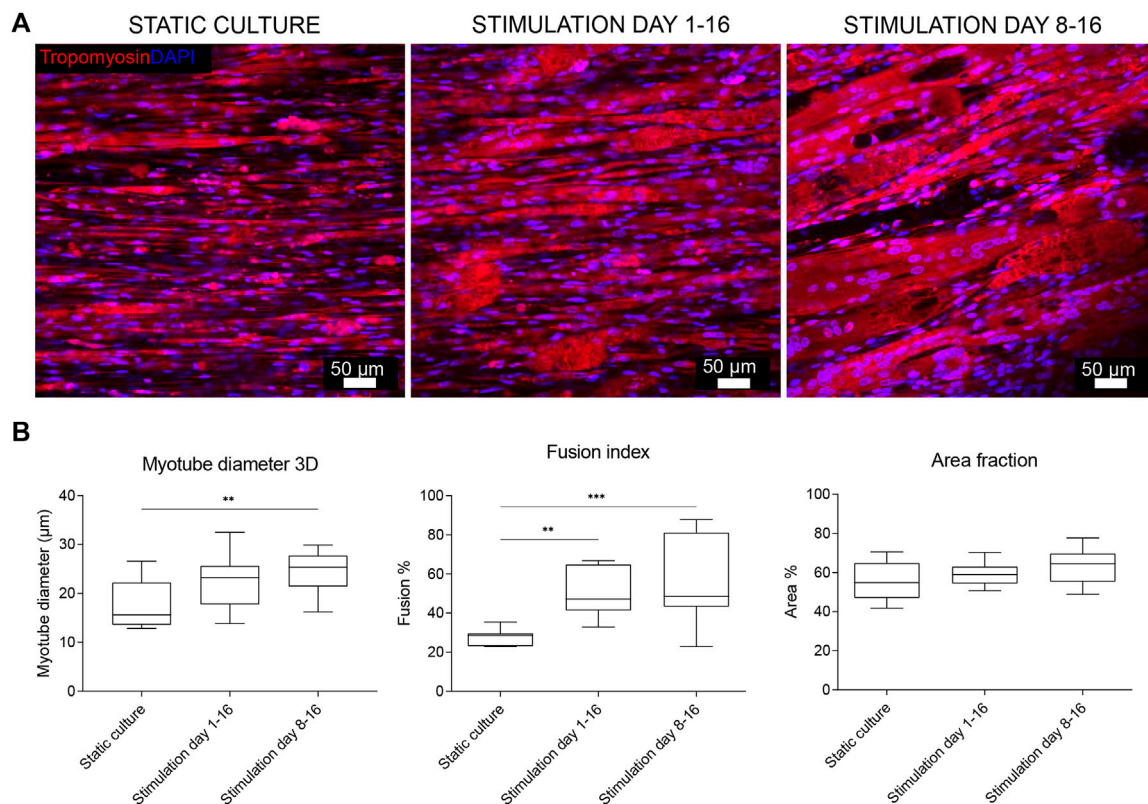


**FIGURE 4 | (A)** Confocal microscopy images of BAMs not stimulated (static culture), PEMF stimulated for 2 h/day during the entire myotube formation (days 1–16) or only after 5 days of unstimulated myoblast fusion (PEMF stimulation days 8–16). Blue: nuclei stained with DAPI; red: myotubes stained for tropomyosin. Scale bar: 50  $\mu$ m. **(B)** Quantifications from the tropomyosin staining images via Fiji software. ( $n = 2$  control,  $n = 3$  stimulated conditions).

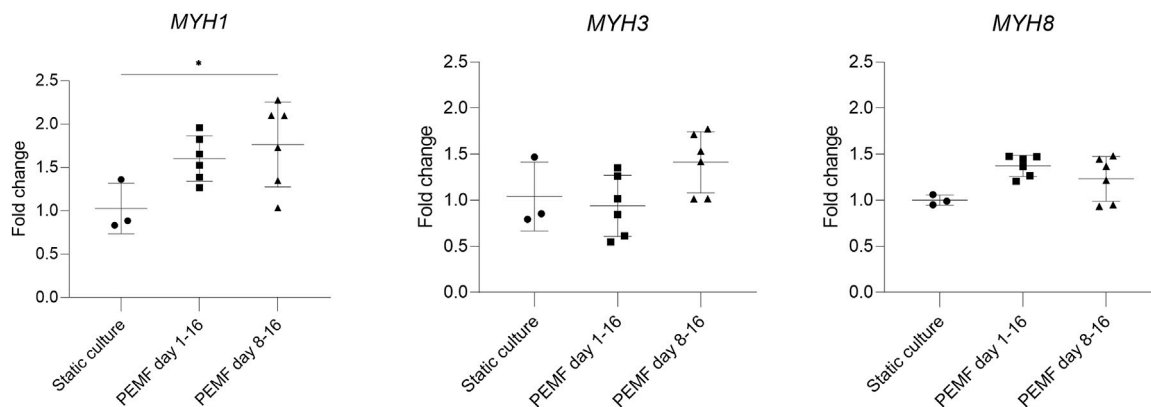


**FIGURE 5 |** RT-qPCR analysis of the constructs ( $n = 3$  control,  $n = 6$  stimulated conditions). PEMF groups were compared to static culture by one-way ANOVA. The difference in expression of *MYH1* indicates a tendency for mature construct formation.

control condition ( $1.0 \pm 0.3$ ,  $n = 3$ ). A similar, yet lower, tendency is observed when continuous stimulation is applied throughout the whole culture period (stimulation applied from day 0 until day 16) ( $1.6 \pm 0.3$ ,  $n = 6$ ). Both PEMF stimulation conditions did not result in a significant difference in the expression of *MYH3* nor *MYH8*.

## DISCUSSION

To enhance myoblast fusion and increase myotube diameter within engineered skeletal muscle, several types of biophysical stimuli have been studied. Mostly, mechanical stimulation (Powell et al., 2002; Boonen et al., 2010; Aguilar-Agon et al., 2019) and electrical

stimulation (Langelaan et al., 2010; Khodabukus et al., 2015; Khodabukus et al., 2019), and the synergistic effects have been explored (Somers et al., 2017; Maleiner et al., 2018). Tissue-engineered skeletal muscle constructs are expected to highly benefit from biophysical stimulation due to their intrinsic adaptive nature to exercise. While PEMF devices are being sold for muscle pain relief, only a few papers have described the influence on skeletal muscle of patients (Kim et al., 2012; Jeon et al., 2015). Interestingly, 30 Hz mechanical vibrations have been suggested to induce muscle hypertrophy in newborn mice *in vivo* and enhance terminal differentiation of satellite cells *in vitro*. Furthermore, high-frequency stimuli (30–90 Hz) have been suggested for musculoskeletal regenerative rehabilitation therapy (Thompson et al., 2016; Jones et al., 2020) which may act through activation of a mechano-sensitive signalling pathway (Uzer et al., 2015). Finally, a systematic review including trials that evaluated the effect of localised vibration on muscle strength in healthy individuals concluded that vibrations (8–300 Hz) can enhance the strength in healthy adults (Alghadir et al., 2018). To our knowledge, however, no studies have described the influence of PEMF on tissue-engineered skeletal muscle development. In this work, we applied the human BAM model to study the effects of PEMF on myoblast fusion, myotube size and myosin heavy chain isoform expression.

The biophysical PEMF stimulation protocol was optimized to enhance the development of human tissue-engineered skeletal muscle. In the first explorative phase, the stimulation was applied on 2D cultured human myoblasts, seeded on gelatin-coated culture plates, to explore the effect of the electromagnetic stimulus. Two different exposure times were selected in this explorative phase: 2 and 22 h, based on what was previously observed on myocytes and osteoblasts (Fassina et al., 2006; Fassina et al., 2009; Ceccarelli et al., 2013). In fact, for the osteoblasts, 24 h of exposure to PEMF increased the extracellular matrix deposition (Fassina et al., 2006; Patterson et al., 2006; Fassina et al., 2009), while 1-h exposure enhanced the proliferation of myofibroblasts in a diabetic cutaneous wound healing model (Cheing et al., 2014) and 3 h enhanced differentiation of C2C12 cells (Liu et al., 2017). For our bioreactor setup, we chose two exposure durations, 2 versus 22 h of PEMF stimulation per day. The cells stimulated for 22 h showed a significant enhancement of myotube diameter, and an increased overall area occupied with tropomyosin positive cells in 2D. Nonetheless, the 2 h PEMF-exposed cells showed an increasing trend of these parameters in comparison to the static culture, albeit non-significant. For both stimulation durations, no difference was found in the myoblast fusion index, however, this may be because the human myoblasts we used already had a high fusion index (>70%) in the unstimulated control, leaving little room for further improvement. To further evaluate the effect of PEMF, we switched to a human 3D bio artificial muscle model which more closely mimics native skeletal muscle. The same PEMF daily stimulation durations ranging from 2 to 22 h were applied and evaluated. Two hours of stimulation was found to enhance the myotube formation within 3D cultured BAMs, demonstrated by a significant increase in myotube diameter. In contrast to the 2D results, a longer stimulation of 22 h per day resulted in a myotube diameter similar to unstimulated control. The different behaviour of cells in 3D is the reason that there is an increasing shift towards using

3D models. Cells experience a different mechanical environment and form other cell-cell and cell-matrix contacts. Therefore, cells have a different arrangement of cytoskeletal organisation which in turn influences signalling; this concept is called tensegrity and it was already described nearly three decades ago (Ingber, 1993; Mammoto and Ingber, 2010). Since the BAMs are based on an initial fibrin hydrogel that surrounds the myoblasts, the tension to which the cells are exposed is very different from adherence to tissue culture plastic. In addition, the value of resting is generally accepted in muscle physiology but not yet studied in the SMTE field. Similar to what is known in sports physiology, resting time is important to allow proper muscle development. Still, the value of resting is not agreed upon in the field and various durations are described. Our 3D model was able to capture a deleterious effects of 22 h stimulation. The model may in the future aid in further dissecting the mechanisms behind positive versus negative effects of stimulation duration.

Using the 2 h of stimulation as the best exposure duration, we questioned whether the outcome could vary with starting the stimulation at different time points during the BAM development process. In literature, different protocols are reported with different starting points in the culture period, but the general tendency is that once the stimulation begins, it is generally applied every day until the end of the experiment (Patterson et al., 2006; Ceccarelli et al., 2013; Cheing et al., 2014; Liu et al., 2017). Since no general guidelines are reported, we compared two different starting points, being stimulation early on before myoblast fusion to myotubes occurred versus starting stimulation only after myotube formation. Myotube formation is typically induced in serum starvation medium for 4–5 days. In our protocol, this fusion induction was from days 3–8. Stimulation from days 8–16 as well as stimulation from days 1–16 resulted in an overall improved myotube formation as compared to the static control. Applying the stimulation after the formation of the myotubes resulted in the largest improvement with myotubes having an increased diameter and a higher area of cells versus the extracellular matrix. Interestingly, the fusion index was further augmented, also in the group where PEMF stimulation only started after fusion for 5 days. This indicates that PEMF is efficient in further stimulating myoblast fusion even when the medium is already returned to a serum-rich growth medium. Further characterization on the molecular level by RT-qPCR analysis for the different myosin heavy chain isoforms showed that the chosen condition displayed an increased expression of the mature form of myosin heavy chain (*MYH1*), indicative of an enhanced myotube formation within the construct.

PEMF stimulation has not been applied thus far in the context of muscle tissue engineering. It was the purpose of this work to establish if this PEMF stimulation affected the early stages of differentiation. The presented findings are encouraging and warrant further follow-up studies in which many other parameters and ultimately more functional analysis can be performed. In this work, we focused on fixed PEMF stimulus to determine solely the impact of exposure duration and starting point. Still, a wide range of PEMF stimulation protocols can be set up by varying other field parameters such as frequency and magnitude. The current study had a well-delineated scope and served to open a novel subfield.



In summary, the present work has studied the use of PEMF stimulation for human skeletal muscle tissue engineering. We demonstrated that PEMF stimulation can enhance myoblast fusion and can increase myotube diameter, with myotubes expressing more of the adult myosin heavy chain isoform. We also show that the BAM model can be used to study the effects of muscle stimulation protocols and that the effects on this 3D model are different from what is observed in 2D.

## DATA AVAILABILITY STATEMENT

The datasets presented in this study can be found in online repositories. The names of the repository/repositories and accession number(s) can be found below: <https://osf.io/59k3g/59k3g>.

## REFERENCES

- Aguilar-Agon, K. W., Capel, A. J., Martin, N. R. W., Player, D. J., and Lewis, M. P. (2019). Mechanical Loading Stimulates Hypertrophy in Tissueengineered Skeletal Muscle: Molecular and Phenotypic Responses. *J. Cell. Physiology* 234 (12), 23547–23558. doi:10.1002/jcp.28923
- Alghadir, A. H., Anwer, S., Zafar, H., and Iqbal, Z. A. (2018). Effect of Localised Vibration on Muscle Strength in Healthy Adults: a Systematic Review. *Physiotherapy* 104 (1), 18–24. doi:10.1016/j.physio.2017.06.006
- Boonen, K. J. M., Langelaan, M. L. P., Polak, R. B., van der Schaft, D. W. J., Baaijens, F. P. T., and Post, M. J. (2010). Effects of a Combined Mechanical Stimulation Protocol: Value for Skeletal Muscle Tissue Engineering. *J. Biomechanics* 43 (8), 1514–1521. doi:10.1016/j.jbiomech.2010.01.039
- Ceccarelli, G., Bloise, N., Mantelli, M., Gastaldi, G., Fassina, L., De Angelis, M. G., et al. (2013). A Comparative Analysis of the In Vitro Effects of Pulsed Electromagnetic Field Treatment on Osteogenic Differentiation of Two Different Mesenchymal Cell Lineages. *BioResearch Open Access* 2 (4), 283–294. doi:10.1089/biores.2013.0016
- Cheing, G. L.-Y., Li, X., Huang, L., Kwan, R. L.-C., and Cheung, K.-K. (2014). Pulsed Electromagnetic Fields (PEMF) Promote Early Wound Healing and Myofibroblast Proliferation in Diabetic Rats. *Bioelectromagnetics* 35 (3), 161–169. doi:10.1002/bem.21832
- Diz-Muñoz, A., Krieg, M., Bergert, M., Ibarlucea-Benitez, I., Muller, D. J., Paluch, E., et al. (2010). Control of Directed Cell Migration *In Vivo* by Membrane-To-Cortex Attachment. *PLoS Biol.* 8 (11), e1000544. doi:10.1371/journal.pbio.1000544
- Fassina, L., Saino, E., Sbarra, M. S., Visai, L., Cusella De Angelis, M. G., Mazzini, G., et al. (2009). Ultrasonic and Electromagnetic Enhancement of a Culture of Human SAOS-2 Osteoblasts Seeded onto a Titanium Plasma-Spray Surface. *Tissue Eng. Part C. Methods* 15 (2), 233–242. doi:10.1089/ten.tec.2008.0398
- Fassina, L., Visai, L., Benazzo, F., Benedetti, L., Calligaro, A., De Angelis, M. G. C., et al. (2006). Effects of Electromagnetic Stimulation on Calcified Matrix Production by SAOS-2 Cells over a Polyurethane Porous Scaffold. *Tissue Eng.* 12 (7), 1985–1999. doi:10.1089/ten.2006.12.1985
- Gholobova, D., Decroix, L., Van Muylder, V., Desender, L., Gerard, M., Carpentier, G., et al. (2015). Endothelial Network Formation within Human Tissue-Engineered Skeletal Muscle. *Tissue Eng. Part A* 21 (19–20), 2548–2558. doi:10.1089/ten.tea.2015.0093
- Gholobova, D., Gerard, M., Decroix, L., Desender, L., Callewaert, N., Annaert, P., et al. (2018). Human Tissue-Engineered Skeletal Muscle: a Novel 3D *In Vitro* Model for Drug Disposition and Toxicity after Intramuscular Injection. *Sci. Rep.* 8 (1), 1–14. doi:10.1038/s41598-018-30123-3
- Gholobova, D., Gerard, M., Terrie, L., Desender, L., Shansky, J., Vandenberg, H., et al. (2019). Coculture Method to Obtain Endothelial Networks within Human Tissue-Engineered Skeletal Muscle. *Methods Mol. Biol.* 1889, 169–183. doi:10.1007/978-1-4939-8897-6\_10

## AUTHOR CONTRIBUTIONS

LTe and MB: experimental design, data generation, data analysis, statistics, data interpretation—SV, LF, and LTh: contribution of critical components, data interpretation—LTh: experimental design, data interpretation, project supervision. All authors critically contributed to writing, editing and reviewing the manuscript.

## FUNDING

This work was funded by Fonds Wetenschappelijk Onderzoek—Vlaanderen (G0D3620N, S002821N and 1133520N), Interreg 3D4Med (including co-financing of the province of West-Flanders and the Hermes fund) and KU Leuven C24E/20/067.

- Gholobova, D., Terrie, L., Mackova, K., Desender, L., Carpentier, G., Gerard, M., et al. (2020). Functional Evaluation of Prevascularization in One-Stage versus Two-Stage Tissue Engineering Approach of Human Bio-Artificial Muscle. *Biofabrication* 12 (3), 035021. doi:10.1088/1758-5090/ab8f36
- Ingber, D. E. (1993). Cellular Tensegrity: Defining New Rules of Biological Design that Govern the Cytoskeleton. *J. Cell Sci.* 104 (3), 613–627. doi:10.1242/jcs.104.3.613
- Jeon, H.-S., Kang, S.-Y., Park, J.-H., and Lee, H.-S. (2015). Effects of Pulsed Electromagnetic Field Therapy on Delayed-Onset Muscle Soreness in Biceps Brachii. *Phys. Ther. Sport* 16 (1), 34–39. doi:10.1016/j.ptsp.2014.02.006
- Jones, G., Smallwood, C., Ruchti, T., Blotter, J., and Feland, B. (2020). A Mathematical Model of Skeletal Muscle Regeneration with Upper Body Vibration. *Math. Biosci.* 327, 108424. doi:10.1016/j.mbs.2020.108424
- Khodabukus, A., Baehr, L. M., Bodine, S. C., and Baar, K. (2015). Role of Contraction Duration in Inducing Fast-To-Slow Contractile and Metabolic Protein and Functional Changes in Engineered Muscle. *J. Cell. Physiol.* 230 (10), 2489–2497. doi:10.1002/jcp.24985
- Khodabukus, A., Madden, L., Prabhu, N. K., Koves, T. R., Jackman, C. P., Muoio, D. M., et al. (2019). Electrical Stimulation Increases Hypertrophy and Metabolic Flux in Tissue-Engineered Human Skeletal Muscle. *Biomaterials* 198, 259–269. doi:10.1016/j.biomaterials.2018.08.058
- Khodabukus, A. (2021). Tissue-Engineered Skeletal Muscle Models to Study Muscle Function, Plasticity, and Disease. *Front. Physiol.* 12. doi:10.3389/fphys.2021.619710
- Kim, S.-B., Kim, J.-Y., Park, S.-W., Lee, N.-R., Kim, Y.-H., Lee, K.-J., et al. (2012). Effects of PEMFs (Pulsed Electromagnetic Fields) Stimulation on Acupoint in Quadriceps Fatigue Recovery. *Int. J. Precis. Eng. Manuf.* 13 (9), 1697–1703. doi:10.1007/s12541-012-0222-0
- Langelaan, M. L. P., Boonen, K. J., Rosaria-Chak, K. Y., van der Schaft, D. W., Post, M. J., and Baaijens, F. P. (2010). Advanced Maturation by Electrical Stimulation: Differences in Response between C2C12 and Primary Muscle Progenitor Cells. *Ann. Am. Thorac. Soc.* 12 (3), 181–204. doi:10.1002/term.345
- Liu, M., Lee, C., Laron, D., Zhang, N., Waldorff, E. I., Ryaby, J. T., et al. (2017). Role of Pulsed Electromagnetic Fields (PEMF) on Tenocytes and Myoblasts—Potential Application for Treating Rotator Cuff Tears. *J. Orthop. Res.* 35 (5), 956–964. doi:10.1002/jor.23278
- Maffioletti, S. M., Sarcar, S., Henderson, A. B. H., Mannhardt, I., Pinton, L., Moyle, L. A., et al. (2018). Three-Dimensional Human iPSC-Derived Artificial Skeletal Muscles Model Muscular Dystrophies and Enable Multilineage Tissue Engineering. *Cell Rep.* 23, 899–908. doi:10.1016/j.celrep.2018.03.091
- Maleiner, B., Tomasch, J., Heher, P., Spadiut, O., Rünzler, D., and Fuchs, C. (2018). The Importance of Biophysical and Biochemical Stimuli in Dynamic Skeletal Muscle Models. *Front. Physiol.* 9, 1–24. doi:10.3389/fphys.2018.01130
- Mammoto, T., and Ingber, D. E. (2010). Mechanical Control of Tissue and Organ Development. *Development* 137 (9), 1407–1420. doi:10.1242/dev.024166
- Marmotti, A., Peretti, G. M., Mattia, S., Mangiavini, L., de Girolamo, L., Viganò, M., et al. (2019). Corrigendum to “Pulsed Electromagnetic Fields Improve

- Tenogenic Commitment of Umbilical Cord-Derived Mesenchymal Stem Cells: A Potential Strategy for Tendon Repair-An *In Vitro* Study". *Stem Cells Int.* 2019, 9761573. doi:10.1155/2019/9761573
- Mognaschi, M. E., Di Barba, P., Magenes, G., Lenzi, A., Naro, F., and Fassina, L. (2014). Field Models and Numerical Dosimetry inside an Extremely-low-Frequency Electromagnetic Bioreactor: the Theoretical Link between the Electromagnetically Induced Mechanical Forces and the Biological Mechanisms of the Cell Tensegrity. *Springerplus* 3 (1), 473. doi:10.1186/2193-1801-3-473
- Osera, C., Fassina, L., Amadio, M., Venturini, L., Buoso, E., Magenes, G., et al. (2011). Cytoprotective Response Induced by Electromagnetic Stimulation on SH-Sy5y Human Neuroblastoma Cell Line. *Tissue Eng. Part A* 17, 2573–2582. doi:10.1089/ten.tea.2011.0071
- Patterson, T. E., Sakai, Y., Grabiner, M. D., Ibiwoye, M., Midura, R. J., Zborowski, M., et al. (2006). Exposure of Murine Cells to Pulsed Electromagnetic Fields Rapidly Activates the mTOR Signaling Pathway. *Bioelectromagnetics* 27 (7), 535–544. doi:10.1002/bem.20244
- Powell, C. A., Smiley, B. L., Mills, J., and Vandenburg, H. H. (2002). Mechanical Stimulation Improves Tissue-Engineered Human Skeletal Muscle. *Am. J. Physiology-Cell Physiology* 283 (5), C1557–C1565. doi:10.1152/ajpcell.00595.2001
- Somers, S. M., Spector, A. A., DiGirolamo, D. J., and Grayson, W. L. (2017). Biophysical Stimulation for Engineering Functional Skeletal Muscle. *Tissue Eng. Part B Rev.* 23 (4), 362–372. doi:10.1089/ten.teb.2016.0444
- Thompson, W. R., Scott, A., Loghmani, M. T., Ward, S. R., and Warden, S. J. (2016). Understanding Mechanobiology: Physical Therapists as a Force in Mechanotherapy and Musculoskeletal Regenerative Rehabilitation. *Phys. Ther.* 96 (4), 560–569. doi:10.2522/ptj.20150224
- Thorrez, L., DiSano, K., Shansky, J., and Vandenburg, H. (2018). Engineering of Human Skeletal Muscle with an Autologous Deposited Extracellular Matrix. *Front. Physiol.* 9, 1–11. doi:10.3389/fphys.2018.01076
- Uzer, G., Thompson, W. R., Sen, B., Xie, Z., Yen, S. S., Miller, S., et al. (2015). Cell Mechanosensitivity to Extremely Low-Magnitude Signals Is Enabled by a LINCed Nucleus. *a LINCed Nucleus* 33 (6), 2063–2076. doi:10.1002/stem.2004.Cell
- Varani, K., Vincenzi, F., Pasquini, S., Blo, I., Salati, S., Cadossi, M., et al. (2021). Pulsed Electromagnetic Field Stimulation in Osteogenesis and Chondrogenesis: Signaling Pathways and Therapeutic Implications. *Int. J. Mol. Sci.* 22 (2), 809–817. doi:10.3390/ijms22020809
- Vigodarzere, G. C., and Mantero, S. (2014). Skeletal Muscle Tissue Engineering: Strategies for Volumetric Constructs. *Front. Physiol.* 5, 1–13. doi:10.3389/fphys.2014.00362
- Wang, T., Wang, P., Cao, Z., Wang, X., Wang, D., Shen, Y., et al. (2017). Effects of BMP9 and Pulsed Electromagnetic Fields on the Proliferation and Osteogenic Differentiation of Human Periodontal Ligament Stem Cells. *Bioelectromagnetics* 38 (1), 63–77. doi:10.1002/bem.22018

**Conflict of Interest:** The authors declare that the research was conducted in the absence of any commercial or financial relationships that could be construed as a potential conflict of interest.

**Publisher's Note:** All claims expressed in this article are solely those of the authors and do not necessarily represent those of their affiliated organizations, or those of the publisher, the editors and the reviewers. Any product that may be evaluated in this article, or claim that may be made by its manufacturer, is not guaranteed or endorsed by the publisher.

Copyright © 2022 Terrie, Burattini, Van Vlierberghe, Fassina and Thorrez. This is an open-access article distributed under the terms of the Creative Commons Attribution License (CC BY). The use, distribution or reproduction in other forums is permitted, provided the original author(s) and the copyright owner(s) are credited and that the original publication in this journal is cited, in accordance with accepted academic practice. No use, distribution or reproduction is permitted which does not comply with these terms.



# Identification of Small-Molecule Inhibitors for Osteosarcoma Targeted Therapy: Synchronizing *In Silico*, *In Vitro*, and *In Vivo* Analyses

Juan Liu<sup>1†</sup>, Qi Yao<sup>1†</sup>, Yu Peng<sup>1</sup>, Zhihong Dong<sup>1</sup>, Lu Tang<sup>1</sup>, Xiaoyu Su<sup>1</sup>, Lishuang Liu<sup>1</sup>, Cheng Chen<sup>1</sup>, Murugan Ramalingam<sup>1,2\*</sup> and Lijia Cheng<sup>1\*</sup>

<sup>1</sup>School of Basic Medical Sciences, Affiliated Hospital, School of Mechanical Engineering, Chengdu University, Chengdu, China, <sup>2</sup>Institute of Tissue Regeneration Engineering, Department of Nanobiomedical Science, BK21 NBM Global Research Center for Regenerative Medicine, Dankook University, Cheonan, South Korea

## OPEN ACCESS

### Edited by:

Anuj Kumar,  
Yeungnam University, South Korea

### Reviewed by:

Atul Dev,  
University of California, Davis,  
United States  
Durgalakshmi Dhinasekaran,  
Anna University, India

### \*Correspondence:

Murugan Ramalingam  
rmurug2000@gmail.com  
Lijia Cheng  
chenglijia@cdu.edu.cn

<sup>†</sup>These authors share first authorship

### Specialty section:

This article was submitted to  
Biomaterials,  
a section of the journal  
Frontiers in Bioengineering and  
Biotechnology

**Received:** 15 April 2022

**Accepted:** 16 May 2022

**Published:** 23 June 2022

### Citation:

Liu J, Yao Q, Peng Y, Dong Z, Tang L, Su X, Liu L, Chen C, Ramalingam M and Cheng L (2022) Identification of Small-Molecule Inhibitors for Osteosarcoma Targeted Therapy: Synchronizing *In Silico*, *In Vitro*, and *In Vivo* Analyses. *Front. Bioeng. Biotechnol.* 10:921107. doi: 10.3389/fbioe.2022.921107

**Objective:** The study aimed to explore a new approach for the treatment of osteosarcoma through combining biomaterials with next-generation small molecule-based targeted therapy.

**Methods:** The model of osteosarcoma was established by 4-hydroxyaminoquinoline 1-oxide (4-HAQO) in mice while the collagen-thermosensitive hydrogel-calcium phosphate (CTC) biocomposites were prepared, and the small molecule inhibitors were virtually screened and synthesized. Then, for the osteosarcoma cell line, MG-63 cells were used to validate our bioinformatic findings *in vitro*, and the mouse osteosarcoma models were treated by combining CTC composites and small-molecule inhibitors after debridement.

**Results:** Five compounds, namely, ZINC150338698, ZINC14768621, ZINC4217203, ZINC169291448, and ZINC85537017, were found in the ZINC database. Finally, ZINC150338698 was selected for chemical synthesis and experimental verification. The results of the MTT assay and Hoechst staining showed that the small-molecule inhibitor ZINC150338698 could significantly induce MG-63 cell death. Furthermore, CTC composites and ZINC150338698 could repair the bone defects well after the debridement of osteosarcoma. In addition, the biomaterials and small-molecule inhibitors have good biocompatibility and biosafety.

**Conclusion:** Our findings not only offer systems biology approach-based drug target identification but also provide new clues for developing novel treatment methods for future osteosarcoma research.

**Keywords:** osteosarcoma, biocomposites, small molecules, virtual screening, targeted therapy

## INTRODUCTION

Osteosarcoma is the most common primary bone cancer in children and adolescents and the third most common in adults (Czarnecka et al., 2020). With the development of surgery and chemotherapy, the survival rate of osteosarcoma patients without distant metastasis has been greatly improved. However, although the treatment of osteosarcoma has improved in the past three decades, the overall survival rate of patients has reached a plateau, and about 30–40% of the patients experienced progressive metastasis and died within 5 years after diagnosis (Fernandez-Pineda et al.,

2011; Liao et al., 2019). Therefore, it is necessary to find new biomarkers and molecular therapeutic targets for osteosarcoma.

Targeted therapy, also referred to as precision medicine, is a relatively new type of cancer treatment, particularly osteosarcoma, and currently, there is tremendous progress toward the development of targeted drugs. The targeted therapy for osteosarcoma using small-molecule drugs would conceptually be more specific than the conventional non-targeted therapy, such as chemotherapy, radiation therapy, and surgical treatment. The reason is that the small-molecule drugs are small enough to enter the targeted cancer cells, but not the normal cells, and can block the pathway that is responsible for the cancer cells to multiply and spread.

In the past decade, molecular therapeutic targets for bone cancer were identified as individual gene products, and various systems biology approaches are being employed that involve unbiased genome sequencing. DAVID is a Database for Annotation, Visualization, and Integrated Discovery (Dennis et al., 2003). GO (Gene Ontology) and KEGG (Kyoto Encyclopedia of Genes and Genomes) pathway analyses can be performed in DAVID. The STRING database is the network and enrichment facilities in STRING that enable the comprehensive characterization of user gene lists and functional genomics datasets and allow the creation of protein–protein interaction (PPI) networks (Szklarczyk et al., 2021). In this study, we selected two microarray datasets (GSE12865 and GSE36001) from the GEO (Gene Expression Omnibus) database for analysis and screened out differentially expressed genes (DEGs) between osteosarcoma patients and normal people. Through comprehensive analysis in DAVID and STRING databases, the key genes of osteosarcoma were obtained. Then, molecular docking was used to screen out the small-molecule inhibitors that may inhibit the growth of osteosarcoma.

In the conventional treatment of osteosarcoma, the tumor part is surgically removed. The large segment of bone defects left behind by surgical debridement would not heal on their own and require bone grafts to be filled (Dang et al., 2020; Feder et al., 2020). There are a variety of biomaterials that have been used for bone repair and regenerative applications. Calcium phosphate-based composite is one of the effective biomaterials with wide application prospects (Schweikle et al., 2019). Our previous experiments have proved that collagen-thermosensitive hydrogel–calcium phosphate (CTC) bio-composites have excellent osteoinductivity, osteoconductivity, and biological activity, which could be used for load-bearing bone repair. Furthermore, we also have previously demonstrated that the osteogenic ability of CTC is stronger than that of traditional calcium phosphate biomaterials, such as hydroxyapatite/tricalcium phosphate (HA/TCP) (Cheng et al., 2021). Keeping these points in view, in this study, we explored a new approach of targeted therapy by combining surgery, biomaterials with small-molecule inhibitors by database screening, which could treat the mouse osteosarcoma constructed with 4-hydroxyaminoquinoline 1-oxide (4-HAQO). This study may open a new avenue and direct the path for developing novel treatment methods for future osteosarcoma research.

## MATERIALS AND METHODS

### Mouse Osteosarcoma Model Construction

Twenty BALB/c mice were purchased from Dossy Biological Technology Company (Chengdu, China). All animals were maintained in a temperature and light-controlled environment ventilated with filtered air. All animals were anesthetized with an intraperitoneal injection of pentobarbital sodium. The hair on both legs was removed using an electric shaver, and the skin underneath was disinfected with 75% ethanol, and then, the skin and muscle were cut open, and the tibia was exposed; then, an incision was made to the tibia to expose the marrow cavity; next, 1 mg 4-HAQO was placed into the incision of the bone marrow with a small scraper in the right leg of the mouse, and the left leg had the tibia cut off without any drugs in the same mouse. Twelve weeks later, the osteosarcoma models were identified by histological staining and used for subsequent treatment. The study is reported in accordance with Animal Research: Reporting of *In Vivo* Experiments (ARRIVE) guidelines version 2.0 (Percie du Sert et al., 2020). The Animal Care and Use Committee of Chengdu University approved the study. The operative procedures and animal care were performed in compliance with ARRIVE guidelines on the care and use of laboratory animals, under the supervision of a licensed veterinarian.

### Targets Screening of Key Genes of Osteosarcoma

Two sets of microarray data from the GEO database set were selected, including GSE12865 and GSE36001. The selection criteria were as follows: 1) osteosarcoma; 2) *Homo sapiens*; 3) tissue or cells containing both normal and tumor types; and 4) DNA copy. GSE36001 was based on the GPL6102 platform (Illumina Human-6 v2.0 Expression Beadchip) and contained 19 osteosarcoma samples and six normal samples (Sadikovic et al., 2009). GSE12865 was based on the GPL6244 platform {(HuGene-1\_0-st) Affymetrix Human Gene 1.0 ST Array [transcript (gene) version]} and contained 12 osteosarcoma samples and two osteoblast samples (Kresse et al., 2012). GEO2R (<https://www.ncbi.nlm.nih.gov/geo/geo2r/>) analysis was used to obtain differentially expressed genes (DEGs). The  $|\text{LogFC}| > 1$  and  $p < 0.05$  were set as DEG cutoff criteria. Gene ontology (GO) and KEGG pathway enrichment analyses were performed using the DAVID (version 6.8) online tool (<https://david.ncifcrf.gov/>) (Dennis et al., 2003). GO can be applied to the functions of genes and proteins in all organisms, and there are mainly three types: biological processes, molecular functions, and cellular components. Next, construction and analysis of protein–protein interaction (PPI) networks were performed by STRING. As shown in **Figure 1A**, the PPI network was visualized by Cytoscape software, and the core network was identified by the MCODE module. Through DAVID and STRING databases, the key genes of osteosarcoma were screened out.



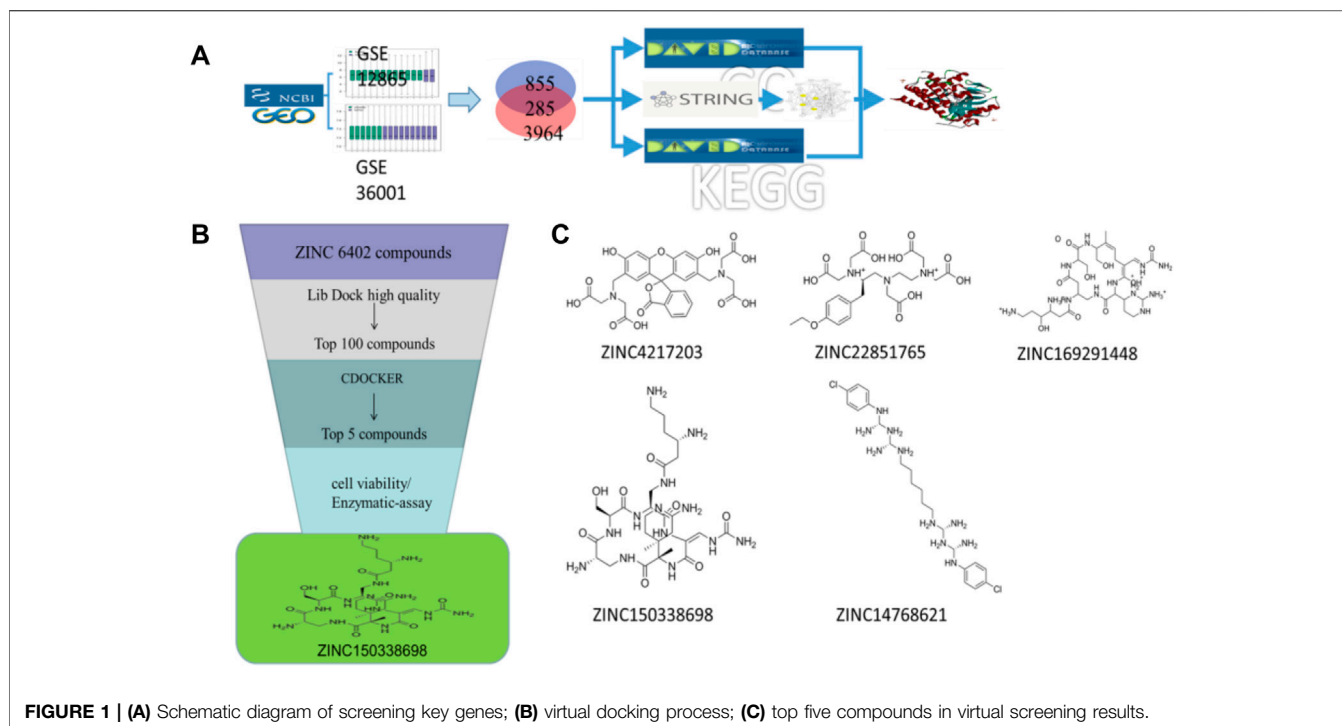


**FIGURE 1 | (A)** Schematic diagram of screening key genes; **(B)** virtual docking process; **(C)** top five compounds in virtual screening results.

## Molecular Docking and Screening of Candidate Compounds

The 3D X-ray crystal structure of CSF1R (PDB ID: 6T2W) was downloaded from the RCSB protein database (<http://www.rcsb.org/>). A total of 6403 candidate compounds were collected from the subset world of the ZINC database (<https://zinc.docking.org/substances/subsets/world/>). Protein 6T2W (receptor) and these compounds (ligands) were used in molecular docking studies by Discovery Studio (DS) to evaluate binding affinities between them. In DS, LibDOCK and CDOCKER programs were adopted for molecular docking for semi-flexible docking. The binding site of the known ligand (Ligand1) in the 6T2W structure is selected and defined as an active pocket, the ligand molecules are prepared, the energy of compounds is minimized, and the LibDOCK program is used for preliminary docking, and the LibDOCK score is an index to evaluate docking results (**Figure 1B**). The top 100 small molecules are selected with the highest scores and different structures; the five compounds with the highest LibDOCK score are selected for the same molecule with different conformations (**Figure 1C**). Next, a second docking was performed using the CDOCKER program provided in DS, and CDOCKER INTERACTION ENERGY evaluated the effectiveness of the docking of different chemicals. CDOCKER ENERGY is best preserved for different conformations of the same compound. In this program, the molecular docking method based on CHARMM was used to dock the ligand with the protein-binding site. When high-temperature molecular dynamics (MD) is used, CDOCKER allows a single protein target to be finely docked to a large

number of ligands, resulting in a random ligand conformation. Last, the compound ZINC150338698 with the best CDOCKER INTERACTION ENERGY was selected for chemical synthesis.

## Cell Culture

MG-63 cells were purchased from American Type Culture Collection (ATCC, Manassas, VA, United States). The cells were cultured in Dulbecco's modified Eagle medium (DMEM) with 10% fetal bovine serum (FBS) and 1% penicillin/streptomycin and maintained in a 5% CO<sub>2</sub>/37°C incubator, respectively. Cells were used with 0.25% trypsin, DMEM, FBS, and antibiotics were purchased from Gibco (Carlsbad, CA, United States).

## (4,5-Dimethyl-2-Thiazolyl)-2,5-Diphenyltetrazolium Bromide (MTT) Assay

For the assay,  $5 \times 10^3$  MG-63 cells were seeded in a 96-well plate, respectively. The small molecule inhibitor ZINC150338698 is dissolved in anhydrous ethanol and then diluted with normal saline. Eighteen hours post-seeding, cells were treated with different concentrations of ZINC150338698 as follows: 0.1 μmol/L, 1 μmol/L, and 10 μmol/L ZINC150338698. Cisplatin was used as a positive control, and untreated cells were set as blank control. Each group was set with three wells. Then, 48 h post drug treatments, the viable cells were stained by adding 20 μl of 5 mg/ml MTT solution per 100 μl of growth medium. After incubating for 4 h at 37°C, the media were removed, and 150 μl DMSO was added to dissolve the formazan. The absorbance of each well was measured by using

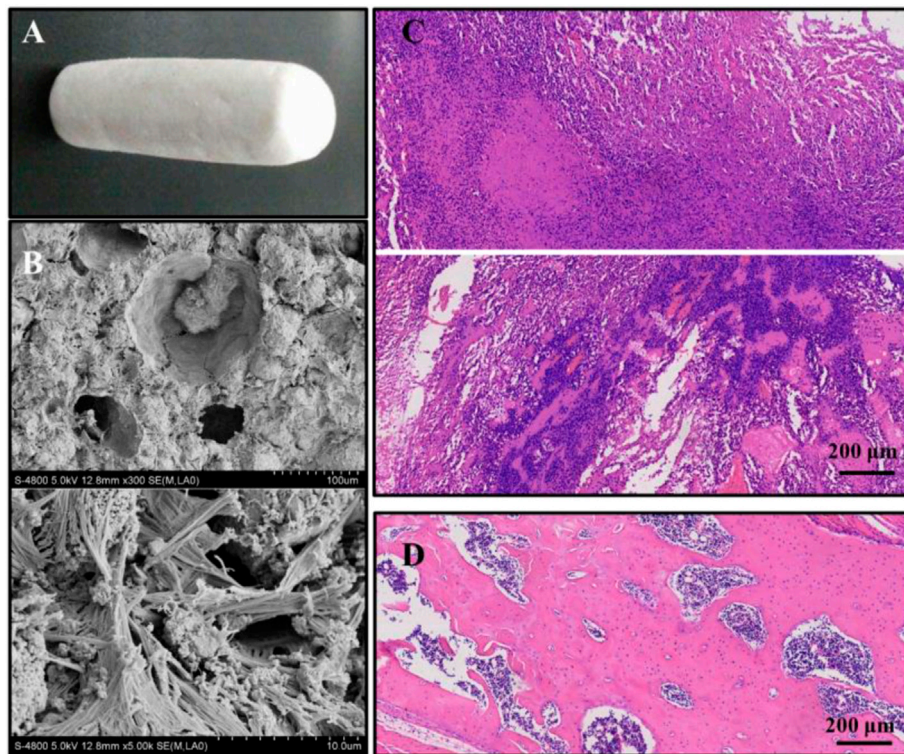


**FIGURE 2 | (A)** Macroscopic structures of collagen-thermosensitive hydrogel-calcium phosphate (CTC) composites; **(B)** microscopic structures by magnification 300 and 5000 times of CTC composites; **(C)** osteosarcoma models were successfully constructed by 4-HAQO, bar: 200  $\mu\text{m}$ ; **(D)** control group without tumors, bar: 200  $\mu\text{m}$ .

a microplate reader, and viable cells are presented as a percentage of the control.

### Hoechst Staining

For staining,  $1 \times 10^5$  MG-63 cells were seeded in a 6-well plate. The cells were treated with different concentrations of small-molecule ZINC150338698 as follows: 0.1  $\mu\text{mol/L}$ , 1  $\mu\text{mol/L}$ , and 10  $\mu\text{mol/L}$  ZINC150338698 after 18 h. Cisplatin was used as positive control, and untreated cells were set as blank control. Each group was set with three wells. Then, 48 h later, cells were stained with a Hoechst kit from Beyotime (Haimen, Jiangsu, China). Cell counting was carried out by ImageJ software from the National Institutes of Health, which is available at <http://rsbweb.nih.gov>. The corresponding cell death rates were calculated according to Hoechst staining.

### Western Blot

The cells were used to extract proteins and then were separated using a 10% polyacrylamide gel. After transferring the protein on a nitrocellulose membrane, the membrane was blocked with a 5% defatted milk solution and probed with the mouse monoclonal antibody against CSF1R (1:2000, Abcam) and GAPDH (1:5000, Chemicon) and then probed with a secondary antibody using ALP-conjugated anti-mouse IgG (1:5000, Chemicon). Last, blots were developed using an ECL Plus kit (GE, United States).

### Preparation of Collagen-Thermosensitive Hydrogel-Calcium Phosphate Composites

The bio-composites used in this study were made up of thermosensitive hydrogel using type I collagen and tricalcium phosphate powder. The ratio of type I collagen (Sigma-Aldrich, United States) to hydrogel solution was 15:25 and stirred for 10 min to obtain the mixture of the collagen-thermosensitive hydrogel. Then, the tricalcium phosphate powder [ $\text{Ca}_3(\text{PO}_4)_2$ , Sigma-Aldrich, United States] was weighed and mixed with the collagen-thermosensitive hydrogel solution in a ratio of 40:60 for 10 min. The collagen-thermosensitive hydrogel-calcium phosphate (CTC) mixture was obtained (Figure 2A). The surface structures of the composites were measured by scanning electron microscopy (SEM) (Figure 2B). The composites were fabricated into a shape corresponding to the debriement of osteosarcoma and steam-sterilized at 121°C for 15 min before implantation.

### Surgery and Targeted Therapy for Osteosarcoma

Ten mouse osteosarcoma models were selected and randomly divided into two groups ( $n = 5$ ): the experimental group and the control group. Then all animals were anesthetized with an intraperitoneal injection of pentobarbital sodium. The hair on

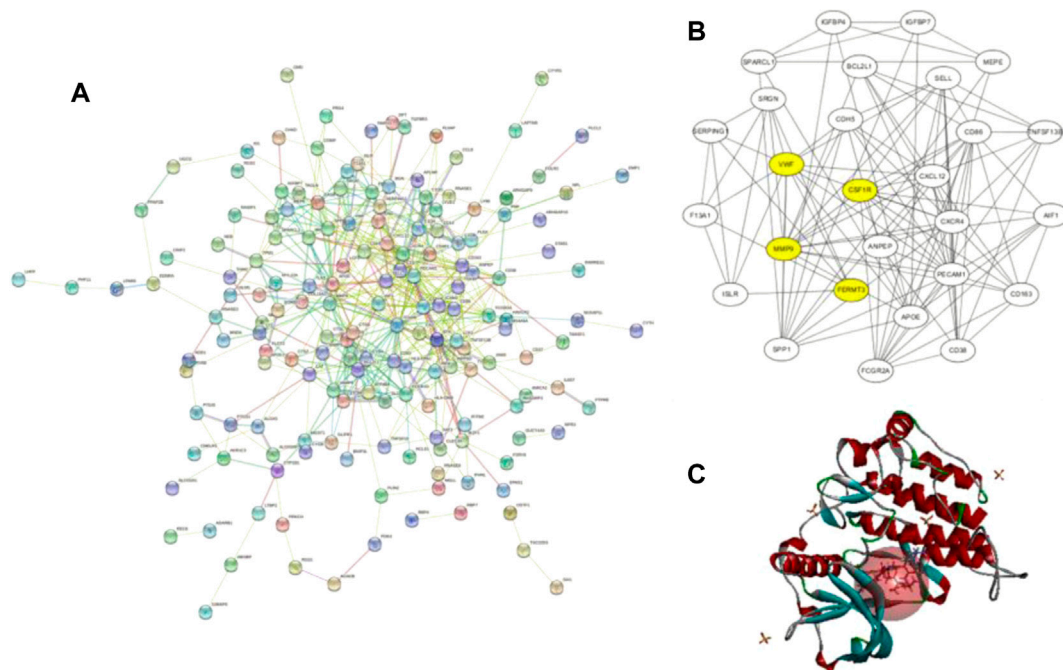


**FIGURE 3 | (A)** Protein–protein interaction network of upregulated genes from the STRING database; **(B)** this interaction network is the core network from **(A)**, which was calculated in Cytoscape. The four yellow core HUB proteins were obtained by comprehensive analysis with KEGG and GO; **(C)** binding diagram of ZINC150338698 to protein 6T2W, and the red ball is the binding site.

the right leg was removed using an electric shaver, and the skin underneath was disinfected with 75% ethanol and cut open. All tumor tissues were removed, including osteomas and sarcomas, and the tibia was amputated. In the experimental group, after debridement is completed, the tibial-shaped CTC composite was grafted to the bone defect and simply fixed. The skin was closed with nylon sutures, and penicillin was injected intramuscularly to prevent infection finally. Next, 50 mg/kg ZINC150338698 was injected through the tail vein from the day of the surgery, and then, the same dose was injected every 3 days, a total of 20 administrations. In the control group, there was no material filling and small-molecule inhibitor administration after debridement, the skin was closed, and penicillin was injected intramuscularly as the experimental group. After 60 days, the mice were sacrificed. The complete tibia was harvested and fixed with a 4% formaldehyde solution to be used for follow-up research.

### Detection of the Therapeutic Effect by Imaging

After fixation in the formaldehyde solution, the samples were stored in alcohol and sent to scan  $\mu$ -CT by a high-resolution Skyscan 1174 (Bruker, Belgium) at 10- $\mu$ m voxel resolution and 55 kV. For three-dimensional analysis by  $\mu$ -CT, 400 images of each sample were three-dimensionally reconstructed with the best threshold, and the overall and cross-section images were produced with their own software. In the meantime, the overall osteogenesis and bone trabecula were automatically analyzed

through the value of total volume (TV), bone volume (BV), BV/TV, structure model index (SMI), trabecular thickness (Tb.Th), trabecular number (Tb.N), trabecular separation (Tb.Sp), and bone mineral density (BMD).

### Detection of the Therapeutic Effect by Histology

After scanning  $\mu$ -CT, all samples were decalcified in 10% ethylene diamine tetraacetic acid (EDTA, pH 7.0) for about 20 days at room temperature, dehydrated, and embedded in paraffin. The embedded samples were cut into 5- $\mu$ m thick histological sections. Then, they were stained with hematoxylin-eosin (HE), Masson-trichrome staining, and tartrate-resistant acid phosphatase staining, according to the manufacturer's instructions. Finally, all tissue slices were imaged under the microscope and analyzed by image analysis software.

### Statistical Analysis

Data were expressed as means  $\pm$  standard deviation and analyzed by paired ANOVA (SPSS 13.0, SPSS, United States).  $p < 0.05$  was considered statistically significant.

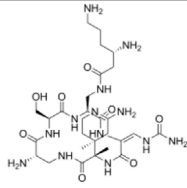
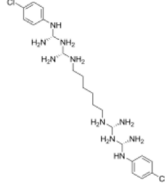
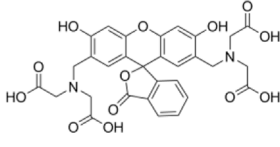
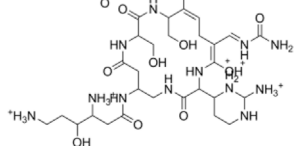
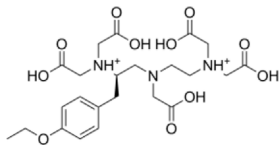
## RESULTS

### Construction of the Osteosarcoma Model

The osteosarcoma models were successfully constructed in 18 of the 20 mice with a success rate of 90% by 4-HAQO. The average



**TABLE 1 |** Top five compounds from virtual screening results.

	Name	2D STRACTION	-LibDOCK score	-CDOCKER INTERACTION ENERGY
1	ZINC150338698		148.955	88.2205
2	ZINC14768621		153.232	82.9094
3	ZINC4217203		169.416	82.0324
4	ZINC169291448		146.643	81.2782
5	ZINC22851765		163.706	80.7144

tumor volume was  $1581 \pm 367 \text{ mm}^3$ , and the average tumor weight was  $3.89 \pm 0.76 \text{ g}$ . In the osteosarcoma models, HE images showed obvious nuclear atypia of tumor cells, which were fusiform or polygonal; the multinucleated giant cells were also observed, and some blood vessels were surrounded by tumor cells (**Figure 2C**), while the fracture had healed and no tumor cells were observed in the control group (**Figure 2D**).

## Target Gene of Osteosarcoma

A total of 855 and 3964 DEGs were identified from GSE36001 and GSE12865 datasets. In total, 215 genes were screened out in two datasets and were selected for further analysis. The upregulated genes were analyzed by the David 6.8 online tool, and the results of Gene Ontology and KEGG pathway enrichment analyses were obtained, respectively. Meanwhile, we analyzed these upregulated genes through a STRING database to obtain a PPI network (**Figure 3A**); the core PPI network obtained by Cytoscape software contained 27 genes. Through the comprehensive integration of GO, KEGG pathway analysis, and Cytoscape software analysis results, four osteosarcoma key genes, *MMP9*, *FERMT3*, *CSF1R*, and *VWF*, were finally identified (**Figure 3B**).

There are some studies on the relationship between *MMP9*, *VWF*, and osteosarcoma. *FERMT3* has barely been studied. In addition, we found some studies on *CSF1R* in osteosarcoma in the past five years. In the study of Fujiwara et al. (2021), the FDA-approved *CSF1R* inhibitor PLX3397 can suppress the growth of osteosarcoma. Smeester et al. (2020) found that *CSF1R* is utilized by OSA cells to promote tumorigenesis. Wen et al. (2017) found that *CSF-1R* inhibition in osteosarcoma cells by RNA interference suppresses cell proliferation and tumor growth in mice. Finally, we chose to make some contributions to the research on *CSF1R* in osteosarcoma.

## Screening of CSF1R Inhibitors

The molecular docking of 6,403 compounds collected in the ZINC database with protein 6T2W was studied. Initial docking with the LibDOCK yielded 1,314,664 compounds, with the 100 compounds with the highest retention scores (all with -LibDOCK score >140). The second docking of these compounds by CDOCKER yielded 4,947 compounds. The top five compounds in docking results were ZINC150338698, ZINC14768621, ZINC4217203, ZINC169291448, and



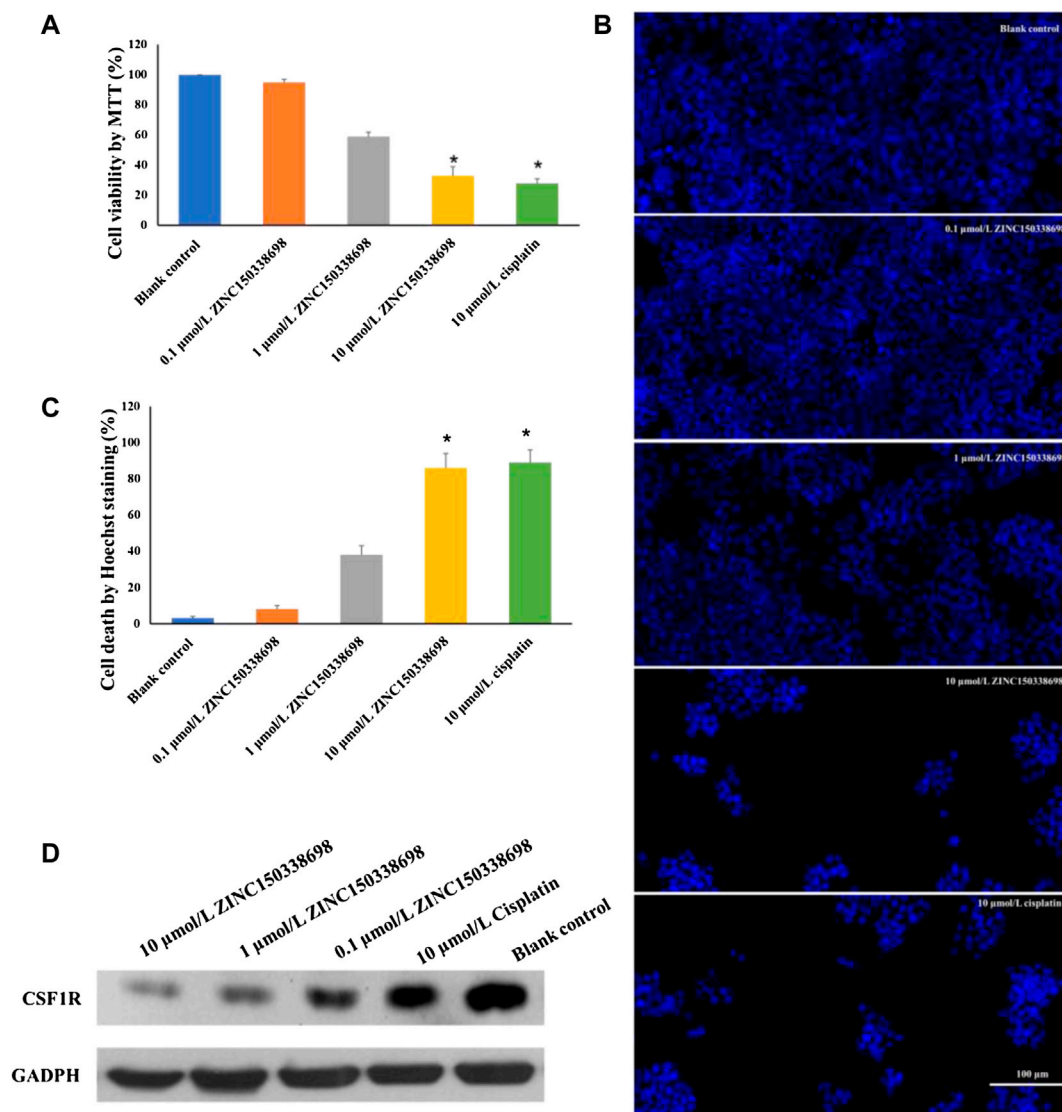


**FIGURE 4 | (A)** Viability of MG-63 cells was detected by MTT assay. The cell growth was significantly inhibited by 10  $\mu\text{mol/L}$  ZINC150338698 at 48 h. **(B)** Percentage of cell death according to Hoechst staining at 48 h. Compared with the blank control group,  $*p < 0.05$ . **(C)** Expression of CSF1R in MG-63 cells after treatment at 48 h; GAPDH was set as a positive control. **(D)** Corresponding gray-scale value of CSF1R based on GAPDH, compared with the blank control group,  $*p < 0.05$ .

ZINC85537017, as shown in **Table 1**, which might have effects on osteosarcoma. Finally, ZINC150338698, the compound with the best CDOCKER INTERACTION ENERGY, was selected for chemical synthesis and experimental verification. **Figure 3C** showed the binding diagram of ZINC150338698 to protein 6T2W.

### Effects of the Compound ZINC150338698 on Osteosarcoma Cell Viability

To determine whether the treatment of ZINC150338698 affected osteosarcoma cell survival abilities, the authors examined the cell viability by MTT assay after drug treatment for 48 h. The results

demonstrated that the cell survival abilities were significantly decreased with 10  $\mu\text{mol/L}$  ZINC150338698 ( $p < 0.05$ ), whose effects were similar to those of the positive control group (**Figure 4A**). To further investigate the effects of ZINC150338698 on the cell survival rate, the authors investigated the percentages of cell death of MG-63 cells, upon ZINC150338698 treatment by Hoechst staining. Compared to the untreated group, the percentage of dead cells was significantly increased in the group treated with 10  $\mu\text{mol/L}$  ZINC150338698 and cisplatin (**Figure 4B**). The expression of CSF1R was inhibited by ZINC150338698, especially by 10  $\mu\text{mol/L}$  ZINC150338698; however, cisplatin did not significantly inhibit the expression of CSF1R (**Figure 4C**). The gray-scale value of each band was

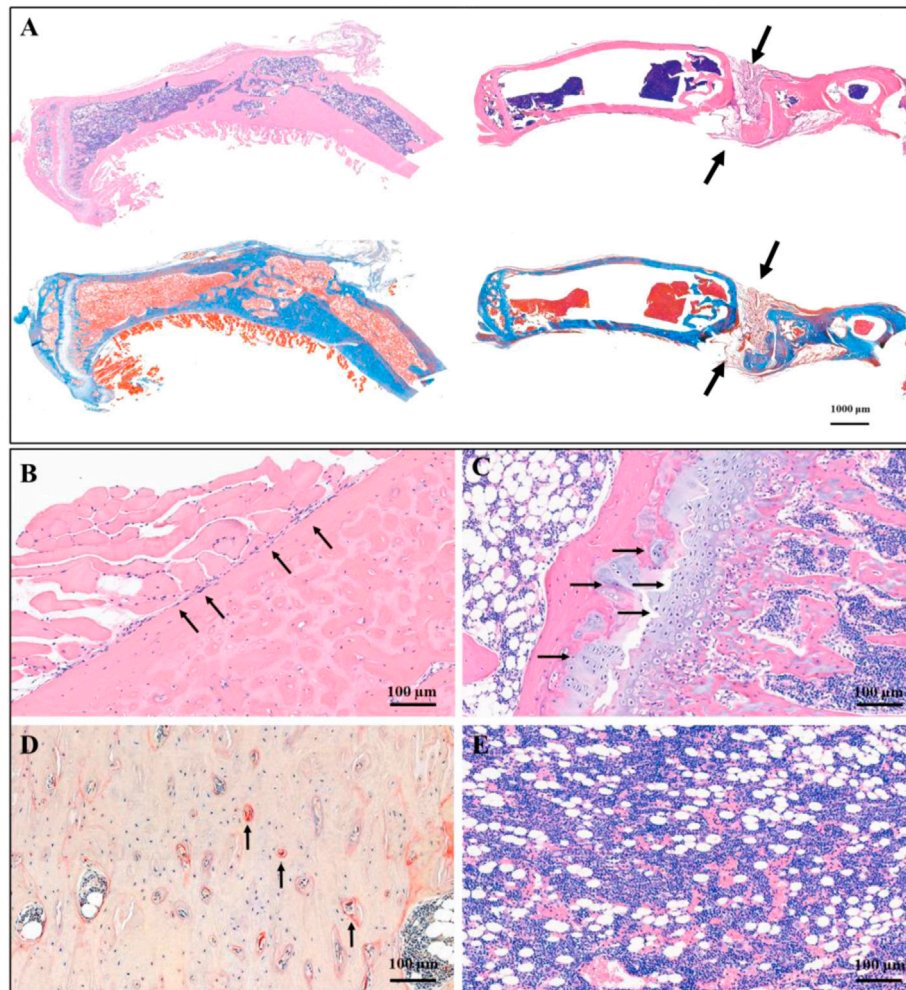


**FIGURE 5 |** Histological staining showed the therapeutic effect of CTC bio-composite engraftment and ZINC150338698 administration on osteosarcoma. **(A)** HE and Masson trichromatic staining showing the entire tibia in the experimental group (left) and the control group (right); the bone defect healed well in the experimental group, while the bone defect showed nonunion in the control group. Arrow: the unhealed bone defect; bar: 1000 μm. **(B)** In the area of new bone formation, the osteoblasts lined up around the new bone tissues by HE staining, arrow: osteoblasts; bar: 100 μm. **(C)** Growth of chondrocytes was detected by HE staining, indicating that the new bone is formed by endochondral ossification. Arrow: chondrocytes; bar: 100 μm. **(D)** Osteoclasts were determined by tartrate-resistant acid phosphatase staining, indicating the dynamic balance between osteoblasts and osteoclasts. Arrow: osteoclasts; bar: 100 μm. **(E)** Mature bone marrow tissue appeared in the marrow cavity. Bar: 100 μm.

converted to the relative expression of CSF1R (**Figure 4D**,  $*p < 0.05$ ). These results indicated that ZINC150338698 could effectively inhibit the osteosarcoma cell survival through the inhibition of CSF1R.

### New Bone Formation After Treatment

The osteosarcoma models were successfully constructed by 4-HAQO, to treat osteosarcoma, a combination of surgery, biomaterial filling, and targeted therapy was used. Two months later, the results showed that the removed tibia was replaced by new bone tissue, which was induced by the CTC composites, and the debridement defects healed well in the experimental group, while the results showed the bone nonunion at the debridement site, and the new bone tissue

grew irregularly in the control group (**Figure 5A**). We also found a balanced and dynamic growth of osteoblasts (**Figure 5B**), chondrocytes (**Figure 5C**), osteoclasts (tartrate-resistant acid phosphatase staining, **Figure 5D**), and marrow cells (**Figure 5E**) in the experimental group.

### Evaluation of the Postoperative Recovery

To reconstruct the real scene of bone healing *in vivo*, the micro-CT was used to reveal the specific and visualized repair results 60 days after surgery. The multi-view of sagittal, coronal, and transverse planes, and the stereogram was captured to show the details. From these pictures, it could be seen that the osteosarcoma was well treated, and no unhealed bone defect remained in the experimental group, while there is a bone nonunion in the control group (**Figure 6**). The results of micro-CT are

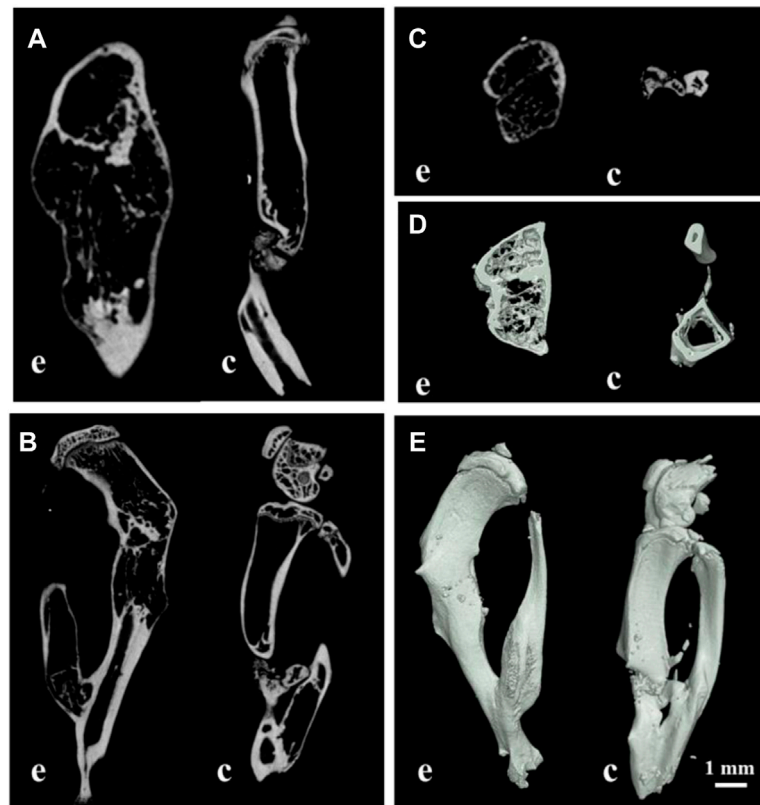


**FIGURE 6 |** Multi-view of sagittal (A), transverse (B), coronal (C), and sectional planes (D), and the stereogram (E) of mouse tibia by micro-CT; (E) the experimental group; (C) the control group; bar: 1 mm.

consistent with those of histological staining. According to the results of micro-CT, the data of osteogenesis and trabecula were analyzed with built-in software of micro-CT in the experimental group and control group, and the unoperated control group was set as a reference (Table 2), for further analysis of therapeutic effects.

### Biological Safety of Materials and Small-Molecule Inhibitors

After treatment of osteosarcoma with a combination of CTC composites and compound ZINC150338698, to detect the side effects of the biomaterials and small-molecule inhibitors, the authors examined the microscopic structure of the heart, liver, spleen, lung, kidney, and the muscle tissues adjacent to cancer tissues in the experimental group and the control group. The results showed that no inflammation, foreign body, or tumor tissue was observed in the two groups (Figure 7), which suggested our biomaterials and small-molecule inhibitors have good biocompatibility and biosafety.

### DISCUSSION

Osteosarcoma is the most common primary malignant bone tumor; the highest incidence is in children and adolescents

(median age of 18) (Corre et al., 2020). These tumors occur mainly in the long bones and less frequently in the skull, jaw, and pelvis. Nowadays, the best treatment options for osteosarcoma include chemotherapy, surgery, radiotherapy, and immunotherapy (Lussier et al., 2015; Yu et al., 2019; Hız et al., 2021); however, the optimal scheme has not yet been defined. Surgical treatment was fundamental, and the complete surgical resection of all sites of tumor tissues remains essential for survival (Kager et al., 2017). Over the past few decades, the prognosis of metastatic and relapsed osteosarcoma has remained stagnant, although several anticancer drugs have been clinically applied (Thanindrarn et al., 2019); the metastatic rate of osteosarcoma is as high as 40% within 5 years after diagnosis, metastasis to the lungs is common, but also to the liver and lymph. To date, new treatment options for osteosarcoma, especially relapsed and metastatic osteosarcoma, are still limited (Chen et al., 2021). Therefore, the development of appropriately targeted therapy drugs may effectively inhibit the metastasis of osteosarcoma.

In the study, by the method of bioinformatics analysis, the possible key genes of osteosarcoma including MMP9, FERMT3, CSF1R, and VWF were screened from two microarray datasets, GSE12865 and GSE36001. These four key genes may be potential targets for the diagnosis and treatment of osteosarcoma. Through consulting relevant literature reports, the four genes were analyzed, and finally, CSF1R was selected for subsequent

**TABLE 2 |** Parameters of osteogenesis in bone healing.

	TV (mm <sup>3</sup> )	BV (mm <sup>3</sup> )	BV/TV (%)	SMI	Tb.Th (mm)	Tb.N (1/mm)	Tb.Sp (mm)	BMD (g/Cm <sup>3</sup> )
Experimental group	18.3522 ± 0.3515	10.2593 ± 0.5796	0.5590 ± 0.0357	1.7965 ± 0.0593	0.1676 ± 0.0136*	2.1551 ± 0.1157*	0.6549 ± 0.0527	1.1546 ± 0.1654*
Control group	21.1975 ± 0.3675	8.5345 ± 0.2707	0.4026 ± 0.0091	2.3477 ± 0.0883	0.1175 ± 0.0070	1.1223 ± 0.0302	0.7019 ± 0.0305	0.6967 ± 0.0173
Unoperated control group	21.4892 ± 0.9957	14.7635 ± 0.6580	0.6870 ± 0.0430	1.6034 ± 0.0243	0.1782 ± 0.0094	2.8746 ± 0.1344	0.6012 ± 0.0442	1.6531 ± 0.1165

The comparison between the experimental group and control group, \*p < 0.05. TV: tissue volume; BV/TV: bone volume fraction; SMI: structural mode index; Tb: trabecular thickness; Tb.N: trabecular number; Tb.Sp: trabecular separation; BMD: bone mineral density.

research. CSF1R is a member of the receptor protein tyrosine kinase (rPTK) family of growth factor receptors (Ries et al., 2014). It has been proved that the infiltration of tumor-associated macrophages (TAMs) was related to the driving force of tumorigenesis and the suppression of antitumor immunity. CSF1R is a cellular receptor for colony-stimulating factor-1 (CSF-1) and interleukin-34 (IL-34), which plays a nuclear role in the manipulation of TAMs (Holmgaard et al., 2016; Xun et al., 2020). In this context, various approaches targeting either the ligands or the receptor are currently in clinical development. His existing inhibitors for CSF1R include PLX3397 and RG7155 (Ries et al., 2014). The FDA-approved CSF1R inhibitor PLX3397 can suppress the growth of osteosarcoma in mice (Fujiwara et al., 2021). We did not find a correlation between RG7155 and osteosarcoma. The protein structure expressed by CSF1R is subjected to molecular docking with compounds downloaded by ZINC in Discovery Studio. ZINC150338698 showed the best docking results when analyzed by LibDOCK and CDOCKER. Therefore, we chose ZINC150338698 small-molecule inhibitors for osteosarcoma *in vitro* and *in vivo*. Our results showed that the small-molecule inhibitor ZINC150338698 could effectively inhibit the proliferation of osteosarcoma cells *in vitro* and promote bone repair after surgery *in vivo*. However, the postoperative evaluation time is too short to directly indicate the effect of targeted therapy, and we will extend the evaluation time in future studies.

Most patients with osteosarcoma required surgical amputation to cure the tumor completely, which needed a bone graft (Zhao et al., 2020; Barr and Howe, 2018; El Beaino et al., 2019). At present, the most advantageous bone graft material was the artificial bone compared to autogenous and allogeneic bone grafts. Calcium phosphate-based composites were the focus of research in the department of orthopedics, stomatology, and plastic surgery in recent years, which could achieve the same effect of autologous bone transplantation with the advantages of economic, wide source, and no immunogenicity (Richter et al., 2019; Birkholz et al., 2016; Waiyawat et al., 2020; Ma et al., 2019). HE and Masson staining showed that the tibia was replaced by new bone tissue induced by the CTC composite. Tricalcium phosphate of CTC composites could degrade to form a hydroxyapatite layer and then serve as a cell scaffold to promote the proliferation of osteoblasts and detect the growth of chondrocytes; however, it needs to be combined with other substances to become osteoinductive, so the addition of type I collagen and temperature-sensitive hydrogel increases the mechanical properties of tricalcium phosphate and enhances its osteogenic properties. Micro-CT and histological staining showed that the material degraded in mice and induced tibial healing. We can speculate that the degradation rate of CTC material in mice is the same as that of bone healing and repair, thus ensuring complete tibial healing. In addition, it can also be inferred that the properties of CTC composites are stable and have no side effects in mice since there was no significant immune response and inflammatory reaction in the heart, liver, spleen, lung, kidney, and the muscle tissues adjacent to cancer tissues. Micro-CT scanning is an effective way to evaluate the effect of bone repair (Kim et al., 2021; Oliviero



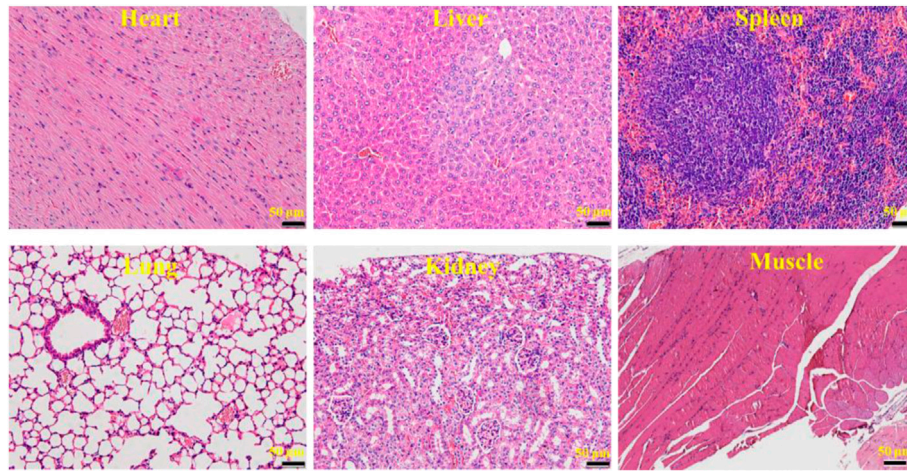


**FIGURE 7 |** HE micrograph showing no inflammation, foreign body, or tumor tissue in the heart, liver, spleen, lung, kidney, and the muscle tissues adjacent to cancer tissues. Bar: 50 µm.

et al., 2019); the values of TV, BV, BV/TV, SMI, Tb.Th, Tb.N, Tb.Sp, and BMD are important indicators for the evaluation of osteogenesis. Through the micro-CT, we observed the more trabecular and cortical bone formation and restoration of basic structure in the area of bone defects compared to the control group. In addition, BV/TV has been used to measure tumor-induced osteolysis (Ohba et al., 2014), we can also find that the value in **Table 2** demonstrates decreased trabecular osteolysis and increased BMD in the experimental group, which showed that the material degraded in mice and induced tibial healing, and the bone repairing effects were consistent with our previous study (Cheng et al., 2021), which indicated that our CTC composites and small-molecule inhibitors have good effects for the treatment of mouse osteosarcoma.

Therefore, the CTC bio-composites were used to fill the defects caused by amputation, and the results showed the new bone tissues induced by the biomaterials repaired the bone defects very well. It is believed that the biomaterials with excellent biological and osteogenic properties, combined with targeted therapy, might effectively reduce the recurrence rate and death rate of osteosarcoma, and the authors will continue to report the related research studies in the future studies.

## CONCLUSION

In this study, differentially expressed genes (DEGs) from two microarray datasets were identified. Then, the up-regulated gene was analyzed by KEGG, GO, and STRING methods. We chose CSF1R as the receptor for molecular docking, and ZINC150338698 showed the best binding result. In addition, we performed *in vitro* and *in vivo* experiments on the effects of ZINC150338698 in mice. A tibia with osteosarcoma established by 4-HAQO was surgically removed, and the defect was filled with CTC biomaterial and our synthetic inhibitor. Experiments proved that the inhibitor ZINC150338698 could inhibit the growth of osteosarcoma cells,

and the bone defects could be repaired by the CTC bio-composite and ZINC150338698. There was no inflammation, foreign body, or tumor tissue observed in mice, suggesting that our biomaterial and small molecule inhibitor had good biocompatibility and biosafety. Our study may be developed as a new candidate drug for the treatment of osteosarcoma in the future.

## DATA AVAILABILITY STATEMENT

The original contributions presented in the study are included in the article/supplementary material; further inquiries can be directed to the corresponding authors.

## ETHICS STATEMENT

The animal study was reviewed and approved by The Animal Care and Use Committee of Chengdu University.

## AUTHOR CONTRIBUTIONS

LC: writing—review and editing, supervision, project administration, and conceptualization; JL: project administration; QY: software, methodology, and writing—original draft; YP: investigation; ZD: resources; LT: validation; XS: data curation; LL: visualization; CC: visualization; MR: supervision.

## FUNDING

This work was supported by the Medical Scientific Research Project of Chengdu City, China (2021043), The Key Laboratory of Medical Clinical Genetics of Sichuan Province,

China (ZD-01-05), the CC National Creative Space Innovation and Entrepreneurship Education Special topic of Chengdu University (ccyg202101008), the Industry-university Collaborative Education Program, Ministry of Education,

China (202101011010), and the College Student Innovation and Entrepreneurship Training Program of Sichuan province, China (S202111079028, S202111079043X, S202111079095, S202111079124X, and S202111079041X).

## REFERENCES

- Barr, S., and Howe, T. E. (2018). Prosthetic Rehabilitation for Older Dysvascular People Following a Unilateral Transfemoral Amputation. *Cochrane Database Syst. Rev.* 10 (10), CD005260. doi:10.1002/14651858.CD005260.pub4
- Birkholz, M.-N., Agrawal, G., Bergmann, C., Schröder, R., Lechner, S. J., Pich, A., et al. (2016). Calcium Phosphate/microgel Composites for 3D Powderbed Printing of Ceramic Materials. *Biomed. Tech. Berl.* 61 (3), 267–279. doi:10.1515/bmt-2014-0141
- Chen, C., Xie, L., Ren, T., Huang, Y., Xu, J., and Guo, W. (2021). Immunotherapy for Osteosarcoma: Fundamental Mechanism, Rationale, and Recent Breakthroughs. *Cancer Lett.* 500, 1–10. doi:10.1016/j.canlet.2020.12.024
- Cheng, L., Lin, T., Khalaf, A. T., Zhang, Y., He, H., Yang, L., et al. (2021). The Preparation and Application of Calcium Phosphate Biomedical Composites in Filling of Weight-Bearing Bone Defects. *Sci. Rep.* 11 (1), 4283. doi:10.1038/s41598-021-83941-3
- Corre, I., Verrecchia, F., Crenn, V., Redini, F., and Trichet, V. (2020). The Osteosarcoma Microenvironment: A Complex but Targetable Ecosystem. *Cells* 9 (4), 976. doi:10.3390/cells9040976
- Czarnecka, A. M., Synoradzki, K., Firlej, W., Bartnik, E., Sobczuk, P., Fiedorowicz, M., et al. (2020). Molecular Biology of Osteosarcoma. *Cancers* 12 (8), 2130. doi:10.3390/cancers12082130
- Dang, W., Ma, B., Li, B., Huan, Z., Ma, N., Zhu, H., et al. (2020). 3D Printing of Metal-Organic Framework Nanosheets-Structured Scaffolds with Tumor Therapy and Bone Construction. *Biofabrication* 12 (2), 025005. doi:10.1088/1758-5090/ab5ae3
- Dennis, G., Sherman, B. T., Hosack, D. A., Yang, J., Gao, W., Lane, H. C., et al. (2003). DAVID: Database for Annotation, Visualization, and Integrated Discovery. *Genome Biol.* 4 (5), P3. doi:10.1186/gb-2003-4-5-p3
- El Beaino, M., Liu, J., and Lin, P. P. (2019). Modular Endoprosthetic Implant for Maximizing Residual Limb Length. *Prosthet. Orthot. Int.* 43 (1), 123–126. doi:10.1177/0309364618805259
- Feder, A.-L., Pion, E., Troebbs, J., Lenze, U., Prantl, L., Htwe, M. M., et al. (2020). Extended Analysis of Intratumoral Heterogeneity of Primary Osteosarcoma Tissue Using 3D-In-Vivo-Tumor-Model. *Ch.* 76 (2), 133–141. doi:10.3233/ch-209204
- Fernandez-Pineda, I., Bahrami, A., Green, J. F., McGregor, L. M., Davidoff, A. M., and Sandoval, J. A. (2011). Isolated Subcutaneous Metastasis of Osteosarcoma 5 Years after Initial Diagnosis. *J. Pediatr. Surg.* 46 (10), 2029–2031. doi:10.1016/j.jpedsurg.2011.06.011
- Fujiwara, T., Yakoub, M. A., Chandler, A., Christ, A. B., Yang, G., Ouerfelli, O., et al. (2021). CSF1/CSF1R Signaling Inhibitor Pexidartinib (PLX3397) Reprograms Tumor-Associated Macrophages and Stimulates T-Cell Infiltration in the Sarcoma Microenvironment. *Mol. Cancer Ther.* 20 (8), 1388–1399. doi:10.1158/1535-7163.mct-20-0591
- Hız, M., Karaismailoglu, B., Ulutas, S., Camurdan, V. B., Gorgun, B., and Oner Dincbas, F. (2021). The Effect of Preoperative Radiotherapy on Local Control and Prognosis in High-Grade Non-metastatic Intramedullary Osteosarcoma of the Extremities. *Arch. Orthop. Trauma Surg.* 141 (7), 1083–1089. doi:10.1007/s00402-020-03494-4
- Holmgaard, R. B., Zamarin, D., Lesokhin, A., Merghoub, T., and Wolchok, J. D. (2016). Targeting Myeloid-Derived Suppressor Cells with Colony Stimulating Factor-1 Receptor Blockade Can Reverse Immune Resistance to Immunotherapy in Indoleamine 2,3-Dioxygenase-Expressing Tumors. *EBioMedicine* 6, 50–58. doi:10.1016/j.ebiom.2016.02.024
- Kager, L., Tamamyan, G., and Bielack, S. (2017). Novel Insights and Therapeutic Interventions for Pediatric Osteosarcoma. *Future Oncol.* 13 (4), 357–368. doi:10.2217/fon-2016-0261
- Kim, Y., Brodt, M. D., Tang, S. Y., and Silva, M. J. (2021). MicroCT for Scanning and Analysis of Mouse Bones. *Methods Mol. Biol.* 2230, 169–198. doi:10.1007/978-1-0716-1028-2\_11
- Kresse, S. H., Rydbeck, H., Skårn, M., Namlø, H. M., Barragan-Polania, A. H., Cleton-Jansen, A.-M., et al. (2012). Integrative Analysis Reveals Relationships of Genetic and Epigenetic Alterations in Osteosarcoma. *PLoS One* 7 (11), e48262. doi:10.1371/journal.pone.0048262
- Liao, Y. X., Yu, H. Y., Lv, J. Y., Cai, Y. R., Liu, F., He, Z. M., et al. (2019). Targeting Autophagy Is a Promising Therapeutic Strategy to Overcome Chemoresistance and Reduce Metastasis in Osteosarcoma. *Int. J. Oncol.* 55 (6), 1213–1222. doi:10.3892/ijo.2019.4902
- Lussier, D. M., Johnson, J. L., Hingorani, P., and Blattman, J. N. (2015). Combination Immunotherapy with  $\alpha$ -CTLA-4 and  $\alpha$ -PD-L1 Antibody Blockade Prevents Immune Escape and Leads to Complete Control of Metastatic Osteosarcoma. *J. Immunother. cancer* 3, 21. doi:10.1186/s40425-015-0067-z
- Ma, C., Ma, Z., Yang, F., Wang, J., and Liu, C. (2019). Poly (Propylene Fumarate)/ $\beta$ -calcium Phosphate Composites for Enhanced Bone Repair. *Biomed. Mat.* 14 (4), 045002. doi:10.1088/1748-605x/ab12ae
- Ohba, T., Cole, H. A., Cates, J. M., Slosky, D. A., Haro, H., Ando, T., et al. (2014). Bisphosphonates Inhibit Osteosarcoma-Mediated Osteolysis via Attenuation of Tumor Expression of MCP-1 and RANKL. *J. Bone Min. Res.* 29 (6), 1431–1445. doi:10.1002/jbmr.2182
- Oliviero, S., Giorgi, M., Laud, P. J., and Dall'Ara, E. (2019). Effect of Repeated *In Vivo* microCT Imaging on the Properties of the Mouse Tibia. *PLoS One* 14 (11), e0225127. doi:10.1371/journal.pone.0225127
- Percie du Sert, N., Hurst, V., Ahluwalia, A., Alam, S., Avey, M. T., Baker, M., et al. (2020). The ARRIVE Guidelines 2.0: Updated Guidelines for Reporting Animal Research. *PLoS Biol.* 18 (7), e3000410. doi:10.1371/journal.pbio.3000410
- Richter, R. F., Ahlfeld, T., Gelinsky, M., and Lode, A. (2019). Development and Characterization of Composites Consisting of Calcium Phosphate Cements and Mesoporous Bioactive Glass for Extrusion-Based Fabrication. *Materials* 12 (12), 2022. doi:10.3390/ma12122022
- Ries, C. H., Cannarile, M. A., Hoves, S., Benz, J., Wartha, K., Runza, V., et al. (2014). Targeting Tumor-Associated Macrophages with Anti-CSF-1r Antibody Reveals a Strategy for Cancer Therapy. *Cancer Cell.* 25 (6), 846–859. doi:10.1016/j.ccr.2014.05.016
- Sadikovic, B., Yoshimoto, M., Chilton-MacNeill, S., Thorner, P., Squire, J. A., and Zielenska, M. (2009). Identification of Interactive Networks of Gene Expression Associated with Osteosarcoma Oncogenesis by Integrated Molecular Profiling. *Hum. Mol. Genet.* 18 (11), 1962–1975. doi:10.1093/hmg/ddp117
- Schweikle, M., Bjørnøy, S. H., van Helvoort, A. T. J., Haugen, H. J., Sikorski, P., and Tiainen, H. (2019). Stabilisation of Amorphous Calcium Phosphate in Polyethylene Glycol Hydrogels. *Acta Biomater.* 90, 132–145. doi:10.1016/j.actbio.2019.03.044
- Smeester, B. A., Slipek, N. J., Pomeroy, E. J., Laoharawee, K., Osum, S. H., Larsson, A. T., et al. (2020). PLX3397 Treatment Inhibits Constitutive CSF1R-Induced Oncogenic ERK Signaling, Reduces Tumor Growth, and Metastatic Burden in Osteosarcoma. *Bone* 136, 115353. doi:10.1016/j.bone.2020.115353
- Szklarczyk, D., Gable, A. L., Nastou, K. C., Lyon, D., Kirsch, R., Pyysalo, S., et al. (2021). The STRING Database in 2021: Customizable Protein-Protein Networks, and Functional Characterization of User-Uploaded Gene/measurement Sets. *Nucleic Acids Res.* 49 (D1), D605–D612. doi:10.1093/nar/gkaa1074
- Thanindrarn, P., Dean, D. C., Nelson, S. D., Hornicek, F. J., and Duan, Z. (2019). Advances in Immune Checkpoint Inhibitors for Bone Sarcoma Therapy. *J. Bone Oncol.* 15, 100221. doi:10.1016/j.jbo.2019.100221
- Waiyawat, J., Kongsema, M., Sinthuvanich, C., Chienthavorn, O., Teanchai, C., and Akkarachaneeyakorn, K. (2020). Fabrication of Calcium Phosphate Composite polymer/SLS-Stabilized Emulsion-Based Bioactive Gels and Their Application

- for Dentine Tubule Occlusion. *J. Oral Biosci.* 62 (1), 64–71. doi:10.1016/j.job.2019.11.002
- Wen, Z. Q., Li, X. G., Zhang, Y. J., Ling, Z. H., and Lin, X. J. (2017). Osteosarcoma Cell-Intrinsic Colony Stimulating Factor-1 Receptor Functions to Promote Tumor Cell Metastasis through JAG1 Signaling. *Am. J. Cancer Res.* 7 (4), 801–815.
- Xun, Q., Wang, Z., Hu, X., Ding, K., and Lu, X. (2020). Small-Molecule CSF1R Inhibitors as Anticancer Agents. *Cmc* 27 (23), 3944–3966. doi:10.2174/1573394715666190618121649
- Yu, D., Zhang, S., Feng, A., Xu, D., Zhu, Q., Mao, Y., et al. (2019). Methotrexate, Doxorubicin, and Cisplatin Regimen Is Still the Preferred Option for Osteosarcoma Chemotherapy. *Med. Baltim.* 98 (19), e15582. doi:10.1097/md.00000000000015582
- Zhao, Z., Jin, Q., Xie, X., Wang, Y., Lin, T., Yin, J., et al. (2020). Plastic Lengthening Amputation with Vascularized Bone Grafts in Children with Bone Sarcoma: a Preliminary Report. *World J. Surg. Onc* 18 (1), 246. doi:10.1186/s12957-020-02020-5

**Conflict of Interest:** The authors declare that the research was conducted in the absence of any commercial or financial relationships that could be construed as a potential conflict of interest.

**Publisher's Note:** All claims expressed in this article are solely those of the authors and do not necessarily represent those of their affiliated organizations, or those of the publisher, the editors, and the reviewers. Any product that may be evaluated in this article, or claim that may be made by its manufacturer, is not guaranteed or endorsed by the publisher.

Copyright © 2022 Liu, Yao, Peng, Dong, Tang, Su, Liu, Chen, Ramalingam and Cheng. This is an open-access article distributed under the terms of the Creative Commons Attribution License (CC BY). The use, distribution or reproduction in other forums is permitted, provided the original author(s) and the copyright owner(s) are credited and that the original publication in this journal is cited, in accordance with accepted academic practice. No use, distribution or reproduction is permitted which does not comply with these terms.



# Physical and Chemical Properties, Biosafety Evaluation, and Effects of Nano Natural Deer Bone Meal on Bone Marrow Mesenchymal Stem Cells

Yongbo Li, Zhe Tan, Jixiang Zhang, Junhan Mu and Han Wu\*

Department of Orthopedics, China-Japan Union Hospital of Jilin University, Changchun, China

## OPEN ACCESS

### Edited by:

Murugan Ramalingam,  
VIT University, India

### Reviewed by:

Ahmed El-Fiqi,  
Dankook University, South Korea  
Xianyi Cai,  
Huazhong University of Science and  
Technology, China

### \*Correspondence:

Han Wu  
wu\_han@jlu.edu.cn

### Specialty section:

This article was submitted to  
Biomaterials,  
a section of the journal  
Frontiers in Bioengineering and  
Biotechnology

Received: 08 March 2022

Accepted: 01 June 2022

Published: 15 July 2022

### Citation:

Li Y, Tan Z, Zhang J, Mu J and Wu H  
(2022) Physical and Chemical  
Properties, Biosafety Evaluation, and  
Effects of Nano Natural Deer Bone  
Meal on Bone Marrow Mesenchymal  
Stem Cells.  
Front. Bioeng. Biotechnol. 10:891765.  
doi: 10.3389/fbioe.2022.891765

At present, bone-based products are abundant, and the main sources are bovine bone and pig bone, but there are few studies on the development of deer bone as a bone repair material. Deer bone has important osteogenic effects in the theory of traditional Chinese medicine. It is rich in protein, ossein, and a variety of trace elements, with the effect of strengthening tendons and bones. Nanomaterials and their application in the repair of bone defects have become a research hotspot in bone tissue engineering. In this study, nano-deer bone meal (nBM), nano-calcined deer bone meal, and nano-demineralized bone matrix were successfully prepared. It was found that the Ca/P ratio in deer bone was significantly higher than that in cow bone and human bone tissue, and deer bone contained beneficial trace elements, such as potassium, iron, selenium, and zinc, which were not found in cow bone. The three kinds of deer bone powders prepared in this study had good biocompatibility and met the implantation standards of medical biomaterials. Cell function studies showed that compared with other bone powders, due to the presence of organic active ingredients and inorganic calcium and phosphate salts, nBM had excellent performance in the proliferation, adhesion, migration, and differentiation of bone marrow mesenchymal stem cells. These findings indicate that nBM can be used as a potential osteoinductive active nanomaterial to enhance bone tissue engineering scaffolds with certain application prospects.

**Keywords:** bone marrow mesenchymal stem cells, nanoparticles, bone powders, osteogenic differentiation, bone tissue engineering

## 1 INTRODUCTION

Bone defects caused by trauma, inflammatory diseases, and tumors are in urgent need of repair (Wang and Yeung, 2017; Baldwin et al., 2019; Simpson et al., 2020). Untreated bone defects may be infiltrated by connective tissue (Li et al., 2019a). Therefore, these problems not only pose challenges to clinicians but also increase the need for bone reconstruction (Zhao et al., 2017; Ho-Shui-Ling et al., 2018). Various surgical approaches have been used to treat bone defects, such as autologous/allogeneic bone grafting, guided bone regeneration, and distraction osteogenesis (Khojasteh et al., 2013). However, several disadvantages limit the use of autologous bone grafting, including additional surgical procedures, insufficient supply, and donor-site morbidity. Despite these complications, it remains the gold standard for bone grafting (Tang et al., 2016; Przekora, 2019). Given the limitations of autologous bone grafting, allografts can overcome the above drawbacks, but it carries risks of



infection transmission, immune response, and rapid resorption (Long et al., 2012). A xenograft is another possible approach because it is similar to human bone in morphological properties (Long et al., 2012). Xenografts can be obtained from different species, including cattle, pigs, camels, and ostriches. Among them, bovine bone is still the first choice for bone reconstruction (Ghanaati et al., 2014; Eliaz and Metoki, 2017; Sonmez et al., 2017). Although xenografts are widely sourced and simple to operate, they have low osteoinductive properties and have potential infectious disease problems, such as bovine spongiform encephalopathy.

Nowadays, abundant products are developed based on bone, and there are many commercial bone meal (BM) brands. These products are divided into two categories. The first category includes BM prepared by strong alkali treatment, high-temperature sintering annealing, and other processes. The main components are hydroxyapatite and other inorganic components with bone conductivity, such as Bio-Oss and Osteobiol. The former comes from cow bone and the latter from pig bone [bab 2065]. The second category is based on conventional Urist preparation methods, such as ether degreasing and hydrochloric acid decalcification. The main components are organic components of demineralized bone matrix (DBM), such as Grafton matrix and Xin Kangchen (XKC), both of which are derived from allogeneic bone. They contain a variety of osteogenic growth factors with osteoinductive properties, such as bone morphogenetic protein (BMP), insulin-like growth factor, and transforming growth factor (TGF), which can promote the migration and differentiation of bone marrow mesenchymal stem cells (BMSCs) and bone tissue regeneration (Urist, 1965; Urist and Strates, 2009). As is known, natural bone tissue is mainly composed of organic components (35%) and inorganic components (65%). The organic components mainly include collagen and cell growth factors, and the inorganic components are hydroxyapatite, various anions and cations (calcium, phosphorus, and magnesium), etc. However, few BM on the market contains both organic and inorganic components.

Deer bone, the skeleton of the deer family, as traditional Chinese medicine occupies an important position in China's medical field. According to the Dictionary of Traditional Chinese Medicine, its pharmacological function is to strengthen the body and tendons and to treat limbs, arthritis, and muscle pain caused by rheumatism. Studies have shown that the long-term administration of deer BM can relieve joint pain in elderly patients and reduce the incidence of osteoporosis. Nowadays, with the development of biochemistry, pharmacology, cell biology, and other disciplines, the analysis of deer bone components has gradually improved, and deer bones have been increasingly widely used in scientific research and clinical work. Deer bone contains a large number of proteins, collagen, phospholipids, chondroitin, and phosphoprotein that are conducive to osteogenesis, promoting the synthesis of collagen and elastin, delaying bone absorption, and promoting endochondral osteogenesis *in vivo* (He, 2011; Ren et al., 2019). Guo et al. studied the nutritional components of sika deer BM and its therapeutic effect on osteoporosis in ovariectomized rats and measured the contents of amino acids, major and trace elements,

and fatty acids in sika deer BM. The results showed that sika deer BM has a good effect for the treatment of osteoporosis (Guo, 2017). Deer bone also contains a large amount of minerals, such as calcium, magnesium, iron, zinc, potassium, copper, phosphorus, selenium, and other elements, covering almost all the nutrients required for the formation of human bone marrow. These provide a suitable microenvironment for bone regeneration, which helps to slow down the aging of the bone marrow, maintain the hardness and toughness of the bones, prevent osteoporosis, and reduce the risk of fractures (Lee et al., 2014; Quan et al., 2015). Wang et al. studied the effects of deer BM on bone microstructure and bone minerals in rats with osteoporosis after ovariectomy, and the results showed that deer BM improved the changes in bone microstructure and serological indexes caused by ovarian removal, suggesting that it can prevent and treat osteoporosis caused by decreased estrogen (Quan et al., 2015). Epimedium bone with deer BM as the main raw material has been reported to improve osteoporosis, and its effect on increasing bone trabecular structural components is very significant (Xudong, 2021). An et al. gave glucocorticoid-induced osteoporosis rats gavage of deer bone polypeptide, and the results showed that deer bone polypeptide can inhibit the imbalance of calcium and phosphorus metabolism induced by dexamethasone, reduce alkaline phosphatase (ALP), increase osteocalcin, inhibit bone resorption and promote bone formation, and improve the pathological changes and microstructure of bone in osteoporotic rats (Li-ping, 2016). In addition, several preclinical studies have shown that deer bone-related products, such as deer BM and deer melon polypeptide, can effectively relieve osteoporosis caused by ovariectomy in rats and promote osteoblast proliferation (He, 2011; Xue et al., 2021).

Due to its small particle size and large specific surface area, nanomaterials exhibit different properties from their monolithic state. Studies have shown that nanoscale materials can promote the proliferation, migration, and adhesion of BMSCs. Nanomaterials have unique microscopic biomimetic structures, good mechanical properties, and superior osteoinduction, osteoconduction, and other biological properties. Nanomaterials and their application in the repair of bone defects have become a research hotspot in bone tissue engineering in recent years (Laschke et al., 2010; Chae et al., 2013; Touri et al., 2013; Aryaei et al., 2014).

At present, there is no basic research on the development of deer bone as a bone repair material. It is innovative and promising to develop deer bone repair materials with nanotechnology.

In this study, three kinds of nano-deer BM (nano-deer BM (nBM), nano-calcined deer BM (nCBM), and nano-DBM (nDBM)) were prepared and compared with two kinds of commercial BM (Bio-Oss, XKC) to analyze the differences in particle size, substance structure, and nutrient content among different BM. The biological safety of nano-sized deer BM was tested. At the same time, the effects of different BM on BMSC proliferation, adhesion, spread, migration, and differentiation were studied to evaluate the possibility of deer BM as a bone repair material in clinical application.

## 2 MATERIALS AND METHODS

### 2.1 Materials

Bio-Oss was purchased from Geistlich Pharmaceuticals Ltd. (Switzerland). KKC was acquired from Beijing Xinkangchen Medical Technology Development Co., Ltd. (China).

### 2.2 Preparation of Nano-Deer Bone Meal

#### 2.2.1 Acquisition of Fresh Deer Bone

The fresh sika deer leg bones used in the experiments were fresh samples taken within 24 h after slaughter, which were provided by the breeding and slaughtering plant in Deer Town, Changchun City, Jilin Province. The soft tissue, fascia layer, periosteum, and marrow in the medullary cavity attached to the surface of the deer leg bone were removed layer by layer, and the articular cartilage around the joint was removed as much as possible, rinsed three times with sterile distilled water, and then cut using a grinding drill into bone blocks with a size of 2 cm×2 cm. The bone blocks were stored at  $-80^{\circ}\text{C}$  for at least 6 h and then thawed in a  $37^{\circ}\text{C}$  water bath. This was repeated for three cycles. The above process was physical freeze-thaw decellularization. The bone blocks were then placed in 1% TritonX-100 and treated with a shaker at a constant speed (100 rpm) for 12 h. The name of this step was chemical decellularization. The decellularized bone blocks were thoroughly washed with sterile distilled water. Finally, the blocks were stored in a  $-80^{\circ}\text{C}$  freezer for future use.

#### 2.2.2 Preparation of Deer Bone Meal and Nano-Deer Bone Meal

The deer bone blocks prepared above were put into a beaker and soaked in ether for 24 h to remove grease; after the ether was poured out, the blocks were soaked in absolute ethanol for 24 h for dehydration and then freeze-dried in a vacuum freeze dryer. First, the blocks were pulverized with a pulverizer and passed through a standard sieve; BM that passed through a 20-mesh standard sieve but failed to pass through a 60-mesh standard sieve was collected, which was deer BM. The BM prepared above was ball-milled using a planetary ball mill, and the BM was placed in a 50 ml agate ball milling jar. There were two kinds of balls, large and small, and the diameter of the large ball was 0.6 cm, accounting for about 20% of the total number of grinding balls. The diameter of the small ball was 0.1 cm, accounting for about 80% of the total mass of the grinding ball. Ball milling conditions were as follows: the ratio of ball to material was 4:1, the ball milling time was 12 h, and the ball milling speed was 550 r/min. The deer BM collected after ball milling was nBM.

#### 2.2.3 Preparation of Calcined Deer Bone Meal and Nano-Deer Bone Meal

The BM prepared above was spread in a ceramic bowl, calcined in a muffle furnace, slowly heated to  $800^{\circ}\text{C}$  at a rate of  $1.5^{\circ}\text{C}/\text{min}$ , maintained for 6 h, and then cooled to room temperature naturally. Then, it was passed through a standard sieve, and BM that passed through a 20-mesh standard sieve but not a 60-mesh standard sieve was collected, which was calcined deer BM

(CBM). The CBM prepared above was ball-milled using a planetary ball mill. The conditions were the same as those for the preparation of nBM. The deer bone powder collected after ball milling was nCBM.

#### 2.2.4 Preparation of Demineralized Bone Matrix and Nano-Demineralized Bone Matrix

DBM was prepared by the modified Urist method (Grgurevic et al., 2017). The prepared deer bone pieces were decalcified with a concentration of 0.6 mmol/L hydrochloric acid; the mixture was stirred and soaked for 72 h, and the hydrochloric acid was replaced every 12 h during the soaking process. It was ensured that the bone pieces were fully in contact with the hydrochloric acid. The bone pieces were rinsed with sterile distilled water 3–5 times and soaked overnight to fully remove the hydrochloric acid. Then, it was soaked in absolute ethanol for 2 h for dehydration, and the ethanol was removed and ether added for 2 h. Next, the ether was removed, and the bone pieces were volatilized in a fume hood overnight; the pieces were then freeze-dried in a vacuum freeze dryer. Preliminary pulverization was done using a pulverizer; BM was passed through a standard sieve, and BM that passed through a 20-mesh standard sieve but failed to pass through a 60-mesh standard sieve was collected, which was DBM. The DBM prepared above was ball-milled using a planetary ball mill. Before ball milling, DBM was lyophilized with liquid nitrogen. The ball milling time was 24 h, and DBM was lyophilized with liquid nitrogen every 3 h. The ball milling conditions were the same as those for nBM. The ball-milled deer bone powder was nDBM.

## 2.3 Characterization of Nano-Deer Bone Meal

### 2.3.1 Characterization of Nano-Deer Bone Meal

The particle size distribution of the three different bone powders was measured using a nanoparticle size analyzer (Zetasizer Nano-ZS90, China) after dispersing the powders in phosphate-buffered saline (PBS) with 100  $\mu\text{g}/\text{ml}$ , and the average particle size was represented by the median particle size D50. The surface micromorphology of the different BM was examined by transmission electron microscopy (TEM, Tecnai G<sup>2</sup>S-Twin, United States). TEM images were taken after dispersing the powder in ethanol with 1  $\text{mg}/\text{ml}$ . XRD measurement was performed on a Rigaku D/MAX-2250 V at  $\text{Cu K}\alpha$  ( $\lambda = 0.154056 \text{ nm}$ ) with a scanning rate of  $4^{\circ} \text{ min}^{-1}$  in the  $2\theta$  range of  $20^{\circ}$ – $60^{\circ}$ . Fourier transform infrared spectroscopy (FTIR, Perkin Elmer, FTIR-2000) was used to determine the chemical structure among different bone powders. For this measurement, the transmission IR spectra were recorded using KBr pellets (1 mg sample/300 mg KBr) over a range of  $400$ – $4000 \text{ cm}^{-1}$  with  $1 \text{ cm}^{-1}$  resolution averaging over 100 scans. The component composition of different bone powders was characterized by thermal gravimetric analysis (TGA) (TA Instruments TGA500, United States). TGA was conducted at  $10^{\circ}\text{C}/\text{min}$  heating speed in an oxidative atmosphere (synthetic air, composed of 80%  $\text{N}_2$  and 20%  $\text{O}_2$ ). The element content of

different BM was analyzed by X-ray photoelectron spectroscopy (ESCALab250i-XL).

### 2.3.2 Basic Components of Nano-Deer Bone Meal

**Mineral content:** Inductively coupled plasma spectrometry, according to GB5009.268-2016. After the sample was digested, it was determined by inductively coupled plasma mass spectrometer, qualitatively determined by the specific mass of the element, and quantitatively analyzed by the external standard method.

**Amino acid content:** Determined by the amino acid full spectrum analyzer.

**Ash content:** Muffle furnace high-temperature burning method, according to GB5009.4-2016. The residual inorganic material after the sample was burned is called ash. The ash value was calculated by burning and weighing.

**Protein content:** Kjeldahl method, according to GB5009.5-2016. The protein in the sample was decomposed under catalytic heating conditions, and the ammonia produced combines with sulfuric acid to form ammonium sulfate. Ammonia was freed by alkalization distillation, absorbed with boric acid, and then titrated with a standard titration solution of sulfuric acid or hydrochloric acid. The nitrogen content was calculated according to the consumption of acid and then multiplied by the conversion factor, that is, the protein content.

**Fat content:** Soxhlet extraction method, according to GB5009.6-2016. Fats are easily soluble in organic solvents. The sample was directly extracted with a solvent such as anhydrous ether or petroleum ether, evaporated to remove the solvent, and dried to obtain the content of free fat.

**Moisture content:** Direct drying method, according to GB5009.3-2016. At 101.3 kPa (one atmospheric pressure) and a temperature of 101°C–105°C, the weight loss on drying in the sample was determined by the volatilization method, and the moisture content was calculated using the weight before and after drying.

## 2.4 Biosafety of Nano-Deer Bone Meal

### 2.4.1 Systemic Acute Toxicity Test

According to the GB/T16886 standard for the systemic acute toxicity test of medical biomaterials, nBM, nCBM, and nDBM were placed in normal saline at a concentration of 0.2 g/ml, and the extracts of nBM, nCBM, and nDBM were obtained in a 37°C incubator for 12 h. Forty Balb/C mice were randomly divided into four groups, namely, nBM, nCBM, nDBM, and PBS groups, with each group having 50% males and 50% females. The mice were injected intraperitoneally at a dose of 50 ml/kg. The experimental group was injected with material extract, and the control group was injected with normal saline. After injection, the mice were raised in separate cages. The general situation, poisoning, and death of the mice were observed 1, 2, and 3 days after injection. The changes in animal body weight were monitored and hematological and biochemical indexes were detected. Toxicity was evaluated according to the following indicators of animal reaction degree: 1) Nontoxic: the animals were in good general condition and had no obvious signs of poisoning. 2) Mild poisoning: The activities of the experimental

animals were normal, but mild dyspnea and abdominal irritation occurred. 3) Obvious poisoning: The experimental animals showed symptoms of difficulty in breathing, severe abdominal irritation, decreased activity and food intake, and mild weight loss. 4) Severe poisoning: cyanosis, tremor, respiratory failure, etc., appeared in experimental animals, and their body weight decreased significantly. 5) Death: The experimental animals died after injection.

### 2.4.2 Skin Sensitization Test

According to the GB/T16886 standard for the skin sensitization test of medical biomaterials, nBM, nCBM, and nDBM were placed in PBS at a concentration of 0.2 g/ml, and the extracts of nBM, nCBM, and nDBM were obtained in a 37°C incubator for 12 h. Twenty-four guinea pigs were randomly divided into five groups—the nBM, nCBM, and nDBM groups, the negative control group, and the positive control group—with six in each group. The back of the experimental animals was shaved, and five points were injected intradermally on both sides of the scapula of the guinea pigs. The experimental group was injected with the extracts. The negative control group was injected with PBS. The positive control group was injected with 2% dinitrofluorobenzene. The local reaction of animal skin was observed 1, 2, and 3 days after injection. The degree of erythema and edema at the injection site was recorded and scored. The scoring criteria are shown in **Supplementary Table S1**.

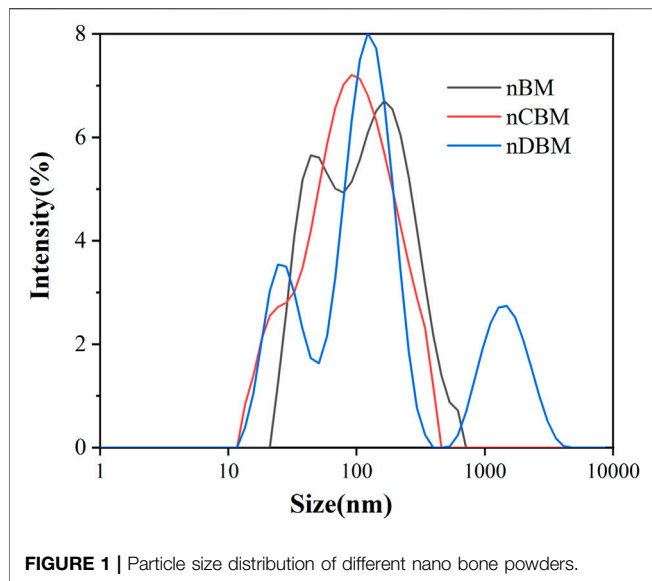
### 2.4.3 *In vitro* Hemolysis Test

Fresh blood was taken from rats and centrifuged at 2500 r/min for 6 min; the supernatant was aspirated to obtain red blood cells, which were then washed with PBS three times and diluted to a final concentration of 2% for later use. The experiment was divided into the nBM, nCBM, nDBM, PBS, and 0.8% triton groups with three test tubes in each group. A 1.5 ml centrifuge tube was taken, 1 ml material extract was first added, and then 0.5 ml diluted red blood cell suspension was added. The centrifuge tube was placed in a shaker at 37°C and 130 r/min for incubation for 1 h, and photos were taken. After centrifugation at 2000 r/min for 5 min, 150 µl of supernatant was taken and placed in a 96-well plate. The absorbance value at 545 nm ( $OD_{545}$ ) was measured using a multifunctional microplate tester. The hemolysis rate was calculated according to the following formula:

$$\text{Hemolysis rate (HR\%)} = \frac{OD\text{Value}(\text{samples}) - OD\text{Value}(\text{PBS})}{OD\text{Value}(\text{triton group}) - OD\text{Value}(\text{PBS})} \times 100\%$$

### 2.4.4 Cytotoxicity Assay

After ultraviolet disinfection for 4 h, nBM, nCBM, and nDBM were placed in Dulbecco's modified Eagle's medium (DMEM)/F12 medium at a ratio of 50 mg/ml at 120 r/min and incubated at 37°C for 24 h. After centrifugation, the supernatant was taken as the extraction solution. BMSCs were cultured on a fresh DMEM/F12 medium for 24 h; the culture medium was then sucked up, and the extract solution, gradient dilution solution



(1/2, 1/4), and medium without the extract (negative control group) were added. Then, the extract was sucked up in the culture box for 24 h, and 10% CCK-8 solution was added into each well. After 2 h of incubation, the absorbance value of each well at 450 nm was measured using a multifunctional microplate analyzer to calculate the relative percentage of the cell proliferation rate:

$$\text{Cell Viability (\%)} = \frac{\text{ODValue (samples)}}{\text{ODValue (control group)}} \times 100\%$$

## 2.5 In Vitro Cell Studies

### 2.5.1 Cell Culture

Cell experiments were performed using rat BMSCs purchased from the Institute of Biochemistry and Cell Biology, Shanghai Institutes for Biological Sciences, Chinese Academy of Sciences. Cells were cultured in DMEM (Gibco) and supplemented with 10% fetal bovine serum (Gibco), 100 U ml<sup>-1</sup> penicillin, and 100 U ml<sup>-1</sup> streptomycin (Sigma) in a humidified incubator of 5% CO<sub>2</sub> at 37°C. Before culturing, the samples were sterilized by immersing in 75% alcohol and exposing to ultraviolet light for 60 min; the samples were rinsed with sterile PBS thrice. The medium of cell culture was refreshed every other day.

### 2.5.2 Cell Proliferation

The CCK-8 assay was employed to quantitatively evaluate the cell proliferation on different bone powders. BMSCs (2 × 10<sup>4</sup> cells/well) were seeded in a 48-well plate and cultured for 24 h. After that, the medium was changed with different bone powders (50 µg/ml) containing medium and the cells were incubated for 24 h, then the cells were refreshed with normal medium and incubated for more 1, 3, and 7 days, respectively. At every prescribed time point, 15 µl/well CCK-8 solution was added to the well. After 2 h of incubation, 200 µl of the medium was transferred to a 96-well plate for measurement. The absorbance was determined at 450 nm using a multifunctional

microplate scanner (Tecan Infinite M200). The complete cell culture medium was used as a control group, and results were averaged over three parallel samples.

Cells were stained with calcein (Calcein-AM) and propidium iodide, which fluoresce green for live cells and red for dead cells. The images were captured by a fluorescent inverted microscope (TE 2000U, Nikon).

### 2.5.3 Cell Morphology

Cell adhesion and morphology were evaluated using phalloidin (Sigma) for live cells (red) and 4,6-diamidino-2-phenylindole (DAPI, Invitrogen) for the cell nucleus (blue). BMSCs (2 × 10<sup>4</sup> cells/well) were seeded in a 48-well plate and cultured for 24 h. After that, the medium was changed with different bone powders (50 µg/ml) containing medium, and the cells were refreshed with normal medium and incubated for 3 days. After 3 days of culture, the cells were fixed with 4% paraformaldehyde and then stained with phalloidin and DAPI. The images were captured by a fluorescent inverted microscope (TE 2000U, Nikon).

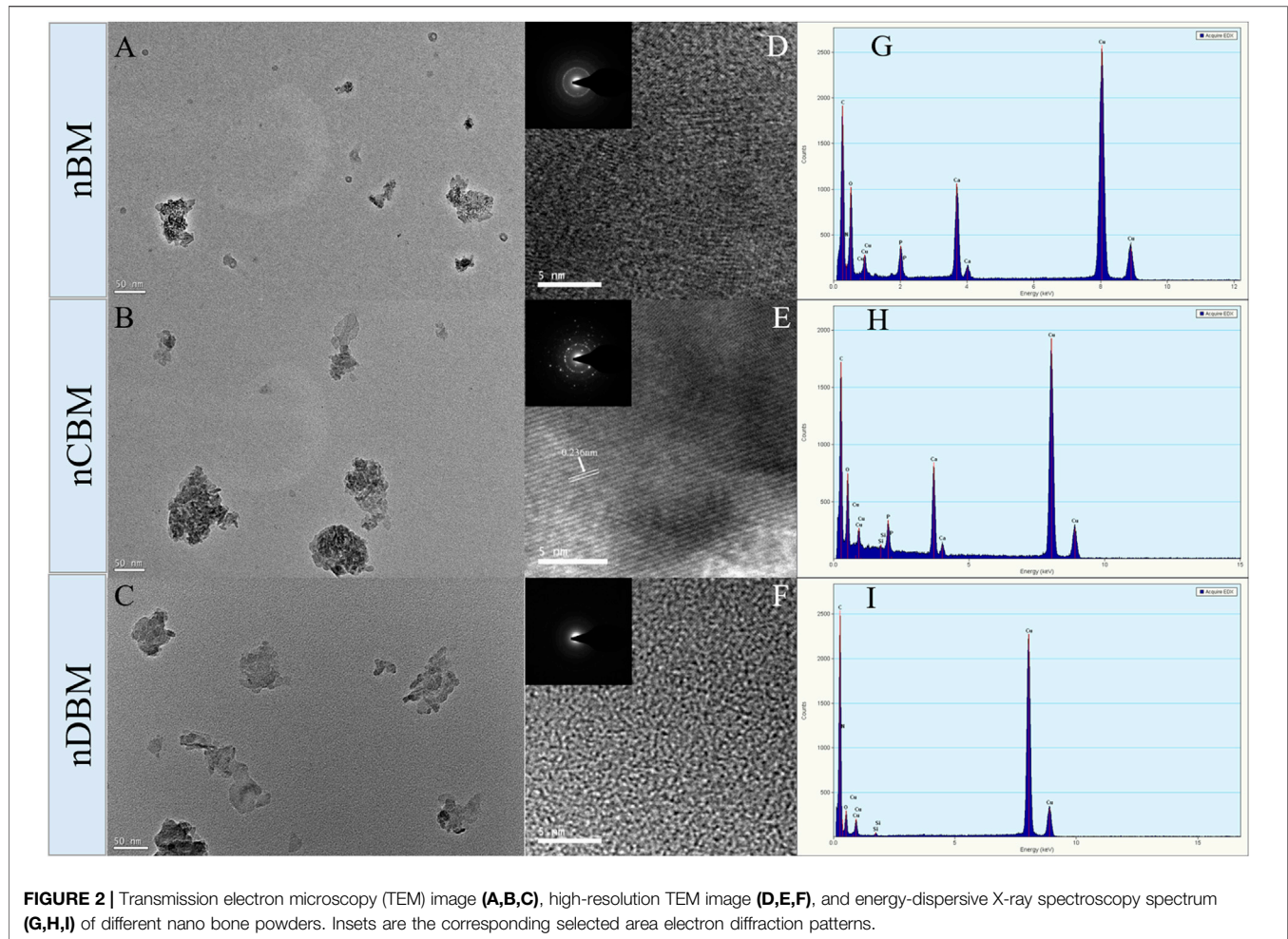
### 2.5.4 Cell Migration

First, 100 µl serum-free medium was absorbed into the upper chamber of the transwell chamber and hydrated for 30 min at 37°C; then, the hydration solution was discarded. Next, 200 µl serum-free medium containing BMSCs (3 × 10<sup>4</sup> cells/well) was added into the upper chamber, and a 600 µl complete medium containing different BM was added into the lower chamber. After PBS washing, the cells in the upper chamber were fixed with 4% paraformaldehyde for 20 min. After PBS washing, cotton swabs were used to wipe the cells in the inner layer of the microporous membrane. Under dark conditions, 500 µl 0.1% crystal violet staining solution was added to each well. Staining at room temperature for 20 min, a fluorescent inverted microscope was used to observe and photograph. Images were taken from five fields randomly selected from each chamber, and cell counts were performed.

### 2.5.5 Alkaline Phosphatase Activity Assay

ALP staining and corresponding quantitative detection were applied to assess the activity of ALP in BMSCs grown onto different BM (Wang et al., 2020; Yao et al., 2020). ALP staining was detected using the BCIP/NBT Alkaline Phosphatase Colour Development Kit (Beyotime, China). When BMSCs were cultured on different samples for 7 and 14 days, cells were washed three times with PBS, fixed with 4% paraformaldehyde for 15 min, and washed with PBS again. Then, 500 µl ALP dye solution was added into wells, and cells were dyed for at least 12 h at room temperature under dark conditions. The extra ALP dye solution was washed away with PBS, and the purple deposition was captured by a fluorescent inverted microscope (TE 2000U, Nikon). The ALP quantitative detection was tested using a modified Alkaline Phosphatase Assay Kit (Beyotime, China). After being cultured on a different BM for 7 and 14 days, BMSCs were washed with PBS three times and split by adding 200 µl of RIPA cell lysis solution, freezing at -80°C for 25 min, and thawing at 37°C. Then,





p-nitrophenol phosphate substrate and BCA solution (Beyotime, China) were added, followed by incubation in the dark for 30 min at 37°C. The absorbances at 405 nm (OD405) and 562 nm (OD562) were read using a multifunctional microplate scanner (Tecan Infinite M200). The corresponding ALP quantitative evaluation was calculated according to the eq. OD 405/OD 562.

### 2.5.6 Alizarin Red Staining for Calcium Deposition

Alizarin red staining and calcium deposit quantification were applied to evaluate mineral deposition in BMSCs cultured on different BM based on a previously published protocol (Li et al., 2019b; Mahmoud et al., 2020). When cells were incubated with different BM for 14 and 21 days, the cells were washed three times with PBS, fixed with 4% PFA for 15 min, and washed with PBS again. Afterward, the cells were immersed in 1% (w/v) Alizarin Red S (ARS, Sigma) solution for 30 min at 37°C. The excess ARS dye was flushed out with PBS, and the presence of mineral deposition was qualitatively evaluated according to the red color intensity observed using an inverted microscope (TE 2000U, Nikon). Furthermore, calcium quantification was performed using a 10% cetylpyridinium chloride (CPC) solution. ARS-stained cells were rinsed with PBS and then

treated with 1 ml CPC solution for 1 h to desorb calcium ions. Absorbance was measured at 540 nm using a multifunction microplate scanner (Tecan Infinite M200).

### 2.5.7 Gene Expression Analysis via Quantitative Reverse Transcription-Polymerase Chain Reaction

Quantitative reverse transcription-polymerase chain reaction (qRT-PCR) was introduced to further investigate the expression levels of runt-related transcription factor 2 (RUNX2), collagen type 1 (COL-1), osteopontin (OPN), and bone morphogenetic protein 2 (BMP-2). TRIzol (Takara Biomedical Technology Co., Ltd., Beijing, China) was used to extract the total RNA of the cells after 7 and 14 days of culture, and reverse transcription was performed according to the PrimeScript™ RT reagent kit with gDNA Eraser (Takara Biomedical Technology Co., Ltd., Beijing, China) to generate the template; it was then mixed with TB Green® Premix Ex Taq™ (Takara Biomedical Technology Co., Ltd., Beijing, China) for PCR on a LightCycler® 480 instrument (Roche Diagnostics Ltd., Shanghai, China). The target gene primer sequences are shown in **Supplementary Table S2**. The resulting mRNA levels were normalized to GAPDH and compared with those of the control group using the  $2^{-\Delta\Delta Ct}$  method.

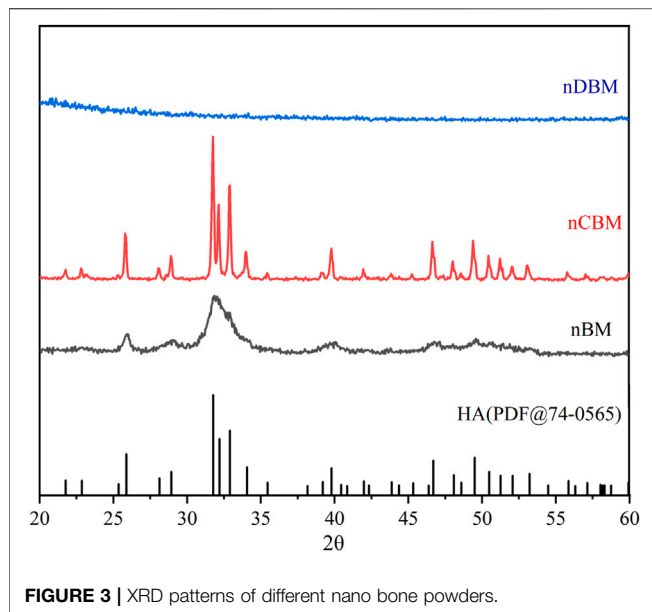


FIGURE 3 | XRD patterns of different nano bone powders.

### 2.5.8 Western Blotting Assay

BMSCs were seeded onto different BM in 6-well culture plates at a density of  $15 \times 10^4$  cells per 2 ml medium per well and then incubated for 7 days. Cells were scraped from different samples and lysed with RIPA buffer (Biosharp, China) containing phenylmethylsulfonyl fluoride. Lysates were freeze/thawed for three cycles and centrifuged at 12,000 rpm for 20 min at 4°C, and the supernatant was collected. The total protein concentration was determined using the BCA Protein Assay Kit (Thermo, United States) afterward. The loading buffer was added to the supernatant, and the mixture was heated to 100°C for 5 min. The protein sample lysates were loaded on a 12% sodium dodecyl sulfate-polyacrylamide gel and transferred to polyvinylidene difluoride membranes (Solarbio, China). The membrane was blocked with 5% skim milk in TBST buffer (0.1 M Tris-HCl and 0.1% Tween-20, pH 7.4) for 1 h and incubated with primary antibodies overnight at 4°C. Finally, the membrane was incubated with secondary antibodies at

room temperature for 1 h. Protein bands were detected using the ECL Western Blotting Substrate (KF005, Affinity) and revealed using a chemiluminescence imaging system (Amersham Imager 600, GE, United States). Band densitometry was analyzed using ImageJ software.  $\beta$ -actin was used as the internal control.

## 2.6 Statistical Analysis

The data presented are the mean (standard deviation  $\pm$  STD). Independent and replicated experiments were used to analyze the statistical variability of the data via one-way analysis of variance, with  $p < 0.05$  being statistically significant ( $*p < 0.05$ ).

## 3 RESULTS AND DISCUSSION

### 3.1 Preparation and Characterization of Nano-Deer Bone Meal

#### 3.1.1 Characterization of Nano-Deer Bone Meal

The BM, CBM, and DBM prepared in this study all passed the screening of 20-mesh and 60-mesh standard sieves; therefore, the particle sizes of the final prepared BM, CBM, and DBM were all in the range of 250  $\mu$ m–850  $\mu$ m. In this study, nanoscale bone powder was prepared by physical ball milling of BM, CBM, and DBM. The average particle size of the three different nano bone powders is shown in **Figure 1**—D50 (nBM) = 106 nm (PDI = 0.372), D50 (nCBM) = 91.3 nm (PDI = 0.231), and D50 (nDBM) = 122 nm (PDI = 0.426). Nanoparticles are prepared via physical and chemical preparation methods. Physical ball milling is widely used because of its advantages of simple operation and large production (Yin et al., 2015). The particle size of prepared nanoparticles is affected by many factors, such as the ratio of ball to material, grinding time, and grinding speed. Nano-sized BM was successfully prepared under the conditions of ball milling in this study.

Microscopically, natural bone tissue is composed of an organic collagen fiber structure and an inorganic apatite framework structure. The basic units of the inorganic structure are needle and columnar apatite crystals. They are intertwined with amorphous collagen fibers, oriented or coiled to form a variety

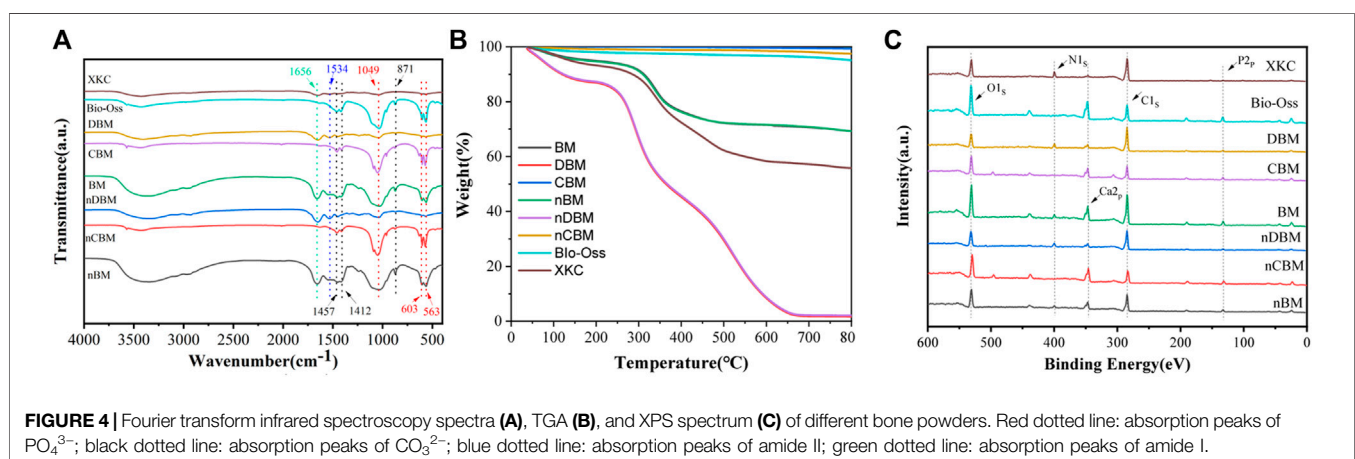


FIGURE 4 | Fourier transform infrared spectroscopy spectra (A), TGA (B), and XPS spectrum (C) of different bone powders. Red dotted line: absorption peaks of  $\text{PO}_4^{3-}$ ; black dotted line: absorption peaks of  $\text{CO}_3^{2-}$ ; blue dotted line: absorption peaks of amide II; green dotted line: absorption peaks of amide I.

**TABLE 1** | Basic component content of different bone powders (%).

	Ash	Protein	Fat	Moisture
BM	68.83±4.14	23.88±1.94	1.69±0.21	5.95±0.88
nBM	69.99±3.54	22.19±1.84	1.64±0.03	5.92±0.2
CBM	99.29±0.38	0	0	0
nCBM	97.50±1.22	0	0	0
DBM	2.34±0.29	81.28±3.19	2.19±0.15	13.82±0.49
nDBM	2.08±0.09	80.5±4.92	2.45±0.11	14.5±0.68
Bio-Oss	94.93±4.33	0	0	0
XKC	55.74±2.96	36.29±1.8	3.21±0.22	4.69±0.29

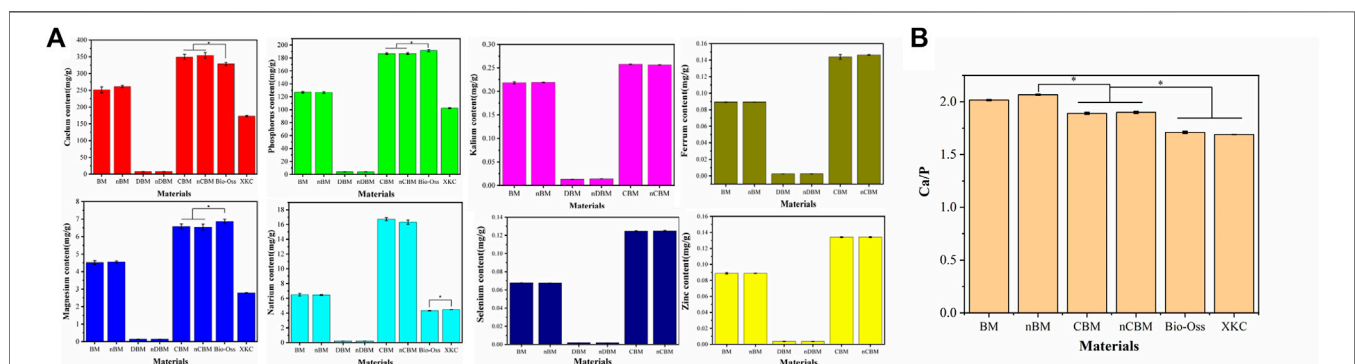
of structures and different functional units (Kumar et al., 2016; Wubneh et al., 2018). As shown in **Figures 2A–C**, nBM had an irregular shape, consisting of needle-stick hydroxyapatite crystals and an amorphous fiber structure, which completely retains the natural bone tissue structure. nCBM was calcined at a high temperature during the preparation process, and the organic collagen fibers in the bone tissue were lost; thus, the morphology was a needle-shaped hydroxyapatite. nDBM had an amorphous fibrous structure because most of the inorganic calcium and phosphorus salts were removed during the preparation process. The corresponding HRTEM images are shown in **Figures 2D–F**. The interplanar distances measured in the segments (fringes) of the HRTEM micrograph of nCBM were ~0.236 nm, corresponding to the interplanar spacing of the (212) plane of the hydroxyapatite. This reveals that nCBM had a compact crystal structure. The HRTEM micrographs of nBM and nDBM suggested that they had no obvious crystal structure. These differences might be attributed to the presence of organic matrix in nBM and nDBM. The corresponding selected area electron diffraction patterns demonstrated similar results. Meanwhile, all the major elements (Ca, P, and N) are shown in the energy-dispersive X-ray spectroscopy spectrum (**Figures 2G–I**). nCBM did not contain N due to the lack of organic components. Because of the removal of inorganic calcium and phosphate salts, nDBM did not have Ca and P. Since nBM had both inorganic and organic components, Ca, P, and N elements appeared in the energy spectrum.

**Figure 3** shows the XRD patterns of different nano bone powders. Characteristic peaks of nCBM corresponded to the

major diffraction peaks of stoichiometric hydroxyapatite (PDF#74-0565). nBM presented a lower intensity and a higher signal-to-noise ratio than nCBM, while nDBM presented an amorphous band. These differences might be attributed to the presence of organic matrix in nBM and nDBM. The XRD results were in good agreement with the TEM observations.

To study the differences in the chemical structures of different BM and the same kind of BM with different particle sizes, FTIR analysis was conducted. As shown in **Figure 4A**, 563 and 603  $\text{cm}^{-1}$  were the bending vibration absorption peaks of  $\text{PO}_4^{3-}$  in hydroxyapatite, 871  $\text{cm}^{-1}$  was the bending vibration absorption peak of  $\text{CO}_3^{2-}$ , 1049  $\text{cm}^{-1}$  was the symmetrical stretching absorption peak of  $\text{PO}_4^{3-}$ , and 1412 and 1457  $\text{cm}^{-1}$  were the stretching vibration absorption peaks of  $\text{CO}_3^{2-}$  (Khoo et al., 2015; Yin et al., 2015). Since most of the inorganic calcium and phosphorus salts were removed in DBM and nDBM, the two BM did not have the above characteristic absorption peaks. For the rest of the bone powders, the above characteristic absorption peaks were detected, and the peak positions of different bone powders were consistent, indicating that no new substances appeared during the ball milling process; in addition, the differences in particle size did not cause differences in the chemical structure of bone powder. Of note, 1534  $\text{cm}^{-1}$  was the N–H bending vibration absorption peak of amide II, and 1656  $\text{cm}^{-1}$  was the C=O stretching vibration absorption peak of amide I (Boutinguiza et al., 2012). Since CBM, nCBM, and Bio-Oss did not contain organic collagen fibers, there were no two characteristic absorption peaks. It could be seen that the chemical structures of CBM, nCBM, and Bio-Oss were mainly phosphate and carbonate, and the chemical structures of DBM, nDBM, and XKC were mainly organic. BM and nBM had both inorganic and organic chemical structures.

The proportion of inorganic and organic compounds in different bone powders could be determined by TGA. As shown in **Figure 4B**, after a high temperature of 800°C, the remaining substance of BM was inorganic. Therefore, CBM, nCBM, and Bio-Oss were almost all inorganic, accounting for 99.29%, 97.50%, and 94.93%, respectively. In DBM and nDBM, the proportion of inorganic matter was

**FIGURE 5** | Mineral content (A) and Ca/P ratio (B) of different bone powders, \* $p < 0.05$ .



**TABLE 2 |** Amino acid composition and content of different bone powders (%).

Amino acid	nBM	nDBM	XKC
Aspartic acid	1.43±0.014	5.33±0.012	2.29±0.014
Threonine*	0.49±0.003	1.83±0.001	0.65±0.001
Serine	0.71±0.069	2.63±0.011	1.08±0.004
Glutamate	2.51±0.013	9.17±0.039	3.86±0.021
Proline	2.70±0.019	10.40±0.021	4.19±0.018
Glycine	4.93±0.005	18.86±0.048	7.96±0.032
Alanine	1.98±0.008	7.37±0.005	3.20±0.012
Valine*	0.67±0.022	2.14±0.009	1.14±0.005
Methionine	0.11±0.019	0.48±0.002	0.13±0.001
Isoleucine*	0.31±0.008	1.27±0.013	0.46±0.048
Leucine*	0.74±0.001	2.94±0.022	1.10±0.021
Tyrosine	0.20±0.005	0.84±0.007	0.20±0.003
Phenylalanine*	0.49±0.029	1.83±0.004	0.73±0.011
Histidine*	0.35±0.007	0.94±0.003	0.27±0.006
Lysine*	0.81±0.012	3.01±0.016	1.21±0.009
Arginine	1.66±0.004	6.55±0.008	2.62±0.015
Essential amino acids	3.86±0.016	13.96±0.183	5.56±0.027
Total	20.11±0.326	75.58±0.481	31.09±0.109

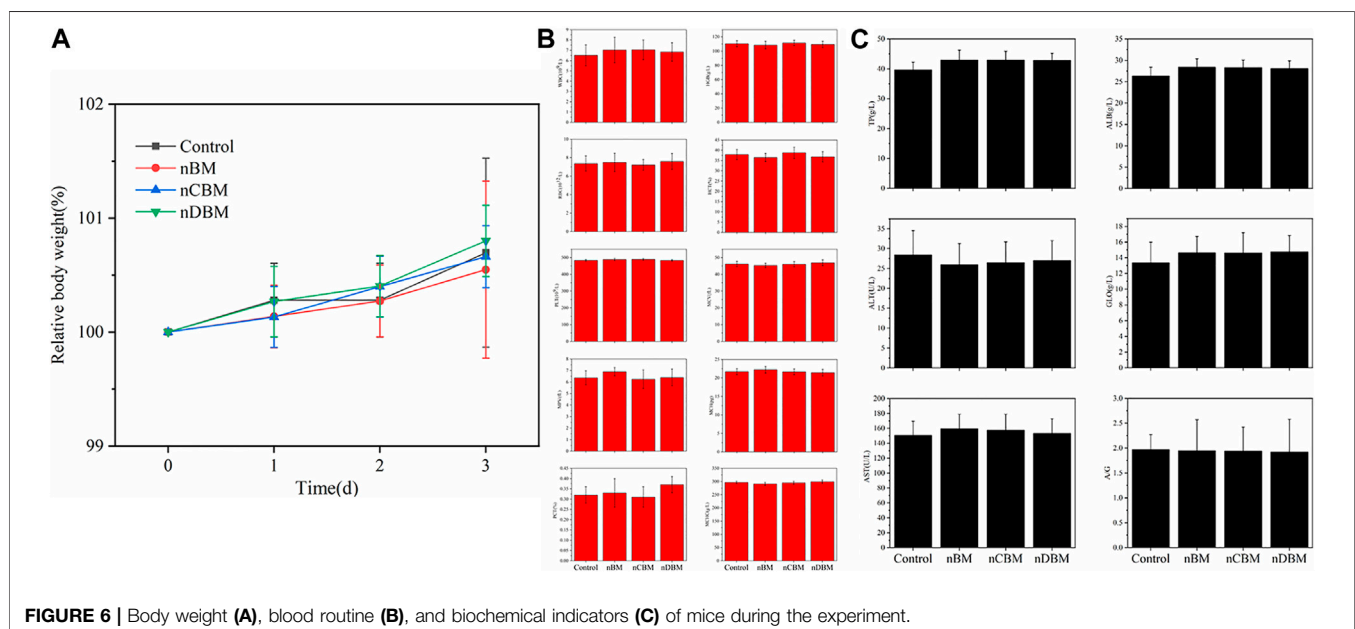
1.72% and 2.08%, respectively. The proportion of inorganic matter in BM, nBM, and XKC was 69.24%, 69.23%, and 55.74%, respectively.

The elemental composition and structure of different BM were further analyzed by XPS. As shown in **Figure 4C**, CBM, nCBM, and Bio-Oss hardly contained organic collagen fibers, so there was no characteristic absorption peak of N element in the XPS energy spectrum. DBM and nDBM hardly contained inorganic calcium and phosphorus salts, so the characteristic absorption peaks of Ca and P elements in the spectrum were very small. Since BM, nBM, and XKC had both inorganic and organic components, characteristic absorption peaks of Ca, P, and N elements appeared in the XPS energy spectrum.

### 3.1.2 Basic Components of Nano-Deer Bone Meal

As shown in **Table 1**, different particle sizes of the same type of BM did not have significant differences in the content of the basic components of BM ( $p > 0.05$ ). This is consistent with the results of the FTIR analysis and TGA. Due to the different preparation processes, the content of the basic ingredients in different bone powders varied greatly. As is widely known, natural bone tissue is mainly composed of organic components (35%) and inorganic components (65%). We found that the proportion of ash in BM and nBM prepared in this study was higher than that in natural bone tissue and the commercial product XKC, while the proportion of protein and fat was lower than that in natural bone tissue and XKC. The ash ratio of CBM and nCBM was also higher than that of Bio-Oss. The different contents of these basic components may have different effects on the proliferation, differentiation, and migration of BMSCs.

Subsequently, we measured and analyzed the main mineral elements of different BM, including calcium, phosphorus, magnesium, sodium, potassium, iron, selenium, and zinc. As shown in **Figure 5A**, different particle sizes of the same type of BM did not have significant differences in the mineral content of BM ( $p > 0.05$ ). The mineral content of different BM varied greatly. In particular, the calcium content in CBM and nCBM was significantly higher than that in Bio-Oss, while the phosphorus and magnesium content was significantly lower than that in Bio-Oss ( $p < 0.05$ ). Potassium, iron, selenium, and zinc were not detected in Bio-Oss and XKC. Therefore, by measuring the mineral content, we found a clear difference in the composition of deer bone and cow bone. In addition, we calculated the Ca/P ratio. As shown in **Figure 5B**, the Ca/P ratio in CBM and nCBM was significantly higher than that in Bio-Oss, and the Ca/P ratio in BM and nBM was significantly higher than that in CBM and nCBM, both of which were much higher than the Ca/P ratio in human bone tissue. Therefore, the Ca/P





ratio in deer bone is significantly higher than that in cow bone and human bone tissue. Deer bone contains trace elements beneficial to the human body, which cow bone does not have; this may be the reason why deer bone can be and has been used as a traditional Chinese medicine for osteogenesis from ancient times to the present.

We selected nBM, nDBM, and XKC to determine the amino acid content. As shown in **Table 2**, different BM have different amino acid contents due to different preparation processes. Seven amino acids are essential amino acids (with \*) and are necessary for human development. An increasing number of studies has shown that amino acids play an important role in the function of osteoblasts. It has been found that glutamine is involved in the matrix calcification process of calvarial precursor cells (Brown

et al., 2011). Glutamine can participate in the tricarboxylic acid cycle and can be converted into citric acid to promote the energy metabolism of osteogenic precursor cells (Karner et al., 2015). A recent study showed that glutamine can promote the proliferation of bone marrow stem cells and their differentiation into osteoblasts (Yu et al., 2019). Atf4, an important regulator of osteogenic differentiation, can increase the uptake of amino acids and the synthesis of collagen. In patients with Coffin–Lowry syndrome caused by Atf4 mutation, both bone mass and bone density are significantly reduced (Yang et al., 2004; Elefteriou et al., 2006). In addition, arginine can promote the osteogenic differentiation of BMSCs (Chevalley et al., 1998). BM and nBM prepared in this study have both inorganic and organic components, both of which can promote osteogenesis.

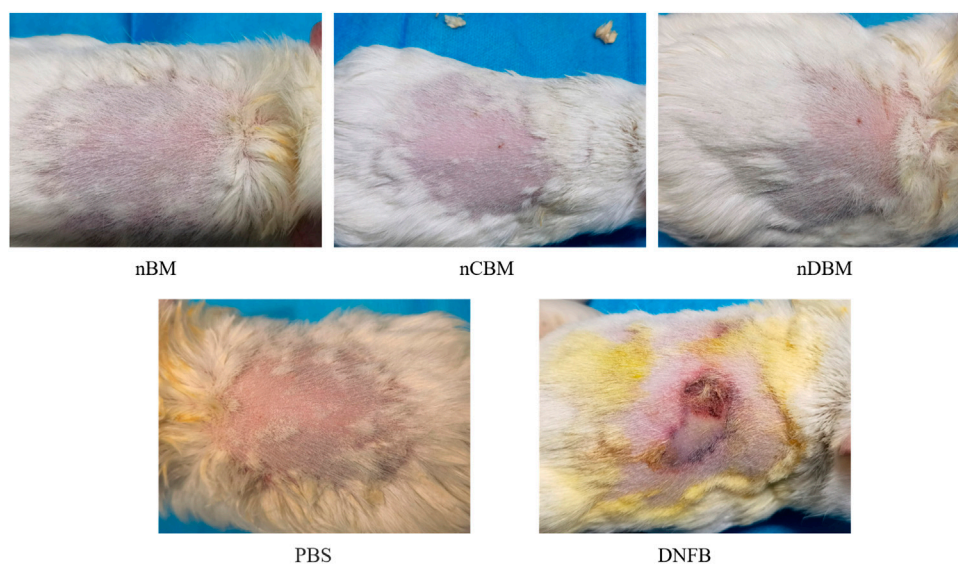


**FIGURE 7 |** Appearance of the guinea pig skin on the 3rd day of the experiment.

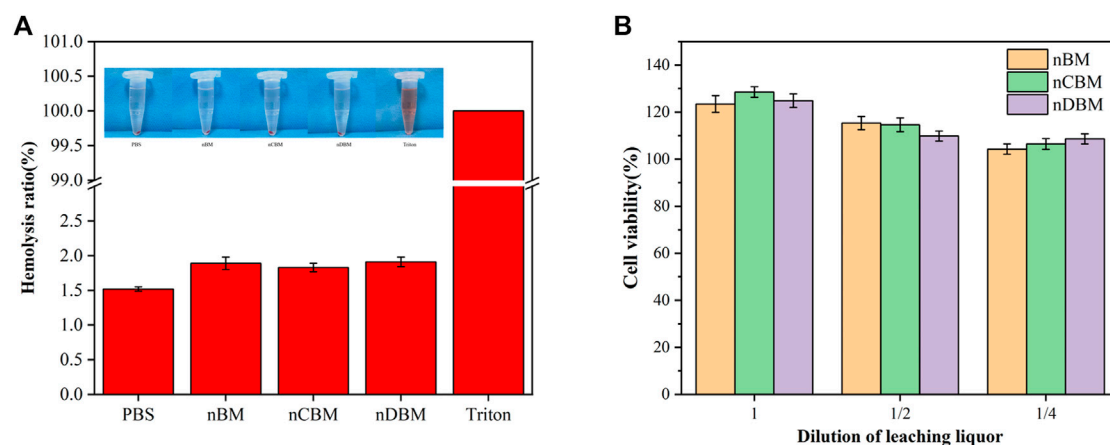
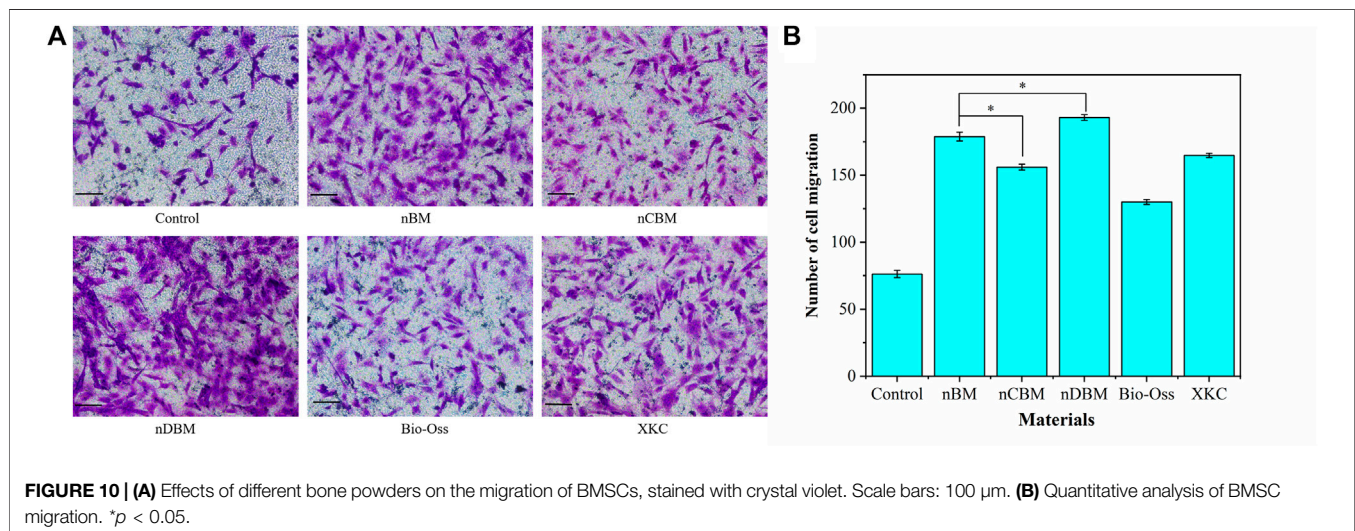
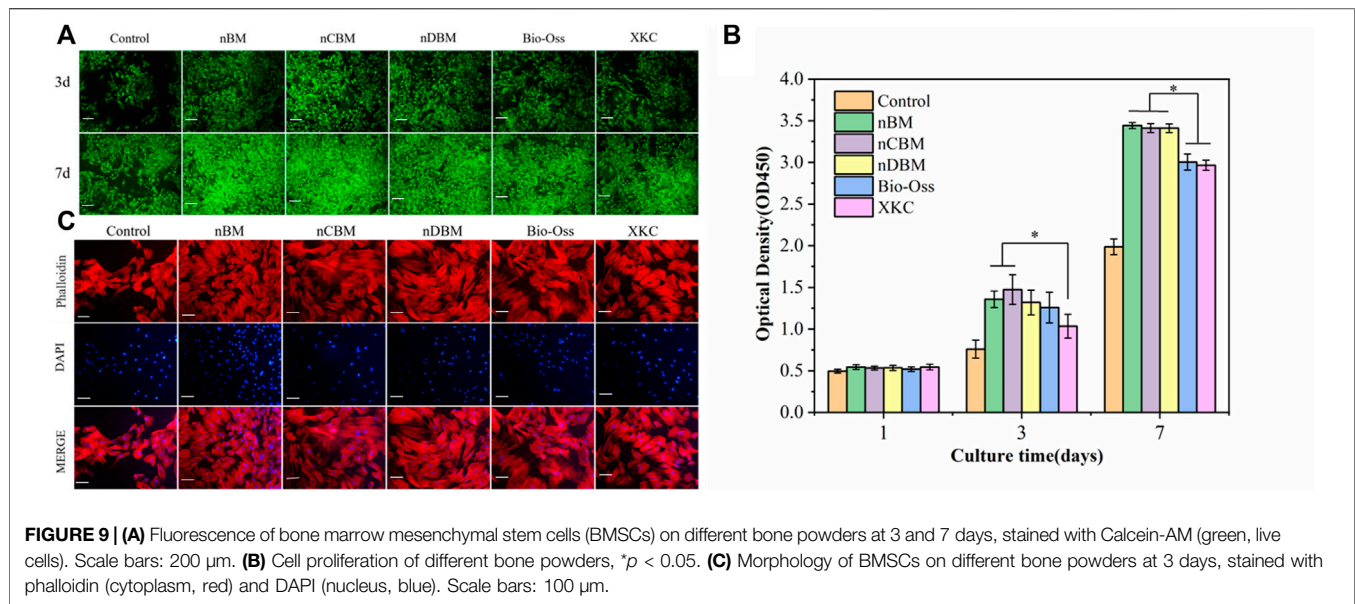


**FIGURE 8 |** Hemolysis rate (A) and cytotoxicity (B) of different bone powders.



Therefore, in theory, they can significantly promote the osteogenic differentiation of BMSCs.

## 3.2 Biosafety of Nano-Deer Bone Meal

### 3.2.1 Systemic Acute Toxicity Test

The systemic acute toxicity test is performed by injecting an extract of the implant material into the blood circulation system of the animal and then observing whether the animal is poisoned, so as to judge the toxicity. General observation: At 30 min, 1, 2, and 3 days after injection, the vital signs of the mice in the experimental and control groups were good without obvious poisoning. At the same time, changes in body weight were detected. As shown in **Figure 6A**, the body weight of mice in the experimental and control groups increased by varying degrees, but there was no significant difference. In addition, blood routine and

blood biochemical tests showed no significant difference in results after 3 days (**Figures 6B and C**). Therefore, the systemic acute toxicity experiments showed that the deer BM prepared in this study was biologically safe.

### 3.2.2 Skin Sensitization Test

The skin sensitization test is used to evaluate possible contact hazards from chemicals released from implant materials. The guinea pigs in the experimental and negative control groups did not have erythema and edema on the skin after injection of the extract, while the guinea pigs in the positive control group had severe erythema (purple) and edema (**Figure 7**). The scoring results are shown in **Supplementary Table S3**. The deer bone powder prepared in this study underwent physical and chemical decellularization treatment to remove substances that can cause immunogenic reactions. Therefore, the skin sensitization



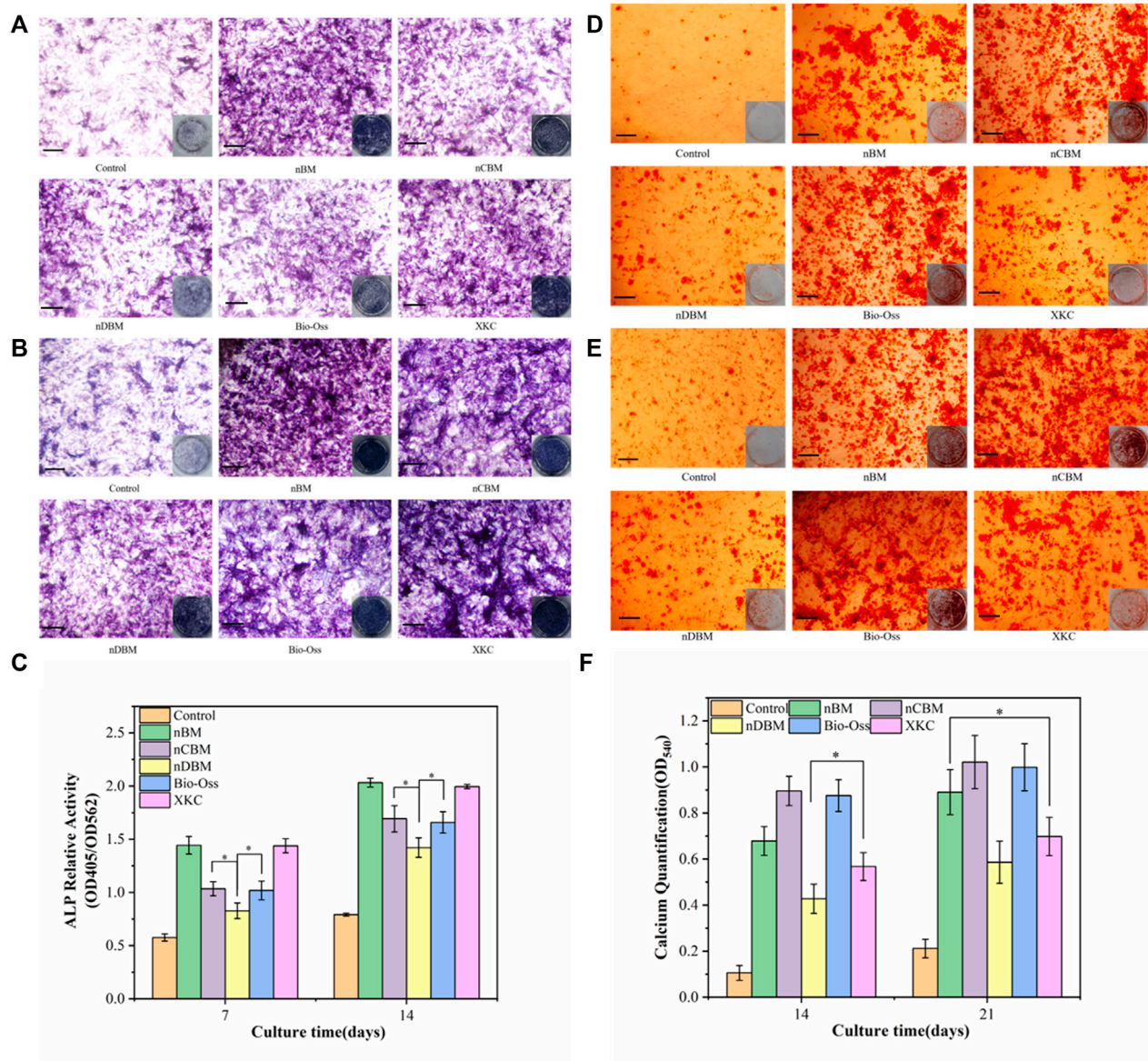


**FIGURE 11 |** Alkaline phosphatase (ALP) staining (**A,B**) and alizarin red staining (**D,E**) in BMSCs cultured on different bone powders for 7 and 14 days (ALP) and 14 and 21 days (AR). (**C**) Corresponding quantitative evaluation of relative ALP activity in BMSCs cultured on different bone powders for 7 and 14 days. (**F**) Corresponding quantitative evaluation of calcium content and mineral deposition in BMSCs cultured on different bone powders for 14 and 21 days. Scale bars: 100  $\mu$ m. \* $p < 0.05$ .

experiments showed that the deer bone powder prepared in this study does not cause contact damage to the skin.

### 3.2.3 *In vitro* Hemolysis Test

The *in vitro* hemolysis test is used to evaluate the effect of implanted material on the blood by detecting the rate of hemolysis after red blood cell rupture. As shown in **Figure 8A**, the red blood cells in the experimental and negative control groups were deposited at the bottom of the centrifuge tube, and no obvious hemolysis occurred, while the positive control group had obvious hemolysis. According to the calculation formula, the hemolysis rate of the extracts in

the experimental group was less than the requirement of 5% (**Figure 8A**). The experimental results showed that the deer BM prepared in this study has no obvious effect on blood and meets the safety standards for medical biomaterials.

### 3.2.4 Cytotoxicity Assay

Cytotoxicity assay is an important method to evaluate the biosafety of implant materials. As shown in **Figure 8B**, compared with the negative control group (medium without extract), the addition of extract and gradient diluent (1/2, 1/4) in the experimental group not only did not inhibit but also promoted the proliferation of BMSCs, and the promoting

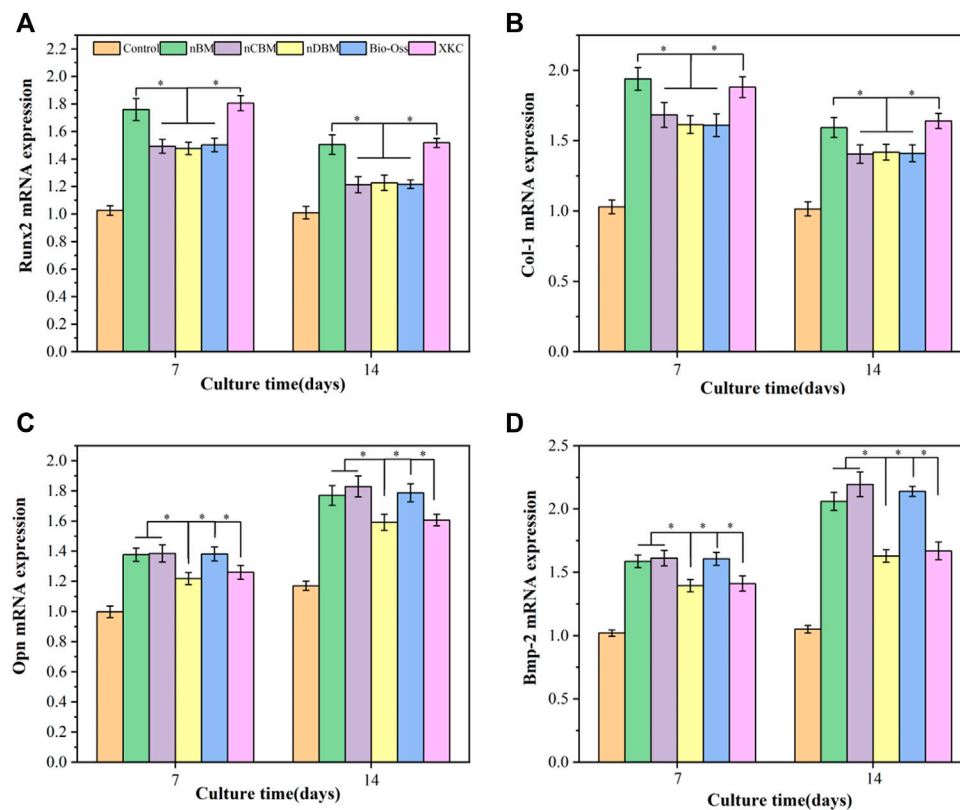


**FIGURE 12 |** qRT-PCR analysis of Runx2 (A), Col-1 (B), Opn (C), and Bmp-2 (D) in BMSCs cultured on different bone powders for 7 and 14 days. \* $p < 0.05$ .

effect decreased with the serial dilution. The results showed that the deer BM prepared in this study has no cytotoxicity.

### 3.3 In vitro Cell Studies

#### 3.3.1 Cell Proliferation and Morphology

During bone repair, BMSC proliferation plays an important role in their function. BMSCs were cultured in media containing different BM, and the number of cells at 1, 3, and 7 days was tested using the CCK-8 method. To observe cell proliferation more intuitively, BMSCs were stained at 3 and 7 days. As shown in **Figure 9B**, the total number of cells in each group increased gradually with the increase in culture time. There was no significant difference in the number of cells in each group at 1 day. At 3 days, the number of cells in the BM group was significantly higher than that in the control group ( $p < 0.05$ ). Among the different BM groups, the number of cells in the nBM and nCBM groups was significantly higher than that in the XKC group ( $p < 0.05$ ), while the number of cells in the other BM groups was not significantly different. At 7 days, the number of cells in the nBM, nCBM, and nDBM groups was significantly higher than that in the Bio-Oss and XKC groups ( $p < 0.05$ ), and the number of cells in all the BM groups was significantly higher than that in the control group ( $p < 0.05$ ). As shown in **Figure 9A**, the cells of 3 and 7 days were stained, and almost all cells showed green fluorescence, indicating that the cells survived normally. As

quantitatively analyzed, the cell density in the nBM, nCBM, and nDBM groups was significantly higher than that in the Bio-Oss and XKC groups at 7 days. In addition, when cultured for 3 days, the BMSC cytoskeleton was observed by staining, and it could be seen that BMSCs in all groups showed a typical spindle structure with a complete cytoskeleton. Compared with the sparse cells in the control group, the cells in the BM group were denser; the cells in the nBM, nCBM, and nDBM groups were more stretched and had more filamentous pseudopodia, and the connections between the cells were closer (**Figure 9C**). According to our analysis, on the one hand, as in the analysis of the composition of BM, the Ca/P ratio in deer bone was significantly higher than that in bovine bone and human bone tissue, and it contains trace elements beneficial to the human body, which bovine bone does not have. On the other hand, the bone powder was prepared at the nanoscale, so that the particle size becomes smaller and the specific surface area increases. In addition, nBM has a natural bone-graded structure. During the preparation process, it was subjected to strong friction and collision, which disrupts the hydroxyapatite structure deposited in the collagen fibrin; thus, it is easier to release calcium and phosphate ions. Therefore, compared with Bio-Oss and XKC, nBM, nCBM, and nDBM prepared in this study were more likely to promote the proliferation and adhesion of BMSCs.



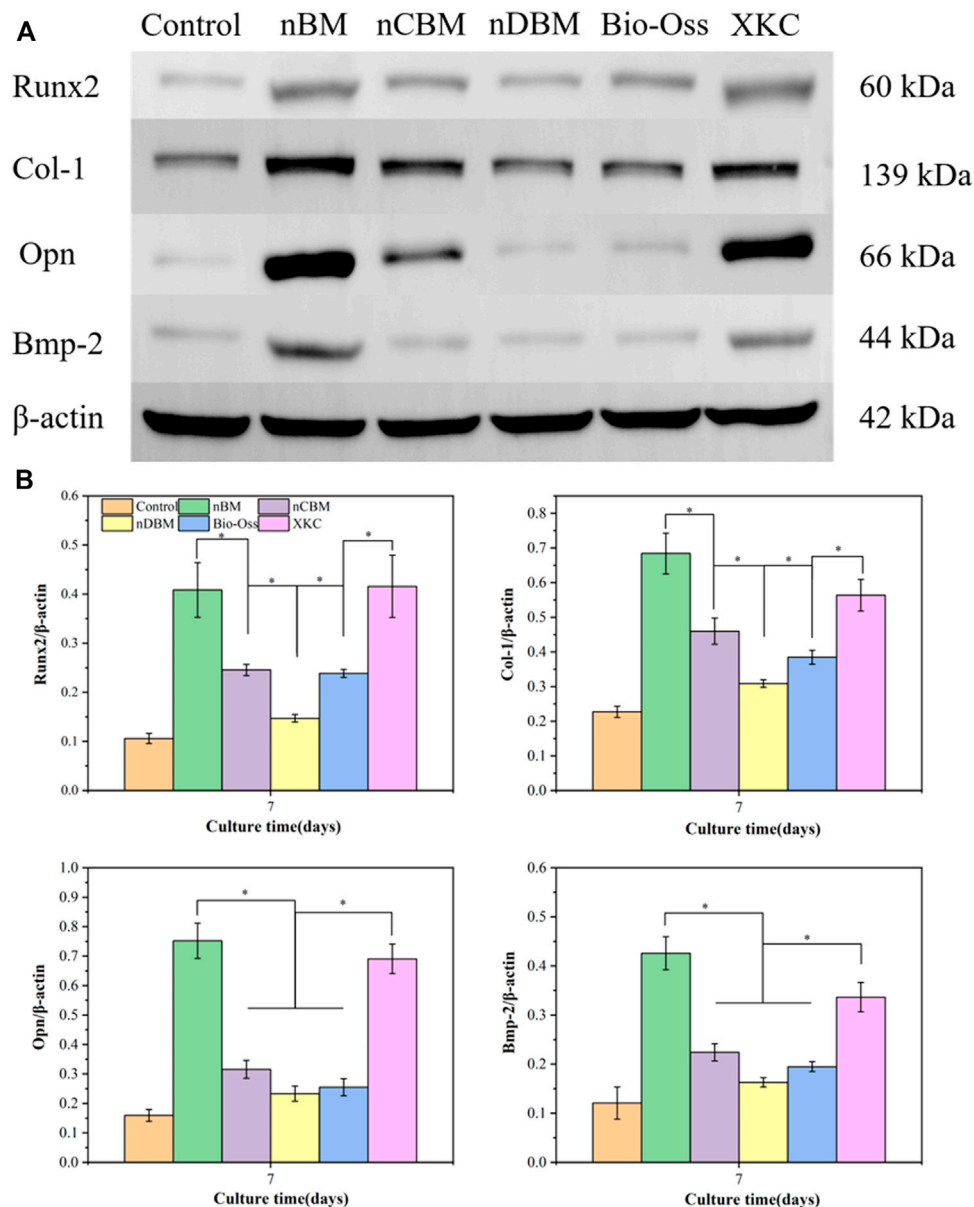


**FIGURE 13 | (A)** Western blotting for protein-level detection of Runx2, Col-I, Opn, and Bmp-2 in different groups of cells for 7 days. **(B)** Band densitometry analysis of Runx2, Col-I, Opn, and Bmp-2 protein for 7 days. \* $p < 0.05$ .

### 3.3.2 Cell Migration

In the process of osteogenic induction, BMSCs are regulated by various factors to differentiate into osteoblasts and migrate into the area of bone regeneration. Therefore, promoting cell migration and enhancing the recruitment of BMSCs are beneficial to bone repair in bone defect areas (Chavakis et al., 2008). As shown in **Figure 10A**, the nDBM group had the highest cell migration density, followed by the nBM and XKC groups, and finally the nCBM and Bio-Oss groups. Quantitative analysis of the number of cells migrated showed that all BM groups significantly promoted cell migration compared with the control group ( $p < 0.05$ ). In the BM group, the number of

cells migrated in the nDBM group was significantly higher than that in the nBM and XKC groups ( $p < 0.05$ ), followed by the nCBM group, and finally the Bio-Oss group (**Figure 10B**). Studies have shown that growth factors such as BMP and TGF can promote the migration of BMSCs (Gamell et al., 2011). nDBM prepared in this study contained these growth factors, which significantly promoted the migration of BMSCs. nBM and XKC were not as effective as nDBM because they contained fewer organic components. nCBM and Bio-Oss did not contain organic active ingredients, so the induction effect was not as good as that of the other three BM groups, while all were better than the control

group. This is because both groups contained calcium ions, which promote cell migration. Some studies suggest that calcium ions may also be chemokines for cell migration (Liu et al., 2018). The calcium ion content in the nCBM group was higher than that in the Bio-Oss group, so the cell migration effect of the nCBM group was better than that of the Bio-Oss group.

### 3.3.3 Alkaline Phosphatase Activity Assay

ALP is a marker of early metaphase differentiation of osteoblasts. As shown in **Figures 11A and B**, in general, with the increase in culture time, the ALP staining effect of each group gradually increased. When the culture time was 7 days, the staining effect of all BM groups was better than that of the control group. In the BM group, the nBM and XKC groups had the best staining results, followed by the nCBM and Bio-Oss groups, and finally the nDBM group. The trend of the staining effect at 14 days of culture was the same as that at 7 days. The ALP quantitative analysis results, presented in **Figure 11C**, verify the above results. After 7 and 14 days of BMSC culture, the ALP activities in the nBM and XKC groups were significantly higher than those in the nCBM and Bio-Oss groups ( $p < 0.05$ ), and the ALP activities in the nCBM and Bio-Oss groups were significantly higher than those in the nDBM group ( $p < 0.05$ ). Therefore, it can be concluded that nBM and XKC with both organic and inorganic components are superior to nCBM, Bio-Oss, and nDBM containing a single component in the early induction of osteogenic differentiation of BMSCs.

### 3.3.4 Alizarin Red Staining for Calcium Deposition

Calcium deposition is a marker of osteoblast differentiation and maturation. As shown in **Figures 11D and E**, in general, with the increase in culture time, the color rendering effect of calcium nodule deposition in each group gradually increased. When cultured for 14 days, almost no calcium nodules were deposited in the control group, while calcium nodules were observed in all BM groups. In the BM group, the nCBM and Bio-Oss groups had the best staining results, followed by the nBM and XKC groups, and finally the nDBM group. The trend of the staining effect at 21 days of culture was the same as that at 14 days. The results of the quantitative analysis of calcium nodules, shown in **Figure 11F**, showed that after 21 days of BMSC culture, there was no significant difference in the number of calcium nodules among the nBM, nCBM, and Bio-Oss groups ( $p > 0.05$ ), but the numbers in these three groups were significantly higher than those in the XKC and nDBM groups ( $p < 0.05$ ). nCBM and Bio-Oss, which are dominated by inorganic calcium and phosphorus salts, contain a large amount of calcium nodule deposition materials, which can promote the deposition of mineralized nodules in the extracellular matrix of BMSCs. nBM also promotes the mineralization of stem cells due to its high Ca/P ratio. Therefore, nBM, nCBM, and Bio-Oss exhibited the ability to promote the osteogenic differentiation of BMSCs at a later stage.

### 3.3.5 Gene Expression Analysis via Quantitative Reverse Transcription-Polymerase Chain Reaction

In the process of natural bone formation, a large number of genes related to osteogenesis are activated. These genes are considered markers in the process of osteogenesis, providing important evidence for the induction of osteogenesis by materials. The difference in cell behavior and the relative expression of osteogenesis-related genes are important evaluation indicators (Wang et al., 2004; Tang et al., 2018). To further explore the effect of different BM on the osteogenic differentiation of BMSCs at the molecular level, we used real-time quantitative PCR to quantitatively measure the osteogenic differentiation-related target genes, Runx2, Col-I, Opn, and Bmp-2. Runx2 is a key gene expressed early in the process of osteogenic differentiation, which plays an important role in the differentiation of osteoblasts, the maturation of chondrocytes, and the production of bone matrix proteins. Col-I is expressed in the early and middle stages of osteogenic differentiation of osteoblasts. It can act as a nucleation site for hydroxyapatite crystals during the mineralization stage of the extracellular matrix of osteoblasts, promote calcium deposition in the matrix, and play an important role in the mineralization of osteoblasts. Opn is a marker expressed in the middle stage of osteogenic differentiation of osteoblasts. As an important part of the extracellular matrix, it can promote the signal transduction between osteoblasts and play a key role in osteogenic induction. Bmp-2 is a growth factor that regulates the development of bone tissue; it can induce the proliferation of stem cells and their directional differentiation to osteoblasts and promote the formation of new bone (Tang et al., 2018).

As shown in **Figure 12**, BMSCs were cocultured with different BM for 7 and 14 days. Compared with the blank control group, the expression levels of the Runx2 and COL-I genes in BMSCs were increased in the BM group, and the expression levels in the nBM and XKC groups were the highest, with no significant difference between the two groups. These results indicate that BM can significantly promote the early osteogenic differentiation of BMSCs, and nBM and XKC have the most significant promoting effect. Regarding Opn and Bmp-2, the expression levels of the Opn and Bmp-2 genes gradually increased with the increase in culture time. Compared with the blank control group, the expression levels of the Opn and Bmp-2 genes in the cells of the BM group increased, among which the nBM, nCBM, and Bio-Oss groups had the highest expression levels. These results indicate that BM can also significantly promote the osteogenic differentiation of BMSCs in the middle and late stages, with nBM, nCBM, and Bio-Oss showing the best effect.

### 3.3.6 Bone-Related Protein Expression by Western Blotting

To further investigate the regulation by different BM of the protein expression and osteogenic factors (Runx2, Col-I, Opn, and Bmp-2) in BMSCs, western blotting was performed, shown in **Figures 13A and B**. Western blotting (**Figure 13A**) and band densitometry (**Figure 13B**) analysis results indicated that compared with the blank control group, the amount of

osteogenic differentiation-related proteins (Runx2, Col-I, Opn, and Bmp-2) produced by BMSCs in all BM groups increased, and the expression levels in the nBM group were the highest. The western blotting results were relatively in accordance with the observations of ALP activity, calcium mineral deposition, and expression of osteogenic-related genes. Overall, nBM can significantly promote the osteogenic differentiation of BMSCs in the early, middle, and late stages.

## 4 CONCLUSION

In this study, nBM, nCBM, and nDBM were successfully prepared. It was found that the Ca/P ratio in deer bone was significantly higher than that in cow bone and human bone tissue, and deer bone contained beneficial trace elements, such as potassium, iron, selenium, and zinc, which were not found in cow bone. The three kinds of deer bone powders prepared in this study had good biocompatibility and met the implantation standards of medical biomaterials. Cell function studies showed that compared with Bio-Oss and XKC, nBM, nCBM, and nDBM prepared in this study were more likely to promote the proliferation and adhesion of BMSCs. In terms of cell migration, nDBM was better than nBM and XKC, followed by nCBM, and finally Bio-Oss. nBM and XKC performed excellently in inducing osteogenic differentiation of BMSCs in the early stage, while nBM, nCBM, and Bio-Oss performed better in promoting the osteogenic differentiation of BMSCs in the later stage. Based on the above results, nBM has excellent performance in the proliferation, adhesion, migration, and differentiation of BMSCs. These findings indicate that nBM can be used as a potential osteoinductive active nanomaterial to enhance bone tissue engineering scaffolds with certain application prospects.

## REFERENCES

- Aryaei, A., Jayatissa, A. H., and Jayasuriya, A. C. (2014). Mechanical and Biological Properties of Chitosan/carbon Nanotube Nanocomposite Films. *J. Biomed. Mat. Res.* 102 (8), 2704–2712. doi:10.1002/jbm.a.34942
- Baldwin, P., Li, D. J., Auston, D. A., Mir, H. S., Yoon, R. S., and Koval, K. J. (2019). Autograft, Allograft, and Bone Graft Substitutes: Clinical Evidence and Indications for Use in the Setting of Orthopaedic Trauma Surgery. *J. Orthop. Trauma* 33 (4), 203–213. doi:10.1097/bot.0000000000001420
- Boutingui, M., Pou, J., Comesaña, R., Lusquinos, F., de Carlos, A., and León, B. (2012). Biological Hydroxyapatite Obtained from Fish Bones. *Mater. Sci. Eng. C* 32 (3), 478–486. doi:10.1016/j.msec.2011.11.021
- Brown, P. M., Hutchison, J. D., and Crockett, J. C. (2011). Absence of Glutamine Supplementation Prevents Differentiation of Murine Calvarial Osteoblasts to a Mineralizing Phenotype. *Calcif. Tissue Int.* 89 (6), 472–482. doi:10.1007/s00223-011-9537-6
- Chae, T., Yang, H., Leung, V., Ko, F., and Troczynski, T. (2013). Novel Biomimetic Hydroxyapatite/alginate Nanocomposite Fibrous Scaffolds for Bone Tissue Regeneration. *J. Mater. Sci. Mater. Med.* 24 (8), 1885–1894. doi:10.1007/s10856-013-4957-7
- Chavakis, E., Urbich, C., and Dimmeler, S. (2008). Homing and Engraftment of Progenitor Cells: A Prerequisite for Cell Therapy. *J. Mol. Cell. Cardiol.* 45 (4), 514–522. doi:10.1016/j.jmcc.2008.01.004
- Chevalley, T., Rizzoli, R., Manen, D., Caverzasio, J., and Bonjour, J. (1998). Arginine Increases Insulin-like Growth Factor-I Production and Collagen

## DATA AVAILABILITY STATEMENT

The original contributions presented in the study are included in the article/**Supplementary Material**; further inquiries can be directed to the corresponding author.

## ETHICS STATEMENT

The animal study was reviewed and approved by the Laboratory Animal Welfare and Ethics Committee, College of Basic Medical Sciences, Jilin University (Changchun, China).

## AUTHOR CONTRIBUTIONS

YL and ZT were involved in the completion of the experiments, data analysis, and manuscript preparation. JM performed the cell culture experiments. JZ helped with the data processing and revision of the manuscript. HW designed the study and contributed to the data analysis and writing of the manuscript. All authors contributed to the article and approved the submitted version.

## FUNDING

This work was supported by a grant from the Science and Technology Development Plan of Jilin Province (No. 20200404187YY).

## SUPPLEMENTARY MATERIAL

The Supplementary Material for this article can be found online at <https://www.frontiersin.org/articles/10.3389/fbioe.2022.891765/full#supplementary-material>

- Synthesis in Osteoblast-like Cells. *Bone* 23 (2), 103–109. doi:10.1016/s8756-3282(98)00081-7
- Elefteriou, F., Benson, M. D., Sowa, H., Starbuck, M., Liu, X., Ron, D., et al. (2006). ATF4 Mediation of NF1 Functions in Osteoblast Reveals a Nutritional Basis for Congenital Skeletal Dysplasias. *Cell Metab.* 4 (6), 441–451. doi:10.1016/j.cmet.2006.10.010
- Eliaz, N., and Metoki, N. (2017). Calcium Phosphate Bioceramics: A Review of Their History, Structure, Properties, Coating Technologies and Biomedical Applications. *Mater. (Basel)* 10 (4). doi:10.3390/ma10040334
- Gamell, C., Susperregui, A. G., Bernard, O., Rosa, J. L., and Ventura, F. (2011). The p38/MK2/Hsp25 Pathway Is Required for BMP-2-Induced Cell Migration. *Plos One* 6 (1), e16477. doi:10.1371/journal.pone.0016477
- Ghanaati, S., Barbeck, M., Booms, P., Lorenz, J., Kirkpatrick, C. J., and Sader, R. A. (2014). Potential Lack of "standardized" Processing Techniques for Production of Allogeneic and Xenogeneic Bone Blocks for Application in Humans. *Acta Biomater.* 10 (8), 3557–3562. doi:10.1016/j.actbio.2014.04.017
- Grgurevic, L., Pecina, M., Vukicevic, S., and Marshall, R. (2017). Marshall R. Urist and the Discovery of Bone Morphogenetic Proteins. *Int. Orthop. (SICOT)* 41 (5), 1065–1069. doi:10.1007/s00264-017-3402-9
- Guo, X. (2017). Nutritional Composition and Anti Osteoporosis Activity of Sika Deer Bone Meal. *J. Econ. Animal* 21 (3). doi:10.13326/j.jea.2017.1179
- He, Z. (2011). Study on Effects of Collagen of Deer Bone on Osteoporosis in Ovariectomized Rats. *Traditional Chin. Med. Pharmacol. Clin.* 27 (5), 76–79. doi:10.13412/j.cnki.zyy.2011.05.027
- Ho-Shui-Ling, A., Bolander, J., Rustom, L. E., Johnson, A. W., Luyten, F. P., and Picart, C. (2018). Bone Regeneration Strategies: Engineered Scaffolds, Bioactive

- Molecules and Stem Cells Current Stage and Future Perspectives. *Biomaterials* 180, 143–162. doi:10.1016/j.biomaterials.2018.07.017
- Karner, C. M., Esen, E., Okunade, A. L., Patterson, B. W., and Long, F. (2015). Increased Glutamine Catabolism Mediates Bone Anabolism in Response to WNT Signaling. *J. Clin. Invest.* 125 (2), 551–562. doi:10.1172/jci78470
- Khojasteh, A., Morad, G., and Behnia, H. (2013). Clinical Importance of Recipient Site Characteristics for Vertical Ridge Augmentation: a Systematic Review of Literature and Proposal of a Classification. *J. Oral Implantol.* 39 (3), 386–398. doi:10.1563/aaid-joi-d-11-00210
- Khoo, W., Nor, F. M., Ardhyana, H., and Kurniawan, D. (2015). “Preparation of Natural Hydroxyapatite from Bovine Femur Bones Using Calcination at Various Temperatures,” in 2nd International Materials, Industrial, and Manufacturing Engineering Conference Bali, INDONESIA, MIMEC2015. doi:10.1016/j.promfg.2015.07.034
- Kumar, A., Mandal, S., Barui, S., Vasireddi, R., Gbureck, U., Gelinsky, M., et al. (2016). Low Temperature Additive Manufacturing of Three Dimensional Scaffolds for Bone-Tissue Engineering Applications: Processing Related Challenges and Property Assessment. *Mater. Sci. Eng. R-Reports* 103, III. doi:10.1016/j.mser.2016.01.001
- Laschke, M. W., Strohe, A., Menger, M. D., Alini, M., and Eglin, D. (2010). *In Vitro* and *In Vivo* Evaluation of a Novel Nanosize Hydroxyapatite Particles/poly(ester-Urethane) Composite Scaffold for Bone Tissue Engineering. *Acta Biomater.* 6 (6), 2020–2027. doi:10.1016/j.actbio.2009.12.004
- Lee, H., Choi, H.-S., Park, Y., Ahn, C. W., Jung, S. U., Park, S. H., et al. (2014). Effects of Deer Bone Extract on the Expression of Pro-inflammatory Cytokine and Cartilage-Related Genes in Monosodium Iodoacetate-Induced Osteoarthritic Rats. *Biosci. Biotechnol. Biochem.* 78 (10), 1703–1709. doi:10.1080/09168451.2014.930317
- Li, C., Wang, Q., Gu, X., Kang, Y., Zhang, Y., Hu, Y., et al. (2019). Porous Se@SiO<sub>2</sub> Nanocomposite Promotes Migration and Osteogenic Differentiation of Rat Bone Marrow Mesenchymal Stem Cell to Accelerate Bone Fracture Healing in a Rat Model. *Ijn* 14, 3845–3860. doi:10.2147/ijn.s202741
- Li, L., Lu, H., Zhao, Y., Luo, J., Yang, L., Liu, W., et al. (2019). Functionalized Cell-free Scaffolds for Bone Defect Repair Inspired by Self-Healing of Bone Fractures: A Review and New Perspectives. *Mater. Sci. Eng. C* 98, 1241–1251. doi:10.1016/j.msec.2019.01.075
- Li-ping, A. (2016). Effect of Deer Bone Polypeptides on Bone Microarchitecture of Dexamethasoneinduced Osteoporosis Rats. *Chin. Traditional Herb. Drugs* 47 (22), 4030–4034.
- Liu, J., Zhou, P., Long, Y., Huang, C., and Chen, D. (2018). Repair of Bone Defects in Rat Radii with a Composite of Allogeneic Adipose-Derived Stem Cells and Heterogeneous Deproteinized Bone. *Stem Cell Res. Ther.* 9, 79. doi:10.1186/s13287-018-0817-1
- Long, B., Dan, L., Jian, L., Yunyu, H., Shu, H., and Zhi, Y. (2012). Evaluation of a Novel Reconstituted Bone Xenograft Using Processed Bovine Cancellous Bone in Combination with Purified Bovine Bone Morphogenetic Protein. *Xenotransplantation* 19 (2), 122–132. doi:10.1111/j.1399-3089.2012.00694.x
- Mahmoud, N. S., Ahmed, H. H., Mohamed, M. R., Amr, K. S., Aglan, H. A., Ali, M. A. M., et al. (2020). Role of Nanoparticles in Osteogenic Differentiation of Bone Marrow Mesenchymal Stem Cells. *Cytotechnology* 72 (1), 1–22. doi:10.1007/s10616-019-00353-y
- Przekora, A. (2019). The Summary of the Most Important Cell-Biomaterial Interactions that Need to Be Considered during *In Vitro* Biocompatibility Testing of Bone Scaffolds for Tissue Engineering Applications. *Mater. Sci. Eng. C* 97, 1036–1051. doi:10.1016/j.msec.2019.01.061
- Quan, W., Ying, M., and Chun-Hui, M. (2015). Treatment of Osteoporosis by Sika Bone Powder Among Rats after Ovariectomy. *China Maternal Child Health* 30 (17).
- Ren, C., Gong, W., Li, F., and Xie, M. (2019). Pilose Antler Aqueous Extract Promotes the Proliferation and Osteogenic Differentiation of Bone Marrow Mesenchymal Stem Cells by Stimulating the BMP-2/Smad1, 5/Runx2 Signaling Pathway. *Chin. J. Nat. Med.* 17 (10), 756–767. doi:10.1016/s1875-5364(19)30092-5
- Simpson, C. R., Kelly, H. M., and Murphy, C. M. (2020). Synergistic Use of Biomaterials and Licensed Therapeutics to Manipulate Bone Remodelling and Promote Non-union Fracture Repair. *Adv. Drug Deliv. Rev.* 160, 212–233. doi:10.1016/j.addr.2020.10.011
- Sonmez, M. M., Armagan, R., Ugurlar, M., and Eren, T. (2017). Allografts versus Equine Xenografts in Calcaneal Fracture Repair. *J. Foot Ankle Surg.* 56 (3), 510–513. doi:10.1053/j.jfas.2017.01.015
- Tang, D., Tare, R. S., Yang, L.-Y., Williams, D. F., Ou, K.-L., and Oreffo, R. O. C. (2016). Biofabrication of Bone Tissue: Approaches, Challenges and Translation for Bone Regeneration. *Biomaterials* 83, 363–382. doi:10.1016/j.biomaterials.2016.01.024
- Tang, Z., Li, X., Tan, Y., Fan, H., and Zhang, X. (2018). The Material and Biological Characteristics of Osteoinductive Calcium Phosphate Ceramics. *Regen. Biomater.* 5 (1), 43–59. doi:10.1093/rb/rbx024
- Touri, R., Moztaaradeh, F., Sadeghian, Z., Bizari, D., Tahriri, M., and Mozafari, M. (2013). The Use of Carbon Nanotubes to Reinforce 45S5 Bioglass-Based Scaffolds for Tissue Engineering Applications. *Biomed. Res. Int.* 2013, 465086. doi:10.1155/2013/465086
- Urist, M. R., and Strates, B. S. (2009). The Classic: Bone Morphogenetic Protein. *Clin. Orthop. Relat. Res.* 467 (12), 3051–3062. doi:10.1007/s11999-009-1068-3
- Urist, M. R. (1965). Bone: Formation by Autoinduction. *Science* 150 (3698), 893–899. doi:10.1126/science.150.3698.893
- Wang, C., Duan, Y., Markovic, B., Barbara, J., Howlett, C. R., Zhang, X., et al. (2004). Phenotypic Expression of Bone-Related Genes in Osteoblasts Grown on Calcium Phosphate Ceramics with Different Phase Compositions. *Biomaterials* 25 (13), 2507–2514. doi:10.1016/j.biomaterials.2003.09.035
- Wang, P., Hao, L., Wang, Z., Wang, Y., Guo, M., and Zhang, P. (2020). Gadolinium-Doped BTO-Functionalized Nanocomposites with Enhanced MRI and X-Ray Dual Imaging to Simulate the Electrical Properties of Bone. *ACS Appl. Mat. Interfaces* 12 (44), 49464–49479. doi:10.1021/acsami.0c15837
- Wang, W., and Yeung, K. W. K. (2017). Bone Grafts and Biomaterials Substitutes for Bone Defect Repair: A Review. *Bioact. Mater.* 2 (4), 224–247. doi:10.1016/j.bioactmat.2017.05.007
- Wubneh, A., Tsekoura, E. K., Ayranci, C., and Uludağ, H. (2018). Current State of Fabrication Technologies and Materials for Bone Tissue Engineering. *Acta Biomater.* 80, 1–30. doi:10.1016/j.actbio.2018.09.031
- Xudong, W. (2021). Effects of Epimedium Rhizoma Drynariae Combined with Bone Nutritional Tonic on Rats with Osteoporosis. *Sci. Technol. Food Industry* 42 (13), 338–344. doi:10.13386/j.issn1002-0306.2020080004
- Xue, C., Pan, W., Lu, X., Guo, J., Xu, G., Sheng, Y., et al. (2021). Effects of Compound Deer Bone Extract on Osteoporosis Model Mice and Intestinal Microflora. *J. Food Biochem.* 45 (6), e13740. doi:10.1111/jfbc.13740
- Yang, X., Matsuda, K., Bialek, P., Jacquot, S., Masuoka, H. C., Schinke, T., et al. (2004). ATF4 Is a Substrate of RSK2 and an Essential Regulator of Osteoblast Biology: Implication for Coffin-Lowry Syndrome. *Cell* 117 (3), 387–398. doi:10.1016/s0092-8674(04)00344-7
- Yao, D., Liu, N.-n., and Mo, B.-w. (2020). Assessment of Proliferation, Migration and Differentiation Potentials of Bone Marrow Mesenchymal Stem Cells Labeling with Silica-Coated and Amine-Modified Superparamagnetic Iron Oxide Nanoparticles. *Cytotechnology* 72 (4), 513–525. doi:10.1007/s10616-020-00397-5
- Yin, T., Park, J. W., and Xiong, S. (2015). Physicochemical Properties of Nano Fish Bone Prepared by Wet Media Milling. *LWT - Food Sci. Technol.* 64 (1), 367–373. doi:10.1016/j.lwt.2015.06.007
- Yu, Y., Newman, H., Shen, L., Sharma, D., Hu, G., Mirando, A. J., et al. (2019). Glutamine Metabolism Regulates Proliferation and Lineage Allocation in Skeletal Stem Cells. *Cell Metab.* 29 (4), 966–978. doi:10.1016/j.cmet.2019.01.016
- Zhao, D., Witte, F., Lu, F., Wang, J., Li, J., and Qin, L. (2017). Current Status on Clinical Applications of Magnesium-Based Orthopaedic Implants: A Review from Clinical Translational Perspective. *Biomaterials* 112, 287–302. doi:10.1016/j.biomaterials.2016.10.017

**Conflict of Interest:** The authors declare that the research was conducted in the absence of any commercial or financial relationships that could be construed as a potential conflict of interest.

**Publisher's Note:** All claims expressed in this article are solely those of the authors and do not necessarily represent those of their affiliated organizations, or those of the publisher, the editors, and the reviewers. Any product that may be evaluated in this article, or claim that may be made by its manufacturer, is not guaranteed or endorsed by the publisher.

Copyright © 2022 Li, Tan, Zhang, Mu and Wu. This is an open-access article distributed under the terms of the Creative Commons Attribution License (CC BY). The use, distribution or reproduction in other forums is permitted, provided the original author(s) and the copyright owner(s) are credited and that the original publication in this journal is cited, in accordance with accepted academic practice. No use, distribution or reproduction is permitted which does not comply with these terms.





## OPEN ACCESS

## EDITED BY

Livia Visai,  
University of Pavia, Italy

## REVIEWED BY

Gabriele Ceccarelli,  
University of Pavia, Italy  
Nora Bloise,  
University of Pavia, Italy  
Kaili Lin,  
Shanghai Jiao Tong University, China

## \*CORRESPONDENCE

Yu-Jue Zhang,  
zhangyujue@126.com  
Feng-Zhen Liu,  
ldcllfz@163.com  
Bin Zhang,  
zhangbinlc@sdu.edu.cn

## SPECIALTY SECTION

This article was submitted to  
Biomaterials,  
a section of the journal  
Frontiers in Bioengineering and  
Biotechnology

RECEIVED 11 April 2022

ACCEPTED 25 July 2022

PUBLISHED 29 August 2022

## CITATION

Li J, Luo X, Lv Z-Y, Qiang H-F, Hou C-Y,  
Liu K, Meng C-X, Zhang Y-J, Liu F-Z and  
Zhang B (2022), Microporous structures  
on mineralized collagen mediate  
osteogenesis by modulating the osteo-  
immune response of macrophages.  
*Front. Bioeng. Biotechnol.* 10:917655.  
doi: 10.3389/fbioe.2022.917655

## COPYRIGHT

© 2022 Li, Luo, Lv, Qiang, Hou, Liu,  
Meng, Zhang, Liu and Zhang. This is an  
open-access article distributed under  
the terms of the [Creative Commons  
Attribution License \(CC BY\)](https://creativecommons.org/licenses/by/4.0/). The use,  
distribution or reproduction in other  
forums is permitted, provided the  
original author(s) and the copyright  
owner(s) are credited and that the  
original publication in this journal is  
cited, in accordance with accepted  
academic practice. No use, distribution  
or reproduction is permitted which does  
not comply with these terms.

# Microporous structures on mineralized collagen mediate osteogenesis by modulating the osteo-immune response of macrophages

Jun Li<sup>1,2</sup>, Xin Luo<sup>2</sup>, Zhao-Yong Lv<sup>2</sup>, Hui-Fen Qiang<sup>3</sup>,  
Cai-Yao Hou<sup>3</sup>, Kun Liu<sup>1,2</sup>, Chun-Xiu Meng<sup>2</sup>, Yu-Jue Zhang<sup>2\*</sup>,  
Feng-Zhen Liu<sup>2,3\*</sup> and Bin Zhang<sup>1,2\*</sup>

<sup>1</sup>Department of Oral and Maxillofacial Surgery, School and Hospital of Stomatology, Shandong University & Shandong Provincial Key Laboratory of Oral Tissue Regeneration & Shandong Engineering Laboratory for Dental Materials and Oral Tissue Regeneration, Jinan, Shandong, China, <sup>2</sup>Liaocheng People's Hospital, Liaocheng Hospital Affiliated to Shandong First Medical University, Liaocheng, China, <sup>3</sup>Department of Materials Science and Engineering, Liaocheng University, Liaocheng, China

It is a new hot pot in tissue engineering and regenerative medicine to study the effects of physicochemical properties of implanted biomaterials on regulating macrophage polarization to promote bone regeneration. In this study, we designed and fabricated mineralized collagen (MC) with different microporous structures via *in vitro* biomimetic mineralization method. The microporous structures, mechanical properties, shore hardness and water contact angle measurements were tested. Live/dead cell staining, CCK-8 assay, phalloidine staining, staining of focal adhesions were used to detect cell behavior. ELISA, qRT-PCR, ALP, and alizarin red staining (ARS) were performed to appraise osteogenic differentiation and investigated macrophage response and their subsequent effects on the osteogenic differentiation. The results showed that RAW264.7 and MC3T3-E1 cells were able to survive on the MC. MC with the microporous structure of approximately 84  $\mu\text{m}$  and 70%–80% porosity could promote M2 macrophage polarization and increase the expression level of TGF- $\beta$  and VEGF. Moreover, the gene expression of the osteogenic markers ALP, COL-1, and OCN increased. Therefore, MC with different microporous structures mediated osteoimmunomodulation in bone regeneration. These data will provide a new idea of biomaterials inducing bone repair and direct the optimal design of novel immune biomaterials, development, and rational usage.

## KEYWORDS

inflammatory response, mineralized collagen, microporous structures, macrophage polarization, osteogenic differentiation

## Introduction

Effective bone tissue repair is critical for all living organisms of the survivals. The physical body is a complex environment, and the implanted biomaterials will inevitably lead to a series of biological reactions. Implantations trigger inflammatory reactions, and the host immune response always leads to failures in clinic (Zhou et al., 2021). Almost all the biomaterials implanted into human beings may induce many host reactions, and the early host reactions and the local microenvironment have an essential influence on bone regeneration and repair (Huang, et al., 2021). After implantation into the body, immune cells acting with the biomaterials surface originate a series of reactions, which decide whether the effective bone repair (Bai et al., 2020; Wei et al., 2022; Gaharwar et al., 2020; Yi et al., 2022). Among all immune cells, macrophages are the primary effector cells because of their significant biodiversity and plasticity. Especially, macrophages are positively involved in the whole stage of bone repair. Depending on context-dependent polarization profiles, macrophage polarized to pro-inflammatory phenotype (M1 macrophage) or pro-tissue regeneration (anti-inflammatory, M2 macrophage) phenotype (Badylak, 2016; Purnell and Hines, 2017; Eming et al., 2017). Therefore, the accurate and quickly conversion from M1 macrophage to M2 macrophage will contribute to positive bone reconstruction and be essential under the bone-forming environment regulating osteoblast differentiation (Brown and Badylak, 2013; Li et al., 2020; Xie et al., 2020).

In the recent, tuning biomaterials properties to modulate macrophage polarization has attracted increasing attention. More and more scholars have turned much attention to how the inflammation response can be controlled to serve the goals of the implantable bracket, particularly with regards to suppressing the immune rejection of exotic bodies and enhancing the integration of scaffolds with native tissue (Chen et al., 2016; Christo et al., 2016; Chen et al., 2017a). Zhao et al. (2020) had demonstrated that calcium-phosphorus phases, with different chemical and physical characteristics modulated the macrophages response (Zhao et al., 2020). Min et al. (2016) found the aggressive inflammatory reaction could be helpful for the origination of osteogenic cascades reaction. However, if the inflammation became overage, it could inhibit the fracture healing (Chen et al., 2018). These indicated that the biomaterials implantations elicited the prominent role of regulating immunoreaction, which should be well guided into them that conduce bone integration. The microporous structures on biological materials were found to have an important moderating role on cell actions. These actions could be operated by adjusting the biophysical performance of the microporous systems (Redlich and Smolen, 2012; Chen et al., 2015). We had previously demonstrated the effects of the

surface energy and coarseness of mineralized collagen (MC) implanted on bone absorption. But until now, no document has reported about the microporous structures of MC adjusted macrophage polarization to influence the osteoblast differentiation of MC3T3-E1.

Mineralized collagen (MC) was fabricated bionic mineralization and displayed absolute merit in degradation fast *in vitro*, high hardness, and accelerating osteogenesis differentiation of hMSCs (Xu et al., 2016; Liu et al., 2017; Li et al., 2020; Meng et al., 2021). Shi et al. (2018) had proved that MC was more easily regulated macrophage M2 polarization than HA. Our previous study had demonstrated that the surface roughness of MC regulated the group and single form as well as the production of cell factors, including tumor necrosis factor- $\alpha$  (TNF- $\alpha$ ), interleukin-6 (IL-6), interleukin-4 (IL-4) and interleukin-10 (IL-10) from macrophage in a time-dependent manner (Li et al., 2020). As far as we know, whether the microporous structures of MC will influence macrophage polarization and function has not been reported till now.

In this study, we investigated the modulatory effects of MC with different microporous structures on bone immune responses to confirm the role of microporous structures on MC mediated bone immune regulation. The schematic diagram of MC with different microporous structures regulating macrophage polarization to mediate osteogenesis was shown in Figure 1. The research will lead to regulating bone immune reaction to induce a reasonable and sufficient osteoimmunology environment for material-mediated bone regeneration, and provide a theoretical basis for developing immunomodulatory biomaterials and bone defect treatment in the clinic.

## Materials and methods

### Preparation of mineralized collagen

Nano-hydroxyapatite (HA)/collagen composites were manufactured by Beijing Allgens Medical Science & Technology Co., Ltd. The products were prepared using purified and deantigenized type I collagen as the template and modulated mineralization on calcium-phosphate solution. The mineral phase was HA containing phosphate, and the crystal size was in the nanometer scale. Type I collagen solution (0.67 g/L) was mixed with a certain proportion of  $\text{CaCl}_2$  and  $\text{H}_3\text{PO}_4$  solutions ( $\text{Ca}/\text{P} = 1.67$ ). The solution was gently stirred and the pH value was adjusted to 7.4 with sodium hydroxide solution at room temperature. 48 h after the reaction, the precipitate was washed and filtered, and then freeze-dried thoroughly and produced porous mineralized collagen (MC). We prepared MC with large, medium, and small pore sizes, named MC-A, MC-B, and MC-C, with pore sizes of  $273 \pm 13 \mu\text{m}$ ,  $84 \pm 3 \mu\text{m}$ , and  $9.7 \pm 0.2 \mu\text{m}$ , and porosities of 80%–90%, 70%–80% and 50%–

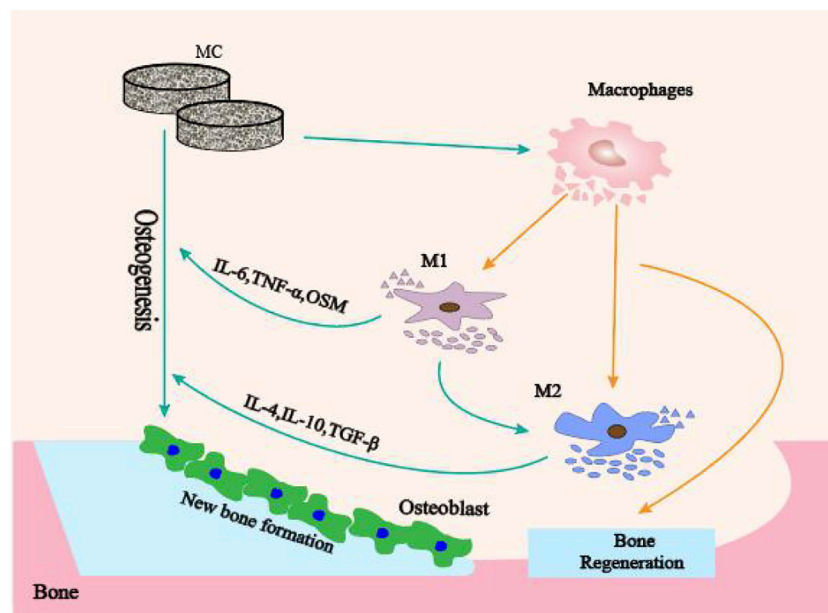


FIGURE 1

The schematic diagram of MC with different microporous structures regulating macrophage polarization to mediate osteogenesis.

60%, respectively. The porosity was related to the collagen content. The porosity of the materials were measured by the porosity analyzer. The obtained materials were similar to natural bone in composition and microstructure.

## Characterizations of mineralized collagen

### Field Emission Scanning Electron Microscopy

The samples were evenly bonded to the conductive adhesive, and a platinum layer was uniformly sprayed by a gold sprayer. The surface morphologies of mineralized collagen (MC) by Field Emission Scanning Electron Microscopy (FESEM) (SU-4800, Hitachi, Japan).

### Measurement of compression mechanics

The initial diameter and thickness of each sample were measured by a vernier caliper. Then the piece was placed in the center of the active platform of the electric universal material testing machine (MTS, E44.304, Co., China). Started the oil supply valve of the test machine, the dynamic forum can be quickly lifted. When the sample contacted the upper-pressure plate, the oil supply should be reduced, and the lifting speed should be slowed to avoid the test failure caused by the excessive compression process. Compression speed was 5 mm/min.

### Shore hardness

Took out the shore hardness tester, pointed to zero, and pressed the surface of the sample with the appropriate force and uniform speed. When the end face of the hardness tester was fully contacted with the surface of the model, recorded the value of the hardness tester table. Three independent tests were performed on each material surface.

### Water contact angle measurements

The surface hydrophilicity of MC was analyzed by measuring the contact angle of the material surface. 10  $\mu$ L of deionized water was added to the surface of the materials. Photographs were taken with a camera within 10 s, and the contact angle was measured by SCA20 software. Three independent tests were carried out on each material surface.

### Cells culture on mineralized collagen with different microporous structures

Mineralized collagen (MC) was cut into discs of 2 mm thickness and then sterilized by irradiation of  $^{60}\text{Co}$  before use. The RAW 264.7 (mouse monocyte/macrophage) was provided by Liaocheng People's Hospital. The MC was put

at a 24-well plate, and cultured in phosphate buffer saline (PBS, Sangon Biotech) for 4 h before RAW 264.7 seeding. For each sample, the  $2 \times 10^5$  RAW 264.7 cells were seeded on the MC. Each substrate was incubated in 1 ml DMEM (Gibco, USA) supplemented with 1% streptomycin/penicillin (Hyclone, USA) and 10% fetal bovine serum (Gibco, USA) for 1, 2 and 3 days, respectively. MC3T3-E1 (mouse embryo osteoblast precursor cells) (ATCC, USA) was inoculated on the surface of different MC in the same way and incubated in  $\alpha$ -MEM complete medium for 1, 3 days and osteogenic induction medium ( $\alpha$ -MEM complete medium supplemented with 10 nM dexamethasone, 50  $\mu$ g/ml vitamin C and 10 mM glycerol phosphate) for 7 days, respectively.

## Live/dead cell staining

MC3T3-E1 cells were seeded on MC surface for calcein-acetyl hydroxymethyl ester/propidium iodide (AM/PI) staining at 1 and 3 days, respectively. The living cells (yellow-green fluorescence) and dead cells (red fluorescence) were observed under an inverted fluorescence microscope at  $490 \pm 10$  nm excitation wavelength. The green fluorescence intensity was detected by Image Pro Plus 7.0 for quantitative analysis.

## Cells viability assay

The proliferation of RAW264.7 and MC3T3-E1 were evaluated by a cell counting kit-8 (CCK-8) assay. MC was placed at the bottom of the 48-well plate, and MC3T3-E1 cells were seeded in culture plates at a density of  $2 \times 10^4$  cells per well. Cells were incubated in DMEM complete medium for 1 day and replaced with macrophage conditioned medium. After 1, 2, and 3 days of incubation, CCK-8 solution was added to each well for an additional 4 h at  $37^\circ\text{C}$ . The cellular activity was assessed by measuring absorbance at a 450 nm wavelength on a microtiter plate reader. In addition, RAW264.7 was seeded on the MC and cultured in DMEM complete medium for 1, 2 and 3 days to detect cellular viability.

## Morphology and micromorphology of macrophagocyte cultured on mineralized collagen

$1 \times 10^6$  cells were inoculated in each well, washed with PBS 3 days later, and fixed in 2.5% glutaraldehyde solution for 20 min. Washed three times and then dehydrated with gradient ethanol solution. Finally, placed in a freeze dryer for 1 h and slowly sealed to room temperature. The sample morphology was observed by FESEM.

## Phalloidine staining of F-actin

Cells were fixed with 4% paraformaldehyde for 30 min and permeabilized with 0.1% Triton X-100 for 20 min at room temperature. Samples were blocked with 1% of bovine serum albumin (BSA; Sigma-Aldrich) and incubated with rhodamine labeled phalloidin for 30 min in the dark environment at room temperature, then washed with PBS for 3 times. The samples were also stained with 4',6-diamidino-2-phenylindole (DAPI) for 30 s in the dark environment at room temperature and washed with PBS 2 times to reveal the nuclei. Cells were observed under a scanning confocal microscope (Nikon, model no. A1R).

## Cell adhesion experiment

### Staining and imaging of focal adhesions

Cells were fixed (4% paraformaldehyde), permeabilized (0.1% Triton X) and blocked (1% BSA). They were then stained with an anti-vinculin antibody (Abcam, ab129002), followed by staining of a corresponding secondary antibody with Alexa 488. Samples were imaged with a confocal microscope (Nikon, model no. A1R).

## Cytokine determinations

Levels of pro-inflammatory cytokines (TNF- $\alpha$ , IL-1 $\beta$ , IL-6), anti-inflammatory cytokine TNF- $\beta$  and VEGF were measured with sandwich enzyme-linked immunosorbent assays (ELISAs) as prescribed by the manufacturer (Abcam).

## Quantitative real-time polymerase chain reaction (qRT-PCR)

Cells were collected to extract RNA and reverse transcribed to cDNA using a reverse transcription kit (Shenggong, China). The mRNA expression was quantified using an

ABI 7500 measuring system and SYBR green supermix (Takara, Japan). All data were normalized to GAPDH expression. At the end of the reaction, the  $2^{-\Delta\Delta C_t}$  method was used as the relative expression of mRNA according to the last measured  $C_t$  value. The primer sequences were shown in Table 1.

## Preparation of macrophage conditioned medium and effect on MC3T3-E1 osteogenesis

MC with different microporous structures were spread in 6-well plates. For each sample,  $1 \times 10^6$  cells were seeded on the



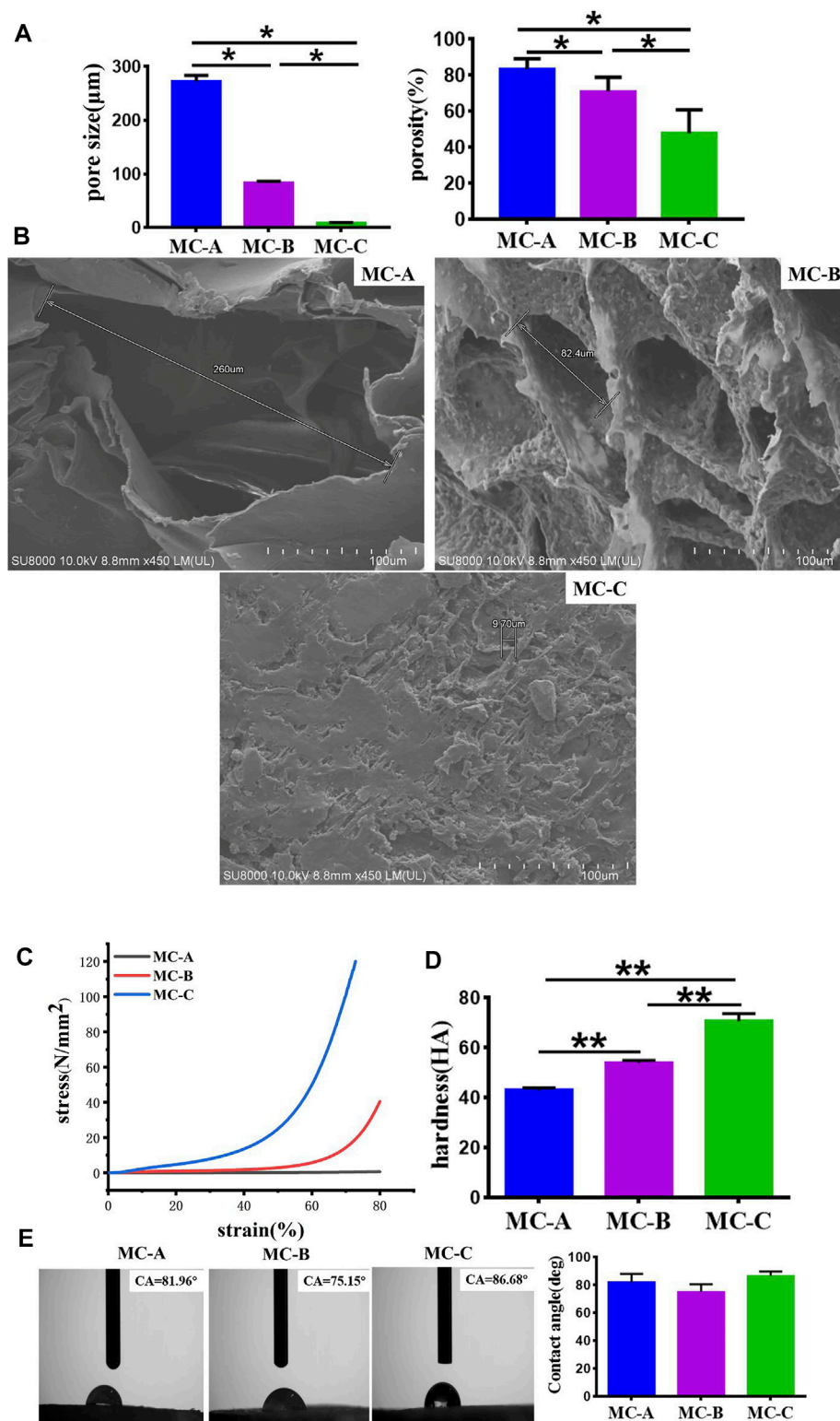


FIGURE 2

Characterizations of mineralized collagen. (A) The pore size and porosity of MC-A, MC-B, and MC-C; (B) FESEM micrographs of MC-A, MC-B, and MC-C (scale bar:100 μm); (C) Compression mechanics of MC-A, MC-B, and MC-C; (D) Shore hardness of MC-A, MC-B and MC-C; (E) Water contact angle of MC-A, MC-B, and MC-C. Data are presented as mean ± SD. \* $p < 0.05$ ; \*\* $p < 0.01$ .

materials surface. Macrophages and materials were co-cultured in complete DMEM medium for 3 days. The supernatant was collected and centrifuged by 1,000 rpm for 5 min to obtain conditioned medium (CM). MC3T3-E1 cells were plated at a density of  $2 \times 10^3 \text{ cm}^{-2}$ . DMEM complete medium was replaced by CM osteogenic induction medium after 1 day. Then the effect of CM on MC3T3-E1 osteogenesis was detected by qRT-PCR, alkaline phosphatase (ALP) staining and activity analysis, alizarin red S staining, and activity analysis.

## ALP staining and activity analysis

After 7 days of MC3T3-E1 culture, ALP expression was detected by 5-Bromo-4-Chloro-3-Indolyl Phosphate/Nitrotetrazolium Blue chloride (BCIP/NBT) Alkaline Phosphatase Color Development Kit (Beyotime, C3206). The color development solution was added sequentially according to the kit instructions, incubated at room temperature without light for 15 min, and then observed and taken photos under the microscope. ALP activity was measured according to the teachings of the Alkaline phosphatase assay kit (Nanjing Jiancheng bioengineering institute).

## Alizarin red S staining and activity analysis

MC3T3-E1 was fixed with 4% paraformaldehyde for 10 min after 21 days in CM osteogenic induction medium and incubated with 0.2% alizarin red S staining solution for 30 min at room temperature. After drying, 10% dodecyl pyridine chloride was added and incubated at room temperature for 1 h. The absorbance at 562 nm was measured on a 96-well plate.

## Statistical analysis

All the analyses were performed using the software SPSS 22.0 (IBM SPSS, Armonk, New York, United States). All the data were expressed as means  $\pm$  standard deviation (SD). Statistical analysis was determined by one-way analysis of variance (ANOVA) and Tukey's post-hoc test. A level of significance was set at  $p < 0.05$ .

## Results

### Characterizations of different mineralized collagen

We had characterized the three groups of mineralized collagen (MC) with microporous structures, the results were as shown in Figure 2. From Figure 2Afig2, the results

showed that the pore size of MC-A was  $273 \pm 13 \mu\text{m}$  and porosity was 80–90%, MC-B was  $84 \pm 3 \mu\text{m}$ , and porosity was 70%–80%, and MC-C was  $9.7 \pm 0.2 \mu\text{m}$ , and porosity was 50%–60%. From FESEM micrographs (Figure 2B), many pores were distributed in the scaffolds with good interconnectivity. According to our previous cooperative research, the porosity of MC was about 70%, and the aperture size was 50–300  $\mu\text{m}$ , which were incredibly similar to the natural bone in both composition and microstructure, and had excellent biocompatibility and biodegradable (Xu et al., 2016; Li et al., 2020). The hydrophilicity, shore hardness, and compression mechanics of MC scaffolds with different pore sizes were tested. The results showed no significant difference in hydrophilicity among the three groups. The compressive strength and shore hardness of MC increased with the decrease of pore sizes (Figures 2C–E).

### Effects of MC with different microporous structure on proliferation, morphology, and osteogenic differentiation of MC3T3-E1

We explored the effects of MC with different microporous structures on the activity, morphology, and osteogenic differentiation of MC3T3-E1. The typical field of vision an inverted fluorescence microscope was selected to observe the staining of live and dead MC3T3-E1 cells at 1 and 3 days. After 1 day, live green cells were predominant in the field of view. On day 3, the number of live cells on the surface of MC increased in all three groups compared with day 1, and the number was significantly more than that of dead cells (Figure 3A). Cells inoculated in MC-A and MC-B with interconnected pseudopods and clear microfilaments. Cells inoculated in MC-B had an increased extension area and enhanced extension ability. Cells inoculated in MC-C had an irregular shapes and bundle-like microfilaments (Figure 3B). OCN is a specific non-collagen protein in bone matrix, which can understand the activity of osteoblasts by OCN level (Komori, 2020). ALP is one of the phenotypic markers of osteoblasts, which can directly reflect the activity or functional status of osteoblasts (Annibali et al., 2021). OPN is involved in bone matrix mineralization and resorption processes (Akram et al., 2018). COL-1 is the most predominantly expressed product during the proliferative phase of osteoblasts (Lin et al., 2019). Therefore, MC3T3-E1 cells were inoculated on MC and cultured under osteogenic induction conditions at 7 days. The expression of osteogenic related genes (ALP, COL-1, OCN, and OPN) was detected by qRT-PCR. It was found that the gene expression level was notably increased in the MC-B group (Figure 3C). Moreover, the MC-B group showed intense ALP staining (Figure 3D). These results suggested that the MC-B group promoted osteogenic differentiation of MC3T3-E1.

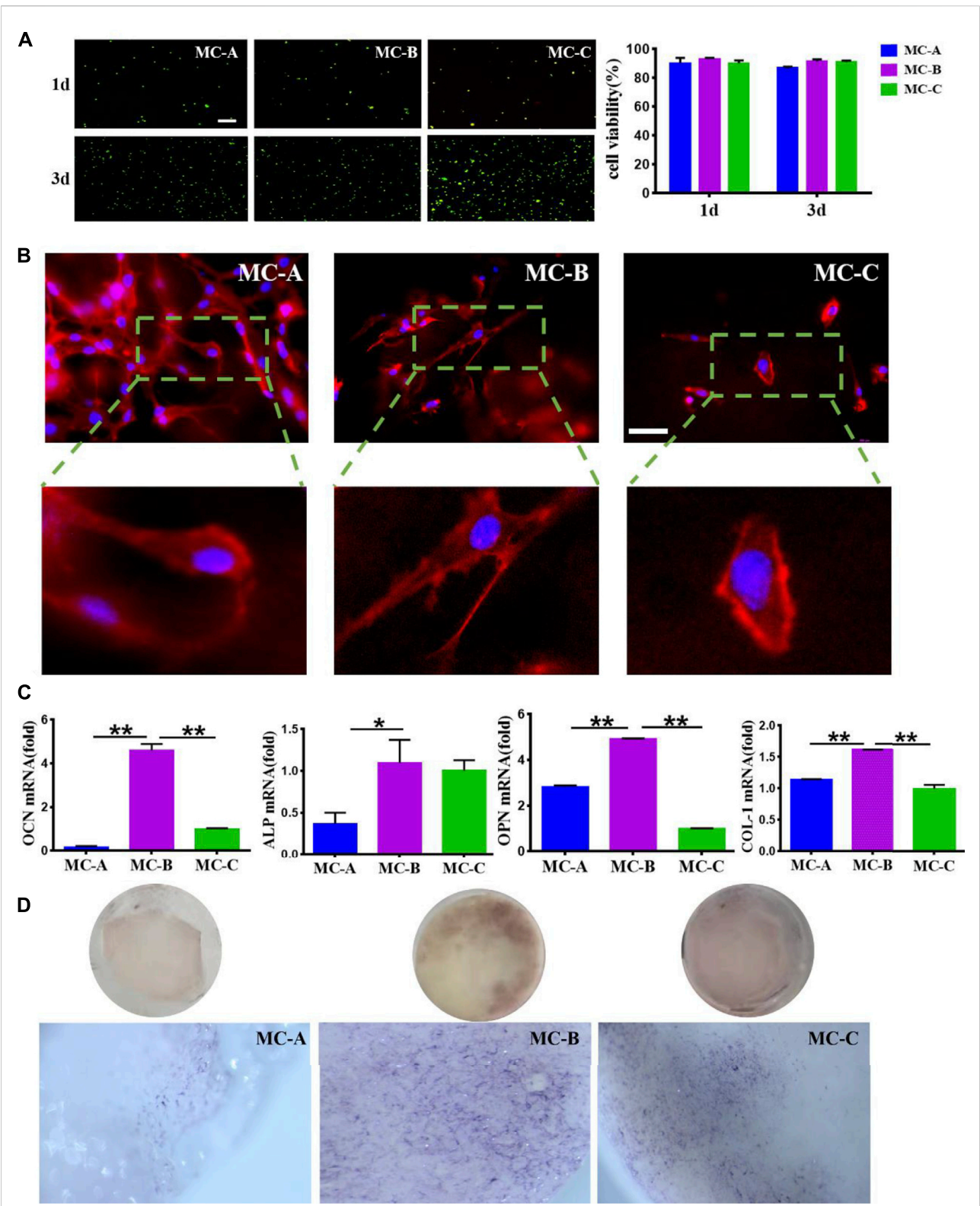


**FIGURE 3**  
Effects of MC-A, MC-B, and MC-C on MC3T3-E1 cells. **(A)** Live/dead cell staining (scale bar: 100  $\mu$ m); **(B)** Effects of MC-A, MC-B, and MC-C on the morphology of MC3T3-E1 cells were detected by rhodamine labeled phalloidin staining (scale bar: 50  $\mu$ m); **(C)** The expression of the osteogenic gene was detected by qRT-PCR; **(D)** ALP staining (stereomicroscope, x60). Data are presented as mean  $\pm$  SD. \* $p$  < 0.05; \*\* $p$  < 0.01.

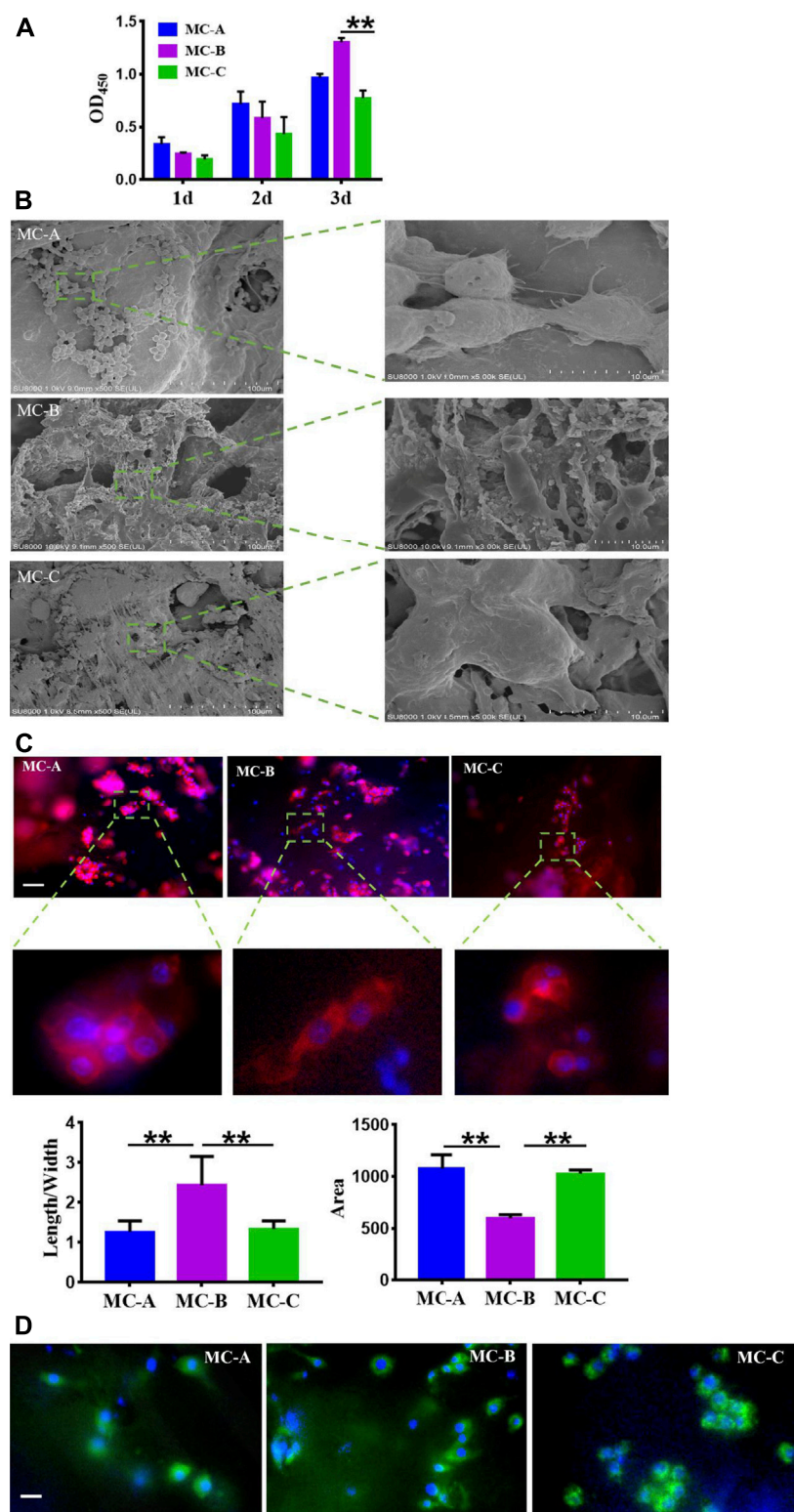


**FIGURE 4** Effects of mineralized collagen with different microporous structures on macrophages morphology. **(A)** CCK-8 cell proliferation experimentation of RAW 264.7 cells after cultured 1 d, 2 d, and 3 days *in vitro*; **(B)** Population and individual morphology of macrophages grown on different mineralized collagen (scale bar:100 µm); **(C)** Detection of the cytoskeleton morphology of macrophages cultured for 3 days by rhodamine labeled phalloidin staining (scale bar: 50 µm); **(D)** Immunofluorescence detection of focal adhesion morphology of macrophages after 3 days of co-culture (scale bar: 50 µm).



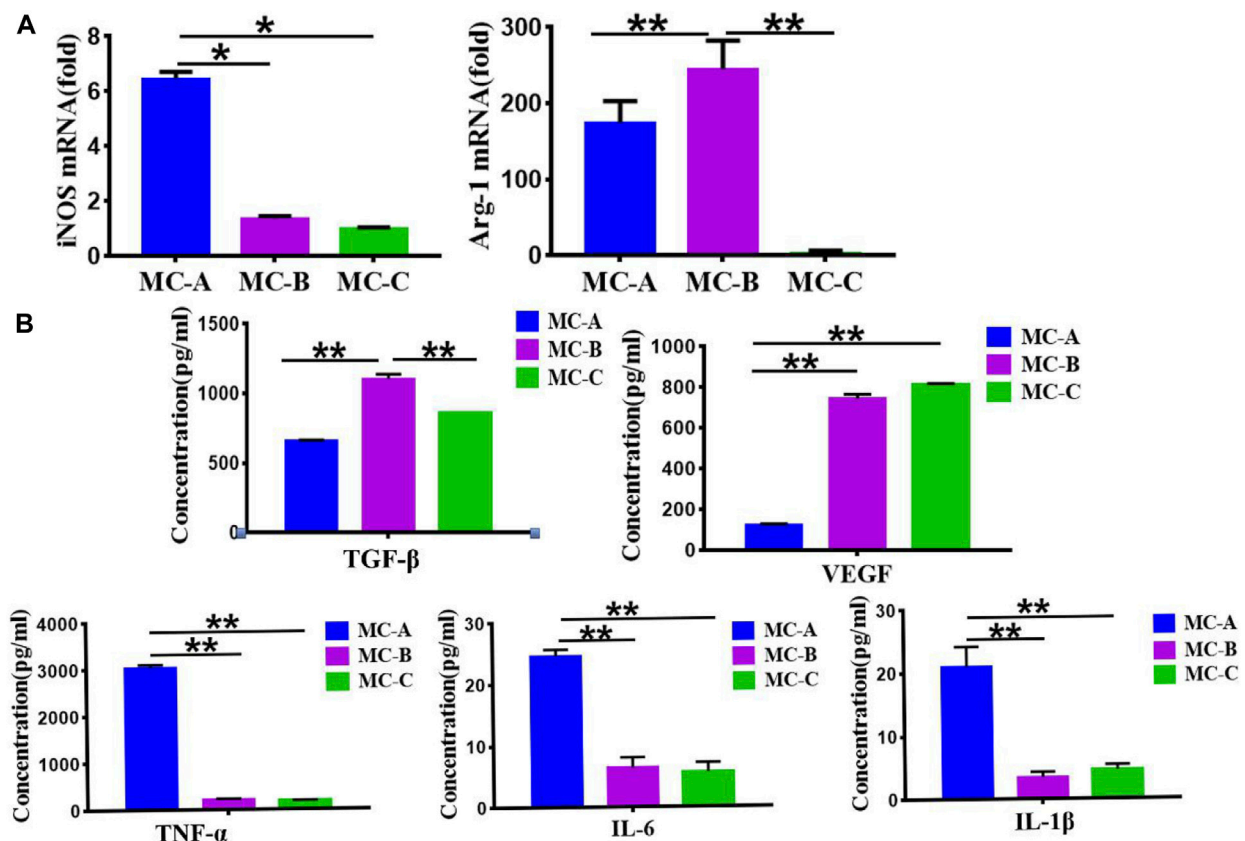


FIGURE 5

Effects of mineralized collagen with different microporous structures on macrophages polarization. (A) Expression of iNOS and Arg-1 marker showing the M1 and M2 polarization of macrophages cultured (M1: iNOS; M2: Arg-1); (B) Secretion of TGF-β, VEGF, and proinflammatory cytokines (TNF-α, IL-6, IL-1β). Data are presented as mean ± SD. \**p* < 0.05; \*\**p* < 0.01.

## Effects of mineralized collagen with different microporous structure on macrophage morphology

To explore the possible role of macrophages in mineralized collagen (MC)-mediated bone formation, RAW264.7 cells were seeded on MC with different pore sizes to analyze the changes of macrophages. The proliferation of RAW264.7 cells inoculated on MC for 1, 2, and 3 days was shown in Figure 4A. We found that the OD values of each group increased gradually with the increase of culture time. Still the cell proliferation ability of the MC-B group was significantly higher than that of the MC-C group at 3 days. The morphology of macrophages in three groups was shown in Figure 4B after 3 days of culture on each surface. Focal adhesion are the sites where cytoskeleton and signal protein structure adhere to extracellular matrix. These signal proteins include vinculin, integrin family members and tyrosine kinase family members. Among them, due to the rich content of vinculin,

the change of adhesion point can be accurately reflected by measuring the expression of vinculin (Han, et al., 2021). From Figures 4C,D, we can see the cytoskeleton morphology and the focal adhesions morphology of macrophages cultured in three groups at 3 days. Based on the above results, there was found that the macrophages in the three groups displayed different shapes. The three groups of RAW264.7 cells all stretched out pseudopods to connect with the biomaterials. On the surface of MC-A, the adherent cells had a sizeable spreading area and different adherent cell morphology, some of which were spindle-shaped or round. On the surface of MC-B, the spreading area of adherent cells was small, and the cells were shuttle-shaped, which was a typical morphology of M2 cells (Liu et al., 2022), on the MC-C surface, the morphology of adhesion cells was irregular and without migrating into the collagen network. RAW264.7 survived on the surface of all three groups of materials, but the medium pore size MC-B promoted cell polarization to M2 macrophage.

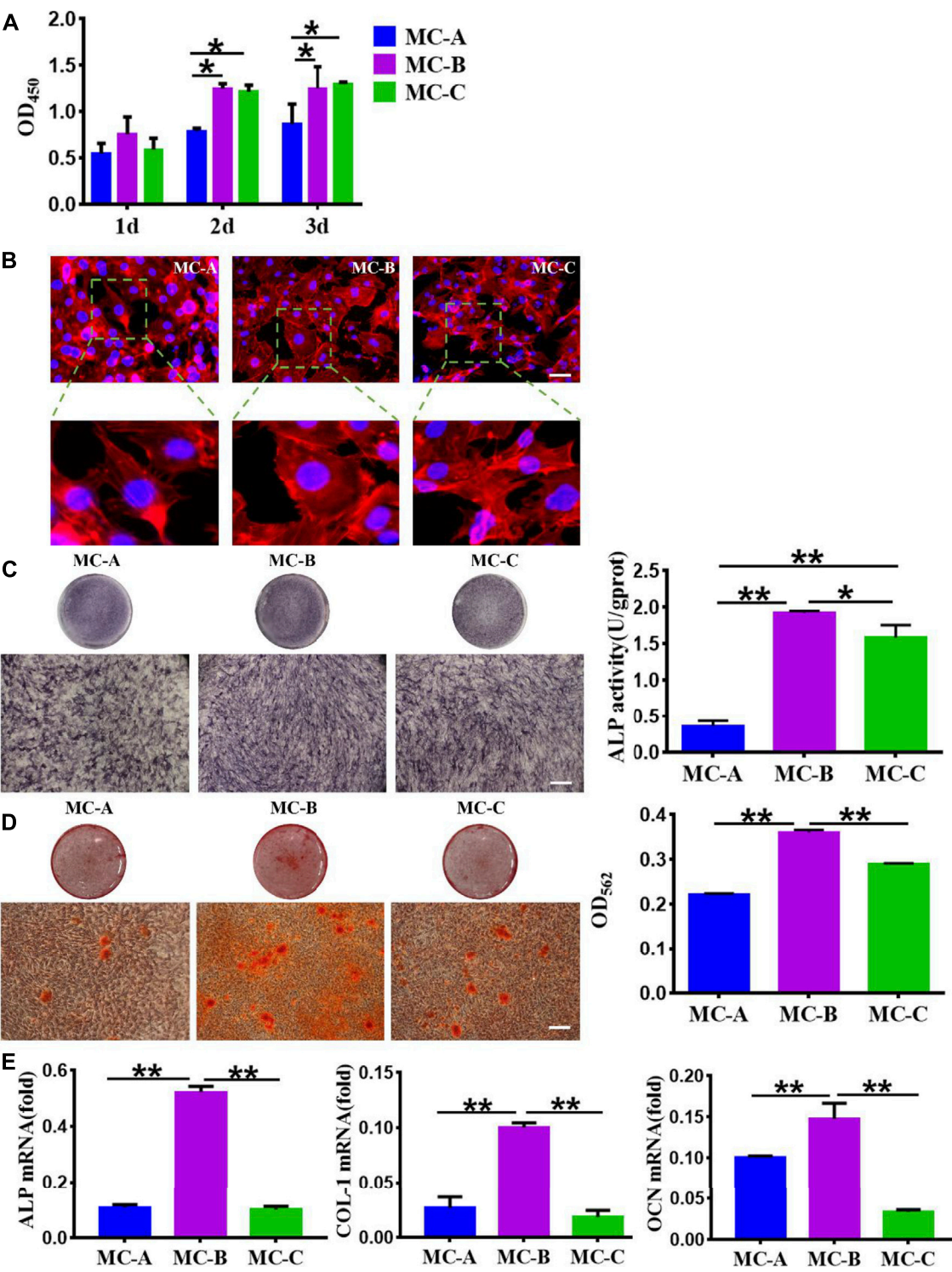


**FIGURE 6** Effect of macrophage conditioned medium produced by mineralized collagen with different pore sizes on MC3T3-E1. (A) CCK-8 cell proliferation experimentation of MC3T3-E1 cells after cultured 1d, 3d, and 7 days *in vitro*; (B) The cytoskeleton morphology of MC3T3-E1 cells cultured on different groups (scale bar: 50  $\mu$ m); (C) ALP staining and quantification in MC3T3-E1 cells (scale bars:100  $\mu$ m); (D) Alizarin red S staining and quantification in MC3T3-E1 cells (scale bars:100  $\mu$ m); (E) The expression of osteogenic gene was detected by qRT-PCR. Data are presented as mean  $\pm$  SD. \* $p$  < 0.05;\*\* $p$  < 0.01.

## Effects of mineralized collagen with different microporous structure on macrophage polarization

Figure 5A showed that the MC-B group increased the expression of Arg-1 (a characteristic marker of M2 macrophage) while the expression of iNOS (a characteristic marker of M1 macrophage) (Li et al., 2019) was significantly increased in the MC-A group. Figure 5B showed that the expression of anti-inflammatory cytokine TGF- $\beta$  and growth factor VEGF were significantly higher in the MC-B group. In comparison the expression of pro-inflammatory cytokines (TNF- $\alpha$ , IL-1 $\beta$ , IL-6) was considerably lower in MC-B and MC-C than in MC-A. According to the above results, we inferred that MC-B promoted MC3T3-E1 osteogenic differentiation by promoting macrophage M2 polarization.

### Osteogenic Differentiation of MC3T3-E1 Cells on Mineralized Collagen with Different Microporous Structures under Osteoimmune Environments

Based on the osteo-immune responses of macrophages, we investigated the effect of macrophages on osteogenic differentiation of MC3T3-E1 cells. Three conditioned media for co-culture of mineralized collagen and macrophages were taken to incubate MC3T3-E1 cells, the results showed in Figure 6. From Figure 6A, we can see that the proliferation of MC3T3-E1 cells incubated in the MC-B, MC-C conditioned medium with small pore size was significantly higher than that of MC-A with a large pore size at 2 and 3 days. Phalloidin staining showed that MC3T3-E1 cells in the MC-B group were densely distributed with large spreading area and clear microfilaments compared with the MC-A and MC-C groups (Figure 6B). We assessed the osteogenic ability of the three groups of MC3T3-E1 cells by ALP staining, alizarin red staining, and osteogenic-related gene expression. The results showed that the MC-B group had more ALP positive cells (Figure 6C), more calcium salt deposition (Figure 6D), and higher expression levels of osteogenic-related genes (Figure 6E). Therefore, we inferred that MC-B could induce macrophage polarization toward the M2 type, which had better performance than MC-A and MC-C in stimulating the inflammatory response of the organism and was more conducive to bone reconstruction. In response to MC-B, M2 macrophage generated osteoimmunology microenvironment, which resulted in outcomes that guide bone regeneration in some situations.

## Discussion

The osteoimmune environment plays an essential role in bone repair, most of the repair process promotes the differentiation of osteoblastic cells on the implanted-biomaterial surfaces generated the microenvironment, but the topics about microporous structures-mediated osteogenesis are

generally neglected (Liu, et al., 2010; Sussman, et al., 2014; Niu, et al., 2020; Sun, et al., 2022). The presence of microporous structures on the biomaterial surface is crucial for bone formation (Kang, et al., 2021). In our study, we investigated the macrophage responses of microporous structures on mineralized collagen (MC) with different porosity and sized pores and the subsequent effects on the osteogenic differentiation of MC3T3-E1 cells. We first analyzed the effect of MC with different microporous structures on MC3T3-E1 cells osteogenic differentiation. It was shown that MC with medium pore size (MC-B) enhanced the extension area and extension capacity as well as osteogenic differentiation of MC3T3-E1 cells. The polarization of macrophage is very sensitive to the physical and chemical properties of biomaterials. These M1 macrophage and M2 macrophage can mediate the host immune response to implanted scaffolds and exert the potential to different degrees in bone regeneration and repair (Chen et al., 2017b; Duan, et al., 2019). We analyzed the effect of microporous structures on macrophage behavior. When RAW 264.7 macrophages were cultured on MC, macrophages maintained surface marker expression and polarized to M1 and M2 phenotypes. Our results indicated that on the surface of MC-B, macrophages polarized into spindle-shaped M2 phenotype. The enhanced M2 polarization on MC-B was further confirmed by qRT-PCR. The expression of M2 type surface marker Arg-1 was the most obvious in RAW264.7 co-cultured with MC-B. In MC with a large pore size (MC-A), the expression of both was reversed. The results of ELISA showed that typical pro-inflammation factors, e.g., IL-6, TNF- $\alpha$ , and IL-1 $\beta$ , were up-regulated on MC-A while growth factors and anti-inflammatory factors, e.g., VEGF and TGF- $\beta$ , were up-regulated on MC-B. ALP staining, alizarin red staining, and qRT-PCR revealed that MC-B significantly enhanced M2 macrophage polarization and subsequently M2 macrophage mediated osteogenic differentiation of MC3T3-E1 cells.

In this study, it was found that the microporous structures and the pore size of biomaterial implantations may be important adhesive cues, affect the spreading and cell shape of macrophages, and modulate the inflammatory response. Because immune cells are frontline cells attinent with inserted biomaterials, their reaction and the immune microenvironment they generate are essential to determine biomaterial-mediated osteogenesis. These impacts demonstrate that biomaterial mediated immunoreaction performed a critical role in micropore structure-mediated osteogenesis (Liao, et al., 2021).

It is essential for the crosstalk between immune cells and the bone forming cells to complete the inflammation stage and initiate the new bone formation (Liu et al., 2022; Yu et al., 2022). Our results indicated the osteoimmunomodulatory property of the microporous structures MC with different sized pores and its critical effects on bone regeneration. This study suggested that osteogenic differentiation of bone

TABLE 1 Primer sequences used in the study.

Gene	Full name	Primer	Sequences (5'-3')
iNOS	Inducible nitric oxide synthase	Forward	CACCAAGCTGAACCTGAGCG
		Reverse	CGTGGCTTTGGGCTCCTC
Arg-1	Arginine-1	Forward	CTCCAAGCCAAAGTCCTTAGAG
		Reverse	AGGAGCTGTCATTAGGGACATC
OCN	Osteocalcin	Forward	CCGGGAGCAGTGTGAGCTTA
		Reverse	AGGCGGTCTTCAAGCCATACT
ALP	Alkaline phosphatase	Forward	AGGGTGGGTAGTCATTTCATAG
		Reverse	GAGGCATACGCCATCACATG
OPN	Osteopontin	Forward	ATCTACCATTCGGATGAGTCT
		Reverse	TGTAGGGACGATTGGAGTGAAA
COL-1	Collagen-1	Forward	GCTGGAGTTTCCGTGCCT
		Reverse	GACCTCGGGGACCCATTG
GAPDH	Glyceraldehyde-3-phosphate dehydrogenase	Forward	TGACCACAGTCCATGCCATC
		Reverse	GACGGACACATTGGGGGTAG

cells was not only determined by the nature of biomaterial implantations, but also influenced by the inflammatory environment generated by the interaction of immune cells and biomaterial implantations significantly. Therefore, creating an osteoimmunology environment that stimulate osteogenesis by biomaterials with optimal design and development and rational application is vital in bone tissue and regeneration.

The early immune environment decides the follow-up action of bone cells (Fernandes et al., 2017; Chen et al., 2018; Sadowska et al., 2018). Nonetheless, better comprehending of this relation requires further *in vitro* investigation of signalling pathways responsible for enhanced osteogenic differentiation of bone forming cells (Fan et al., 2021). Therefore, further *in vivo* experiments designed to research the interaction between immune and bone cells should be conducted to sufficient support driven presupposition.

## Conclusion

Microporous structures have apparent regulatory effects on macrophages responses. The osteo-immune environment promoted by the mineralized collagen (MC) with about 85  $\mu\text{m}$  microporous structure and 70% porosity was conducive to the osteogenic differentiation of MC3T3-E1 cells, suggesting a favorable osteo-immunomodulatory effect, which could be favorable for increasing the osteogenesis capability of biomaterials for bone regeneration. Microporous structures on MC elicited notable influence on regulating the immunological reaction. The induced osteoimmunology environment significantly regulated osteoblast differentiation, which may suggest a new orientation for

systemic research. We need further study to acquire more particulars on the biomaterials dependent response of macrophages on the level of the molecular and the function of immunoregulatory function of biomaterials in bone tissue and engineering. The science gained from this research can supply clues for the intending development of improved immune therapy for bone biomaterials applications and highlight emerging concepts that may expand therapeutic perspectives in bone repair and regeneration.

## Data availability statement

The original contributions presented in the study are included in the article/Supplementary Material, further inquiries can be directed to the corresponding authors.

## Author contributions

XL, Z-YL, H-FQ, C-YH, KL, and C-XM, assisted JL completed all preliminary work of this article. JL wrote the manuscript. F-ZL reviewed the manuscript. Y-JZ, F-ZL, and BZ contributed to the conception of the program.

## Funding

This work was in part supported by Science Foundation of Shandong Province of China (Grant no: ZR2021MH026) and the National Key R&D Program of China (Grant no: 2020YFC1107601) and Medicine and Health Science Technology Development plan of Shandong Province of



China (Grant no: 202108020440) and Liaocheng People's Hospital Youth Fund Project (Grant no: LYQN201914).

## Conflict of interest

The authors declare that the research was conducted in the absence of any commercial or financial relationships that could be construed as a potential conflict of interest.

## References

- Akram, P. M., Seyed, H. G., Mohsen, N., Hosein, K. F., Mohammad, V., Saeed, M., et al. (2018). OPN b and c isoforms doubtless veto anti-angiogenesis effects of curcumin in combination with conventional AML regiment. *Asian Pac. J. Cancer Prev.* 18 (9), 2591–2599. doi:10.22034/APJCP.2017.18.9.2591
- Annibali, O., Petrucci, M. T., Santini, D., Bongarzoni, V., Russano, M., Pisani, F., et al. (2021). Alkaline phosphatase (alp) levels in multiple myeloma and solid cancers with bone lesions: Is there any difference? *J. Bone Oncol.* 26, 100338. doi:10.1016/j.jbo.2020.100338
- Badylak, S. F. (2016). A scaffold immune microenvironment. *Science* 352, 298. doi:10.1126/science.aaf7587
- Bai, J. X., Wang, H. Y., Chen, H., Ge, G. R., Wang, M., Gao, A., et al. (2020). Biomimetic osteogenic peptide with mussel adhesion and osteoimmunomodulatory functions to ameliorate interfacial osseointegration under chronic inflammation. *Biomaterials* 255, 120197. doi:10.1016/j.biomaterials.2020.120197
- Brown, B. N., and Badylak, S. F. (2013). Expanded applications, shifting paradigms and an improved understanding of host-biomaterial interactions. *Acta Biomater.* 9, 4948–4955. doi:10.1016/j.actbio.2012.10.025
- Chen, Z., Bachhuka, A., Han, S., Wei, F., Lu, S., Visalakshan, R. M., et al. (2017a). Tuning chemistry and topography of nanoengineered surfaces to manipulate immune response for bone regeneration applications. *ACS Nano* 11, 4494–4506. doi:10.1021/acsnano.6b07808
- Chen, Z., Chen, L., Liu, R., Lin, Y., Chen, S., Lu, S., et al. (2018). The osteoimmunomodulatory property of a barrier collagen membrane and its manipulation via coating nanometer-sized bioactive glass to improve guided bone regeneration. *Biomater. Sci.* 6, 1007–1019. doi:10.1039/c7bm00869d
- Chen, Z., Han, S., Shi, M., Liu, G., Chen, Z., Chang, J., et al. (2018c). Immunomodulatory effects of mesoporous silica nanoparticles on osteogenesis: From nanoimmunotoxicity to nanoimmunotherapy. *Appl. Mater. Today* 10, 184–193. doi:10.1016/j.apmt.2017.12.003
- Chen, Z., Klein, T., Murray, R. Z., Crawford, R., Chang, X., Wu, C., et al. (2016). Osteoimmunomodulation for the development of advanced bone biomaterials. *Mater. Today* 19, 304–321. doi:10.1016/j.mattod.2015.11.004
- Chen, Z., Ni, S., Han, S., Crawford, R., Lu, S., Wei, F., et al. (2017b). Nanoporous microstructures mediate osteogenesis by modulating the osteo-immune response of macrophages. *Nanoscale* 9, 706–718. doi:10.1039/c6nr06421c
- Chen, Z., Yuen, J., Crawford, R., Chang, J., Wu, C., and Xiao, Y. (2015). The effect of osteoimmunomodulation on the osteogenic effects of cobalt incorporated  $\beta$ -tricalcium phosphate. *Biomaterials* 61, 126–138. doi:10.1016/j.biomaterials.2015.04.044
- Christo, S. N., Bachhuka, A., Diener, K. R., Mierczynska, A., Hayball, J. D., and Vasilev, K. (2016). The role of surface nanotopography and chemistry on primary neutrophil and macrophage cellular responses. *Adv. Healthc. Mat.* 5, 956–965. doi:10.1002/adhm.201500845
- Duan, R., van Dijk, L. A., van Dijk, D., Barbieri, F., de Groot, H., Yuan, J. D., et al. (2019). Accelerated bone formation by biphasic calcium phosphate with a novel sub-micron surface topography. *eCM* 37, 60–73. doi:10.22203/eCM.v037a05
- Eming, S. A., Wynn, T. A., and Martin, P. (2017). Inflammation and metabolism in tissue repair and regeneration. *Science* 356, 1026–1030. doi:10.1126/science.aam7928
- Fan, Q., Bai, Jinyu, Shan, Huajian, Fei, Ziyang, Chen, Hao, Xu, Jialu, et al. (2021). Implantable blood clot loaded with BMP-2 for regulation of osteoimmunology and enhancement of bone repair. *Bioact. Mater.* 6, 4014–4026. doi:10.1016/j.bioactmat.2021.04.008
- Fernandes, K. R., Zhang, Y., Magri, A., Renno, A., and van den Beucken, J. (2017). Biomaterial property effects on platelets and macrophages: An *in vitro* study. *ACS Biomater. Sci. Eng.* 3, 3318–3327. doi:10.1021/acsbomaterials.7b00679
- Gaharwar, A. K., Singh, I., and Khademhosseini, A. (2020). Engineered biomaterials for *in situ* tissue regeneration. *Nat. Rev. Mater* 5, 686–705. doi:10.1038/s41578-020-0209-x
- Han, S. J., Azarova, E. V., Whitewood, A. J., Bachir, A., Guttierrez, E., Groisman, A., et al. (2021). Pre-complexation of talin and vinculin without tension is required for efficient nascent adhesion maturation. *Elife* 10, e66151. doi:10.7554/eLife.66151
- Huang, J. Y., Li, R. Q., Yang, J. H., Cai, M., Lee, Y. C., Wang, A. X., et al. (2021). Bioadaptation of implants to *in vitro* and *in vivo* oxidative stress pathological conditions via nanotopography-induced FoxO1 signaling pathways to enhance Osteoimmunological regeneration. *Bioact. Mater.* 6, 3164–3176. doi:10.1016/j.bioactmat.2021.02.023
- Kang, I. S., Kim, R. I., and Kim, C. (2021). Carbon monoxide regulates macrophage differentiation and polarization toward the M2 phenotype through upregulation of heme oxygenase 1. *Cells* 10, 3444. doi:10.3390/cells10123444
- Komori, T. (2020). Functions of osteocalcin in bone, pancreas, testis, and muscle. *Ijms* 21, 7513. doi:10.3390/ijms21207513
- Li, J., Zhang, Y. J., Lv, Z. Y., Liu, K., Meng, C. X., Zou, B., et al. (2020). The observed difference of macrophage phenotype on different surface roughness of mineralized collagen. *Regen. Biomater.* 7, 203–211. doi:10.1093/rb/rbz053
- Li, M. Y., Xu, J. Y., Mei, X. L., Chi, G. F., Li, L. S., Song, Y. L., et al. (2019). Regulatory effects of dermal papillary pluripotent stem cells on polarization of macrophages from M1 to M2 phenotype *in vitro*. *Transpl. Immunol.* 52, 57–67. doi:10.1016/j.trim.2018.11.003
- Liao, Z. C., Dong, L., and Wang, C. M. (2021). Modulating, instead of suppressing, foreign body responses for biomaterials design. *Eng. Regen.* 2, 91–95. doi:10.1016/j.engreg.2021.08.002
- Lin, Y. C., Zhang, L., Liu, Q. N., Yao, Q. Q., Van Handel, V. B., Xu, Y., et al. (2019). *In vitro* behavior of tendon stem/progenitor cells on bioactive electrospun nanofiber membranes for tendon-bone tissue engineering applications. *Ijn* Vol. 14, 5831–5848. doi:10.2147/IJN.S21050910.2147/ijn.s210509
- Liu, F. Z., Wang, D. W., Zhang, Y. J., Lv, Z. Y., Sun, X. D., Li, K. Y., et al. (2017). Comparison of rabbit rib defect regeneration with and without graft. *J. Mater. Sci. Mater. Med.* 28 (2), 1–5. doi:10.1007/s10856-016-5807-1
- Liu, K., Luo, X., Lv, Z. Y., Zhang, Y. J., Meng, Z., Li, J., et al. (2022). Macrophage-derived exosomes promote bone mesenchymal stem cells towards osteoblastic fate through microRNA-21a-5p. *Front. Bioeng. Biotechnol.* 9, 801432. doi:10.3389/fbioe.2021.801432
- Liu, X., Wang, X. M., Chen, Z., Cui, F. Z., Liu, H. Y., Mao, K., et al. (2010). Injectable bone cement based on mineralized collagen. *J. Biomed. Mat. Res.* 9999B, NA. doi:10.1002/jbm.b.31625
- Meng, C. X., Liu, K., Lv, Z. Y., Zhang, Y. J., Li, J., Luo, X., et al. (2021). Inflammation and immunity gene expression profiling of macrophages on mineralized collagen. *J. Biomed. Mater. Res.* 109, 1328–1336. doi:10.1002/jbm.a.37124
- Min, J., Choi, K. Y., Dredgen, E. C., Padera, R. F., Braatz, R. D., Spector, M., et al. (2016). Designer dual therapy nanolayered implant coatings eradicate biofilms and accelerate bone tissue repair. *ACS Nano* 10, 4441–4450. doi:10.1021/acsnano.6b00087
- Niu, Y., Wang, Z., Shi, Y., Dong, L., and Wang, C. (2021). Modulating macrophage activities to promote endogenous bone regeneration: Biological mechanisms and engineering approaches. *Bioact. Mater.* 6, 244–261. doi:10.1016/j.bioactmat.2020.08.012
- Purnell, B. A., and Hines, P. J. (2017). Repair and regeneration. *Science* 356, 1020–1021. doi:10.1126/science.356.6342.1020

## Publisher's note

All claims expressed in this article are solely those of the authors and do not necessarily represent those of their affiliated organizations, or those of the publisher, the editors and the reviewers. Any product that may be evaluated in this article, or claim that may be made by its manufacturer, is not guaranteed or endorsed by the publisher.

- Redlich, K., and Smolen, J. S. (2012). Inflammatory bone loss: Pathogenesis and therapeutic intervention. *Nat. Rev. Drug Discov.* 11, 234–250. doi:10.1038/nrd3669
- Sadowska, J. M., Guillem-Marti, J., Espanol, M., Stähli, C., Döbelin, N., and Ginebra, M. P. (2018). *In vitro* response of mesenchymal stem cells to biomimetic hydroxyapatite substrates: A new strategy to assess the effect of ion exchange. *Acta biomater.* 76, 319–332. doi:10.1016/j.actbio.2018.06.025
- Shi, X. D., Chen, L. W., Li, S. W., Sun, X. D., Cui, F. Z., and Ma, H. M. (2018). The observed difference of RAW264.7 macrophage phenotype on mineralized collagen and hydroxyapatite. *Biomed. Mat.* 13, 041001. doi:10.1088/1748-605X/aab523
- Sun, J., Huang, Y. K., Zhao, H., Niu, J. J., Ling, X. W., Zhu, C., et al. (2022). Bio-clickable mussel-inspired peptides improve titanium-based material osseointegration synergistically with immunopolarization-regulation. *Bioact. Mater.* 9, 1–14. doi:10.1016/j.bioactmat.2021.10.003
- Sussman, E. M., Halpin, M. C., Muster, J., Moon, R. T., and Ratner, B. D. (2014). Porous implants modulate healing and induce shifts in local macrophage polarization in the foreign body reaction. *Ann. Biomed. Eng.* 42, 1508–1516. doi:10.1007/s10439-013-0933-0
- Wei, H., Cui, J., Lin, K., Xie, J., and Wang, X. (2022). Recent advances in smart stimuli-responsive biomaterials for bone therapeutics and regeneration. *Bone Res.* 10, 17. doi:10.1038/s41413-021-00180-y
- Xie, Y., Hu, C., Feng, Y., Li, D., Ai, T., Huang, Y., et al. (2020). Osteoimmunomodulatory effects of biomaterial modification strategies on macrophage polarization and bone regeneration. *Regen. Biomater.* 7, 233–245. doi:10.1093/rb/rbaa006
- Xu, S. J., Qiu, Z. Y., Wu, J. J., Kong, X. D., Weng, X. S., Cui, F. Z., et al. (2016). Osteogenic differentiation gene expression profiling of hMSCs on hydroxyapatite and mineralized collagen. *Tissue Eng. Part A* 22, 170–181. doi:10.1089/ten.tea.2015.0237
- Yi, J., Liu, Q., Zhang, Q., Chew, T. G., and Ouyang, H. (2022). Modular protein engineering-based biomaterials for skeletal tissue engineering. *Biomaterials* 282, 121414. doi:10.1016/j.biomaterials.2022.121414
- Yu, W. W., Wan, Q. Q., Wei, Y., Li, Y. T., Li, Q. H., Ye, T., et al. (2022). Engineered extracellular vesicles: Regulating the crosstalk between the skeleton and immune system. *Eng. Regen.* 3, 270–282. doi:10.1016/j.engreg.2022.06.004
- Zhao, D. W., Liu, C., Zuo, K. Q., Su, P., Li, L., Xiao, G.-Y., et al. (2020). Strontium-zinc phosphate chemical conversion coating improves the osseointegration of titanium implants by regulating macrophage polarization. *Chem. Eng. J.* 408, 127362. doi:10.1016/j.cej.2020.127362
- Zhou, P. Y., Xia, D. M., Ni, Z. X., Ou, T. L., Wang, Y., Zhang, H. Y., et al. (2021). Calcium silicate bioactive ceramics induce osteogenesis through oncostatin M. *Bioact. Mater.* 6, 810–822. doi:10.1016/j.bioactmat.2020.09.018



## OPEN ACCESS

## EDITED BY

Junjie Li,  
Innovation Centre of NanoMedicine  
(iCONM), Japan

## REVIEWED BY

Xiaoyuan Li,  
Northeast Normal University, China  
Qinghao Zhou,  
University of Science and Technology of  
China, China

## \*CORRESPONDENCE

Murugan Ramalingam,  
rmurug2000@gmail.com  
ShuYang Xie,  
shuyangxie@aliyun.com  
RanRan Wang,  
wangrr@bzmc.edu.cn

<sup>†</sup>These authors have contributed equally  
to this work

## SPECIALTY SECTION

This article was submitted  
to Biomaterials,  
a section of the journal  
Frontiers in Bioengineering and  
Biotechnology

RECEIVED 28 July 2022

ACCEPTED 19 August 2022

PUBLISHED 13 September 2022

## CITATION

Li X, Gao Y, Liu X, Hu X, Li Y, Sun J,  
Wang P, Wu H, Kim H, Ramalingam M,  
Xie S and Wang R (2022), Ultrasound and  
laser-promoted dual-gas nano-  
generator for combined photothermal  
and immune tumor therapy.  
*Front. Bioeng. Biotechnol.* 10:1005520.  
doi: 10.3389/fbioe.2022.1005520

## COPYRIGHT

© 2022 Li, Gao, Liu, Hu, Li, Sun, Wang,  
Wu, Kim, Ramalingam, Xie and Wang.  
This is an open-access article  
distributed under the terms of the  
[Creative Commons Attribution License](#)  
(CC BY). The use, distribution or  
reproduction in other forums is  
permitted, provided the original  
author(s) and the copyright owner(s) are  
credited and that the original  
publication in this journal is cited, in  
accordance with accepted academic  
practice. No use, distribution or  
reproduction is permitted which does  
not comply with these terms.

# Ultrasound and laser-promoted dual-gas nano-generator for combined photothermal and immune tumor therapy

XinYu Li<sup>1,2†</sup>, Yong Gao<sup>3†</sup>, XinZheng Liu<sup>1,2</sup>, XiaoQian Hu<sup>1</sup>,  
YunMeng Li<sup>1</sup>, JunXi Sun<sup>1</sup>, PingYu Wang<sup>4</sup>, Hongkai Wu<sup>5</sup>,  
HaeWon Kim<sup>6,7,8</sup>, Murugan Ramalingam<sup>6,7,8,9\*</sup>, ShuYang Xie<sup>4\*</sup>  
and RanRan Wang<sup>1,2\*</sup>

<sup>1</sup>Institute of Rehabilitation Medicine, School of Rehabilitation Medicine, Binzhou Medical University, Yantai, China, <sup>2</sup>Shandong Laboratory of Advanced Materials and Green Manufacturing, Yantai, China, <sup>3</sup>Binzhou Medical University Hospital, Binzhou, China, <sup>4</sup>Key Laboratory of Tumor Molecular Biology, Binzhou Medical University, Yantai, China, <sup>5</sup>Department of Chemistry, The Hong Kong University of Science and Technology, Hong Kong, China, <sup>6</sup>Institute of Tissue Regeneration Engineering, Dankook University, Cheonan, Korea, <sup>7</sup>Department of Nanobiomedical Science, BK21 NBM Global Research Center for Regenerative Medicine, Dankook University, Cheonan, Korea, <sup>8</sup>Mechanobiology Dental Medicine Research Center, Dankook University, Cheonan, Korea, <sup>9</sup>School of Basic Medical Sciences, Chengdu University, Chengdu, China

The combination of photothermal therapy (PTT) and immune tumor therapy has emerged as a promising avenue for cancer treatment. However, the insufficient immune response caused by inefficient immunogenic cell death (ICD) inducers and thermal resistance, immunosuppression, and immune escape resulting from the hypoxic microenvironment of solid tumors severely limit its efficacy. Herein, we report an ultrasound and laser-promoted dual-gas nano-generator (calcium carbonate-polydopamine-manganese oxide nanoparticles, CPM NPs) for enhanced photothermal/immune tumor therapy through reprogramming tumor hypoxic microenvironment. In this system, CPM NPs undergo reactive decomposition in a moderately acidic tumor, resulting in the generation of calcium, manganese ions, carbon dioxide (CO<sub>2</sub>), and oxygen (O<sub>2</sub>). Calcium and manganese ions act as adjuvants that trigger an immune response. The cancer cell membrane rupture caused by sudden burst of bubbles (CO<sub>2</sub> and O<sub>2</sub>) under ultrasound stimulation and the photothermal properties of PDA also contributed to the ICD effect. The generation of O<sub>2</sub> alleviates tumor hypoxia and thus reduces hypoxia-induced heat resistance and immunosuppressive effects, thereby improving the therapeutic efficacy of combination PTT and immune therapy. The present study provides a novel approach for the fabrication of a safe and effective tumor treatment platform for future clinical applications.

## KEYWORDS

CaCO<sub>3</sub>-PDA-MnO<sub>2</sub> nanoparticles, dual-gas nano-generator, ultrasound and laser, photothermal, immunotherapy

## Introduction

Cancer is the second most common cause of death, seriously threatening human health (Liu J et al., 2019; Soerjomataram and Bray, 2021). Various treatment modalities such as surgery, radiotherapy, and chemotherapy have been used to eliminate tumors. However, the disadvantages of severe trauma, poor selectivity, and drug resistance greatly limit the application of these methods. Photothermal therapy (PTT) as an effective tumor treatment modality with non-invasive, highly targeted, low systemic toxicity and few side effects has got widespread attentions. PTT kills tumor cells by converting light energy into heat energy, and has received extensive attention (Li et al., 2018). However, in addition to effective tumor growth inhibition, avoiding tumor recurrence is crucial for effective tumor treatment. Immunotherapy, a rapidly developing therapeutic approach that inhibits tumor growth and prevents tumor recurrence and metastasis by activating the immune system, is considered to be one of the most promising therapeutic techniques for tumors. Since immunogenic cell death (ICD) plays a significant role in initiating antitumor immune responses, the development of potent ICD inducers is required to improve the efficacy of immunotherapy (Duan et al., 2019; Liu P et al., 2019; Chattopadhyay et al., 2020; Ding et al., 2020). Various ICD inducers have been reported, including radiation (Chao et al., 2018), photosensitizers (Deng et al., 2020), and chemotherapeutic drugs (Nam et al., 2018). However, X-rays and drug molecules can cause systemic toxicity and drug resistance, thereby increasing the risk of treatment. Therefore, development of mild and non-drug ICD inducers is required for safe and efficient immunotherapy. Currently, in addition to selecting efficient ICD inducers, remodeling the tumor hypoxic microenvironment is another important strategy to improve the immunotherapy efficiency (Hu et al., 2020; Li and Kataoka, 2021). Recently,  $\text{Ca}^{2+}$  has been reported to serve as an ICD inducer in immunotherapy. ICD effects are attributed to mitochondrial  $\text{Ca}^{2+}$  overload and the subsequent upregulation of the reactive oxygen species (ROS) levels (Zheng et al., 2021). Furthermore, exogenous ultrasound (US) stimuli can enhance  $\text{Ca}^{2+}$  overload by promoting  $\text{Ca}^{2+}$  influx from the extracellular fluid to the cytoplasm, resulting in enhanced ICD (Samal et al., 2000; Parvizi et al., 2002; Park et al., 2010). Another report showed that the sudden burst  $\text{CO}_2$  bubbles in the tumor microenvironment can also stimulate efficient immunogenicity by inducing membrane rupture of cancer cells (Jeon et al., 2022). Several studies have demonstrated that PTT can not only directly destroy tumor cells but also indirectly stimulate systemic immunity (Jiao et al., 2021; Yasothamani et al., 2021); therefore, the combined treatment using PTT and an ICD-inducer is anticipated to improve the efficiency of immunotherapy. Nevertheless, the hypoxic characteristics of tumors impair the efficiency of PTT and immunotherapy. For example, the hypoxic characteristics of tumor tissue leading to

thermal resistance, reducing the efficiency of photothermal treatment (Meng et al., 2018; Wen et al., 2020; Dai et al., 2021; Lv et al., 2021). Moreover, hypoxia can lead to immune suppression and escape (Riera-Domingo et al., 2020; Zhou et al., 2020).  $\text{MnO}_2$  nanoparticles with tumor microenvironment-responsive degradation characteristics and catalase properties can react with excess  $\text{H}_2\text{O}_2$  present in tumor tissue, producing  $\text{O}_2$  and  $\text{Mn}^{2+}$  to alleviate tumor hypoxia (Fan et al., 2015; Yang et al., 2017; Duan et al., 2020). In addition, recent studies have shown that  $\text{MnO}_2$  can be used as an immune adjuvant to trigger ICD by dual induction of  $\text{Mn}^{2+}$ -triggered chemodynamic therapy (CDT) and glutathione (GSH)-depleting ferroptosis (Lv et al., 2020). CDT and ferroptosis can stimulate dying cancer cells to produce damage-associated molecular patterns (DAMPs), thereby eliciting ICD (Chen Y et al., 2019; Wen et al., 2019; Zhang et al., 2019).

In this study, we constructed ultrasonication- and laser-promoted dual-gas nanogenerators based on calcium carbonate ( $\text{CaCO}_3$ ), polydopamine (PDA), and manganese oxide ( $\text{MnO}_2$ ) nanoparticles for combined photothermal/immune tumor therapy.  $\text{CaCO}_3$  has the characteristics of accessibility, good biocompatibility, and pH sensitivity and can decompose at the tumor site, generating carbon dioxide ( $\text{CO}_2$ ) and  $\text{Ca}^{2+}$  (Feng et al., 2018; Yu et al., 2018; Sun et al., 2019; Wang et al., 2020). The inherent photothermal properties of PDA make it suitable for PTT (Wang et al., 2018; Chen Q et al., 2019; Li et al., 2020).  $\text{MnO}_2$  can decompose into oxygen and manganese ions in the tumor microenvironment. Therapeutic systems do not involve chemical drugs, preventing drug resistance. When delivered to the tumor site, the CPM NPs undergo reactive decomposition in a moderately acidic tumor microenvironment, resulting in the generation of  $\text{Ca}^{2+}$ ,  $\text{Mn}^{2+}$ ,  $\text{CO}_2$ , and  $\text{O}_2$ . The generated  $\text{Ca}^{2+}$  and  $\text{Mn}^{2+}$  act as immune adjuvants to trigger ICD. The cancer cell membrane rupture caused by sudden burst of  $\text{CO}_2$ ,  $\text{O}_2$ , and the photothermal properties of PDA also contributed to ICD. The generation of  $\text{O}_2$  alleviates tumor hypoxia and thus reduces the hypoxia-induced heat resistance and immunosuppressive effects, thereby improving the therapeutic efficacy of PTT and immune therapy. In this treatment system, the combination of photothermal therapy and immunity can not only greatly inhibit tumor growth but also avoid tumor metastasis and secondary recurrence through immune effects. Finally, the tumor microenvironment-responsive degradation of the nanoparticles ensures their biosafety.

## Experimental details

### Materials

$\text{CaCl}_2$  and  $\text{NH}_4\text{HCO}_3$  were provided by Sinopharm Chemical Reagent Co., Ltd. (China). Dopamine was obtained



from Sigma-Aldrich. Manganese chloride ( $\text{MnCl}_2$ ) was provided by J and K Chemical Co. Singlet oxygen sensor green reagent was purchased from Meilunbio. Sodium hydroxide ( $\text{NaOH}$ ) was provided by Tianjin Yongda Chemical Reagent Co., Ltd. Calcein-AM/propidium iodide (PI) was purchased from SolarBio. RPMI-1640 medium was purchased from Thermo Fisher Scientific, Inc. Fluorescein isothiocyanate (FITC) was provided by Biological Technology Co., Ltd. Lyso-Tracker Red and Fluo-4 AM were purchased from KeyGen Biotech Co., Ltd. 5,5',6,6'-Tetrachloro-1,1',3,3'-tetraethylbenzimidazoly carbocyanine chloride (JC-1) and mitochondrial extraction kit were purchased from Solarbio.

## Characterization

The morphology and size of the CPM NPs were analyzed using a JEM-1400 transmission electron microscope (TEM, JEOL, Japan). The size and surface charge of the  $\text{CaCO}_3$ -PDA (CP) and CPM NPs were analyzed using a Malvern Zetasizer Nano-ZS90 instrument (United Kingdom). X-ray photoelectron spectroscopy (XPS) spectra were obtained using a Thermo Fisher Scientific ESCALAB 250Xi XPS system. The concentration of  $\text{Ca}^{2+}$  in the CPM NPs was determined using inductively coupled plasma mass spectrometry (ICP-MS, Jena, PlasmaQuant® MS). Cell uptake was measured using a confocal laser-scanning microscope (CLSM ZEISS LSM 780, Carl Zeiss, Jena, Germany).

## Cell culture and animal studies

4T1 cells were cultured in RPMI-1640 medium containing 10% fetal bovine serum. Then, the cells were placed in an incubator containing 5%  $\text{CO}_2$  at 37°C. Healthy female BALB/c mice aged 5–7 weeks were provided by GemPharmatech Co., Ltd. (Nanjing, China). All animals were euthanized by dislocation of cervical vertebra after the treatments.

## Synthesis of calcium carbonate-polydopamine-manganese oxide nanoparticles

CP NPs were prepared *via* a one-pot gas diffusion method following previously reported procedures with some modifications (Dong et al., 2018). Briefly,  $\text{CaCl}_2$  (150 mg) mixed with dopamine (10 mg) was fully dissolved in anhydrous ethanol (100 ml). Then, the samples were transferred into a flask with  $\text{NH}_4\text{HCO}_3$  (5 g) and kept at 40°C for 24 h. Subsequently, CP NPs were obtained *via* centrifugation. To obtain CPM NPs, CP NPs (180 mg) were slowly dropped into an ethanol solution (30 ml) containing  $\text{MnCl}_2$  (360 mg). After stirring for 4 h, the Mn-ion-adsorbed CP nanoparticles were

collected by centrifugal purification. Then,  $\text{NaOH}$  (1 M) was mixed with the solution by adjusting the pH to 11 to obtain CPM NPs.

## Oxygen and reactive oxygen species generation *in vitro*.

The oxygen probe was immersed in different solutions (100  $\mu\text{M}$   $\text{H}_2\text{O}_2$ , pH 7.4 + CPM, pH 6.5 + CPM, pH 7.4 + CPM+100  $\mu\text{M}$   $\text{H}_2\text{O}_2$ , pH 6.5 + CPM+100  $\mu\text{M}$   $\text{H}_2\text{O}_2$ , and CPM 1 mg  $\text{ml}^{-1}$ ) to determine the oxygen concentration. ROS levels were assessed using an ROS probe (reagent singlet oxygen sensor green, SOSG). SOSG methanol solution (10  $\mu\text{L}$ , 2.5 M) was mixed into various solutions with CPM NPs (1 mg  $\text{ml}^{-1}$ ). Then, a 1,064 nm laser (1 W  $\text{cm}^{-2}$ , 5 min) and/or US (1.0 MHz, 20% duty cycle, 0.5 W  $\text{cm}^{-2}$ , 2 min) were applied to the mixture. Finally, a fluorescence spectrophotometer (Hitachi F-2700, Japan) was used to assess the SOSG signals of various groups.

## Investigation of $\text{Ca}^{2+}$ Release from calcium carbonate-polydopamine-manganese oxide nanoparticles *in vitro*.

CPM NPs (1 mg) were immersed in PBS (10 ml) at 37°C and different pH (7.4, 6.5, and 5.5). Supernatants were collected from each sample at 0, 4, 8, 12, and 16 h. The amount of released  $\text{Ca}^{2+}$  was measured by Inductively coupled plasma mass spectrometry (ICP-MS). The release fractions of  $\text{Ca}^{2+}$  were calculated as the amount of released  $\text{Ca}^{2+}$  from CPM NPs divided by the total amount of  $\text{Ca}^{2+}$  in CPM NPs.

## Antitumor therapy *in vitro*

The antitumor effect and biocompatibility of the CPM NPs were determined using the MTT assay. 4T1 cells were co-cultured with CPM NPs at various concentrations for 12 h. The antitumor effect of CPM NPs was measured after the treatment with a 1,064 nm laser (1 W  $\text{cm}^{-2}$ , 5 min) and/or US (1.0 MHz, 20% duty cycle, 0.5 W  $\text{cm}^{-2}$ , 2 min). Thereafter, the cell survival rate was measured after adding a medium containing MTT and incubating for 4 h. For live/dead staining, CPM NPs were co-incubated with 4T1 cells for 12 h. Subsequently, the Calcein-AM/PI probe was added to the cell medium after the treatment with the laser and/or ultrasonication and was incubated for 30 min. Finally, images were obtained by CLSM. For apoptosis, CPM NPs (20  $\mu\text{g}$   $\text{ml}^{-1}$ ) were added to the 4T1 cells and cultured for 12 h. Thereafter, various treatments were applied to the cells. After 2 h, the cells were stained with annexin V-FITC/PI for flow cytometry detection.

## Detection of intracellular reactive oxygen species levels

Various conditions were detected using dichloro-dihydro-fluorescein diacetate (DCFH-DA) reagent (PBS, CPM, CPM + US, CPM + L, CPM + US + L, CPM: 20  $\mu\text{g ml}^{-1}$ , 1,064 nm laser: 1  $\text{W cm}^{-2}$ , 5 min and US: 1.0 MHz, 20% duty cycle, 0.5  $\text{W cm}^{-2}$ , 2 min) to generate intracellular ROS. The 4T1 cells plated on confocal dishes were co-incubated with CPM NPs for 12 h in the dark. Thereafter, the cells were treated by various treatments. Finally, CLSM was used to examine the fluorescence images.

## Lysosome escape

CPM NPs (labeled with FITC; 20  $\mu\text{g ml}^{-1}$ ) were added to 4T1 cells and incubated for 0.5, 1, and 4 h. Then, the cells were labeled with Lyso-Tracker Red (1  $\mu\text{M}$ ). After 4 h, a 1,064 nm laser (1  $\text{W cm}^{-2}$ , 5 min) and/or US (1.0 MHz, 20% duty cycle, 0.5  $\text{W cm}^{-2}$ , 2 min) were applied to the cells, and 4% paraformaldehyde solution was added to fix the cells. After 10 min of fixation, DAPI was added to stain the cells. Fluorescence images were obtained by CLSM after 10 min.

## JC-1 Staining to Measure Mitochondrial Membrane Potential

CPM NPs (20  $\mu\text{g ml}^{-1}$ ) were incubated with the 4T1 cells for 12 h. After various treatments, JC-1 (10  $\mu\text{g ml}^{-1}$ ) was incubated with cells within 10 min. Subsequently, the mitochondrial membrane potentials were visualized using CLSM images.

## Mitochondrial swelling study

The 4T1 cells were incubated with CPM NPs (20  $\mu\text{g ml}^{-1}$ ) for 12 h. After various treatments, the mitochondria of the 4T1 cells in various groups were extracted using a mitochondrial extraction kit, and mitochondrial swelling was analyzed by UV-Vis-NIR spectrophotometry to determine the optical intensity of the mitochondria at 540 nm.

## Intracellular $\text{Ca}^{2+}$ detection in 4T1 cells

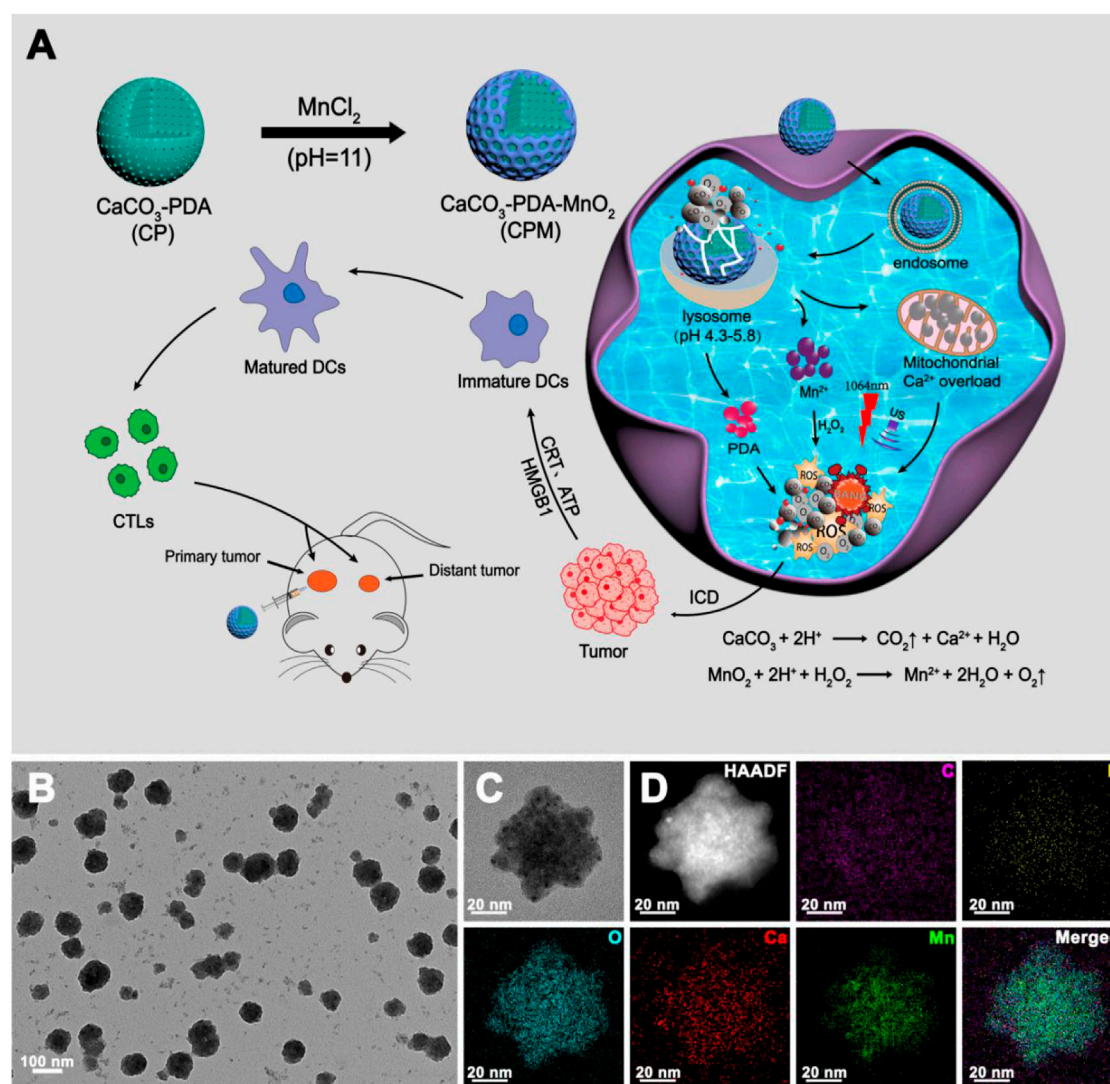
CPM NPs (20  $\mu\text{g ml}^{-1}$ ) were cultured with 4T1 cells for 0, 1, and 4 h. Subsequently, Fluo-4 AM (1  $\mu\text{M}$ ) was used to label cells after incubation for 4 h. Then, a 1,064 nm laser (1  $\text{W cm}^{-2}$ , 5 min) and/or US (1.0 MHz, 20% duty cycle, 0.5  $\text{W cm}^{-2}$ , 2 min) were applied to the cells. Finally, fluorescence images were visualized by CLSM after co-incubation with Hoechst 33,342 for 10 min.

## Immunogenic cell death and dendritic cell maturation *in vitro*

To evaluate calreticulin (CRT) expression after various treatments, 4T1 cells were incubated with CPM NPs (20  $\mu\text{g ml}^{-1}$ ) for 12 h. After a treatment with a 1,064 nm laser (1  $\text{W cm}^{-2}$ , 5 min) and/or US (1.0 MHz, 20% duty cycle, 0.5  $\text{W cm}^{-2}$ , 2 min), the 4T1 cells were incubated with CRT antibodies (1:100; Abcam, EPR3924) for 30 min. After washing three times with PBS, Cy5-labeled goat anti-mouse IgG (H + L) (1:400, Abbkine, A23320) was added to the cells and incubated at 37°C for 2 h. Finally, CLSM was used to visualize the cells after staining with DAPI for 15 min. The release of ATP and HMGB1 was examined using the Chemiluminescence ATP Determination Kit (Solarbio, BC0300) and the HMGB1 enzyme-linked immunosorbent assay (ELISA) Kit (CUSABIO, CSB-E08225M). Briefly, 4T1 cells were incubated with 20  $\mu\text{g ml}^{-1}$  CPM NPs for 12 h. Then, after a treatment with a 1,064 nm laser (1  $\text{W cm}^{-2}$ , 5 min) and/or US (1.0 MHz, 20% duty cycle, 0.5  $\text{W cm}^{-2}$ , 2 min), the release level of HMGB1 in the cell culture medium was detected using an HMGB1 ELISA Kit. Similarly, the release of ATP was measured using an ATP ELISA kit. To determine DCs maturation, 4T1 cells were cultured with CPM NPs (20  $\mu\text{g ml}^{-1}$ ) for 12 h. After a 1,064 nm laser (1  $\text{W cm}^{-2}$ , 5 min) and/or US (1.0 MHz, 20% duty cycle, 0.5  $\text{W cm}^{-2}$ , 2 min) treatment, the supernatant in the 6-well plate of the 4T1 cells was added to the 6-wall plates seeded with DC cells (derived from the bone marrow of BALB/c mice after stimulation with GM-CSF) and then cultivated for 24 h. The control group was cultured in a fresh medium. DCs were detected using flow cytometry after staining with anti-CD11c-PE (BioLegend, 117,308), anti-CD80-PE/Cy5.5 (Biolegend, 104,722), and anti-CD86-APC (BioLegend, 105,012).

## *In vivo* antitumor efficiency

When the primary tumor volume grew to approximately 80  $\text{mm}^3$ , BALB/c mice were randomly divided into five groups: PBS (100  $\mu\text{l}$ ), CPM (CPM: 100  $\mu\text{l}$ , 1  $\text{mg ml}^{-1}$ ), CPM + US (1.0 MHz, 20% duty cycle, 2  $\text{W cm}^{-2}$ , 2 min), CPM + L (1  $\text{W cm}^{-2}$ , 5 min), CPM + US + L, and were subcutaneously injected with four injections of CPM NPs or PBS on days 0, 2, 4, and 6. The temperature of the tumor area was recorded using an infrared thermal imager (FLIR E8). Tumor weight and volume were monitored on alternating days for 15 days. After treatment, the mice were euthanized by dislocation of cervical vertebra and all major organs and tissues were removed and stained with hematoxylin and eosin. To further investigate immune responses during photothermal and immune tumor therapy, tumor-draining lymph nodes, spleens, and tumors were collected after 15 days of treatment. To assess the maturity of DCs *in vivo*, single-cell suspensions obtained after lymph node grinding were stained with anti-CD11c-PE (BioLegend, 117,308), anti-CD80-PE/Cy5.5 (Biolegend, 104,722), and anti-CD86-APC (BioLegend, 105,012), and then were analyzed by flow



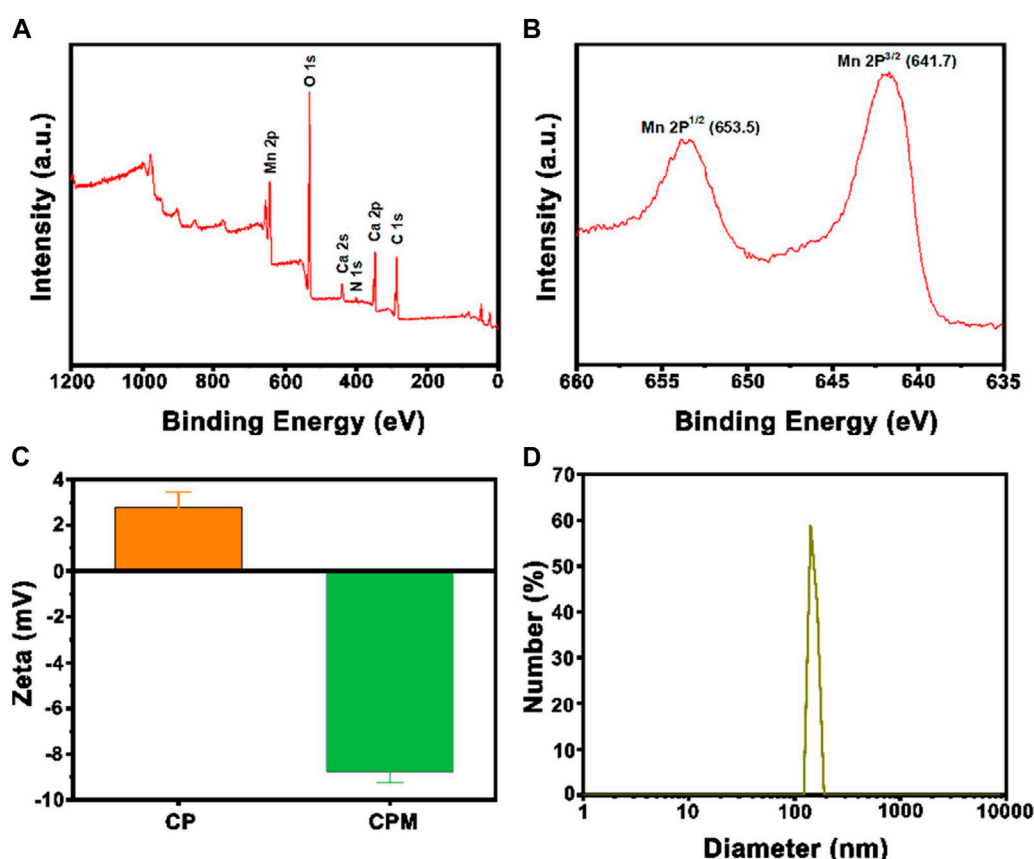


FIGURE 1

(A) XPS spectra of CPM NPs. (B) XPS high-resolution scans of Mn2p peaks in CPM NPs. (C) The average zeta potentials of CP NPs and CPM NPs. (D) Size distribution of CPM NPs.

diffusion method according to a previous report with minor modifications (Dong et al., 2018). Then,  $\text{MnO}_2$  was introduced to the surface of the CP NPs by the reaction of  $\text{MnCl}_2$  and NaOH to form CPM NPs. TEM was used to investigate the morphology and size of the CPM NPs. As shown in Schemes 1B,C, the CPM NPs with irregular spherical shapes exhibited a size of  $\sim 150$  nm. This size is suitable for cellular uptake. The corresponding elemental mapping demonstrated the homogeneous elemental distributions of C, O, N, Ca, and Mn in the CPM NPs (Scheme 1D). XPS analysis also confirmed the presence of C, N, O, Ca, and Mn in the CPM-NPs (Figure 1A). Moreover, the characteristic peaks at 653.5 and 641.7 eV in the high-resolution Mn 2p spectrum correspond to the Mn (IV)  $2p_{1/2}$  and Mn (IV)  $2p_{3/2}$  spin-orbit peaks of  $\text{MnO}_2$ , respectively (Figure 1B), illustrating the successful synthesis of CPM NPs (Chen et al., 2015; Zhao et al., 2015; Liu J et al., 2021). We also measured the zeta potentials of the CP and CPM NPs. As shown in Figure 1C, CPM NPs exhibited a lower average zeta potential ( $-8.76$  mV) than CP NPs ( $2.79$  mV). Negatively charged CPM NPs prolong blood circulation *in vivo*. To evaluate the dispersity of CPM NPs

in water, dynamic light scattering (DLS) was used to detect the hydrodynamic diameter of the CPM NPs. As illustrated in Figure 1D, the CPM NPs showed an average hydrodynamic diameter of  $\sim 150$  nm, demonstrating the superior dispersibility of CPM NPs in water. We further investigated the colloidal stability of CPM NPs by immersing CPM NPs in various solutions. After 7 days of immersion in water, phosphate-buffered saline (PBS, pH 7.4), FBS, and Medium, the digital photograph of CPM NPs did not display any obvious precipitation (Supplementary Figure S1). Homoplasticly, the hydrodynamic diameter of CPM NPs showed non-significant change after immersion in water for a week (Supplementary Figure S2). These results clearly revealed the excellent stability of CPM NPs. Notably, CPM NPs were stable in the presence of excess FBS protein, suggesting that CPM NPs can be stable in the blood stream (Hwang et al., 2008).

As the bubble generation ability of CPM NPs is crucial for this therapeutic system, we evaluated its bubble generation ability carefully under various conditions in the following study. Theoretically, in a simulated tumor environment with slightly



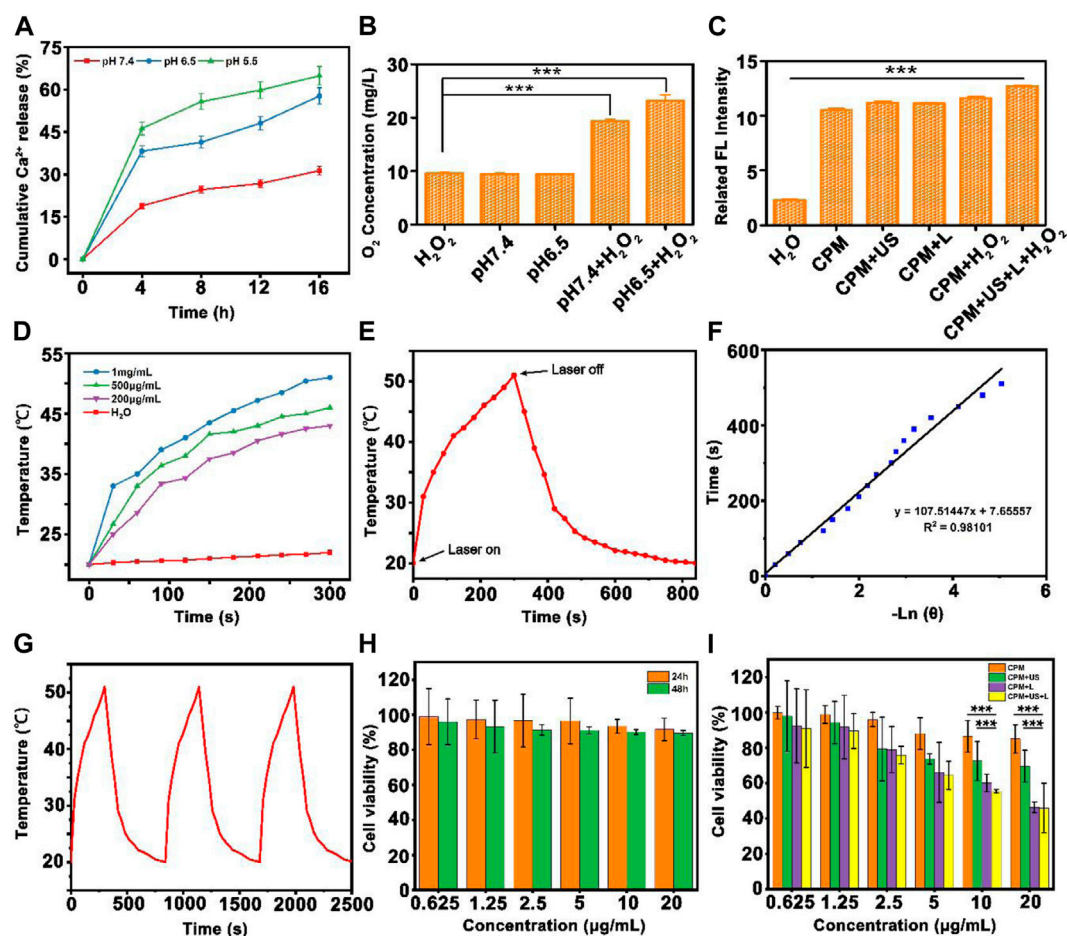


FIGURE 2

The physicochemical characterization of CPM NPs. (A) Time-dependent release profiles of  $\text{Ca}^{2+}$  from CPM NPs in PBS at different pH values 5.5, 6.5, and 7.4. The release percentages were calculated as the amount of release of  $\text{Ca}^{2+}$  from CPM NPs/the total amount of  $\text{Ca}^{2+}$  in CPM NPs. (B) The oxygen concentrations produced by CPM NPs at different pH values in  $\text{H}_2\text{O}_2$  solution (100  $\mu\text{M}$ ). (C) SOSG fluorescence intensities of materials under different conditions. (D) Heating curves of different concentrations of CPM NPs under 1,064 nm laser irradiation. (E) Temperature record of CPM NPs (1 mg  $\text{ml}^{-1}$ ) under laser irradiation. (F) Linear-time data versus  $-\ln(\theta)$  obtained from the cooling period of NIR laser off. (G) The photothermal conversion cycling test of CPM NPs (1 mg  $\text{ml}^{-1}$ ) during three laser on/off cycles. (H) Viability of 293T after being treated with different concentrations of CPM NPs for 24 and 48 h. (I) Cell survival rate of 4T1 cells after being treated by different treatment groups.

acidic and high levels of hydrogen peroxide,  $\text{CaCO}_3$  nanoparticles can be decomposed to produce  $\text{CO}_2$  and  $\text{Ca}^{2+}$  by the following reaction:  $\text{CaCO}_3 + 2\text{H}^+ \rightarrow \text{CO}_2 + \text{Ca}^{2+} + \text{H}_2\text{O}$ . At the same time,  $\text{MnO}_2$  nanoparticles can be disintegrated to generate  $\text{O}_2$  and  $\text{Mn}^{2+}$  ions by the following reaction:  $\text{MnO}_2 + 2\text{H}^+ + \text{H}_2\text{O}_2 \rightarrow \text{Mn}^{2+} + 2\text{H}_2\text{O} + \text{O}_2$  (Sun et al., 2021). As shown in Supplementary Figure S3, both CP NPs and CPM NPs showed a certain bubble generating ability in pH 6.5 solutions with the existence of  $\text{H}_2\text{O}_2$ . The stimulation of laser or ultrasound promote the generation of bubbles both in CP NPs and CPM NPs. Obviously, the CPM + US + L +  $\text{H}_2\text{O}_2$  group produced the largest number of bubbles compared to the other groups. Hence, it is reasonable to speculate that the dual gas production of  $\text{O}_2$  and  $\text{CO}_2$  in CPM NPs solutions greatly contributes to the large

amounts of bubbles compared to CP NPs solution that only produces  $\text{CO}_2$ .

Since pH-responsive  $\text{Ca}^{2+}$  release from CPM NPs is crucial for the calcium-overload-induced cancer immune therapy, we evaluated the  $\text{Ca}^{2+}$  release ability at various pH (5.5, 6.5, and 7.4). As shown in Figure 2A, time-related release behavior of  $\text{Ca}^{2+}$  from CPM NPs was observed. CPM NPs in the pH 5.5 solutions showed the highest calcium release rate (65%) compared to the pH 7.4 (31%) and pH 6.5 (58%) solutions. These results demonstrate the pH-dependent release behavior of CPM NPs. Therefore, CPM NPs are promising for  $\text{Ca}^{2+}$ -induced immunotherapy.

As previously reported,  $\text{MnO}_2$  nanoparticles can trigger the decomposition of  $\text{H}_2\text{O}_2$  to produce oxygen and  $\text{Mn}^{2+}$  by

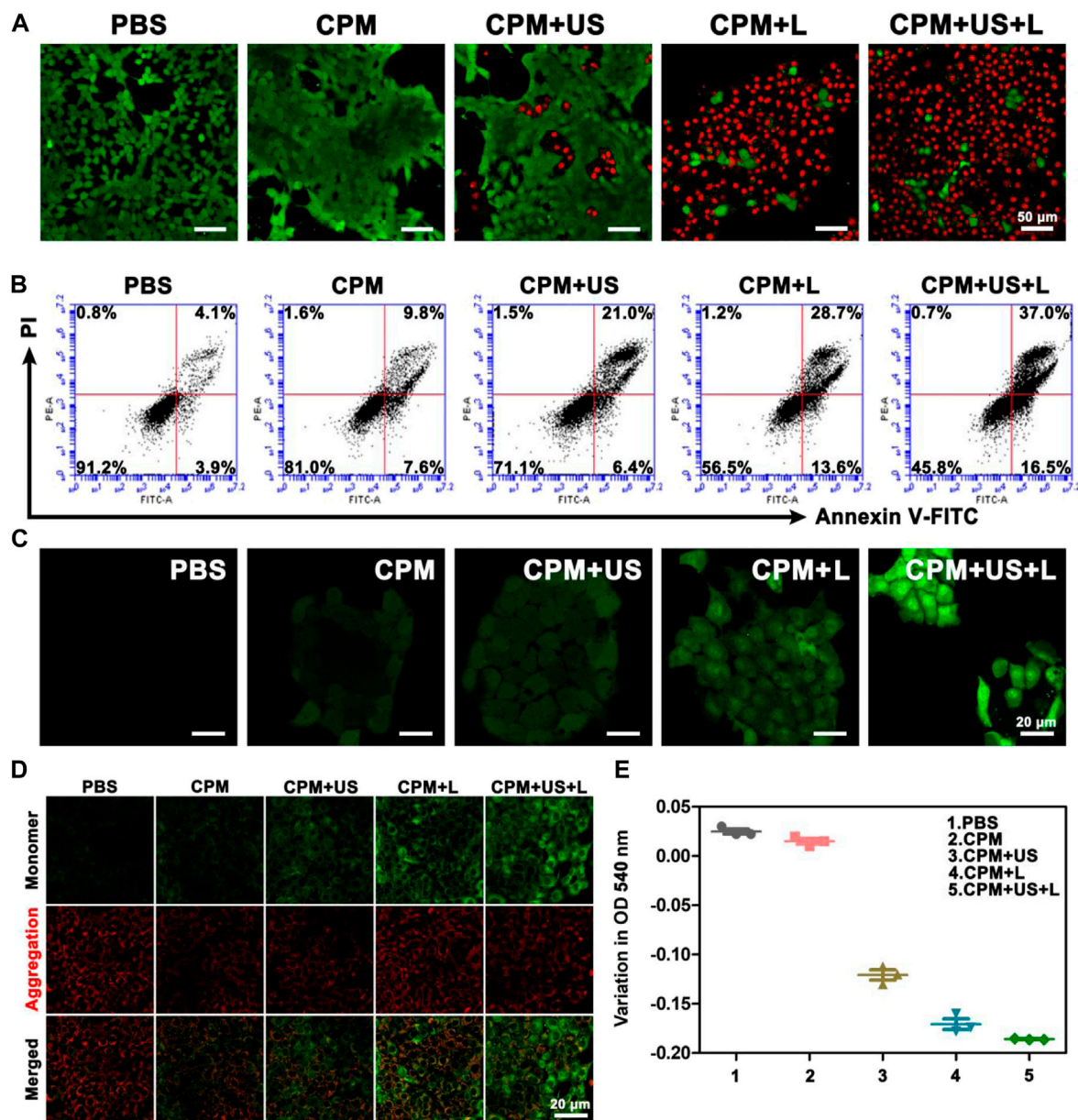


FIGURE 3

(A) Live/dead staining assay (green, live cells; red, dead cells) and (B) apoptosis analysis of 4T1 cells after various treatments. (C) Intracellular ROS detected by DCFH-DA probe. (D) CLSM images of 4T1 cells that received various treatments and then stained with JC-1 dye. (E) The optical density of 4T1 cells mitochondria at 540 nm after various treatments.

consuming  $H^+$  ions (Liu Y et al., 2019). Using a portable oxygen-dissolving apparatus, we further investigated the oxygen generation capability of CPM NPs at different pH with and without  $H_2O_2$  (100  $\mu M$ ). A similar oxygen content of approximately 10 mg/L was observed in the pure  $H_2O_2$  and PBS (pH 7.4) group (CPM NPs dissolved in pH 7.4 PBS solution) and the pH 6.5 group (and the CPM NPs dissolved in pH 6.5 PBS solution). When  $H_2O_2$  was added, the pH 7.4 +

$H_2O_2$  group exhibited significantly increased oxygen levels ( $\sim 20$  mg/L). Compared to the other groups, the pH 6.5 +  $H_2O_2$  group exhibited the highest oxygen content ( $\sim 24$  mg/L) (Figure 2B). These results demonstrated the potential of CPM to eliminate tumor hypoxia. Then, the ROS generation capability of CPM NPs in pH 6.5 solution under various conditions was investigated. The fluorescence intensity was clearly increased in the presence of CPM NPs under various treatments

compared to that in the pure H<sub>2</sub>O group (Figure 2C). However, the highest fluorescence intensity was obtained by the implementation of laser and ultrasound irradiation with H<sub>2</sub>O<sub>2</sub>. The above results show that laser and ultrasound irradiation can promote the production of ROS along with CPM NPs in the tumor microenvironment.

### ***In vitro* photothermal effect of calcium carbonate-polydopamine-manganese oxide nanoparticles**

As reported in previous studies, both PDA and MnO<sub>2</sub> exhibit excellent photothermal conversion capability (Farokhi et al., 2019; Liu Y et al., 2021), which inspired us to evaluate the photothermal properties of the CPM NPs. We examined the heating curves of CPM NPs at different concentrations under 1,064 nm laser irradiation (1,064 nm, 1 W cm<sup>-2</sup>). The CPM NPs exhibited both time- and concentration-dependent photothermal heating (Figure 2D). After 15 min of laser stimulation, the temperature of the CPM NPs with a concentration of 1 mg ml<sup>-1</sup> increased significantly from 20°C to 51°C while the temperature of the CPM NPs with a concentration of 200 µg ml<sup>-1</sup> increased to 43°C. Subsequently, we calculated the photothermal conversion efficiency of CPM NPs to be 26.31% (Figures 2E,F). As depicted in Figure 2G, no apparent temperature decrease was observed during the 1,064 nm laser irradiation for three on/off cycles, indicating the excellent photothermal stability of the CPM NPs.

### **Antitumor effects *in vitro***

To evaluate the combined antitumor photothermal and immunity effect *in vitro*, the cytotoxic effect of CPM NPs on tumor cells under various conditions was investigated. A low toxicity to normal cells is a necessary requirement for the application of CPM NPs in biological systems. We used normal human renal epithelial cells (293T) to evaluate the biosafety of CPM NPs by incubating the cells with different concentrations of CPM NPs for 24 or 48 h. It was found that the cell survival rate exceeded 90% even for incubation with the highest concentration (20 µg ml<sup>-1</sup>) for 48 h (Figure 2H), reflecting the excellent biocompatibility of CPM NPs. The antitumor effects of CPM NPs were further investigated. Various concentrations (0.625, 1.25, 2.5, 5, 10, and 20 µg ml<sup>-1</sup>) of CPM NPs were co-incubated with 4T1 cells and treated with 1,064 nm laser irradiation (1 W cm<sup>-2</sup>, 5 min) and US (1.0 MHz, 20% duty cycle, 0.5 W cm<sup>-2</sup>, 2 min). As shown in Figure 2I, the CPM group exhibited weak killing ability (85%) of 4T1 cells (20 µg ml<sup>-1</sup>) compared to the CPM + US (69.6%) and CPM + L groups (46.3%). The decreased cell viability of the CPM + US group may be attributed to the ultrasound-promoted calcium

overload. Hyperthermia triggered by the photothermal effect of CPM NPs under laser irradiation also promoted cell death. The CPM + US and CPM + L groups exhibited concentration-dependent cell viability. As expected, the 4T1 cells treated with CPM + US + L showed the highest cell lethality (45.9%), indicating the most severe cell damage.

To depict cell viability more intuitively, calcein-AM/PI was employed to conduct a living/dead assay by staining dead cells and living cells to red and green, respectively. As depicted in Figure 3A, only bright green fluorescence, representing live cells, appeared in the CPM and PBS groups, confirming the negligible killing effect. A few dead cells appeared in the CPM + US group, while more dead cells were observed in the CPM + L group, proving that the cytotoxic effect of photothermal therapy is better than that of ultrasound. As expected, the CPM + US + L group showed the highest number of dead cells compared to the other groups. This result was consistent with that of the MTT assay (Figure 2I). Additionally, we investigated the apoptosis induced by CPM NPs under various treatments. As shown in Figure 3B, the apoptosis rates in the CPM, CPM + US, and CPM + L groups were 17.4%, 27.4%, and 42.3%, respectively. Under the application of both laser and ultrasound irradiation, the CPM + US + L group showed the highest apoptosis rate (53.5%). These results are in agreement with those of the MTT and living/dead assays. The above results demonstrated the superior antitumor effect of CPM + US + L. Subsequently, a series of experiments were conducted to elucidate the therapeutic mechanism. Alleviating hypoxia in the tumor microenvironment is critical for tumor therapy. Therefore, we firstly detected the effect of CPM NPs for hypoxia remission in cells. Red fluorescence indicates cell hypoxia. As revealed in Supplementary Figure S4, almost no red fluorescence was exhibited in the normal environment with or without CPM NPs. Under hypoxia environment, the obvious red fluorescence signal appears without CPM NPs. In contrast, the CPM-treated cells only exhibited faint red fluorescence, proving the effective hypoxia remission. The generation of ROS in 4T1 cells was evaluated using a DCFH-DA probe, with green fluorescence as the ROS indicator. CPM-treated cells showed weak fluorescence, which may be ascribed to the ROS production during MnO<sub>2</sub>-induced CDT and mitochondrial Ca<sup>2+</sup> overload (Wang et al., 2019). When either laser or ultrasound irradiation was applied, CPM-treated cells showed stronger fluorescence intensity (Figure 3C), suggesting that both laser irradiation and ultrasound promoted ROS production. This result may be caused by ultrasound-enhanced mitochondrial Ca<sup>2+</sup> overload and laser-promoted CDT (Zhang et al., 2021). As anticipated, the CPM + US + L group showed the strongest green fluorescence compared to the CPM + US and CPM + L groups, suggesting the superiority of the combination therapy. Mitochondrial Ca<sup>2+</sup> overload can damage the mitochondria, triggering a decrease in the mitochondrial membrane potential. We further determined the degree of mitochondrial damage after various treatments using JC-1 (mitochondrial membrane potential probe). J-aggregates with red fluorescence and monomers with green fluorescence were found in normal and damaged mitochondrial membranes, respectively. As



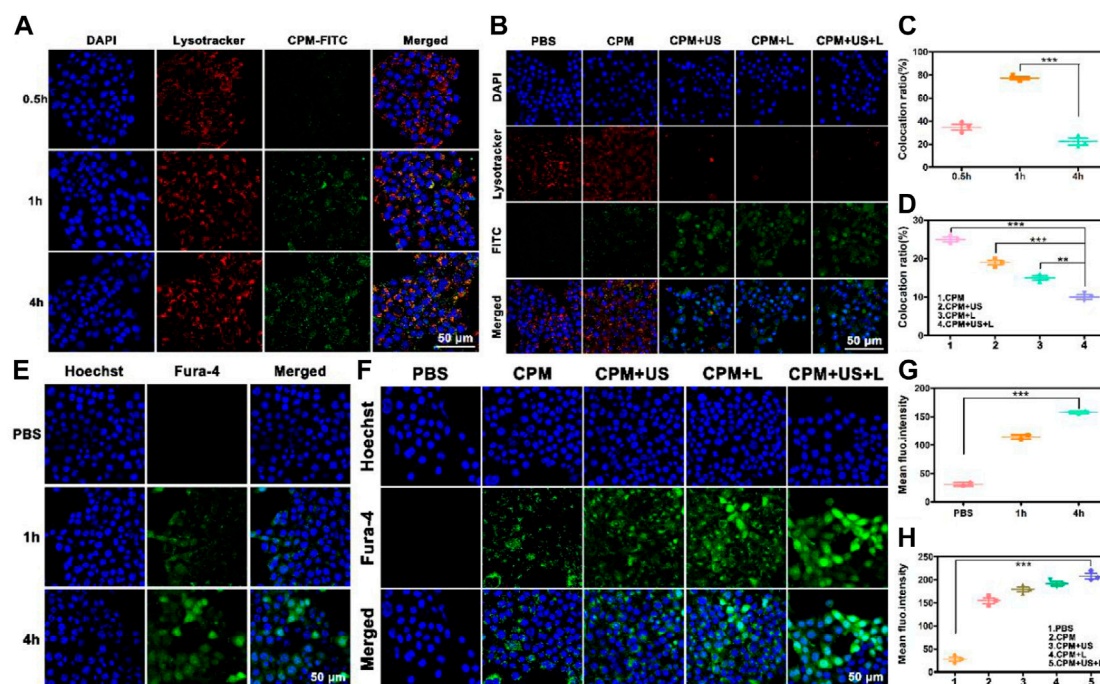


FIGURE 4

(A) The CLSM of CPM NPs (labeled with FITC,  $20 \mu\text{g ml}^{-1}$ ) with lysosomes in 4T1 cells after incubation with CPM NPs for 0.5, 1, and 4 h, respectively. (B) The CLSM of CPM NPs (labeled with FITC,  $20 \mu\text{g ml}^{-1}$ ) with lysosomes in 4T1 cells being various treatments. (C) The co-location ratio of CPM NPs with lysosomes in 4T1 cells after incubated with CPM for 0.5, 1, and 4 h, respectively. (D) The co-location ratio of CPM NPs with lysosomes in 4T1 cells after various treatments. (E) Confocal images of 4T1 cells incubated with CPM NPs ( $20 \mu\text{g ml}^{-1}$ ) at different time points and stained with an intracellular  $\text{Ca}^{2+}$  indicator, Fluo-4 AM (5  $\mu\text{M}$ ). (F) Confocal images of 4T1 cells being various treatments after incubated with CPM NPs ( $20 \mu\text{g ml}^{-1}$ ) for 4 h and stained with an intracellular  $\text{Ca}^{2+}$  indicator, Fluo-4 AM (5  $\mu\text{M}$ ). (G) Mean fluorescence intensity (MFI) of intracellular  $\text{Ca}^{2+}$  level in 4T1 cells. (H) MFI of intracellular  $\text{Ca}^{2+}$  level in 4T1 cells after various treatments.

shown in Figure 3D, weak green fluorescence appeared in the cells of the CPM group, confirming slight mitochondrial damage. The green fluorescence signal was enhanced under laser and ultrasound stimulation, indicating that the application of US and laser increased mitochondrial damage. As expected, the cells in the CPM + US + L group showed the strongest green fluorescence signal, suggesting that the combination of laser irradiation and ultrasound resulted in the most severe mitochondrial damage. In addition to decreased mitochondrial membrane potential, mitochondrial swelling is an important indicator of mitochondrial damage. Therefore, we performed a mitochondrial swelling assay to verify the mitochondrial damage. Normal mitochondria show strong ultraviolet-visible (UV-vis) absorption at 540 nm, whereas the absorbance at 540 nm decreases when mitochondria are damaged. As shown in Figure 3E, the absorbance values of the cells at 540 nm were significantly decreased after treatment with laser irradiation or ultrasound compared to the PBS and CPM groups, indicating that both laser irradiation and ultrasound can induce strong mitochondrial swelling. As anticipated, the CPM + US + L group exhibited the most obvious mitochondrial swelling, which was consistent with the results of the mitochondrial membrane potential assay.  $\text{Ca}^{2+}$  is considered a key factor in the regulation

of mitochondrial activity (Giorgi et al., 2018; Nemani et al., 2018; Rossi et al., 2019). This inspired us to explore whether mitochondrial damage was related to  $\text{Ca}^{2+}$  overload. First, we used FITC-labeled CPM NPs and red Lyso-Tracker to investigate the internalization and lysosomal escape of CPM NPs in 4T1 cells. As indicated in Figure 4A, the green fluorescence intensity of CPM-FITC gradually increased with prolonged co-culture time of CPM-FITC with 4T1 cells. Notably, when CPM-FITC was co-incubated with 4T1 cells for 4 h, the green fluorescence of CPM-FITC separated from the lysosomal red fluorescence was clearly observed unlike for those at 0.5 and 1 h. The co-localization rate of CPM-FITC fluorescence and lysosomal fluorescence was calculated using ImageJ analysis. As shown in Figure 4C, the colocalization rate of CPM-FITC fluorescence and lysosomal fluorescence reached 77% after 1 h incubation, but subsequently decreased to 22% after 4 h of incubation, confirming that CPM NPs underwent effective lysosomal escape. We then explored the internalization and lysosomal escape of 4T1 cells under various treatments after co-culture with CPM-FITC for 4 h. Compared to the CPM group, the green fluorescence of 4T1 cells was significantly enhanced after laser or ultrasound irradiation (Figure 4B), verifying that laser and ultrasound irradiation promoted the cellular uptake of CPM NPs.



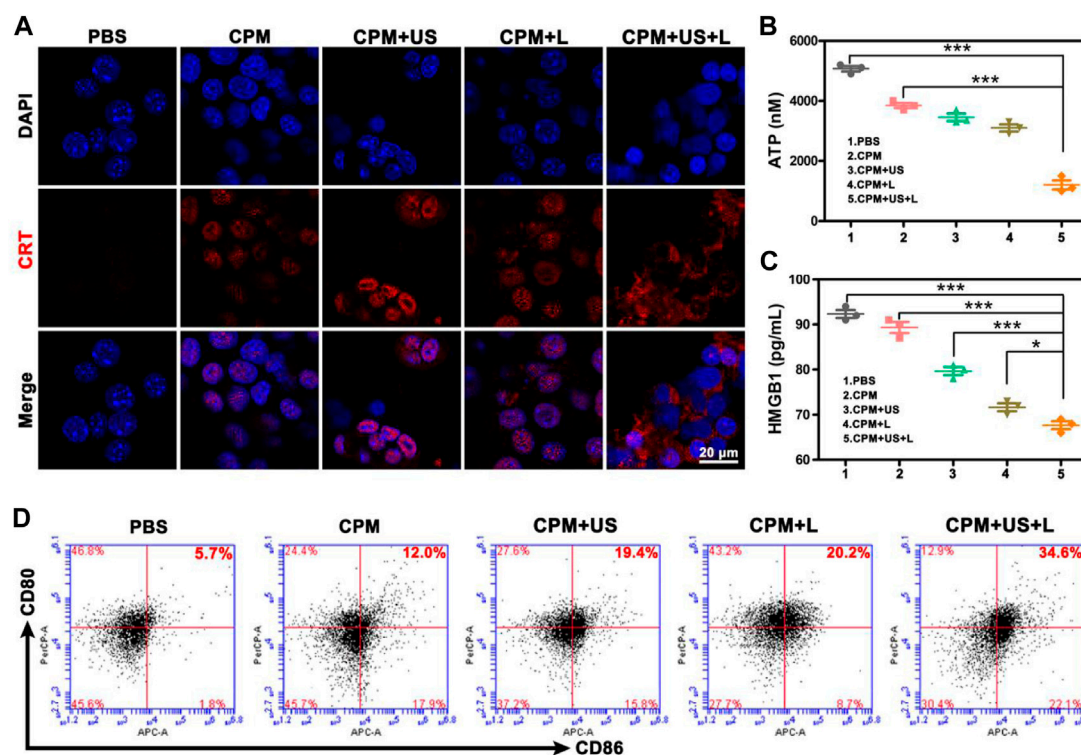


FIGURE 5

(A) CRT exposure. (B) Intracellular ATP and (C) HMGB1 release from 4T1 cells after various treatments. Data are means  $\pm$  SD, \* $p$  < 0.05, \*\* $p$  < 0.01, and \*\*\* $p$  < 0.001. (D) Flow cytometry analysis of the expression of CD80<sup>+</sup>/CD86<sup>+</sup> DC cells (markers for maturation) on the surface of DCs after various treatments.

This is attributed to the higher cell permeability caused by the photothermal effect and ultrasonic vibration, which facilitates the entry of nanoparticles into cells (Hu et al., 2020).

In addition, most of the separated green fluorescence was observed in the CPM + US + L group. As shown in Figure 4D, the fluorescence colocalization rates of CPM, CPM + US, CPM + L, and CPM + US + L groups were calculated to be 25%, 19%, 15%, and 10%, respectively. Notably, red fluorescence was significantly reduced in the CPM + US, CPM + L, and CPM + US + L groups, indicating strong lysosomal damage caused by the release of CPM NPs into the cytoplasm (Weyergang et al., 2014; Huang et al., 2019). These results demonstrated that laser and ultrasound irradiation accelerated lysosomal escape, and the combination treatment further promotes this process. Then, we detected the Ca<sup>2+</sup> uptake by CPM NPs after co-culture with 4T1 cells for 4 h. The green fluorescence of Fluo-4 AM was used as the Ca<sup>2+</sup> probe. The intracellular Ca<sup>2+</sup> fluorescence intensity increased in a time-dependent manner in 4T1 cells (Figures 4E,G). To study the effects of laser and ultrasound irradiation on intracellular Ca<sup>2+</sup> content, we treated 4T1 cells after culturing with CPM NPs for 4 h. As shown in Figure 4F, both the CPM + US and CPM + L groups exhibited brighter green fluorescence than the CPM group, proving that laser and

ultrasound irradiation facilitated Ca<sup>2+</sup> internalization by 4T1 cells. The strongest Ca<sup>2+</sup> fluorescence intensity in the CPM + US + L group confirmed the superiority of the combined laser and ultrasound treatment for Ca<sup>2+</sup> uptake. Moreover, quantitative analysis of the fluorescence intensity of Ca<sup>2+</sup> also proved this conclusion (Figure 4H). The above results indicate that CPM NPs under laser and ultrasound irradiation effectively increase intracellular Ca<sup>2+</sup> content, resulting in Ca<sup>2+</sup> overload and thereby inducing mitochondrial damage.

To assess the antitumor immune response to CPM NPs under various treatments, we explored ICD. The release of DAMPs from tumor cells is an important step in triggering ICD in tumor immunotherapy. During ICD, DAMPs, including CRT, ATP, and HMGB1, can be exposed to the membrane surface of tumor cells to facilitate DC maturation and stimulate optimal antigen presentation. Confocal microscopy was used to observe the level of CRT secretion on the surface of 4T1 cells after treatment, and the levels of intracellular ATP and HMGB1 release were determined using the ATP and HMGB1 ELISA kits, respectively. We found that CRT expression on the cell surface of the CPM group was enhanced compared to that in the PBS group, which may be caused by the Ca<sup>2+</sup>- and Mn<sup>2+</sup>-evoked ICD (Figure 5A). When laser or ultrasound irradiation was applied, a higher CRT exposure was observed. As

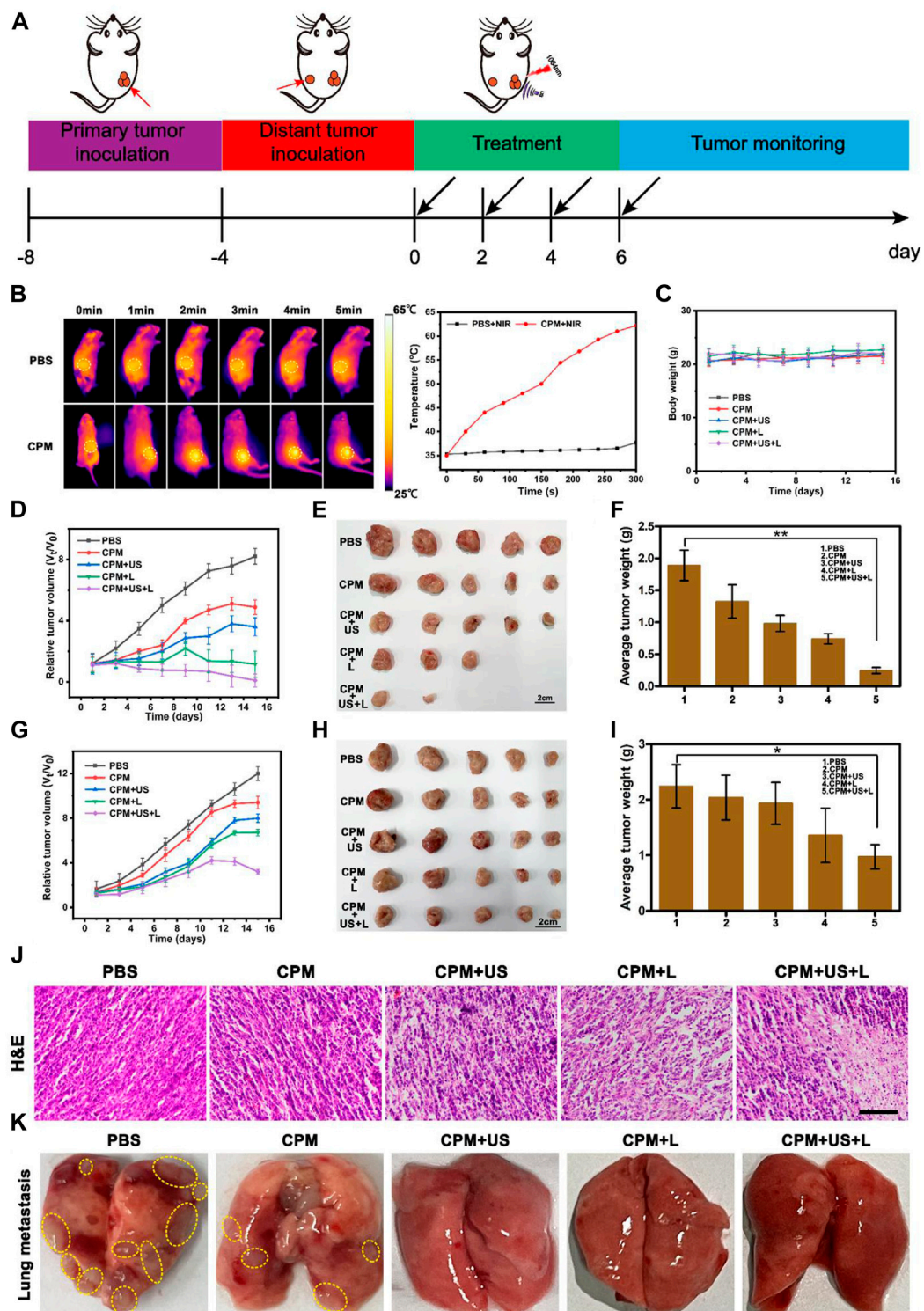


FIGURE 6

(A) Schematic illustration of the animal tumor model and treatment process. (B) Infrared thermographic images of mice in PBS + NIR and CPM + NIR groups and the corresponding temperatures curves of mice. (1,064 nm, 1 W cm<sup>-2</sup>, 5 min). (C) Average body weight curves during treatment. (D) Relative tumor volumes-time curves of 4T1 primary tumors in mice after various treatments. (E) Representative tumor pictures of 4T1 primary tumor and (F) average tumor weights obtained on the 15 th day. (G) Relative tumor volumes-time curve of 4T1 distant tumors in mice after various treatments. (H) Representative tumor pictures of 4T1 distant tumor and (I) average tumor weights obtained on the 15 th day. Data are means  $\pm$  SD, \* $p$  < 0.05. (J) H and E staining images of primary tumors tissues. (Scale bar: 100  $\mu$ m). (K) Representative photographs of lung tissues after various treatments.

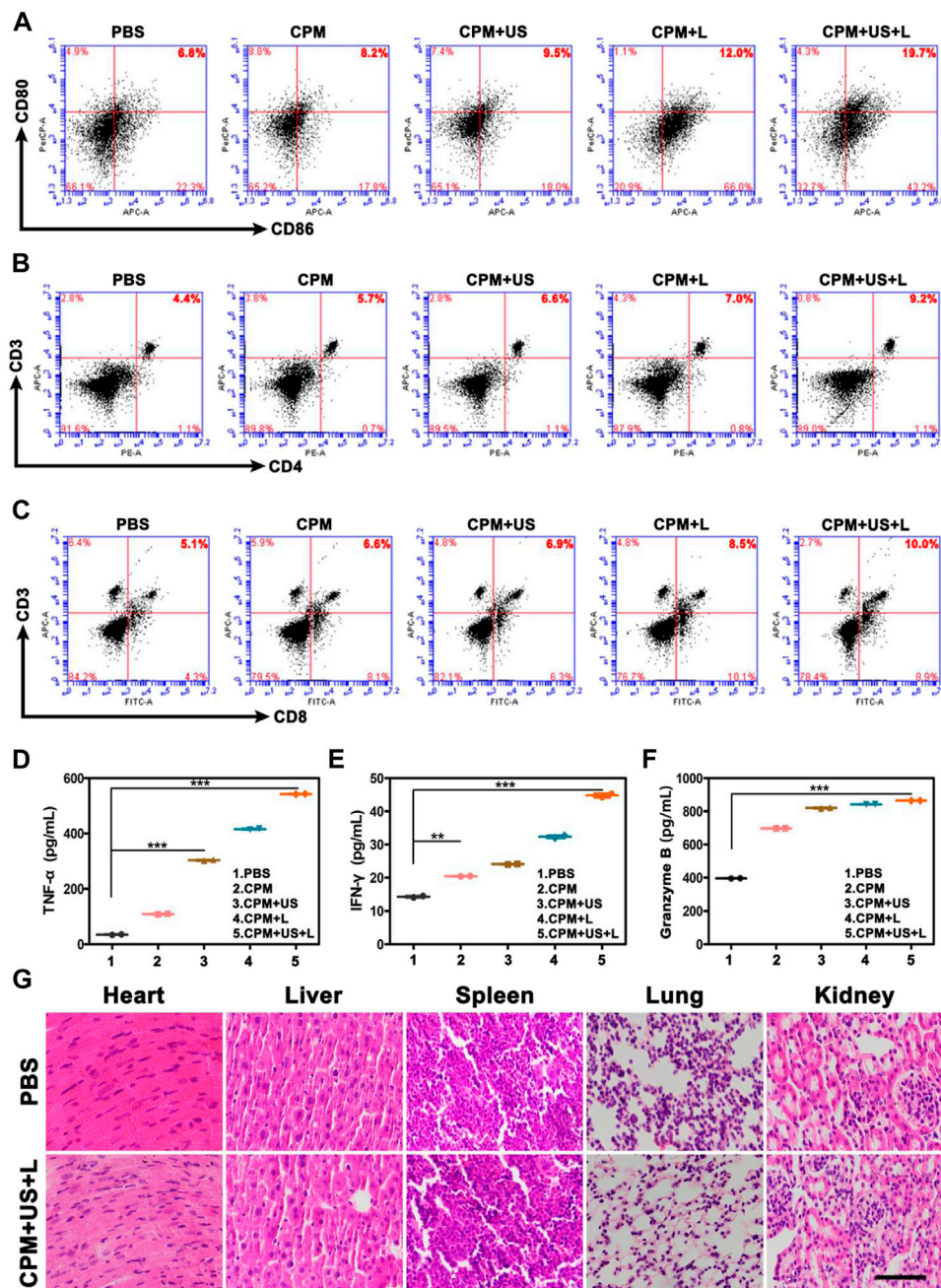


FIGURE 7

Representative flow cytometry profiles of (A) CD80<sup>+</sup>/CD86<sup>+</sup> DC cells after indicated procedures in the lymph nodes, (B) CD3<sup>+</sup>/CD4<sup>+</sup> T cells in the spleen and (C) CD3<sup>+</sup>/CD8<sup>+</sup> T cells in the spleen. (D–F) The ELISA analysis of intraserosal cytokine levels of TNF-α, IFN-γ, and Granzyme B after different treatments on day 15. (G) H and E-stained images of major organs of BALB/c mice in various groups. (Scale bar: 100 μm).

expected, the CPM + US + L group showed the highest CRT exposure, demonstrating that the laser and ultrasound irradiation promoted immune responses. HMGB1 and ATP have been identified as other ICD biomarkers in 4T1 cells. As illustrated in Figures 5B,C, the intracellular release of HMGB1 and ATP significantly decreased in the CPM + US + L, CPM + US, and

CPM + L groups compared to the PBS and CPM groups. Among these, CPM + US + L exhibited the most significant decrease. These results confirmed that CPM + US and CPM + L can trigger an effective ICD that was further promoted by the combination of laser and ultrasound irradiation. Numerous studies have demonstrated that DAMPs released from necrotic or apoptotic tumor cells can



stimulate DCs maturation. DCs maturation was measured using flow cytometry. The mean percentage of mature DCs in the CPM + US + L group (34.6%) was significantly higher than that in the PBS (5.7%), CPM (12.0%), CPM + US (19.4%), and CPM + L (20.2%) groups (Figure 5D). These results verified that laser and ultrasound irradiation with CPM NPs can effectively induce ICD and promote DC maturation, thereby activating the antitumor immune response.

## ***In vivo* synergistic photothermal therapy and immune therapy**

Tumor therapy *in vivo* strictly followed the experimental scheme (Figure 6A). First, the therapeutic efficiency of the treatment system for primary and distant tumors was assessed simultaneously using a bilateral 4T1 tumor model. Different numbers of 4T1 cells ( $2 \times 10^6$  cells per mouse and  $1 \times 10^6$  cells per mouse) were inoculated into both the right (defined as the primary tumor) and left (defined as the distant tumor) flank regions of BALB/c mice on days -8 and -4, respectively. CPM NPs (100  $\mu$ l, 1 mg ml<sup>-1</sup>) were injected into the primary tumor region of BALB/c mice prior to each irradiation of the BALB/c primary tumors with 1,064 nm laser (1 W cm<sup>-2</sup>, 5 min) or US (1.0 MHz, 20% duty cycle, 2 W cm<sup>-2</sup>, 2 min). First, the photothermal effect of the laser-irradiated BALB/c mice was assessed using an infrared thermal imaging camera. After the injection of PBS or CPM NPs, mouse tumor areas were irradiated with a 1,064 nm laser (1 W cm<sup>-2</sup>), and temperature changes were recorded every 30 s using an infrared camera. Photothermal photographs of the mice showed that the CPM group exhibited time-dependent heating. The temperature of the CPM group increased from 35 to 62.2°C after 5 min of laser irradiation, showing a strong photothermal performance (Figure 6B). By contrast, the temperature for the PBS group only increased by 2.4°C within 5 min of laser exposure. Body weight changes (Figure 6C) and tumor volumes of each mouse were measured every 2 days. The relative volume curves of the tumors (including primary and distant tumors) were plotted according to the records. After 15 days of treatment, the mice were euthanized by dislocation of cervical vertebra and the primary and distant tumors were imaged and weighed. Unlike the malignant proliferation of 4T1 cells in the PBS group, the CPM + US and CPM + L groups showed significant inhibitory effects on tumor growth; notably, the inhibition of tumor growth was most pronounced in the CPM + US + L group (Figure 6D). The tumor images and weights showed the same trend (Figures 6E,F). These results suggest that the combination of photothermal therapy and immunity can significantly inhibit tumor growth, which is consistent with its outstanding antitumor effect *in vitro*. As expected, the growth of distant tumors in mice exhibited the same trend

as the growth of the primary tumor. Notably, the CPM + US + L group displayed obvious inhibition compared to the other groups (Figures 6G–I). Histological analysis of the primary tumor was performed to detect tissue damage. As illustrated in Figure 6J, after different treatments, different degrees of apoptosis in tumor cells with shrunken and broken nuclei were observed. The CPM + US and CPM + L groups exhibited more severe apoptosis than the CPM and PBS groups. It is important to note that CPM + US + L showed the greatest tumor cell damage, further confirming the antitumor efficacy of the different treatments.

## ***In vivo* anti-lung metastasis ability and immunity of synergistic photothermal therapy and immune therapy**

To comprehensively evaluate the antitumor ability of CPM, we also investigated the anti-lung metastasis ability of CPM *in vivo*. As shown in Figure 6K, the lungs of the mice in the PBS group exhibited a large number of pulmonary nodules that were significantly reduced in the CPM group. Additionally, the lung surfaces of the mice in the CPM + US, CPM + L, and CPM + US + L groups were flat, further demonstrating the superior antitumor metastasis ability of this therapeutic platform.

After the ability of CPM NPs to induce ICD and facilitate DC cell maturation was verified *in vitro*, we further investigated the antitumor immune responses of CPM NPs after various treatments *in vivo*. Flow cytometry was used to determine the DCs maturation (CD11c<sup>+</sup>/CD80<sup>+</sup>/CD86<sup>+</sup>) levels in the draining lymph nodes. As expected, the highest secretion level of DCs maturation (19.7%) was observed in the CPM + US + L group compared to the CPM (8.2%), CPM + US (9.5%), and CPM + L (12%) groups (Figure 7A), indicating that the combined laser and ultrasound therapy with CPM NPs effectively induced DCs maturation and improved the immune response *in vivo*. In addition, CD4<sup>+</sup> and CD8<sup>+</sup> T lymphocytes in the spleen were detected using flow cytometry. As shown in Figures 7B,C, the CPM + US + L group exhibited the strongest T cell-mediated immune response (CD4<sup>+</sup>/CD8<sup>+</sup> T cells: 9.2% and 10%) compared to the PBS (4.4% and 5.1%), CPM (5.7% and 6.6%), CPM + US (6.6% and 6.9%), and CPM + L (7.0% and 8.5%) groups, suggesting that combined treatment with CPM NPs promotes CD4<sup>+</sup> and CD8<sup>+</sup> T lymphocyte proliferation and infiltration. Subsequently, immune-mediated tumor killing was assessed by determining the levels of typical immune-related pro-inflammatory cytokines secreted by mature DC. The levels of cytokines TNF- $\alpha$ , IFN- $\gamma$ , and granzyme B in mouse serum were measured by enzyme-linked immunosorbent assay. As illustrated in Figures 7D–F, the highest cytokine levels



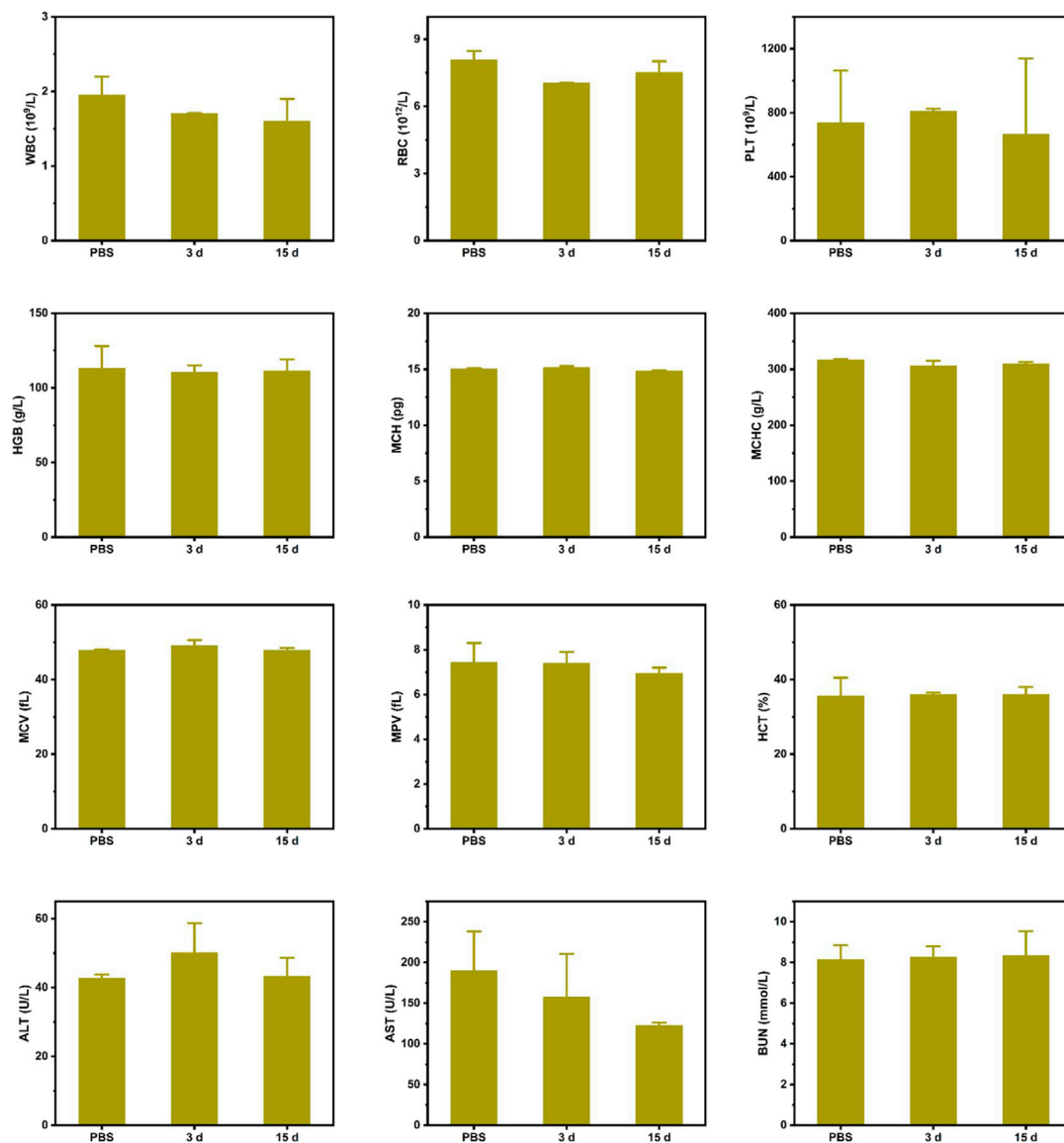


**FIGURE 8**  
Major blood routine indexes, liver and kidney function indexes of mice after various treatments.

were found in the CPM + US + L group. Furthermore, the immune cell response against the tumor was also evaluated by immunohistochemistry analysis of tumor sections from mice. As expected, the highest proportion of CD4<sup>+</sup> and CD8<sup>+</sup> T cell infiltration in the tumor tissues were found in the CPM + US + L group (Supplementary Figure S4), suggesting that the combination of laser and ultrasound treatment could further promote the infiltration and proliferation of CD4<sup>+</sup> and CD8<sup>+</sup> T cells. These results indicated that the regimen of the combination photothermal and immune tumor therapy significantly enhanced the antitumor immune response.

## Systemic toxicity evaluation

Furthermore, to assess the biosafety of CPM, we performed histological analysis of major organs, including the heart, liver, spleen, lungs, and kidneys. As shown in Figure 7G, H and E-stained images of organ sections from the different treatment groups showed negligible abnormalities. Furthermore, the mice did not experience significant weight loss during the treatment period (Figure 6C), indicating the excellent biocompatibility of CPM NPs and the safety of the combined treatment procedure. Moreover, the functional indicators of the blood samples in the

CPM + US + L group were tested to assess the potential toxicity of CPM *in vivo*. As shown in Figure 8, compared to the PBS group, the CPM + US + L group showed negligible abnormalities in the relevant functional indicators on day 3 and at the end of treatment. The routine blood indices in the CPM + US + L group were found to be normal compared to those in the PBS group, indicating that no significant systemic infection or inflammation appeared during the entire evaluation period. The measured parameters, including alanine aminotransferase (ALT), aspartate aminotransferase (AST), and urea nitrogen (BUN), were within the normal range, indicating that the nanoparticles exhibited little toxicity to the liver. These results demonstrated the excellent compatibility and negligible adverse effects of the CPM + US + L treatment on the organism.

## Conclusion

In summary, a combined photothermal and immune tumor therapy platform was fabricated based on dual-gas nanogenerators (CPM NPs). The CPM NPs underwent responsive degradation in the tumor, resulting in the generation of  $\text{Ca}^{2+}$ ,  $\text{Mn}^{2+}$ ,  $\text{CO}_2$ , and  $\text{O}_2$ .  $\text{Ca}^{2+}$  and  $\text{Mn}^{2+}$  act as immune adjuvants that trigger ICD for immunotherapy. The relieved tumor hypoxia and cancer cell membrane rupture caused by sudden burst of bubbles ( $\text{CO}_2$  and  $\text{O}_2$ ) all contributed to ICD. The application of laser and ultrasound promoted the  $\text{Ca}^{2+}$  overload in mitochondria and explosion of  $\text{CO}_2$  and  $\text{O}_2$  bubbles by photothermal effects and ultrasonic waves thus improved immunotherapy effect. Superior PTT and immune synergistic therapeutic capabilities were demonstrated in both *in vitro* and *in vivo* experiments. Thus, this strategy based on CPM NPs dual-gas nano-generators is promising for future clinical cancer treatment.

## Data availability statement

The original contributions presented in the study are included in the article/Supplementary Material, further inquiries can be directed to the corresponding authors.

## Ethics statement

The animal study was reviewed and approved by Binzhou Medical University Animal Ethics Committee.

## Author contributions

XYL and YG, Data curation, Project administration, Writing-original draft. XZL and XH, Investigation, Project administration. YL and JS, Project administration. PW, HW, and HK, Project administration. MR, Conceptualization, Project administration. Writing-review and editing. SX, Resources, Funding acquisition, Writing-review and editing. RW, Conceptualization, Funding acquisition, Writing-review and editing. All authors read and approved the final manuscript.

## Funding

This work was supported by the National Natural Science Foundation of China (Grant Numbers 51903015 and 81772281), Science Fund of Shandong Laboratory of Advanced Materials and Green Manufacturing (Yantai) (AMGM 2021F03), and Shandong Science and Technology Committee (No. ZR2019MH022, ZR2020KH015), the Scientific Research Foundation of Binzhou Medical University (Project No. 50012304274), and Shandong Province Taishan Scholar Project (No. ts201712067), and Hong Kong RGC (GRF# 16308818, 16309920 and 16309421).

## Conflict of interest

The authors declare that the research was conducted in the absence of any commercial or financial relationships that could be construed as a potential conflict of interest.

## Publisher's note

All claims expressed in this article are solely those of the authors and do not necessarily represent those of their affiliated organizations, or those of the publisher, the editors and the reviewers. Any product that may be evaluated in this article, or claim that may be made by its manufacturer, is not guaranteed or endorsed by the publisher.

## Supplementary material

The Supplementary Material for this article can be found online at: <https://www.frontiersin.org/articles/10.3389/fbioe.2022.1005520/full#supplementary-material>

## References

- Chao, Y., Xu, L., Liang, C., Feng, L., Xu, J., Dong, Z., et al. (2018). Combined local immunostimulatory radioisotope therapy and systemic immune checkpoint blockade imparts potent antitumor responses. *Nat. Biomed. Eng.* 2 (8), 611–621. doi:10.1038/s41551-018-0262-6
- Chattopadhyay, S., Liu, Y. H., Fang, Z. S., Lin, C. L., Lin, J. C., Yao, B. Y., et al. (2020). Synthetic immunogenic cell death mediated by intracellular delivery of STING agonist nanoshells enhances anticancer chemo-immunotherapy. *Nano Lett.* 20 (4), 2246–2256. doi:10.1021/acs.nanolett.9b04094
- Chen Q, Q., Liu, L., Lu, Y., Chen, X., Zhang, Y., Zhou, W., et al. (2019). Tumor microenvironment-triggered aggregated magnetic nanoparticles for reinforced image-guided immunogenic chemotherapy. *Adv. Sci.* 6 (6), 1802134. doi:10.1002/advs.201802134
- Chen, Y., Ai, W., Guo, X., Li, Y., Ma, Y., Chen, L., et al. (2019). Mitochondria-targeted polydopamine nanocomposite with AIE photosensitizer for image-guided photodynamic and photothermal tumor ablation. *Small* 15 (30), e1902352. doi:10.1002/sml.201902352
- Chen, Y., Qin, W., Fan, R., Wang, J., and Chen, B. (2015). Hydrothermal synthesis and electrochemical properties of spherical  $\alpha$ -MnO<sub>2</sub> for supercapacitors. *J. Nanosci. Nanotechnol.* 15 (12), 9760–9765. doi:10.1166/jnn.2015.10490
- Dai, Y., Zhao, H., He, K., Du, W., Kong, Y., Wang, Z., et al. (2021). NIR-II excitation phototheranostic nanomedicine for fluorescence/photoacoustic tumor imaging and targeted photothermal-photonic thermodynamic therapy. *Small* 17 (42), e2102527. doi:10.1002/sml.202102527
- Deng, H., Zhou, Z., Yang, W., Lin, L. S., Wang, S., Niu, G., et al. (2020). Endoplasmic reticulum targeting to amplify immunogenic cell death for cancer immunotherapy. *Nano Lett.* 20 (3), 1928–1933. doi:10.1021/acs.nanolett.9b05210
- Ding, B., Zheng, P., Jiang, F., Zhao, Y., Wang, M., Chang, M., et al. (2020). MnOx nanospikes as nanoadjuvants and immunogenic cell death drugs with enhanced antitumor immunity and antimetastatic effect. *Angew. Chem. Int. Ed.* 59 (38), 16381–16384. doi:10.1002/anie.202005111
- Dong, Z., Feng, L., Hao, Y., Chen, M., Gao, M., Chao, Y., et al. (2018). Synthesis of hollow biomineralized CaCO<sub>3</sub>-polydopamine nanoparticles for multimodal imaging-guided cancer photodynamic therapy with reduced skin photosensitivity. *J. Am. Chem. Soc.* 140 (6), 2165–2178. doi:10.1021/jacs.7b11036
- Duan, H., Guo, H., Zhang, R., Wang, F., Liu, Z., Ge, M., et al. (2020). Two-dimensional silicene composite nanosheets enable exogenous/endogenous-responsive and synergistic hyperthermia-augmented catalytic tumor theranostics. *Biomaterials* 256, 120206. doi:10.1016/j.biomaterials.2020.120206
- Duan, X., Chan, C., and Lin, W. (2019). Nanoparticle-mediated immunogenic cell death enables and potentiates cancer immunotherapy. *Angew. Chem. Int. Ed.* 58 (3), 670–680. doi:10.1002/anie.201804882
- Fan, W., Bu, W., Shen, B., He, Q., Cui, Z., Liu, Y., et al. (2015). Intelligent MnO<sub>2</sub> nanosheets anchored with upconversion nanoprobe for concurrent PH-/H<sub>2</sub>O<sub>2</sub>-responsive UCL imaging and oxygen-elevated synergetic therapy. *Adv. Mat.* 27 (28), 4155–4161. doi:10.1002/adma.201405141
- Farokhi, M., Mottaghtalab, F., Saeb, M. R., and Thomas, S. (2019). Functionalized theranostic nanocarriers with bio-inspired polydopamine for tumor imaging and chemo-photothermal therapy. *J. Control. Release* 309, 203–219. doi:10.1016/j.jconrel.2019.07.036
- Feng, Q., Zhang, W., Yang, X., Li, Y., Hao, Y., Zhang, H., et al. (2018). pH/ultrasound dual-responsive gas generator for ultrasound imaging-guided therapeutic inertial cavitation and sonodynamic therapy. *Adv. Health. Mat.* 7 (5), 1700957. doi:10.1002/adhm.201700957
- Giorgi, C., Marchi, S., and Pinton, P. (2018). The machineries, regulation and cellular functions of mitochondrial calcium. *Nat. Rev. Mol. Cell Biol.* 19 (11), 713–730. doi:10.1038/s41580-018-0052-8
- Hu, Q., Huang, Z., Duan, Y., Fu, Z., and Liu, B. (2020). Reprogramming tumor microenvironment with photothermal therapy. *Bioconj. Chem.* 31 (5), 1268–1278. doi:10.1021/acs.bioconjchem.0c00135
- Huang, X., Wu, J., He, M., Hou, X., Wang, Y., Cai, X., et al. (2019). Combined cancer chemo-photodynamic and photothermal therapy based on ICG/PDA/TPZ-Loaded nanoparticles. *Mol. Pharm.* 16 (5), 2172–2183. doi:10.1021/acs.molpharmaceut.9b00119
- Hwang, H. Y., Kim, I. S., Kwon, I. C., and Kim, Y. H. (2008). Tumor targetability and antitumor effect of docetaxel-loaded hydrophobically modified glycol chitosan nanoparticles. *J. Control. Release* 128 (1), 23–31. doi:10.1016/j.jconrel.2008.02.003
- Jeon, J., Yoon, B., Song, S. H., Um, W., Song, Y., Lee, J., et al. (2022). Chemiluminescence resonance energy transfer-based immunostimulatory nanoparticles for sonoimmunotherapy. *Biomaterials* 283, 121466. doi:10.1016/j.biomaterials.2022.121466
- Jiao, X., Sun, L., Zhang, W., Ren, J., Zhang, L., Cao, Y., et al. (2021). Engineering oxygen-deficient ZrO<sub>2</sub>-x nanoplateform as therapy-activated "immunogenic cell death (ICD)" inducer to synergize photothermal-augmented sonodynamic tumor elimination in NIR-II biological window. *Biomaterials* 272 120787. doi:10.1016/j.biomaterials.2021.120787
- Li, B., Gong, T., Xu, N., Cui, F., Yuan, B., Yuan, Q., et al. (2020). Improved stability and photothermal performance of polydopamine-modified Fe<sub>3</sub>O<sub>4</sub> nanocomposites for highly efficient magnetic resonance imaging-guided photothermal therapy. *Small* 16 (45), e2003969. doi:10.1002/sml.202003969
- Li, J., and Kataoka, K. (2021). Chemo-physical strategies to advance the *in vivo* functionality of targeted nanomedicine: The next generation. *J. Am. Chem. Soc.* 143 (2), 538–559. doi:10.1021/jacs.0c09029
- Li, X., Peng, X. H., Zheng, B. D., Tang, J., Zhao, Y., Zheng, B. Y., et al. (2018). New application of phthalocyanine molecules: From photodynamic therapy to photothermal therapy by means of structural regulation rather than formation of aggregates. *Chem. Sci.* 9 (8), 2098–2104. doi:10.1039/c7sc05115h
- Liu, J., Feng, L., and Wu, Y. (2021). Enzymatically synthesised MnO<sub>2</sub> nanoparticles for efficient near-infrared photothermal therapy and dual-responsive magnetic resonance imaging. *Nanoscale* 13 (25), 11093–11103. doi:10.1039/d1nr02400k
- Liu, J., Zhang, R., and Xu, Z. P. (2019). Nanoparticle-based nanomedicines to promote cancer immunotherapy: Recent advances and future directions. *Small* 15 (32), e1900262. doi:10.1002/sml.201900262
- Liu, P., Zhao, L., Pol, J., Levesque, S., Petrazzuolo, A., Pfirschke, C., et al. (2019). Crizotinib-induced immunogenic cell death in non-small cell lung cancer. *Nat. Commun.* 10 (1), 1486. doi:10.1038/s41467-019-09415-3
- Liu, Y., Pan, Y., Cao, W., Xia, F., Liu, B., Niu, J., et al. (2019). A tumor microenvironment responsive biodegradable CaCO<sub>3</sub>/MnO<sub>2</sub>-based nanoplateform for the enhanced photodynamic therapy and improved PD-L1 immunotherapy. *Theranostics* 9 (23), 6867–6884. doi:10.7150/thno.37586
- Liu, Y., Yu, B., Dai, X., Zhao, N., and Xu, F. J. (2021). Biomineralized calcium carbonate nanohybrids for mild photothermal heating-enhanced gene therapy. *Biomaterials* 274, 120885. doi:10.1016/j.biomaterials.2021.120885
- Lv, M., Chen, M., Zhang, R., Zhang, W., Wang, C., Zhang, Y., et al. (2020). Manganese is critical for antitumor immune responses via cGAS-STING and improves the efficacy of clinical immunotherapy. *Cell Res.* 30 (11), 966–979. doi:10.1038/s41422-020-00395-4
- Lv, W., Cao, M., Liu, J., Hei, Y., and Bai, J. (2021). Tumor microenvironment-responsive nanozymes achieve photothermal-enhanced multiple catalysis against tumor hypoxia. *Acta Biomater.* 135, 617–627. doi:10.1016/j.actbio.2021.08.015
- Meng, X., Zhang, J., Sun, Z., Zhou, L., Deng, G., Li, S., et al. (2018). Hypoxia-triggered single-molecule probe for high-contrast NIR II/PA tumor imaging and robust photothermal therapy. *Theranostics* 8 (21), 6025–6034. doi:10.7150/thno.26607
- Nam, G. H., Lee, E. J., Kim, Y. K., Hong, Y., Choi, Y., Ryu, M. J., et al. (2018). Combined rho-kinase inhibition and immunogenic cell death triggers and propagates immunity against cancer. *Nat. Commun.* 9 (1), 2165. doi:10.1038/s41467-018-04607-9
- Nemani, N., Shanmughapriya, S., and Madesh, M. (2018). Molecular regulation of MCU: Implications in physiology and disease. *Cell Calcium* 74, 86–93. doi:10.1016/j.ceca.2018.06.006
- Park, J., Fan, Z., Kumon, R. E., El-Sayed, M. E., and Deng, C. X. (2010). Modulation of intracellular Ca<sup>2+</sup> concentration in brain microvascular endothelial cells *in vitro* by acoustic cavitation. *Ultrasound Med. Biol.* 36 (7), 1176–1187. doi:10.1016/j.ultrasmedbio.2010.04.006
- Parvizi, J., Pappas, V., Greenleaf, J. F., and Bolander, M. E. (2002). Calcium signaling is required for ultrasound-stimulated aggrecan synthesis by rat chondrocytes. *J. Orthop. Res.* 20 (1), 51–57. doi:10.1016/S0736-0266(01)00069-9
- Riera-Domingo, C., Audigé, A., Granja, S., Cheng, W. C., Ho, P. C., Baltazar, F., et al. (2020). Immunity, Hypoxia, and Metabolism—the Ménage à Trois of Cancer: Implications for Immunotherapy. *Physiol. Rev.* 100 (1), 1–102. doi:10.1152/physrev.00018.2019
- Rossi, A., Pizzo, P., and Filadi, R. (2019). Calcium, mitochondria and cell metabolism: A functional triangle in bioenergetics. *Biochimica Biophysica Acta - Mol. Cell Res.* 1866 (7), 1068–1078. doi:10.1016/j.bbamcr.2018.10.016
- Samal, A. B., Adzerikho, I. D., Mrochek, A. G., and Loiko, E. N. (2000). Platelet aggregation and change in intracellular Ca<sup>2+</sup> induced by low frequency ultrasound *in vitro*. *Eur. J. Ultrasound* 11 (1), 53–59. doi:10.1016/s0929-8266(99)00077-4

- Soerjomataram, I., and Bray, F. (2021). Planning for tomorrow: Global cancer incidence and the role of prevention 2020–2070. *Nat. Rev. Clin. Oncol.* 18 (10), 663–672. doi:10.1038/s41571-021-00514-z
- Sun, S., Sun, S., Sun, Y., Wang, P., Zhang, J., Du, W., et al. (2019). Bubble-manipulated local drug release from a smart thermosensitive cerasome for dual-mode imaging guided tumor chemo-photothermal therapy. *Theranostics* 9 (26), 8138–8154. doi:10.7150/thno.36762
- Sun, W., Yu, H., Wang, D., Li, Y., Tian, B., Zhu, S., et al. (2021). MnO<sub>2</sub> nanoflowers as a multifunctional nano-platform for enhanced photothermal/photodynamic therapy and MR imaging. *Biomater. Sci.* 9 (10), 3662–3674. doi:10.1039/d1bm00033k
- Wang, M., Zhou, B., Wang, L., Zhou, F., Smith, N., Saunders, D., et al. (2020). Biodegradable pH-responsive amorphous calcium carbonate nanoparticles as immunoadjuvants for multimodal imaging and enhanced photoimmunotherapy. *J. Mat. Chem. B* 8 (36), 8261–8270. doi:10.1039/d0tb01453b
- Wang, Y., Bi, K., Shu, J., Liu, X., Xu, J., and Deng, G. (2019). Ultrasound-controlled DOX-SiO<sub>2</sub> nanocomposites enhance the antitumor efficacy and attenuate the toxicity of doxorubicin. *Nanoscale* 11 (10), 4210–4218. doi:10.1039/c8nr08497a
- Wang, Z., Duan, Y., and Duan, Y. (2018). Application of polydopamine in tumor targeted drug delivery system and its drug release behavior. *J. Control. Release* 290, 56–74. doi:10.1016/j.jconrel.2018.10.009
- Wen, G., Li, X., Zhang, Y., Han, X., Xu, X., Liu, C., et al. (2020). Effective phototheranostics of brain tumor assisted by near-infrared-II light-responsive semiconducting polymer nanoparticles. *ACS Appl. Mat. Interfaces* 12 (30), 33492–33499. doi:10.1021/acsami.0c08562
- Wen, M., Ouyang, J., Wei, C., Li, H., Chen, W., and Liu, Y. N. (2019). Artificial enzyme catalyzed cascade reactions: Antitumor immunotherapy reinforced by NIR-II light. *Angew. Chem. Int. Ed.* 58 (48), 17425–17432. doi:10.1002/anie.201909729
- Weyergang, A., Cheung, L. H., Rosenblum, M. G., Mohamedali, K. A., Peng, Q., Waltenberger, J., et al. (2014). Photochemical internalization augments tumor vascular cytotoxicity and specificity of VEGF (121)/rGel fusion toxin. *J. Control. Release* 180, 1–9. doi:10.1016/j.jconrel.2014.02.003
- Yang, G., Xu, L., Chao, Y., Xu, J., Sun, X., Wu, Y., et al. (2017). Hollow MnO<sub>2</sub> as a tumor-microenvironment-responsive biodegradable nano-platform for combination therapy favoring antitumor immune responses. *Nat. Commun.* 8 (1), 902. doi:10.1038/s41467-017-01050-0
- Yasothamani, V., Karthikeyan, L., Shyamsivappan, S., Haldorai, Y., Seetha, D., and Vivek, R. (2021). Synergistic effect of photothermally targeted NIR-responsive nanomedicine-induced immunogenic cell death for effective triple negative breast cancer therapy. *Biomacromolecules* 22 (6), 2472–2490. doi:10.1021/acs.biomac.1c00244
- Yu, L., Hu, P., and Chen, Y. (2018). Gas-generating nanoplatfroms: Material Chemistry, multifunctionality, and gas therapy. *Adv. Mat.* 30 (49), e1801964. doi:10.1002/adma.201801964
- Zhang, F., Li, F., Lu, G. H., Nie, W., Zhang, L., Lv, Y., et al. (2019). Engineering magnetosomes for ferroptosis/immunomodulation synergism in cancer. *ACS Nano* 13 (5), 5662–5673. doi:10.1021/acsnano.9b00892
- Zhang, W. X., Hao, Y. N., Gao, Y. R., Shu, Y., and Wang, J. H. (2021). Mutual benefit between Cu (II) and polydopamine for improving photothermal-chemodynamic therapy. *ACS Appl. Mat. Interfaces* 13 (32), 38127–38137. doi:10.1021/acsami.1c12199
- Zhao, H., Zhang, G., Chong, S., Zhang, N., and Liu, Y. (2015). MnO<sub>2</sub>/CeO<sub>2</sub> for catalytic ultrasonic decolorization of methyl orange: Process parameters and mechanisms. *Ultrason. Sonochem.* 27, 474–479. doi:10.1016/j.ultsonch.2015.06.009
- Zheng, P., Ding, B., Jiang, Z., Xu, W., Li, G., Ding, J., et al. (2021). Ultrasound-augmented mitochondrial calcium ion overload by calcium nanomodulator to induce immunogenic cell death. *Nano Lett.* 21 (5), 2088–2093. doi:10.1021/acs.nanolett.0c04778
- Zhou, T., Liang, X., Wang, P., Hu, Y., Qi, Y., Jin, Y., et al. (2020). A hepatocellular carcinoma targeting nanostrategy with hypoxia-ameliorating and photothermal abilities that, combined with immunotherapy, inhibits metastasis and recurrence. *ACS Nano* 14 (10), 12679–12696. doi:10.1021/acsnano.0c01453





## OPEN ACCESS

EDITED BY  
Gabriella Cusella,  
University of Pavia, Italy

REVIEWED BY  
Bikesh Kumar Nirala,  
Baylor College of Medicine,  
United States  
Flavio Lorenzo Ronzoni,  
Humanitas University, Italy

\*CORRESPONDENCE  
Lieven Thorrez,  
lieven.thorrez@kuleuven.be

<sup>†</sup>These authors have contributed equally  
to this work and share first authorship

SPECIALTY SECTION  
This article was submitted to  
Biomaterials,  
a section of the journal  
Frontiers in Bioengineering and  
Biotechnology

RECEIVED 08 June 2022  
ACCEPTED 18 July 2022  
PUBLISHED 21 September 2022

CITATION  
Wüst R, Terrie L, Muntefering T, Ruck T  
and Thorrez L (2022), Efficient co-  
isolation of microvascular endothelial  
cells and satellite cell-derived myoblasts  
from human skeletal muscle.  
*Front. Bioeng. Biotechnol.* 10:964705.  
doi: 10.3389/fbioe.2022.964705

COPYRIGHT  
© 2022 Wüst, Terrie, Muntefering, Ruck  
and Thorrez. This is an open-access  
article distributed under the terms of the  
[Creative Commons Attribution License](https://creativecommons.org/licenses/by/4.0/)  
(CC BY). The use, distribution or  
reproduction in other forums is  
permitted, provided the original  
author(s) and the copyright owner(s) are  
credited and that the original  
publication in this journal is cited, in  
accordance with accepted academic  
practice. No use, distribution or  
reproduction is permitted which does  
not comply with these terms.

# Efficient co-isolation of microvascular endothelial cells and satellite cell-derived myoblasts from human skeletal muscle

Rebecca Wüst<sup>1†</sup>, Lisanne Terrie<sup>1†</sup>, Thomas Muntefering<sup>2</sup>,  
Tobias Ruck<sup>2</sup> and Lieven Thorrez<sup>1\*</sup>

<sup>1</sup>Tissue Engineering Lab, Dep. Development and Regeneration, KU Leuven Kulak, Kortrijk, Belgium  
<sup>2</sup>Department of Neurology, Medical Faculty, Heinrich-Heine-University, Düsseldorf, Germany

Vascularization of tissue-engineered constructs remains a key challenge in the field of skeletal muscle tissue engineering. One strategy for vascularizing organoids is *in vitro* pre-vascularization, relying on *de novo* assembly of undifferentiated endothelial cells into capillaries, a process termed vasculogenesis. In most endothelial cell research to date, human umbilical vein endothelial cells have been used primarily because of their availability. Nevertheless, this endothelial cell type is naturally not occurring in skeletal muscle tissue. Since endothelial cells display a tissue-specific phenotype, it is of interest to use muscle-specific microvascular endothelial cells to study pre-vascularization in skeletal muscle tissue engineering research. Thus far, tissue biopsies had to be processed in two separate protocols to obtain cells from the myogenic and the endothelial compartment. Here, we describe a novel, detailed protocol for the co-isolation of human skeletal muscle microvascular endothelial cells and satellite cell-derived myoblasts. It incorporates an automated mechanical and enzymatic tissue dissociation followed by magnetically activated cell sorting based on a combination of endothelial and skeletal muscle cell markers. Qualitative, quantitative, and functional characterization of the obtained cells is described and demonstrated by representative results. The simultaneous isolation of both cell types from the same donor is advantageous in terms of time efficiency. In addition, it may be the only possible method to isolate both cell types as the amount of tissue biopsy is often limited. The isolation of the two cell types is crucial for further studies to elucidate cell crosstalk in health and disease. Furthermore, the use of muscle-specific microvascular endothelial cells allows a shift towards engineering more physiologically relevant functional tissue, with downstream applications including drug screening and regenerative medicine.

## KEYWORDS

cell isolation, microvascular endothelial cells, myoblasts, co-isolation, human, skeletal muscle

# 1 Introduction

In native skeletal muscle, vascular supply is provided by a highly organized extensive capillary network throughout the fibers to meet the high metabolic demands. The fundamental role of the microvascular network is to deliver oxygen and nutrients throughout the tissue. To vascularize engineered muscle, two core vascularization strategies are being explored. The first approach involves *in vivo* angiogenesis, which exploits the ingrowth of host vessels coming from sprouting endothelial cells (ECs) from pre-existing vessels. However, the rate of spontaneous ingrowth through angiogenesis is slow (approximately 5  $\mu\text{m}/\text{h}$ ) (Orr et al., 2003), which may limit the thickness of the tissue that can be transplanted. Since passive diffusion of metabolic products and gases is also limited, necrosis may occur before sprouts from the host blood vessels can reach the inner core. To overcome this, another strategy focuses on *in vitro* pre-vascularization through *de novo* blood vessel formation. This so-called vasculogenesis strategy uses ECs that coat the inner wall of vascular networks (Gholobova et al., 2020). The majority of research carried out to date, involving endothelial cells, uses human umbilical vein endothelial cells (HUVECs) (Wang et al., 2019). HUVECs are known to be robust and can be obtained from discarded umbilical cord tissue which is abundant. Also, their commercial availability is widespread and researchers can rely on years of accumulated knowledge (Hauseret al., 2017). HUVECs have the capacity to assemble into a capillary network within a 3-dimensional (3D) hydrogel, which was first described by Schechner et al. (2000), and afterwards extensively studied by others in the tissue engineering field. Indeed, also in muscle tissue engineering research, we have used HUVECs to study *in vitro* pre-vascularization thus far (Gholobova et al., 2015; Gholobova et al., 2019).

However, ECs are not only creating a passive conduit for blood delivery. Increasing insights in crosstalk between tissue-specific cell types (Rafii et al., 2016) and the growing evidence for the endothelium as a regulator of regenerative processes in an organ/tissue-specific manner (Rafii et al., 2016) promote the use of tissue-specific cells. These complex tasks are regulated by capillary EC-derived paracrine factors, which create an instructive organ-specific niche for repopulating stem and progenitor cells (Verma et al., 2018). In fact, satellite cells that express Pax7 and Myf5 were found to be positioned near ECs (Chiristov et al., 2007). In addition, the same study established that ECs specifically enhance satellite cell growth, while differentiating myogenic cells were found to be proangiogenic.

Thus, skeletal muscle microvascular endothelial cells (SkMVECs), which are naturally occurring in skeletal muscle, are of high interest for engineering pre-vascularized skeletal muscle. To date, only a few papers have been published on the isolation of SkMVECs. Chen et al. (1995) described a method for isolating primary rat SkMVECs avoiding enzymatic and mechanical

isolation by outgrowth of the cells from tissue pieces within 60 h. Since fibroblasts and other cells are described to grow out of the muscle pieces only after 72 h, this would result in a pure population of SkMVECs. However, no clear numbers in terms of cell purity nor cell yield were given. Another protocol, focusing on murine skeletal muscle tissue, described an approach using fluorescence-activated cell sorting (FACS) to isolate Sca1<sup>+</sup>, CD31<sup>+</sup>, CD34<sup>dim</sup> and CD45<sup>-</sup> cells (Ieronimakis et al., 2008). In this protocol, the capacity of the isolated cells to take up acetylated low-density lipoprotein, to produce nitric oxide, and to form vascular tubes was described even after several passages in culture. However, in our specific case, magnetic-activated cell sorting (MACS) offered advantages compared to FACS such as a lower device cost, higher throughput and faster processing time (Tomlinson et al., 2013; Sutermaster and Darling 2019; Pan and Wan 2020). The most recent work on the isolation of primary murine SkMVECs was published by Müntefering et al. (2019). There, a protocol was established yielding CD31-positive murine SkMVECs with a purity of up to 95% using MACS (Müntefering et al., 2019). Taken together, only a few protocols have been published describing the isolation of primary SkMVECs and none of those has been applied to human tissue. Moreover, for co-culturing approaches in skeletal muscle tissue engineering, a protocol on the combined isolation of both primary myoblasts and primary SkMVECs from the same biopsy is not existing. Therefore, originally based on the protocol of Müntefering et al. (2019), we developed a protocol for the co-isolation of SkMVECs and satellite cell-derived myoblasts from the same human skeletal muscle tissue biopsy.

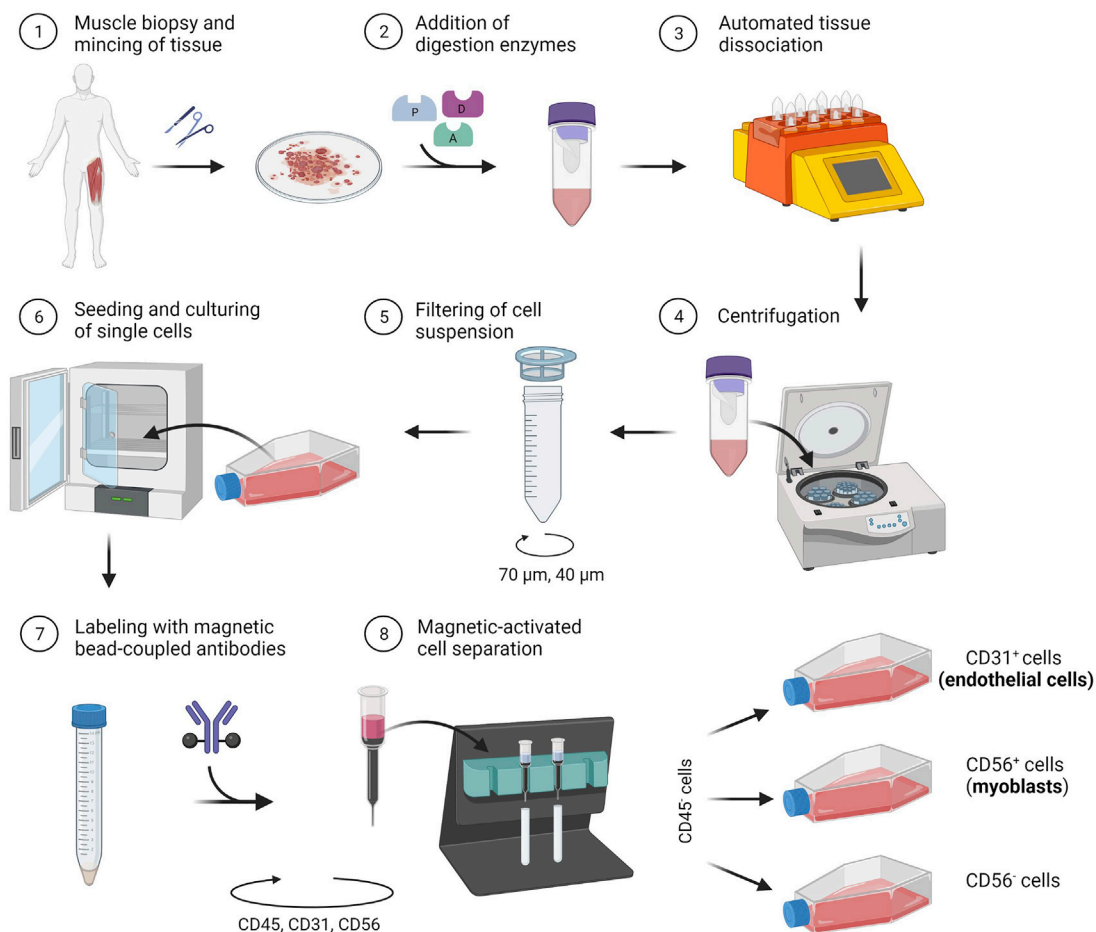
# 2 Materials and methods

In the following section, we describe a detailed protocol for the co-isolation and characterization of SkMVECs and satellite cell-derived myoblasts from human skeletal muscle tissue. Fresh human muscle biopsies were obtained from the Human Body Donation Program of KU Leuven, at campus KULAK, Belgium (ethical approval number: NH019-2020-04-02). A schematic overview of the protocol is represented in Figure 1 (created with BioRender.com). The magnetic-activated cell sorting strategy for the co-isolation of endothelial cells and myoblasts is displayed in more detail in Figure 2. Lastly, a detailed list of used materials and reagents can be found in Table 1.

## 2.1 Buffer and media compositions

### 2.1.1 Ammonium-Chloride-Potassium lysing buffer

- 150 mM NH<sub>4</sub>Cl
- 10 mM KHCO<sub>3</sub>
- 0.1 mM EDTA
- Filter sterilize (0.22  $\mu\text{m}$  filter).

**FIGURE 1**

Schematic representation of the developed protocol for the co-isolation of microvascular endothelial cells (CD31<sup>+</sup>) and satellite cell-derived myoblasts (CD56<sup>+</sup>) from human skeletal muscle tissue.

### 2.1.2 Blocking buffer

PBS supplemented with:

- 1% (w/v%) BSA
- 0.2% Triton X-100

### 2.1.3 Cell sorting buffer

- 90% PBS
- 10% FBS

→ Filter sterilize (0.22 µm filter).

### 2.1.4 Skeletal muscle growth medium

DMEM Glutamax supplemented with:

- 10% FBS
- 1% Ultrosor G serum substitute
- 0.1% gentamicin

→ Filter sterilize (0.22 µm filter).

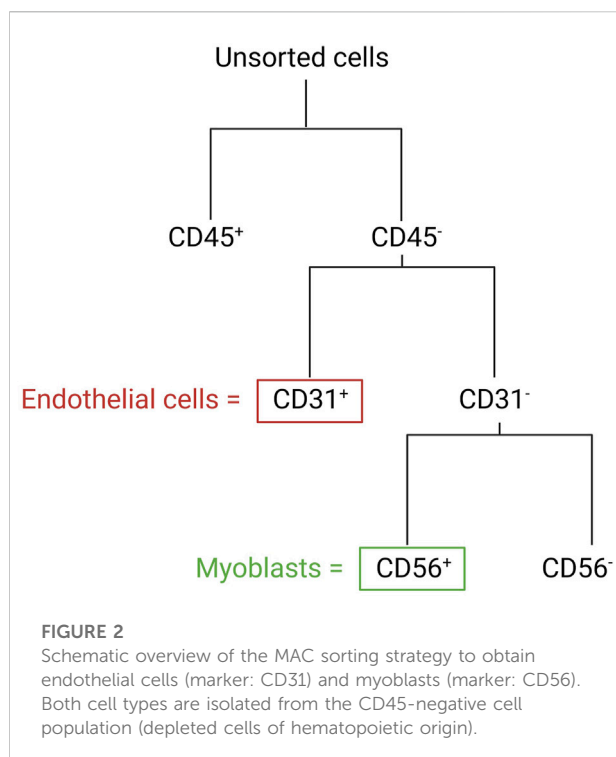
### 2.1.5 Skeletal muscle fusion medium

DMEM Glutamax supplemented with:

- 10 ng/ml hEGF
  - 10 µg/ml insulin
  - 50 µg/ml BSA
  - 50 µg/ml gentamicin
- Filter sterilize (0.22 µm filter).

## 3 Harvest of skeletal muscle tissue

1. Disinfect the area of dissection with 70% ethanol.
2. Make a small longitudinal incision using sterile forceps.
3. Dissect at least 1 g of skeletal muscle tissue (recommended: vastus lateralis muscle).
4. Sterilize the muscle tissue by holding it for 3 s in 70% ethanol.



5. Wash the tissue 3 times for 5 min with PBS.
6. Place the tissue in DMEM+1% P/S until tissue digestion.

## 4 Automated enzymatic and mechanical tissue digestion using gentleMACS™ Octo Dissociator with Heaters

1. Cut the tissue into small pieces (2–4 mm) using sterile scissors and scalpel blades.
2. Prepare the enzyme mix from Miltenyi Biotec skeletal muscle dissociation kit.

Preparation for 1 g muscle tissue:

- 200 µl of Enzyme D
- 50 µl of Enzyme P
- 36 µl of Enzyme A

Mix all three enzymes in 4.70 ml of DMEM (pre-warmed at 37°C).

3. Transfer muscle pieces with a sterile spatula into a gentleMACS™ C Tube containing the enzyme mix and close tube tightly.
4. Place the C Tube upside down onto the gentleMACS™ device and add the heater.

5. Run the program 37C\_mr\_SMDK\_1 on the gentleMACS™ Octo Dissociator with Heaters.

## 5 Seeding of isolated (unsorted) cell population

1. Coat a T75 cell culture flask by incubating with 6 ml of Ultrapure water with 0.1% gelatin for 30 min at room temperature (RT).
2. Remove the coating solution from the cell culture flask.
3. Add 14 ml of EGM-MV medium and store the flask in the incubator (37°C, 5% CO<sub>2</sub>).
4. Perform a short centrifugation step of the gentleMACS™ C Tube to collect the single cell suspension at the tube bottom.
5. Resuspend the cells and apply the suspension to a 70 µm cell strainer.  
Note: Moisturize the cell strainer upfront with 1–2 ml of DMEM.
6. Wash the cell strainer with 10 ml of DMEM.
7. Discard the cell strainer and centrifuge the cell suspension for 20 min at 300 × g.
8. Aspirate the supernatant carefully.
9. Resuspend the cell pellet in 1 ml DMEM+10% FBS.
10. Apply the cell suspension to a 40 µm cell strainer.  
Note: Moisturize the cell strainer upfront with 1–2 ml of DMEM.
11. Wash the cell strainer with 10 ml of DMEM.
12. Centrifuge the cell suspension for 10 min at 300 × g.
13. Resuspend the cell pellet in 1 ml Ammonium-Chloride-Potassium (ACK) lysing buffer (see Section 2.1) for 30 s at RT to lyse erythrocytes.
14. Inactivate the reaction by adding 9 ml DMEM+10% FBS.
15. Perform a centrifugation step for 10 min at 300 × g.
16. Discard the supernatant and resuspend the cell pellet in 1 ml EGM-MV medium.
17. Seed the cells in 15 ml EGM-MV medium in the coated T75 culture flask.
18. Refresh the EGM-MV medium every second day until cells reach approximately 80% confluency.

## 6 Magnetic-activated cell sorting of isolated cells

At a cell confluency of approximately 80%, detach the cells with 5 ml 0.125% Trypsin-EDTA for 3 min at 37°C, followed by inactivation with 15 ml DMEM+10% FBS. Centrifuge the cell suspension for 10 min at 300 × g, resuspend the cells in EGM-MV medium and determine the cell number using an automated cell counter.

Note: Alternatively, determine the cell number using a Burkert cell counting chamber.



TABLE 1 Materials and reagents.

**Materials**

Cell strainers, 40-µm	(VWR Corning, catalog number: 734-2760)
Cell strainers, 70-µm	(VWR Corning, catalog number: 734-2761)
GentleMACS™ C Tubes	(Miltenyi Biotec, catalog number: 130-093-237)
Large magnetic columns	(Miltenyi Biotec, catalog number: 130-042-401)
MACS® MultiStand	(Miltenyi Biotec, catalog number: 130-042-303)
Medium magnetic columns	(Miltenyi Biotec, catalog number: 130-042-201)
MidiMACS™ Separator	(Miltenyi Biotec, catalog number: 130-042-302)
MiniMACS™ Separator	(Miltenyi Biotec, catalog number: 130-042-102)

**Reagents**

Aprotinin	(Carl Roth, catalog number: A1624)
Bovine serum albumin (BSA)	(Sigma-Aldrich, catalog number: A2153)
CD31 MicroBeads, human	(Miltenyi Biotec, catalog number: 130-091-935)
CD45 MicroBeads, human	(Miltenyi Biotec, catalog number: 130-045-801)
CD56 MicroBeads, human	(Miltenyi Biotec, catalog number: 130-055-401)
Calcein AM	(Hello Bio, catalog number: HB0720)
Collagenase II	(Worthington Biochemical Corp., catalog number: LS004176)
DAPI	(Thermo Fisher, catalog number: D1306)
Dispase II	(Roche Diagnostics, catalog number: 4942078001)
Dulbecco's Modified Eagle Medium (DMEM)	(Biowest, catalog number: L0103-500mL)
EDTA	(Sigma-Aldrich, catalog number: 2854)
EGF human	(Peprotech, catalog number: AF-100-15)
EGM-MV™	(Lonza, catalog number: CC-4147)
Fetal Bovine Serum (FBS)	(Biowest, catalog number: SS 1810-500)
Fibrinogen	(Merck, catalog number: 341576)
Gentamicin	(Gibco, catalog number: 15750037)
Growth factor reduced Matrigel	(BD Biosciences, catalog number: 354230)
Insulin	(Sigma-Aldrich, catalog number: I9278-5ML)
KHCO <sub>3</sub>	(Sigma-Aldrich, catalog number: 1.04854)
Methylcellulose	(Carl Roth, catalog number: 8421.1)
NH <sub>4</sub> Cl	(Sigma-Aldrich, catalog number: 12125-02-9)
Phosphate Buffered Saline (PBS)	(Invitrogen, catalog number: 10010023)
Skeletal muscle dissociation kit	(Miltenyi Biotec, catalog number: 130-098-305)
Thrombin	(Stago, catalog number: HT1002a)
Tranexamic acid	(Sigma-Aldrich, catalog number: 857653)
Triton X-100 (10% in water)	(Sigma-Aldrich, catalog number: 93443)
Trypan Blue	(Fisher Scientific, catalog number: 15-250-061)
Trypsin/EDTA	(Invitrogen, catalog number: 15090046)
Tween-20	(Acros, catalog number: 233360010)
Ultrapure water with 0.1% gelatin	(Millipore, EmbryoMax, catalog number: ES 006B)
Ultrosor G serum substitute	(Sartorius, catalog number: 15950-017)

**Antibodies**

Alexa Fluor 488 goat anti-mouse	(Invitrogen, catalog number: A-11029)
Alexa Fluor 633 goat anti-rabbit	(Invitrogen, catalog number: A21070)
Anti-(human) CD31/PECAM-1 antibody	(Santa Cruz, catalog number: sc-376764)
Anti-(human) desmin antibody	(Invitrogen, catalog number: D1033)
Anti-(human) phalloidin-iFluor 488	(Abcam, catalog number: ab176753)
Anti-(human) tropomyosin antibody	(Invitrogen, catalog number: T9283)
Anti-(human) vWF antibody	(Dako, catalog number: A0082)
APC anti-human CD31 antibody	(Thermo Fisher, catalog number: 17-0319-42)
APC anti-human CD56 antibody	(Thermo Fisher, catalog number: A15704)

## 6.1 Depletion of CD45<sup>+</sup> cells

(Adapted from Miltenyi Biotec protocol)

1. Resuspend the cell pellet (up to 10<sup>7</sup> cells) in 80 µl cell sorting buffer (see [Section 2.1](#)).
2. Add 20 µl of anti-human CD45 MicroBeads and incubate for 15 min at 4°C.
3. Add 1–2 ml of cell sorting buffer to wash the cells.
4. Centrifuge the suspension for 10 min at 300 × g.
5. Discard the supernatant and resuspend the cell pellet in 500 µl cell sorting buffer.
6. Place an LS magnetic column onto a MACS™ separator using a magnet of respective size.
7. Moisturize the magnetic column with 3 ml of cell sorting buffer.
8. Apply 500 µl of the labeled cell suspension onto the column and let it completely run through the column.
9. Wash the magnetic column three times with 3 ml cell sorting buffer.
10. Centrifuge the collected flow-through for 10 min at 300 × g and continue with [Section 6.2](#).

Note: The column with CD45<sup>+</sup> cells can be discarded.

## 6.2 Enrichment of CD31<sup>+</sup> cells (microvascular endothelial cells)

(Adapted from Miltenyi Biotec protocol)

1. Coat a T25 culture flask by adding 2 ml Ultrapure water with 0.1% gelatin for 30 min at RT.
2. Remove the coating solution from the cell culture flask.
3. Add 5 ml of EGM-MV medium and store the flask in the incubator (37°C, 5% CO<sub>2</sub>).
4. Resuspend the CD45<sup>+</sup> cell pellet (obtained in [Section 6.1](#)) (up to 10<sup>7</sup> cells) in 80 µl cell sorting buffer.
5. Add 20 µl of anti-human CD31 MicroBeads and incubate for 15 min at 4°C.
6. Add 1–2 ml of cell sorting buffer to wash the cells.
7. Centrifuge the cell suspension for 10 min at 300 × g.
8. Discard the supernatant and resuspend the cell pellet in 500 µl cell sorting buffer.
9. Place an MS magnetic column onto a MACS™ separator using a magnet of respective size.
10. Moisturize the magnetic column with 500 µl cell sorting buffer.
11. Apply 500 µl of the labeled cell suspension onto the column and let it completely run through the column.
12. Wash the column three times with 500 µl cell sorting buffer.
13. Centrifuge the collected flow-through for 10 min at 300 × g and keep on ice until continuing with [Section 6.3](#).

Note: This cell fraction represents the CD31<sup>+</sup> cells, which will be used for the subsequent sorting step for CD56 (see [Section 6.3](#)).

14. Place the MS column containing accumulating CD31<sup>+</sup> cells onto a 15 ml-falcon tube.
15. Apply 1 ml cell sorting buffer onto the column and collect magnetically labeled CD31<sup>+</sup> cells by rapidly pushing the plunger into the column.
16. Centrifuge the CD31<sup>+</sup> cell suspension for 10 min at 300 × g.
17. Resuspend the cell pellet in 1 ml EGM-MV medium and seed the cells in the coated T25 culture flask.

Note: To increase the yield of CD31<sup>+</sup> cells, we recommend repeating [Section 6.2](#) as a purification step of isolated microvascular ECs once cells have reached approximately 80% confluency. Post a second MAC sorting, culture cells until approximately 80% confluency and subsequently proceed with [Section 7](#).

## 6.3 Enrichment of CD56<sup>+</sup> cells (myoblasts)

(Adapted from Miltenyi Biotec protocol)

1. Coat a T175 culture flask by adding 15 ml Ultrapure water with 0.1% gelatin for 30 min at RT.
2. Remove the coating solution from the cell culture flask.
3. Add 30 ml of Skeletal Muscle Growth Medium (SkGM, see [Section 2.1](#)) and store the flask in the incubator (37°C, 5% CO<sub>2</sub>).
4. Resuspend the cell pellet (up to 10<sup>7</sup> cells) from [Section 6.2](#) in 80 µl cell sorting buffer.
5. Add 20 µl of anti-human CD56 MicroBeads and incubate for 15 min at 4°C.
6. Add 1–2 ml of cell sorting buffer to wash the cells.
7. Centrifuge the suspension for 10 min at 300 × g.
8. Discard the supernatant and resuspend the cell pellet in 500 µl cell sorting buffer.
9. Place an LS magnetic column onto a MACS™ separator using a magnet of respective size.
10. Moisturize the magnetic column with 3 ml cell sorting buffer.
11. Apply 500 µl of the labeled cell suspension onto the column and let it completely run through the column.
12. Wash the column three times with 3 ml cell sorting buffer.
13. Store the collected flow-through on ice until CD56<sup>+</sup> cells are collected.

Note: This cell fraction represents the CD56<sup>+</sup> cells.

14. Place the LS column containing accumulating CD56<sup>+</sup> cells onto a 15 ml-falcon tube.
15. Apply 5 ml of cell sorting buffer onto the column and collect magnetically labeled CD56<sup>+</sup> cells by rapidly pushing the plunger into the column.
16. Centrifuge both cell suspensions (CD56<sup>+</sup> and CD56<sup>−</sup> separately) for 10 min at 300 × g.

17. Resuspend each cell pellet in 1 ml SkGM and seed the CD56<sup>+</sup> cells in the coated T175 culture flask.  
Note: For CD56<sup>-</sup> cells, no coating is required.
18. Refresh the culture medium every second day until cells reach approximately 80% confluency.
19. At a cell confluency of approximately 80%, harvest the cells and proceed with the characterization of the cells (Section 7).

## 7 Characterization of isolated endothelial cells and myoblasts

### 7.1 Immunofluorescence staining (qualitative)

For a qualitative characterization of isolated cells, perform an immunofluorescence staining. The following protocol describes the characterization of isolated ECs using the endothelial cell markers CD31 and von Willebrand factor (vWF). Isolated myoblasts are characterized by the expression of desmin.

1. Seed 5,000 cells per well in a 24-well plate.
  2. Culture cells until:
    - (i) ECs: 90%–100% confluency.
    - (ii) myoblasts: 50%–60% confluency.
  3. Rinse the cells 3 times for 5 min with PBS and fix:
    - (i) ECs: for 10 min with 4% paraformaldehyde at RT.
    - (ii) myoblasts: for 10 min with a 1:1 solution of acetone: methanol at −20°C.
  4. Wash the cells 3 times for 5 min with PBS.
  5. Incubate the cells for 1 h with blocking buffer (see Section 2.1) at RT.
  6. Incubate overnight at 4°C with the respective primary antibody:
    - (i) ECs: mouse anti-human CD31, rabbit anti-vWF (10 µg/ml in blocking buffer).
    - (ii) myoblasts: mouse anti-human desmin, (1:100 in blocking buffer).
- Note: Keep one well on blocking buffer as a negative control.
7. Wash the cells 3 times for 5 min with PBS.
  8. Incubate the cells for 30 min at RT with the respective secondary antibody:
    - (i) ECs: Alexa Fluor 488-labeled goat anti-mouse antibody, Alexa Fluor 488-labeled goat anti-rabbit antibody (1:200 in PBS).
    - (ii) myoblasts: Alexa Fluor 488-labeled goat anti-mouse antibody (1:200 in PBS).
  9. Wash the cells 3 times for 5 min with PBS.
  10. Incubate the cells for 30 min at RT with DAPI solution (1:10,000 in PBS).
  11. Replace the DAPI solution with PBS.
  12. Image the cells using a fluorescence microscope.

### 7.2 Flow cytometry analysis (quantitative)

For quantitative analysis of isolated cells, perform flow cytometry analysis. Isolated SkMVECs can be assessed according to the percentage of CD31<sup>+</sup> cells and isolated myoblasts according to the expression of CD56. The preparation for flow cytometry, including a recommended gating strategy (Figure 3), is described in the following.

1. Centrifuge cells (approximately  $2.0 \times 10^5$  cells per tube) for 5 min at 300 × g in three falcon tubes to prepare:
    - cells stained for the respective cell marker (here: CD31, CD56).
    - fluorescence-minus-one (FMO) control.
    - negative control of Calcein AM staining.
- Note: Calcein AM staining is applied for the gating for living cells.
2. Preparation of stained cells and FMO control for APC:
 

Resuspend each cell pellet in 100 µl cold PBS+10% FBS. Add 5 µl of APC-labeled anti-human CD56 (for myoblasts) or CD31 (for SkMVECs) antibody to the cells to be stained. No antibody is added to the FMO control tube. Incubate for 30 min at 4°C.
  3. Preparation of negative control for Calcein AM staining:
 

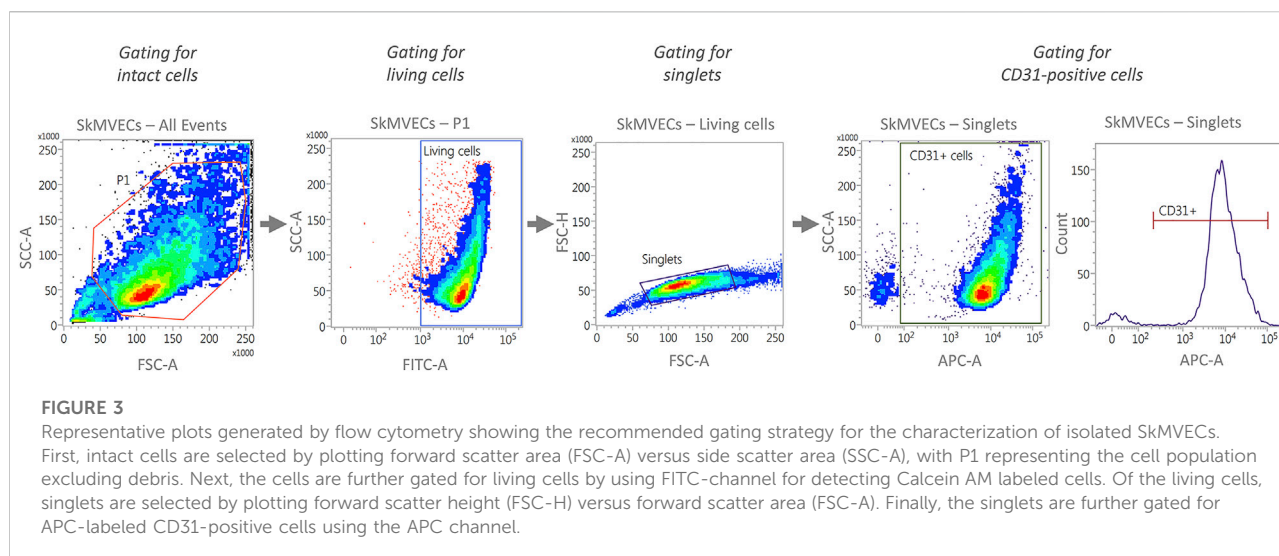
Resuspend the cell pellet in 1 ml PBS, transfer it to an Eppendorf tube, and incubate the cell suspension for 10 min at 65°C.
  4. Wash all three samples by adding 1 ml of cold PBS+10% FBS and centrifuge for 10 min at 300 × g.
  5. Resuspend each cell pellet in 1 ml of Calcein AM staining solution (0.1 µM in PBS).
  6. Incubate for 15–20 min at RT in the dark.
  7. Centrifuge the cells for 10 min at 300 × g.
  8. Resuspend each cell pellet in 200 µl of cold PBS+3% FBS and transfer to a FACS tube.
  9. Analyze cells with a flow cytometer using the recommended gating strategy as shown in Figure 3.

## 8 Functional characterization of isolated cells

### 8.1 Functional characterization of isolated endothelial cells

#### 8.1.1 Endothelial network formation on Matrigel (tube formation assay)

1. Thaw the required amount of growth factor reduced Matrigel in the fridge. Calculate for each well of a 48-well plate 150 µl. Once the Matrigel is liquid, store it on ice.
2. Place the 48-well plate and pipette tips in the fridge before the assay.



3. Add 150  $\mu$ l growth factor reduced Matrigel per well and place for 30 min in the incubator (37°C, 5% CO<sub>2</sub>).
4. Detach cells using 0.125% trypsin/EDTA and incubate for 3 min in the incubator (37°C, 5% CO<sub>2</sub>).
5. Inactivate trypsin with DMEM+10% FBS.
6. Centrifuge for 5 min at 200  $\times$  g and resuspend the cell pellet in EGM-MV medium.
7. Determine the cell number and pellet down the required number of cells: 45,000 cells per well of a 48-well plate.
8. Resuspend the cells in 250  $\mu$ l EGM-MV medium per well of a 48-well plate.
9. Seed the cells on solidified Matrigel and place them in the incubator (37°C, 5% CO<sub>2</sub>).  
Note: Tubes will start forming within 2 h post-seeding and can be visualized up to 12 h post-seeding. Cells should not be kept longer in culture than 24 h.
10. For fixation of the tubes, wash for 5 min with PBS and incubate with 4% paraformaldehyde for 10 min at RT. Wash 3 times with PBS.
6. Harvest the spheroids by gently washing the plastic dishes with PBS containing 10% FBS.
7. Transfer to a 50 ml tube and centrifuge first 5 min at 300  $\times$  g followed by 3 min at 500  $\times$  g at RT.
8. Aspirate the supernatants carefully.
9. Resuspend the spheroids gently in 1 ml of 2 mg/ml fibrinogen solution.
10. Add 4 U/ml thrombin and pipet 2 times up and down to mix.
11. Transfer into a 12-well plate rapidly.
12. Place the 12-well plate for 1 h at 37°C to allow the fibrin (1 mg/ml) hydrogel to solidify.
13. Add 1 ml EGM-MV medium containing tranexamic acid (final concentration 400  $\mu$ M) and aprotinin (final concentration 92.5  $\mu$ g/ml).
14. After 24 h, fix the spheroids for 30 min at RT with 4% paraformaldehyde.
15. Wash 2 times with PBS.
16. Permeabilize with PBS containing 1% Tween20 for 10 min.
17. Stain for 1 h at RT with phalloidin (1:250 in PBS) and DAPI (1:10,000 in PBS).
18. Wash 3 times with PBS.
19. Image using fluorescence microscopy.

### 8.1.2 Endothelial sprouting formation in fibrin hydrogel (spheroid-based sprouting assay)

1. Detach cells using 0.125% trypsin/EDTA and incubate for 3 min in the incubator (37°C, 5% CO<sub>2</sub>).
2. Determine the cell number and pellet down the required number of cells.
3. Resuspend 100,000 ECs in EGM-MV medium containing 20% methylcellulose.
4. Transfer to a multichannel pipette reservoir and pipet spheroids of 25  $\mu$ l each on non-adherent plastic dishes to generate spheroids containing each 1,000 cells.
5. Turn the plate upside down and culture at 37°C and 5% CO<sub>2</sub> overnight.

## 8.2 Functional characterization of isolated myoblasts

### 8.2.1 Myotube formation in a 24-well plate (fusion assay)

(Adapted from protocol described in [Gholobova et al. \(2019\)\)](#).

1. Seed 50,000 cells per well in a 24-well plate.
2. Continue to expand the cells, refresh SkGM every 2 days until cells reach 90%–100% confluency.



3. Change the medium to Skeletal Muscle Fusion medium (SkFM, see [Section 2.1](#)) for 4 days.
4. Refresh the medium every second day.
5. After 7 days, fix the cells with 4% paraformaldehyde for 10 min at RT.
6. Rinse the cells 3 times for 5 min with PBS.
7. Fix the cells with ice-cold methanol for 10 min at  $-20^{\circ}\text{C}$ .
8. Rinse the cells 3 times for 5 min with PBS.
9. Incubate the cells for 1 h with blocking buffer at RT.
10. Incubate overnight at  $4^{\circ}\text{C}$  with a primary mouse anti-human sarcomeric tropomyosin antibody (1:100 in blocking buffer).
11. Rinse the cells 3 times for 5 min with PBS.
12. Incubate with Alexa Fluor 488-labeled goat anti-mouse antibody (1:200 in blocking buffer) for 1 h at RT.
13. Rinse the cells 3 times for 5 min with PBS.
14. Incubate for 30 min at RT with DAPI solution (1:10,000 in PBS).
15. Image DAPI-stained nuclei and tropomyosin-positive myotubes using fluorescence microscopy.

## 9 Lentiviral vector transduction of isolated skeletal muscle microvascular endothelial cells

1. Seed SkMVECs in a T25 (approximately 200,000 cells) and let cells proliferate until 80% cell confluency. Refresh EGM-MV medium every second day.
2. Remove the medium and add 50  $\mu\text{l}$  of lentiviral vector ( $5.2 \times 10^8$  pg p24/ml) in 2 ml of EGM-MV medium to the cells. Viral vector: pCH-EF1a-eGFP-Ires-Puro  
Note: Retroviral vectors were produced by the Leuven Viral Vector Core as described in [Ibrahimi et al. \(2009\)](#). The transfer plasmid used encoded eGFP IRES Puromycin resistance cassette driven by the human elongation factor 1 alpha promoter (EF1a) (pCH-EF1a-eGFP-Ires-Puro). The integrity of all plasmids was verified by digestion and DNA sequencing prior to vector production. Titer (measured by quantifying p24 enzyme linked immunosorbent assay (ELISA) (HIV-1 core profile ELISA, DuPont)) and transducing units following transduction of 293T cells:  $5.2 \times 10^8$  pg p24/ml– $2.1 \times 10^9$  TU/ml.
3. Allow viral vector to transduce cells for 24 h at  $37^{\circ}\text{C}$ , 5%  $\text{CO}_2$ .
4. Remove EGM-MV medium supplemented with viral vector and perform a selection of the transduced cells by incubating cells for 48 h in EGM-MV medium supplemented with 2  $\mu\text{g/ml}$  puromycin.
5. Use selected cells for subsequent experiments or cryo-preserve in liquid nitrogen.

## 10 Alternatives

If for the application of this protocol specific products or devices of Miltenyi Biotec are not available, following alternatives may be applied:

### 10.1 Magnetic-activated cell sorting buffer

As an alternative to using MACS buffer, PBS+10% FBS can be used for the cell sorting steps. In addition, for the final sorting steps before seeding the cells in culture plates, the respective medium for the cell type of interest can be used for this sorting step.

### 10.2 Magnetic-activated cell sorting enzymes

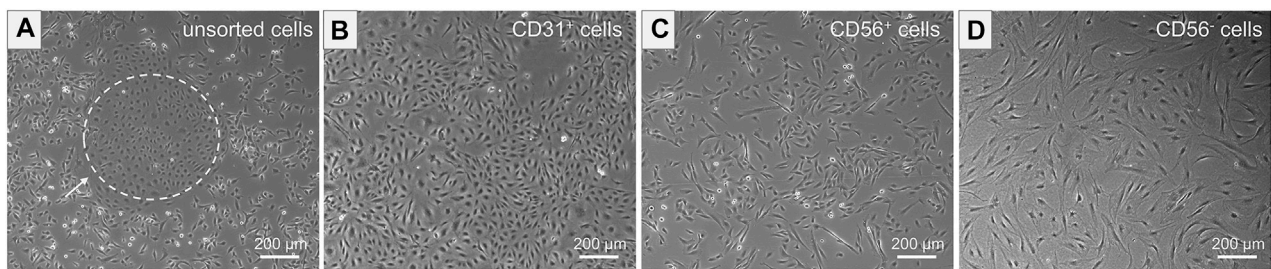
As an alternative for the enzymes A, D and P which come along with the skeletal muscle dissociation kit of Miltenyi Biotec, a combination of the two enzymes Collagenase II (1.5 mg/ml) and Dispase II (4 mg/ml) can be used for the tissue dissociation step using gentleMACS™ Octo Dissociator with Heaters.

### 10.3 GentleMACS™ Dissociator

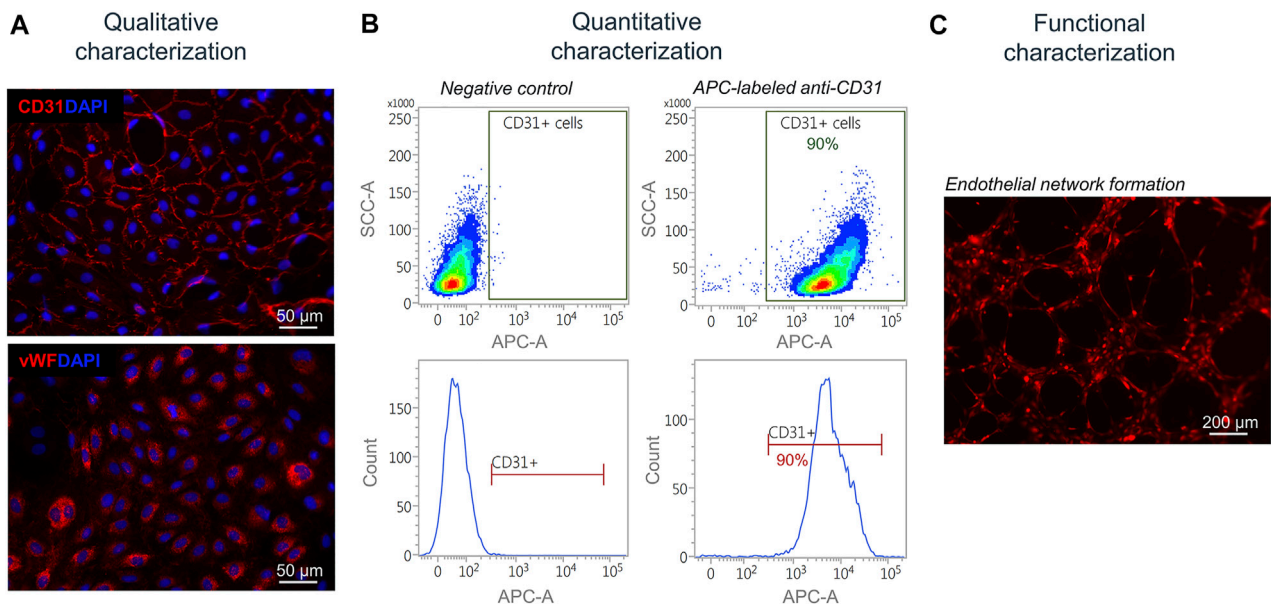
If the gentleMACS™ Dissociator (with or without heaters) is not available, we advise to use the manual dissociation procedure described in [Müntefering et al. \(2019\)](#) as an alternative. Briefly, the tissue pieces are resuspended in the dissociation enzyme solution and placed in the incubator ( $37^{\circ}\text{C}$ , 5%  $\text{CO}_2$ ) for 1.5 h. Every 20 min, the suspension is mixed using a 1 ml syringe.

## 11 Representative results

The unsorted cell population, obtained after tissue digestion, was cultured in a cell culture flask until a cell confluency of approximately 80% was reached. The distinct morphologies of isolated cells prior to MAC sorting observed in microscopic images of unsorted cells is shown in [Figure 4A](#). SkMVECs were found to grow in clusters between the surrounding cell types (marked with a white dashed circle, [Figure 4A](#)). Post MAC sorting, the separated cell types, SkMVECs, myoblasts, and the remaining  $\text{CD}56^{-}$  cell fraction (primarily fibroblasts and pericytes) were subsequently cultured in different cell culture flasks in their respective culture medium. The label of the cells indicates the

**FIGURE 4**

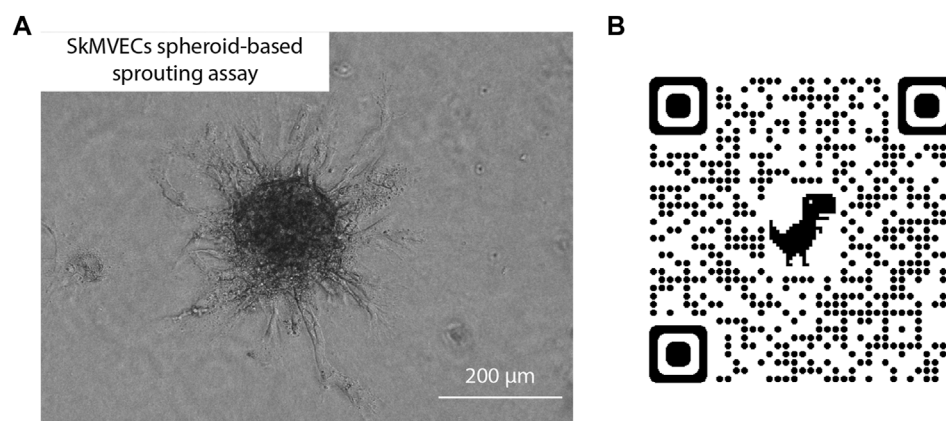
Morphology of isolated cells. Microscopic images represent the morphology of the different isolated cell types. **(A)** Unsorted cells containing multiple cell types of distinct morphologies. Dashed white circle indicates SkMVECs. **(B)** Isolated CD31<sup>+</sup> cells, SkMVECs, displaying a typical round, cobblestone-shaped morphology. **(C)** Isolated CD56<sup>+</sup> cells, satellite cell-derived myoblasts, appearing as more elongated, oval-shaped cells. **(D)** Remaining CD56<sup>-</sup> cells, including fibroblasts and pericytes, displaying a larger cell size and irregular shape, partially with protrusions.

**FIGURE 5**

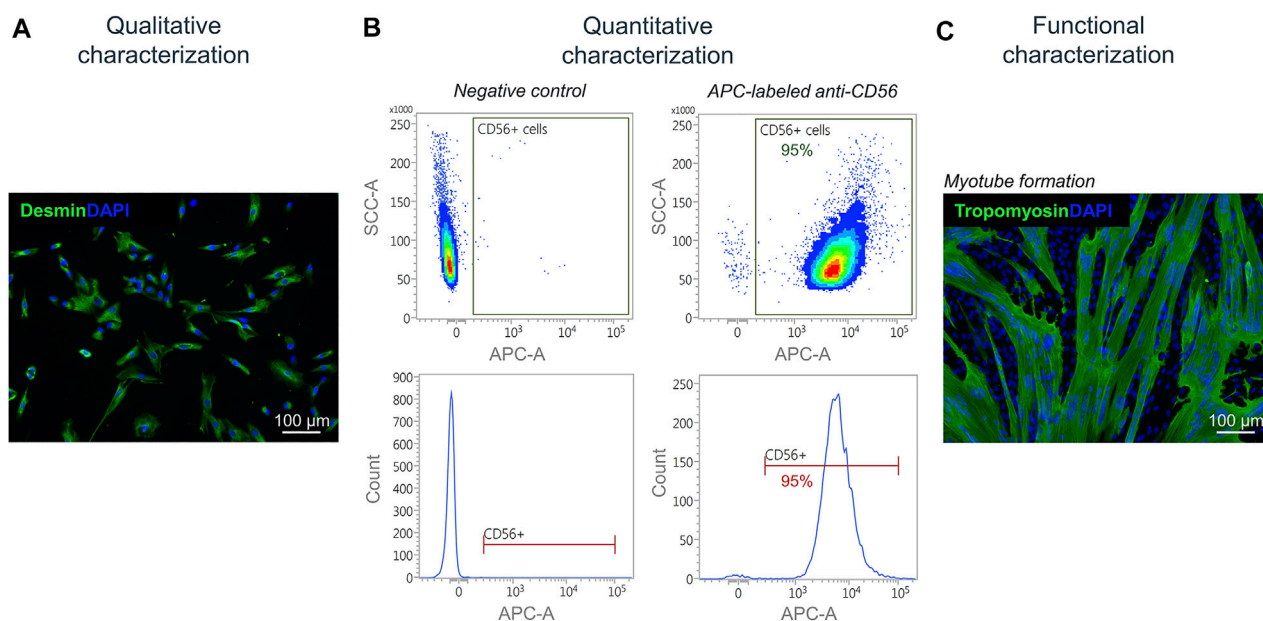
Characterization of isolated SkMVECs. **(A)** Immunofluorescence staining of isolated SkMVECs for the endothelial cell markers CD31 (pseudo-color red) and vWF (pseudo-color red). Nuclei are DAPI-stained (blue) **(B)** Quantitative characterization by flow cytometry for CD31. **(C)** Tube formation assay of GFP-labeled isolated SkMVECs on growth factor reduced Matrigel imaged after 4 h showing endothelial networks formed *in vitro* (pseudo-color red).

marker that was used for MAC sorting: microvascular ECs are indicated as CD31-positive (CD31<sup>+</sup>), myoblasts as CD56-positive (CD56<sup>+</sup>), and the remaining CD31-negative and CD56-negative (short: CD56<sup>-</sup>) cell fraction containing cells such as fibroblasts and pericytes. Isolated SkMVECs can be recognized by their cobblestone shape as demonstrated in Figure 4B. Isolated satellite cell-derived myoblasts display a typical spindle-shaped morphology (Figure 4C). Lastly, the remaining CD56<sup>-</sup> cells appear as larger, irregularly shaped cells, partially displaying protrusions (Figure 4D).

Next, isolated and separated cells were characterized qualitatively, quantitatively, and functionally. Isolated SkMVECs were fixed and qualitatively characterized by immunofluorescence staining for the two endothelial cell markers CD31 and vWF (Figure 5A). For a quantitative characterization, the number of CD31<sup>+</sup> cells was determined by flow cytometry using an APC-labeled antibody against human CD31. Results showed a purity of about 90% of isolated SkMVECs after a second MAC sorting (Figure 5B). By performing a tube formation assay, it was

**FIGURE 6**

(A) Light microscopic image of human SkMVECs spheroid-based sprouting assay in a fibrin hydrogel analyzed after 24 h. (B) QR-code linked to 3D visualization of spheroid-based sprouting assay captured with confocal microscopy.

**FIGURE 7**

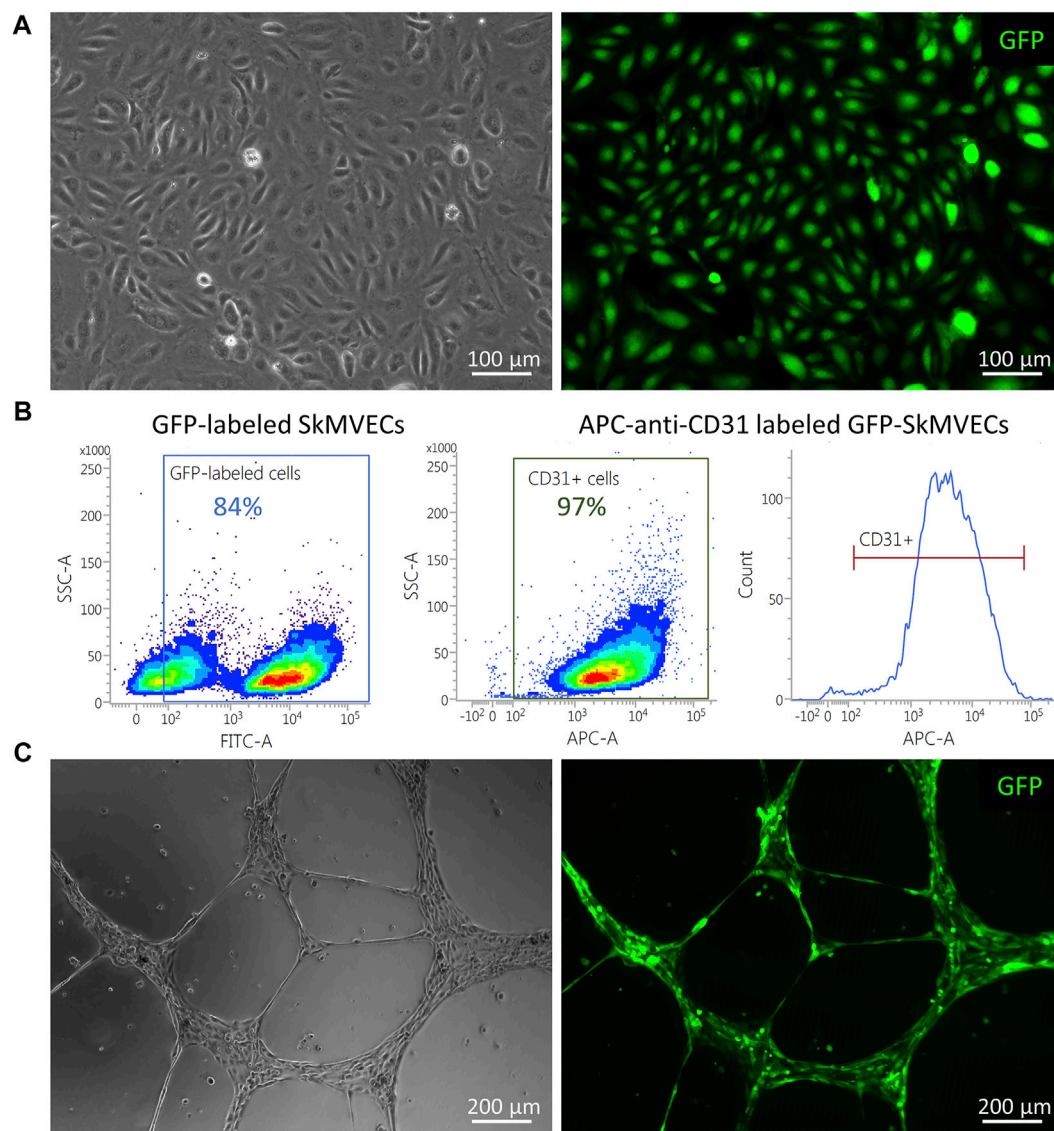
Characterization of isolated myoblasts. (A) Immunofluorescence staining of isolated satellite cell-derived myoblasts for the muscle cell marker desmin (green). Nuclei are DAPI-stained (blue). (B) Quantitative characterization by flow cytometry for CD56. (C) Fusion assay of isolated satellite cell-derived myoblasts showing the formation of multinucleated (DAPI-stained, blue) tropomyosin-positive myotubes (green) after 7 days of culturing *in vitro*.

demonstrated that isolated SkMVECs form endothelial networks *in vitro* (Figure 5C).

In addition, a spheroid-based sprouting assay was performed. This assay is a widely used *in vitro* angiogenesis assay that allows the evaluation of the sprout formation capacity of the isolated endothelial cells. Similar to the tube formation assay, this

sprouting assay can be used to quantify and evaluate angiogenesis *in vitro*. The advantage of the sprouting assay over the tube formation assay is the 3D culture technique which better reflects the *in vivo* angiogenesis. Using this assay, the sprouting of the isolated SkMVECs was shown (Figure 6).



**FIGURE 8**

GFP-expressing SkMVECs. **(A)** Microscopic image of cobblestone-shaped isolated SkMVECs (left image) showing GFP expression post viral vector transduction (green, right image). **(B)** Flow cytometry analysis result showing out of 84% GFP-expressing cells, 97% are positive for the endothelial cell marker CD31. **(C)** Tube formation assay on growth factor reduced Matrigel showing formation of endothelial networks (left image) by isolated GFP-expressing SkMVECs (green, right image).

Isolated satellite cell-derived myoblasts were qualitatively characterized by immunofluorescence staining for the muscle-specific marker desmin (Figure 7A). For a quantitative characterization, flow cytometry was performed using an APC-labeled antibody against human CD56. Results showed a purity of cells of up to 95% post MAC sorting (Figure 7B). By performing a fusion assay, it was demonstrated that the isolated satellite cell-derived myoblasts fuse and form multinucleated myotubes *in vitro* (Figure 7C).

For the use of isolated SkMVECs to create vascularized 3D bioartificial tissue constructs, it can be advantageous to use fluorescent protein expressing cells, especially for multilineage tissue engineering which requires multi-staining to detect the different cell types. Therefore, we tested whether the isolated SkMVECs can successfully be transduced with a lentiviral vector encoding for green fluorescent protein (GFP). Immunofluorescent imaging demonstrated GFP-expression of transduced SkMVECs (Figure 8A). Flow cytometry analysis confirmed 84% GFP-expressing cells with a high purity of



97% CD31-expressing cells (Figure 8B). In addition, performing a tube formation assay verified that the endothelial network formation capacity of GFP-expressing SkMVECs was not affected by the lentiviral vector transduction (Figure 8C).

## 12 Discussion

The vascularization of tissue-engineered constructs remains a key challenge in the field of skeletal muscle tissue engineering. So far, HUVECs have been the predominantly used EC type for generating vascular networks within an engineered tissue. These cells are the best-characterized EC type and can easily be isolated from human umbilical cords, a non-invasive harvesting method. However, HUVECs are not a representative EC type for every application (Hauser et al., 2017). ECs are known to display a great heterogeneity (Garlanda and Dejana 1997) and show tissue- and organ-specific characteristics (Rafi et al., 2016). Both the expression profile and the functional responses have been reported to vary between ECs from different origins (Hauser et al., 2017). For example, Dib et al. (2012) compared the proteome profile of HUVECs to human microvascular pulmonary and dermal ECs, and reported a noticeable difference, reflecting different biological properties. Therefore, the use of skeletal muscle-specific microvascular endothelial cells (SkMVECs) may have great potential for improving *in vitro* pre-vascularization of engineered muscle. A limitation thus far has been the lack of a reliable protocol to isolate human SkMVECs. Engineering a vascular network within a tissue construct can be achieved by co-culturing ECs with myoblasts in a 3D co-culture setting. The endothelial cells have the capacity to self-assemble into a vascular network, a process called vasculogenesis. Considering the tissue-specificity of ECs, different groups have started investigating the interaction between endothelial cells and muscle satellite cells (Chiristov et al., 2007; Osaki et al., 2018; Verma et al., 2018). For studying this cross-talk and setting up a co-culture, it may be beneficial to obtain both cell types from the same biological origin. For this, we developed a protocol to co-isolate microvascular endothelial cells and myoblasts from human skeletal muscle tissue.

For the isolation of myoblasts from skeletal muscle tissue, several protocols exist for human tissue and tissues of another origin. In contrast, the number of protocols that can be found for the isolation of microvascular endothelial cells is limited. Focusing on microvascular endothelial cells from human tissues, protocols have been published for the isolation of, inter alia, dermal microvascular ECs (Mason et al., 2007), pulmonary microvascular ECs (Hewett and Murray 1993), brain microvascular ECs (Navone et al., 2013), or microvascular ECs from adipose tissue (Hewett et al.,

1993). However, no protocol has been described for the isolation of human skeletal muscle-derived microvascular ECs.

With this work, we not only demonstrate the successful isolation of SkMVECs, but also the simultaneous co-isolation of human satellite cell-derived myoblasts. Both isolated cell types were characterized by immunofluorescence staining for specific cell markers. SkMVECs were shown to be positive for CD31, the platelet endothelial cell adhesion molecule (PECAM-1), and for the von Willebrand factor (vWF). Isolated satellite cell-derived myoblasts were positive for desmin. These results were verified and quantified by performing flow cytometry, showing that approximately 95% of myoblasts were positive for CD56 and approximately 90% of isolated ECs positive for CD31 post a second sorting for CD31. This second CD31 MAC sorting step was performed as a purification step to achieve a higher yield of CD31<sup>+</sup> cells, since after the first sorting only around 70% of the cells were CD31<sup>+</sup> (data not shown). If the purity of isolated SkMVECs is lower than expected, an additional purification step (third MAC sorting) is recommended to be performed. After the dissociation of muscle tissue, the resulting single cell suspension may also contain leucocytes, erythrocytes, pericytes and fibroblasts, besides the two cell types of interest (SkMVECs and myoblasts) (Birbrair et al., 2013). Therefore, after one or even multiple rounds of MAC sorting, a minor fraction of these other cell types may still be present. In the first MAC sorting step in this protocol, cells of hematopoietic origin are removed by depleting CD45<sup>+</sup> cells. Since CD45 is not expressed on mature erythrocytes, these cells are removed before the sorting by an incubation step with an ACK lysing buffer. After the removal of these cells and the enrichment of the cells of interest by performing MAC sorting, the remaining CD56<sup>+</sup> cell fraction primarily represents fibroblasts and/or pericytes. For further application in vascularization research, it may be advantageous to maintain this cell fraction in culture. Indeed, fibroblasts and pericytes have been demonstrated to play important roles in the engineering of microvascular networks *in vitro*, as for example described in Levenberg et al. (2005).

In addition to the qualitative and quantitative characterization, the functional characteristics of the isolated cells, which are of interest for the engineering of vascularized tissue, were evaluated. Isolated SkMVECs were found to self-assemble and form vascular networks when seeded onto growth factor reduced Matrigel. Isolated satellite cell-derived myoblasts were demonstrated to fuse and form multinucleated myotubes. Performing an immunofluorescence staining demonstrated that the formed myotubes were positive for tropomyosin. Although this protocol was developed for human skeletal muscle, it may also be applied for the isolation of SkMVECs and co-isolation of satellite cell-derived myoblasts from skeletal muscle tissue from other species. Furthermore, the described protocol may be applicable to isolate microvascular ECs and surrounding tissue-specific cells of different tissue types by adapting the choice of respective cell-specific markers for MAC sorting.

To conclude, using the developed and in detail described protocol allows the efficient isolation of SkMVECs and satellite cell-derived myoblasts simultaneously from the same human skeletal muscle biopsy. Demonstrated by the functional characteristics, these cells will be of great interest for downstream applications in vascularization research, specifically in skeletal muscle tissue engineering, but also in other domains such as fundamental endothelial cell research.

## Data availability statement

The raw data supporting the conclusions of this article will be made available by the authors, without undue reservation.

## Author contributions

LTh contributed to the conception and designed the project. Experiments were performed and data collected by LTe and RW. LTe and RW wrote the manuscript with input from all authors. LTh supervised the project. All authors read and approved the manuscript.

## Funding

This work was funded by Fonds Wetenschappelijk Onderzoek—Vlaanderen (1133520N mandate to Lianne

Terrie and G0D3620N) and KU Leuven C24E/20/067. TR was funded by the Deutsche Forschungsgemeinschaft (DFG) (RU 2169/2-1).

## Acknowledgments

The authors are grateful to prof. Evie Vereecke and Elise Lesage for human skeletal muscle samples, to prof. Rik Gijsbers for kindly providing the viral vectors, and Sigrid Vanryckeghem for administrative support.

## Conflict of interest

The authors declare that the research was conducted in the absence of any commercial or financial relationships that could be construed as a potential conflict of interest.

## Publisher's note

All claims expressed in this article are solely those of the authors and do not necessarily represent those of their affiliated organizations, or those of the publisher, the editors and the reviewers. Any product that may be evaluated in this article, or claim that may be made by its manufacturer, is not guaranteed or endorsed by the publisher.

## References

- Birbrair, Alexander, Tan, Zhang, ZhongWang, Min, Messi, Maria Laura, Enikolopov, Grigori N., Mintz, Akiva, et al. (2013). Skeletal muscle pericyte subtypes differ in their differentiation potential. *Stem Cell Res.* 10 (1), 67–84. doi:10.1016/j.scr.2012.09.003
- Chen, Si Feng, Xia, Fei, and ShaoLi, Hua (1995). A new simple method for isolation of microvascular endothelial cells avoiding both chemical and mechanical injuries. *Microvasc. Res.* 50 (1), 119–128. doi:10.1006/MVRE.1995.1044
- Christov, Christo, Chrétien, Fabrice, Abou-Khalil, Rana, Bassez, Guillaume, Vallet, Grégoire, Jérôme Authier, François, et al. (2007). Muscle satellite cells and endothelial cells: Close neighbors and privileged partners. *Mol. Biol. Cell* 18 (4), 1397–1409. doi:10.1091/MBE06-08-0693
- Dib, Hanadi, Chafey, Philippe, Clary, Guilhem, Federici, Christian, Le Gall, Morgane, Dwyer, Julie, et al. (2012). Proteomes of umbilical vein and microvascular endothelial cells reflect distinct biological properties and influence immune recognition. *Proteomics* 12 (15–16), 2547–2555. doi:10.1002/PMIC.201200060
- Garlanda, Cecilia, and Dejana, Elisabetta (1997). Heterogeneity of endothelial cells. *Arterioscler. Thromb. Vasc. Biol.* 17 (7), 1193–1202. doi:10.1161/01.ATV.17.7.1193
- Gholobova, D., Decroix, L., Van Muylder, V., Desender, L., Gerard, M., Carpentier, G., et al. (2015). Endothelial network formation within human tissue-engineered skeletal muscle. *Tissue Eng. Part A* 21 (19–20), 2548–2558. doi:10.1089/ten.TEA.2015.0093
- Gholobova, Dacha, Gerard, Melanie, Terrie, Lianne, Desender, Linda, Shansky, Janet, Vandenburg, Herman, et al. (2019). Coculture method to obtain endothelial networks within human tissue-engineered skeletal muscle. *Methods Mol. Biol.* 169–183. doi:10.1007/978-1-4939-8897-6\_10
- Gholobova, D., Terrie, L., Gerard, M., Declercq, H., and Thorrez, L. (2020). Vascularization of tissue-engineered skeletal muscle constructs. *Biomaterials* 235, 119708. doi:10.1016/j.biomaterials.2019.119708
- Hauser, Sandra, Jung, Friedrich, and Pietzsch, Jens (2017). Human endothelial cell models in biomaterial research. *Trends Biotechnol.* 35 (3), 265–277. doi:10.1016/j.tibtech.2016.09.007
- Hewett, P. W., and Murray, J. C. (1993). Human lung microvessel endothelial cells: Isolation, culture, and characterization. *Microvasc. Res.* 46 (1), 89–102. doi:10.1006/MVRE.1993.1037
- Hewett, P. W., Murray, J. C., Price, E. A., Watts, M. E., and Woodcock, M. (1993). Isolation and characterization of microvessel endothelial cells from human mammary adipose tissue. *Vitro Cell. Dev. Biol. - Animal* 29 (4), 325–331. doi:10.1007/BF02633961
- Ibrahimi, A. Vande Velde, G.Reumers, V., Toelen, J., Thiry, Irina, Vandeputte, Caroline, et al. (2009). Highly efficient multicistronic lentiviral vectors with peptide 2A sequences. *Hum. Gene Ther.* 20 (8), 845–860. doi:10.1089/hum.2008.188
- Ieronimakakis, N, Balasundaram, G, and Reyes, M (2008). Direct isolation, culture and transplant of mouse skeletal muscle derived endothelial cells with angiogenic potential. *PLOS ONE* 3 (3), e0001753. doi:10.1371/JOURNAL.PONE.0001753
- Levenberg, St, Rouwkema, J, Macdonald, M, Garfein, E, S, Kohane, D S., Darland, D C., et al. (2005). Engineering vascularized skeletal muscle tissue. *Nat. Biotechnol.* 23 (7), 879–884. doi:10.1038/NBT1109
- Mason, J C., Lidington, E A., and Yarwood, H (2007). Isolation and analysis of large and small vessel endothelial cells. *Methods Mol. Med.* 135, 305–321. doi:10.1007/978-1-59745-401-8\_19

- Müntefering, T, Michels, A P. E., Pfeuffer, S, Meuth, S G., and Ruck, T (2019). Isolation of primary murine skeletal muscle microvascular endothelial cells. *J. Vis. Exp.* 2019 (145), e58901. doi:10.3791/58901
- Navone, S E., Marfia, G, Invernici, Ga, Cristini, S, Nava, S, Balbi, S, et al. (2013). Isolation and expansion of human and mouse brain microvascular endothelial cells. *Nat. Protoc.* 8 (9), 1680–1693. doi:10.1038/NPROT.2013.107
- Orr, A. W, Elzie, C A., Kucik, D F., and Murphy-Ullrich, Joanne E. (2003). Thrombospondin signaling through the calreticulin/LDL receptor-related protein Co-complex stimulates random and directed cell migration. *J. Cell Sci.* 116 (14), 2917–2927. doi:10.1242/JCS.00600
- Osaki, T, Sivathanu, V, and Kamm, R D. (2018). Crosstalk between developing vasculature and optogenetically engineered skeletal muscle improves muscle contraction and angiogenesis. *Biomaterials* 156, 65–76. doi:10.1016/j.BIOMATERIALS.2017.11.041
- Pan, J, and Wan, J (2020). Methodological comparison of FACS and MACS isolation of enriched microglia and astrocytes from mouse brain. *J. Immunol. Methods* 486, 112834. doi:10.1016/j.JIM.2020.112834
- Rafii, S, Butler, J M., and Ding, Bi Sen (2016). Angiocrine functions of organ-specific endothelial cells. *Nature* 529 (7586), 316–325. doi:10.1038/NATURE17040
- Schechner, J. S., Nath, A. K., Zheng, L., Kluger, M. S., Hughes, C. C., Sierra-Honigsmann, M. R., et al. (2000). *In vivo* formation of complex microvessels lined by human endothelial cells in an immunodeficient mouse. *Proc. Natl. Acad. Sci. U.S.A.* 97 (16), 9191–9196. doi:10.1073/pnas.150242297
- Sutermaster, B A., and Darling, E M. (2019). Considerations for high-yield, high-throughput cell enrichment: Fluorescence versus magnetic sorting. *Sci. Rep.* 9 (1), 227. doi:10.1038/S41598-018-36698-1
- Tomlinson, M J., Tomlinson, S, Yang, X B., and Jennifer, K (2013). Cell separation: Terminology and practical considerations. *J. Tissue Eng.* 4 (1), 204173141247269–14. doi:10.1177/2041731412472690
- Verma, M, Asakura, Y, Rohit Murakonda, B S, Pengo, T, Latroche, C, Chazaud, B, McLoon, L K., et al. (2018). Muscle satellite cell cross-talk with a vascular niche maintains quiescence via VEGF and notch signaling. *Cell Stem Cell* 23 (4), 530–543.e9. doi:10.1016/j.STEM.2018.09.007
- Wang, K, Lin, R Z, and Melero-Martin, J M. (2019). Bioengineering human vascular networks: Trends and directions in endothelial and perivascular cell sources. *Cell. Mol. Life Sci.* 76 (3), 421–439. doi:10.1007/S00018-018-2939-0



## OPEN ACCESS

## EDITED BY

Lorenzo Fassina,  
University of Pavia, Italy

## REVIEWED BY

Maowen Chen,  
Anhui University of Chinese Medicine,  
China  
Livia Visai,  
University of Pavia, Italy

## \*CORRESPONDENCE

Tiantian Wang,  
✉ tiantianwang@scu.edu.cn

<sup>†</sup>These authors have contributed equally  
to this work

## SPECIALTY SECTION

This article was submitted to  
Biomaterials,  
a section of the journal  
Frontiers in Bioengineering and  
Biotechnology

RECEIVED 20 November 2022

ACCEPTED 21 February 2023

PUBLISHED 03 March 2023

## CITATION

Zhang T, Zhao Z and Wang T (2023),  
Pulsed electromagnetic fields as a  
promising therapy for glucocorticoid-  
induced osteoporosis.  
*Front. Bioeng. Biotechnol.* 11:1103515.  
doi: 10.3389/fbioe.2023.1103515

## COPYRIGHT

© 2023 Zhang, Zhao and Wang. This is an  
open-access article distributed under the  
terms of the [Creative Commons  
Attribution License \(CC BY\)](#). The use,  
distribution or reproduction in other  
forums is permitted, provided the original  
author(s) and the copyright owner(s) are  
credited and that the original publication  
in this journal is cited, in accordance with  
accepted academic practice. No use,  
distribution or reproduction is permitted  
which does not comply with these terms.

# Pulsed electromagnetic fields as a promising therapy for glucocorticoid-induced osteoporosis

Tianxiao Zhang<sup>1†</sup>, Zhiliang Zhao<sup>1†</sup> and Tiantian Wang<sup>2,3\*†</sup>

<sup>1</sup>Innovation Center for Wound Repair, West China Hospital, Sichuan University, Chengdu, China, <sup>2</sup>Key Laboratory of Rehabilitation Medicine, West China Hospital, Sichuan University, Chengdu, Sichuan, China, <sup>3</sup>Institute of Rehabilitation Medicine, West China Hospital, Sichuan University, Chengdu, Sichuan, China

Glucocorticoid-induced osteoporosis (GIOP) is considered the third type of osteoporosis and is accompanied by high morbidity and mortality. Long-term usage of glucocorticoids (GCs) causes worsened bone quality and low bone mass via their effects on bone cells. Currently, there are various clinical pharmacological treatments to regulate bone mass and skeletal health. Pulsed electromagnetic fields (PEMFs) are applied to treat patients suffering from delayed fracture healing and non-unions. PEMFs may be considered a potential and side-effect-free therapy for GIOP. PEMFs inhibit osteoclastogenesis, stimulate osteoblastogenesis, and affect the activity of bone marrow mesenchymal stem cells (BMSCs), osteocytes and blood vessels, ultimately leading to the retention of bone mass and strength. However, the underlying signaling pathways via which PEMFs influence GIOP remain unclear. This review attempts to summarize the underlying cellular mechanisms of GIOP. Furthermore, recent advances showing that PEMFs affect bone cells are discussed. Finally, we discuss the possibility of using PEMFs as therapy for GIOP.

## KEYWORDS

GIOP, PEMFs, bone cells, angiogenesis, mechanism

## 1 Introduction

Glucocorticoids (GCs) are used as a treatment to suppress inflammation, as well as for various inflammation-mediated diseases, including ankylosing spondylitis (AS) and rheumatoid arthritis (RA) (Crawford et al., 2003). However, prolonged GC therapy can cause glucocorticoid-induced osteoporosis (GIOP), which is considered the third type of osteoporosis (Schorlemmer et al., 2005). At present, the main negative effects of excess GCs on the skeleton are considered to be exerted on bone cells directly, affecting osteoblasts, osteoclasts, osteocytes, and bone marrow mesenchymal stem cells (BMSCs) (Wang et al., 2018). BMSCs have the potential to differentiate into different kinds of cells (Chamberlain et al., 2007). In bone tissue, there is a dynamic balance between differentiation into adipocytes and osteoblasts. The balance plays an important role in lipid metabolism and bone homeostasis. In addition, some groups reported that excessive GC use could disturb the balance between lipid metabolism and bone remodeling (Takano-Murakami et al., 2009) by upregulating adipogenesis and downregulating osteogenesis of BMSCs (Yin et al., 2006). GCs increase the expression of adipogenesis-associated genes, such as peroxisome proliferator-activated receptor- $\gamma$ 2 (PPAR- $\gamma$ 2), but decrease osteogenic gene expression, especially Runt-related transcription factor 2 (Runx2) (Li et al., 2005). Moreover, chronic GC treatment may



lead to metabolic defects, resulting in lower serum insulin levels, higher blood glucose, and enhancement of visceral obesity (Lee et al., 2007). These factors might be related to GC-induced obesity and diabetes, which in turn cause severe osteoporosis.

At present, for the treatment of GIOP, calcium and vitamin D are the basic treatments, while bisphosphonates and terlipatide are the main treatment drugs, which increase bone density and reduce fracture risk in GIOP patients. Calcitonin is mainly used to relieve bone pain and is applicable to patients who do not tolerate or have contraindications to the above drugs (Pereira et al., 2020). However, long-term use of these antiosteoporosis drugs can also cause potential side effects, including osteonecrosis of the jaw, gastrointestinal complaints, and typical subtrochanteric or diaphyseal femoral fractures (Canalis et al., 2007). In addition to pharmacotherapy, physical therapy is a non-invasive and safe biophysical countermeasure, which should be the highest recommendation in clinical practice. Pulsed electromagnetic fields (PEMFs) have been proven to exert anti-inflammatory effects and are efficient in treating many bone disorders, including fresh fractures, non-union and delayed fractures, osteoporosis, diabetic osteopenia, and osteonecrosis (Liu et al., 2013; Liu et al., 2017; Wang et al., 2019a; Wang et al., 2019b). At present, the application of PEMFs to GIOP is not yet popularized in clinical practice, but some animal experiments have shown promising results. For example, one group found that PEMF therapy might alleviate bone loss and reduce serum lipid levels without negative effects in GIOP rats. The process depends on the Wnt/ $\beta$ -catenin signaling pathway (Jiang et al., 2016). Our group reported that PEMFs eliminated senescent cells to rescue bone loss in GIOP mice (Wang et al., 2021; Wang et al., 2022a). Furthermore, PEMFs also eliminate the side effects of GCs on osteoblasts (Esmail et al., 2012). We can infer that PEMF treatment may be an effective, safe, and non-invasive therapy for GIOP and might provide some potential benefits for patients with GIOP.

In this review, we first summarize the underlying cellular mechanisms of GIOP. Moreover, recent advances have shown that PEMFs affect bone cells. Finally, we discuss the possibility of using PEMFs as a therapy for GIOP.

## 2 PEMFs

PEMFs are low-frequency magnetic fields with a specific amplitude and waveform characterized by a stable variation in the amplitude of the magnetic field over time. In exposed tissue, PEMFs create a secondary electric field, which is similar to the one naturally generated during the conversion of mechanical energy into electrical energy (Zhu et al., 2017). Two methods, inductive or capacitive coupling, can be used to apply PEMFs in biological tissues. In direct capacitive coupling, the electrodes must be placed on the tissue, but in inductive coupling (non-direct capacitive coupling) they may not be in direct contact with the tissue. The reason is that the electric field produces a magnetic field, and then a current can be produced in the conductive tissues in the body (Ross et al., 2019). PEMFs are a non-invasive method of physical therapy for skeletal diseases. In 1978, Martin found that PEMFs have therapeutic effects in osteoporosis (Matsunaga et al., 1996). Recently, PEMFs have also been proven to improve bone

mineral density in the spine, distal radius, and knee in osteoporosis patients (Roozbeh and Abdi, 2018). PEMFs have widespread application with rapid effects, easy operation, and no adverse effects. It has been demonstrated that PEMF therapy is a safe, non-invasive, and easy method to treat inflammation, dysfunctions, and pain related to osteoarthritis (OA) and RA (Ganesan et al., 2009). Waldorff et al. (2017) also reported that PEMF increased the speed of bone healing when used as a treatment for fracture patients. Additionally, PEMFs have been proven to be beneficial in enhancing bone mechanical strength and improving bone microstructure by promoting bone formation and suppressing bone resorption in a study of a New Zealand white rabbit model of osteoporosis (Qian et al., 2021). Moreover, PEMF therapy attenuated bone resorption, enhanced BMD, and promoted osteogenesis in rats with disuse osteoporosis. In an ovariectomy (OVX)-induced osteoporosis mouse model, a PEMF modulated the anabolic and catabolic activity of bone, upregulated the expression of osteogenesis-related genes, and promoted trabecular bone formation (Wang et al., 2022b).

## 3 Bone

Bone is a metabolically-active tissue related to the physiological processes of locomotion, providing structural support and movement facilitation by providing storage of minerals and growth factors, regulation of mineral and acid-base homeostasis, protection of important structures, muscle levers, and a site for hematopoiesis. A central marrow space surrounded by periosteum and bone tissue is the general structure of a long bone (Buck and Dumanian, 2012). Bone remodeling is a process that involves replacing old bone with newly-formed bone periodically at the same location and is involved in osteoporosis (Siddiqui and Partridge, 2016). Bone is composed of various cell types that undergo continuous remodeling (Raggatt and Partridge, 2010; Buck and Dumanian, 2012; Siddiqui and Partridge, 2016).

BMSCs, or marrow stromal cells (MSCs), were confirmed to be precursors for several different cell lineages, such as chondrocytes, osteoblasts, adipocytes, myoblasts, and fibroblasts (Kfoury and Scadden, 2015), which are regulated by Wnt signaling pathways and bone morphogenetic proteins (BMPs) (Chen et al., 2016). Under the stimulation of multiple factors, activated osteoblasts proliferate in large numbers at the depression of bone resorption, secrete a variety of bone formation-related proteins, combine with extracellular crystalline hydroxyapatite and other inorganic components to form mature bone matrix, and gradually mineralize to form new bone (Kylmaja et al., 2016). Osteoclasts are the primary functional cells of bone resorption and play a vital role in bone growth, development, repair and reconstruction. Osteoclasts, which express receptor activator of nuclear factor kappa-B (NF- $\kappa$ B) ligand (RANKL) and macrophage colony stimulating factor (M-CSF), originate from the blood mononuclear macrophage system and are special terminally-differentiated cells. Fusion of mononuclear precursor cells forms giant multinucleated cells in various ways (Xu and Teitelbaum, 2013). Mature osteoclasts are multinuclear cells produced by the fusion of tartrate-resistant acid phosphatase-positive (TRAP<sup>+</sup>) mononuclear cells, termed preosteoclasts (POCs), and are the

main source of platelet-derived growth factor-BB (PDGF-BB) (Boyle et al., 2003; Xu and Teitelbaum, 2013; Kusumbe et al., 2014; Xie et al., 2014; Zhen et al., 2021). Type H vessels are located abundantly in the metaphysis adjacent to the growth plate, are linked with bone formation, and are double-positive for CD31 and *Emcn* (Peng et al., 2020a; Zhen et al., 2021). PDGF-BB, released by POCs, promotes angiogenesis of type H vessels and osteogenesis (Peng et al., 2020a). Osteocytes are terminally-differentiated osteoblasts embedded in the bone matrix, which are a major source of sclerostin (SOST) and RANKL, regulating osteoblast and osteoclast formation, respectively (Goldring, 2015; Wang et al., 2019c). Additionally, osteoclasts lay down minerals and create the collagen-rich bone matrix, transforming mechanical inputs into biochemical signals (Bidwell et al., 2008).

GIOP can be induced as a primary side effect of the application of GCs based on various mechanisms. It is reported that GCs might be toxic to genes related to cell regulation (osteoblasts, etc.) through combining with the promoter region of GC response elements, eventually resulting in changes of protein regulation and synthesis (Adami and Saag, 2019). Moreover, GCs can be harmful to bone formation *via* two main pathways: enhancing expression of peroxisome proliferator-activated receptor gamma 2 (PPAR $\gamma$ 2) and suppressing the typical Wnt/ $\beta$  catenin signaling pathway (Adami and Saag, 2019). Previous evidence has proven that GCs induce apoptosis of osteocytes and osteoblasts, impairing the function and differentiation of osteoblasts directly. In addition, another study showed that T cells could also lead to bone loss through the RANKL pathway and regulation of CXCL10, resulting in GIOP (Song et al., 2020). The details of GC targeting of bone are discussed below.

## 4 Potential targets of PEMFs in GIOP

### 4.1 BMSCs

A faulty early mesenchymal precursor, presumably an MSC, will cause a reduction in the production of osteoprogenitor cells and may be responsible for a variety of musculoskeletal problems, including osteoporotic syndromes (Bonyadi et al., 2003). BMSCs are a critical cellular target of GCs in developing bone turnover (Shen et al., 2018). GC treatment increases the number and size of bone marrow adipocytes, switching the fate of BMSCs from osteogenesis to adipogenesis (Bujalska et al., 1999). This process has been demonstrated to depend on transactivation of CCAAT/enhancer binding protein in murine stromal cells (Pereira et al., 2002; Canalis et al., 2004) accompanied by an upregulation of PPAR $\gamma$ 2 and downregulation of Runx2 (Canalis et al., 2007), leading to increased bone marrow adipose tissue, fewer mature osteoblasts and decreased cancellous bone (Weinstein and Manolagas, 2000). In addition, GCs stimulate preadipocyte conversion to mature adipocytes, resulting in the hyperplasia of adipose tissue. In a GC-treated model, a two-fold increase was found in the cancellous adipocyte area (Weinstein and Manolagas, 2000). Stimulation of osteogenic MSCs is a relatively new concept in medicine that could potentially be achieved by the use of PEMFs. PEMFs have the potential to prevent aberrant and promote healthy MSC function. PEMFs (75 Hz, 1.5 mT, 28 days) have been shown to

exert suppressive effects on the expression of adipogenic genes (Jansen et al., 2010; Lu et al., 2015) and induce osteogenesis through the enhancement of ALP activity and the expression of Runx2 in BMSCs (Ongaro et al., 2014), accompanied by a delayed increase in cell proliferation. Stimulation of osteogenesis through application of a PEMF alleviated bone loss in GIOP models (Wang et al., 2022a). The Wnt/ $\beta$ -catenin pathway might be involved in this process. For example, GCs disturb the BMSC differentiation balance by upregulating adipogenesis-related genes and downregulating osteogenesis-associated genes by suppressing the Wnt/ $\beta$ -catenin pathway (Li et al., 2013). The mRNA and protein expression levels of Wnt10b, LRP5, and  $\beta$ -catenin were significantly upregulated in GIOP rats after PEMF stimulation for 12 weeks (50 Hz, 4.0 mT, 40 min per day), suggesting that the canonical Wnt signaling pathway was activated during PEMF stimulation, which is in agreement with previous reports (Ding et al., 2011; Jing et al., 2013; Jiang et al., 2016). In addition, the mTOR signaling pathway plays a crucial role in a variety of diseases, including GIOP (Wang et al., 2020; Ge and Zhou, 2021). Suppressing mTOR signaling induces osteoblastic differentiation and reduces adipogenic potential (Martin et al., 2015). One group reported that exposure to PEMFs reversed the reduced mineralization of the extracellular matrix (ECM) induced by rapamycin, an inhibitor of TORC1 (receptor of mTOR) (Sarbasov et al., 2006), suggesting that PEMFs might stimulate BMSC commitment to the osteoblast lineage *via* the mTOR pathway (Ferroni et al., 2018). Whether mTOR participates in the rescue of GIOP by PEMFs requires further study.

Recently, cellular senescence, characterized by loss of replicative potential, has been shown to have a crucial role in GIOP (Liu et al., 2021; Wang et al., 2021; Wang et al., 2022c). For example, in young mice, Nestin-expressing (Nestin<sup>+</sup> cells), a type of MSC in postnatal bones, are primarily of endothelial and osteoblast lineages (Ono et al., 2014) and undergo senescence in response to GCs (Li et al., 2017; Su et al., 2020). In addition, LepR<sup>+</sup> MSCs of adult mice are also susceptible to GC treatment (Wang et al., 2021). Our group reported that LepR<sup>+</sup> cells exhibit a senescent phenotype based on flow cytometry and immunostaining analysis (Wang et al., 2021; Wang et al., 2022a). Clearance of senescent cells by PEMF treatment (8 Hz, 3.8 mT, 1 h per day) for 4 weeks rescued GC-induced bone loss (Wang et al., 2021; Wang et al., 2022a). In particular, PEMFs exerted anti-senescence effects on LepR<sup>+</sup> MSCs through the EZH2–H3K27me3 axis (Wang et al., 2022a).

In conclusion, PEMFs play an important role in regulating the balance of BMSC production and differentiation through various pathways either directly or indirectly. Thus, there is potential to apply PEMFs to the treatment of GIOP in future.

### 4.2 Osteoblast function

The effects of PEMFs on osteoblast function remain debatable; it is well known that PEMFs have a window effect and produce repeatable osteogenic effects (Matsunaga et al., 1996). Different PEMF intensities and different time-points chosen for analysis can cause different effects. However, most studies assumed that PEMFs could enhance osteoblast activity, leading to an increase in cellular differentiation (Diniz et al., 2002).

There are many assumptions related to the mechanism of how PEMFs affect osteoblast lineages in response to GCs. First, osteoblast orientation and morphology can be regulated by PEMFs. A PEMF (60 Hz, 0.7 mT, 24 h) was shown to mediate osteoblast differentiation by inducing morphological changes, making osteoblastic cells smaller, shorter and rounder in comparison to sham treatment (Lee and McLeod, 2000), which should be tested in GIOP. In support of this, our experiments showed that long-term GC treatment caused detrimental effects on osteoblasts, which could be reversed by PEMF therapy (8 Hz, 3.8 mT, 1 h per day) (Wang et al., 2021; Wang et al., 2022a). The Wnt signaling pathway might also account for this. For instance, GCs suppresses the synthesis and release of transcription factors of the Wnt signaling pathway in mature osteoblasts (Mak et al., 2009), such as  $\beta$ -catenin and Runx2, impairing osteoblast differentiation. Specifically, therapeutic concentrations of GCs upregulate the expression of glycogen synthase kinase 3 $\beta$  (GSK-3 $\beta$ ), resulting in  $\beta$ -catenin degradation (Wang et al., 2009). Meanwhile, high levels of GCs also promote the expression of Wnt inhibitors such as SOST and DKK1 (Mak et al., 2009). PEMFs have been demonstrated to increase the expression of genes associated with the Wnt signaling pathway, including Wnt1a, Wnt3a, Lrp5, and Lrp6, both *in vivo* and *in vitro*. In addition, a PEMF (50 Hz, 4.0 mT, 40 min per day) also downregulated DKK1, which antagonized the Wnt signaling pathway (Zhou et al., 2015; Jiang et al., 2016) in a rat model. The role of the canonical Wnt signaling pathway was investigated after PEMF treatment in a GIOP model (50 Hz, 4.0 mT, 40 min per day for 12 weeks) (Jiang et al., 2016). A PEMF reversed the decreased expression of Wnt10b, LRP5, and  $\beta$ -catenin induced by GCs (Jiang et al., 2016).

In addition, BMP-2, a regulator of osteoblast differentiation, is suppressed by high concentrations of GCs (Yao et al., 2008). Moreover, therapeutic levels of GCs enhance the expression of BMP-2 antagonists, such as follistatin and Dan family members (Hayashi et al., 2009). Li et al. (2007) showed that a PEMF (7.5 Hz, 108  $\mu$ T, 20 min per day for 4 days) upregulated the mRNA production of TGF- $\beta$ , BMP2, osteocalcin, osteoprotegerin, ALP, Runx2, NF- $\gamma$ B ligand, matrix metalloproteinase-1 and -3 (Chen et al., 2010), and bone sialoprotein. These studies suggested that osteogenic differentiation of osteoprogenitor cells could be stimulated by PEMFs directly *via* the BMP2 signaling pathway (Schwartz et al., 2008). To clarify the mechanism of PEMF therapy, further studies should evaluate the role of BMP2 in bone loss induced by GCs.

Furthermore, GCs inhibit the synthesis of type I collagen (COL1A), resulting in decreased bone matrix formation *in vitro* (Canalis, 1983; Harris et al., 2013). In addition, PEMFs may not only upregulate genes involved in bone and matrix component formation but also downregulate various genes related to ECM degradation (Sollazzo et al., 2010). Sollazzo et al. (2010) reported that PEMFs (75 Hz, 2 mT, 18 h) increase the expression of genes related to bone formation, including AKT1 and HOXA10; genes associated with transduction activation, such as P2RX7 and CALM 1; genes encoding organic ECM components, such as SPARC and COL1A2; and genes correlated with cytoskeletal components, including VCL and FNI. Smith et al. (2004) found that PEMFs (2 min or 1 h) might suppress the expression of genes for matrix degradation, such as downregulation of phosphatase 4 (DUSP4) and matrix metalloproteinase 11 (MMP-11). Although *in vivo* and

*in vitro* studies showed promising effects of PEMFs on matrix mineralization, this speculation has not been tested in GIOP models, which need further study in future.

### 4.3 Osteocytes

Recent experiments have reported that osteocytes act as the main targets for excessive GCs in bone (O'Brien et al., 2004). Osteocytes are thought to control the fate of both osteoclasts and osteoblasts (Weinstein et al., 2002; Weinstein, 2007). GCs induce osteocyte autophagy during the initial period (Xia et al., 2010), while prolonged usage of GCs causes osteocyte death, resulting in a decrease in osteocyte number, accompanied by significantly impaired bone quality. However, autophagy induction in osteocytes cannot rescue the negative effects of GCs on bone metabolism (Piemontese et al., 2015). Exposure to high levels of GCs may induce osteocyte apoptosis, causing them to secrete more DKK1 and SOST, thereby suppressing the combination between Wnt and LPR5/-6 (Hayashi et al., 2009), leading to reduced bone formation. On the other hand, dying osteocytes secrete more TNF- $\alpha$ , IL-6, HMGB1, and RANKL to stimulate osteoclastogenesis. Cai found that the GC-treated group contained a considerably higher proportion of apoptotic osteocytes than the control group based on the results of TUNEL immunofluorescence staining, and the PEMF group rescued this progression. Moreover, PEMF partially mitigated the increase in the gene expression of SOST and DKK1, suggesting that PEMFs (15 Hz, 2.0 mT, 2 h per day for 6 weeks) attenuated the apoptosis of osteocytes stimulated by GCs (Cai et al., 2020).

In addition to signaling pathway connections, osteocytes also regulate osteoblasts and osteoclasts *via* gap junction intercellular communication (GJIC), including Cx43, which is negative for osteoclasts and positive for osteoblasts (Wang et al., 2018). Other small molecules, including prostaglandin E2 (PGE2) and nitric oxide (NO), might also be related to the communication between osteoblasts and osteocytes. PGE2 plays an important role in ECM synthesis and osteoblast differentiation, which is stimulated by TGF- $\beta$ 1. Moreover, NO $_2^-$  inhibits osteoblast activity, stimulates apoptosis, and promote bone resorption (Wang et al., 2018). The gap junctions at the tips of osteocyte cytoplasmic processes respond to alterations of the mechanical environment *via* stimulation including mechanical loading, and deliver signals through the osteocyte network to osteoblasts. In response to fluid flow, functional gap junctions between osteocytes and osteoblasts are created, which then stimulate osteoblastic development. Thus, blocking GJIC suppresses mechanical signal transmission from osteocytes to osteoblasts, leading to impairment of osteoblastic differentiation (Loiselle et al., 2013). GCs impair osteocyte-osteoblast communication by triggering Cx43 degradation, causing severe adverse skeletal effects. GCs inhibit  $\beta$ -catenin stabilization and production of cyclooxygenase-2 (COX-2) and PGE2 (Wang et al., 2018). Loiselle et al. (2013) found that PEMFs (15 Hz, 8 h per day, 4 days) upregulated total TGF- $\beta$ 1 and PGE2 in cells of the murine long bone osteocyte-Y4 cell line (Murine Long bone Osteocyte-Y4; MLO-Y4) over time, which is dependent on the prostaglandin mechanism, including COX-1 (Lohmann et al., 2003). In addition, PEMF stimulation mediates NO $_2^-$  in a time-dependent manner (Lohmann et al., 2003). Based on the evidence detailed above, PEMFs might rescue GIOP by mediating the communication between



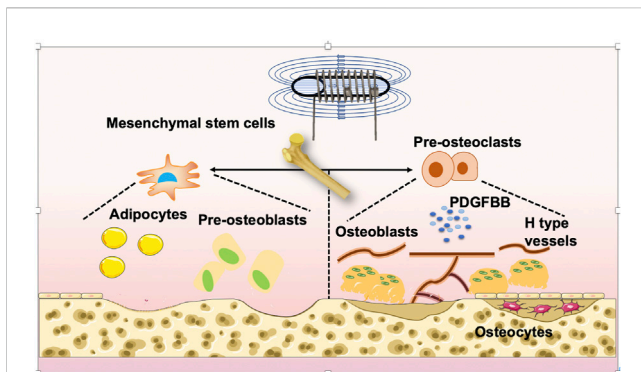


**FIGURE 1**

Mechanism of PEMF-treated OP. PEMFs may be considered a potential and non-side-effect therapy for GIOP. PEMFs stimulate osteoblastogenesis, suppress osteoclastogenesis, and influence the activity of bone marrow mesenchymal stem cells (BMSCs), osteocytes and angiogenesis. Finally, it leads to the retention of bone mass and strength.

osteoblasts/osteoclasts and osteocytes. In future, more studies are needed to test this hypothesis in GIOP models.

## 4.4 Osteoclasts

Decreased osteoclast number and viability induced by PEMFs might account for the antagonistic effects against GCs (He et al., 2015; Tschon et al., 2018). Specifically, GC treatment stimulates bone resorption, accompanied by the upregulation of osteoclast number and activity observed in humans and mice (Dovio et al., 2004; Yao et al., 2008). Excess GCs stimulate bone resorption directly by extending the lifespan of mature osteoclasts (Lin et al., 2016). For example, compared with normal rats, rats with GIOP have lower ALP levels and higher TRAP levels in serum (Jiang et al., 2016). Jiang et al. found that PEMF (50 Hz, 4.0 mT, 40 min per day) stimulation significantly decreased serum TRAP levels and increased serum ALP levels (Jiang et al., 2016), suggesting that PEMFs could be an efficient therapy for GIOP. The mechanism needs to be clarified.

Over the past several years the RANK/RANKL/OPG system has been shown to play a vital role in bone remodeling (Borsje et al., 2010). Osteocytes and osteoblasts primarily express RANKL, a cell surface protein that combines with a specific receptor (RANK) located on the osteoclast membrane, contributing to osteoclastogenesis. Osteoblast-derived OPG inhibits osteoclastogenesis by suppressing osteoclast maturation (Lacey et al., 1998). GC treatment stimulates the production of RANKL and decreases the expression of the RANKL decoy receptor osteoprotegerin (OPG) (Sivagurunathan et al., 2005). Disturbing the RANKL/OPG ratio results in increased osteoclast activity and bone resorption. Jiang et al. found that the OPG/RANKL ratio, which is decreased in GIOP, improved after PEMF treatment (Jiang et al., 2016), indicating that the OPG/RANKL/RANKL signaling pathway might participate in this process. PEMFs inhibit RANKL expression and enhance OPG expression, leading to upregulation of the OPG/RANKL ratio (Jiang et al., 2016). This process might involve activation of the canonical Wnt signaling pathway after PEMF stimulation in GIOP rats.

Proinflammatory cytokines might accelerate osteoclastogenesis and this could be alleviated by PEMF stimulation, which has been demonstrated in other osteoporosis models. For example, Chang et al. (2004) found that in OVX rats, PEMF treatment (7.5 Hz, 0.8  $\mu$ T, 9 days) inhibited osteoclastogenesis accompanied by reduced levels of interleukin 1 beta (IL-1 $\beta$ ), tumor necrosis factor-alpha (TNF- $\alpha$ ), and interleukin 6 (IL-6) in primary bone marrow. To clarify the mechanism of PEMF stimulation, further experiments are in progress to evaluate the role of proinflammatory cytokines in bone metabolism in GIOP models.

## 4.5 Blood vessels

The vasculature plays a critical role in the growing skeleton, and angiogenesis is intimately coupled to osteogenesis. As an essential part of skeletal development, osseointegration, and bone formation, the formation of blood vessels is important in transporting growth factors to achieve cell viability and interaction (Diomedea et al., 2020). High doses of GCs are known to inhibit angiogenesis and induce osteoporosis and growth failure (Sivaraj and Adams, 2016). Liu reported that GC treatment induced vascular endothelial cell senescence in young mice, and alleviation of this alteration not only improved GC-impaired bone angiogenesis with coupled osteogenesis but also bone loss. GC treatment inhibits ANG, a ribonuclease secreted by metaphyseal osteoclasts, leading to blood vessel cell senescence and bone loss through binding to PLXNB2 in vascular cells (Liu et al., 2021). Peng demonstrated that chronic GC exposure led to reduced POC numbers and PDGF-BB and thus inhibited type H vessel formation, ultimately resulting in osteoporosis, bone growth retardation, and osteonecrosis (Peng et al., 2020b). In addition, exposure to GCs inhibits the angiogenic molecule VEGF (Pufe, 2003; Athanasopoulos et al., 2007) and stimulates the angiostatic glycopeptide thrombospondin-1 (Rae et al., 2009). We can infer that excess GC causes a decrease in bone water volume and skeletal blood flow (Goans et al., 1995; Drescher et al., 2000) and contributes to a reduced mineral apposition rate (Reeve et al., 1988). Recently, our studies found that the type H vessel number was significantly reduced in the GC group compared to the controls, while PEMFs (8 Hz, 3.8 mT, 1 h per day for 4 weeks) maintained this change, suggesting that PEMFs can show angiogenic-osteogenic effects on bone marrow during GC treatment (Wang et al., 2021; Wang et al., 2022a). Another study performed by Wang demonstrated that PEMFs (15 Hz, 2.4–2.6 mT, 1 h per day for 8 weeks) substantially countered OVX-induced bone loss by inducing coupling promotion of osteogenesis and type H vessels in a mouse model. This beneficial effect might be mediated by HIF-1 $\alpha$  signaling in type H vessels (Wang et al., 2022b). These results open up new directions for research into the therapeutic effects of PEMFs on the reversal of osteoporosis by targeting angiogenesis. This speculation needs to be tested in GIOP models in both young and adult mice in the future.

## 5 Evidence for therapeutic effects

PEMFs prevent bone loss because of piezoelectrical effects, modulating calcium deposits in bone and regulating mineral



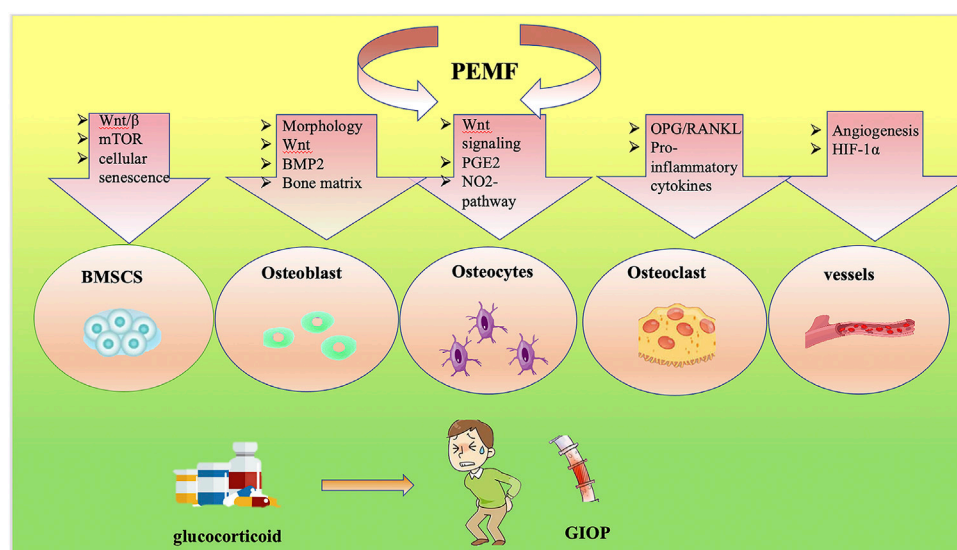


**FIGURE 2**  
Signaling pathway of PEMF-treated GIOP.

metabolism. For example, our team found that PEMFs reduce bone loss in postmenopausal women and improve their pain and balance function (Liu et al., 2013). Moreover, PEMFs improve bone loss in OVX osteoporosis animal models, enhance the biomechanical properties of bone, and inhibit inflammation [!!! INVALID CITATION !!! (3 and 4)]. In addition to OVX-induced bone loss, other groups found that PEMFs also acted as a therapy for osteoporosis induced by diabetes-mellitus and disuse (Chang and Chang, 2003; Liu et al., 2013). At present, the application of PEMFs to GIOP is not yet popularized in clinical applications, but some animal experiments have shown promising results. Jiang et al. (2016) reported that PEMF therapy antagonized the negative effects of GCs in bone by activating the Wnt/ $\beta$ -catenin signaling pathway. Our group found that PEMFs rescued bone loss in GIOP models by eliminating senescent cells (Wang et al., 2021; Wang et al., 2022a). Furthermore, PEMFs eliminate the side-effects of GCs on osteoblasts (Esmail et al., 2012). Based on the evidence, we conclude that PEMF treatment may be an effective, safe, and non-invasive therapy for GIOP and might provide some potential benefits for patients with GIOP.

There are many potential mechanisms that could account for this. Bone mass maintenance is attributed to a balance between osteoblastic bone formation and osteoclastic bone resorption. Numerous studies have reported that the RANKL–RANK signaling and Wnt signaling pathways are two of the most necessary pathways regulating bone quality and bone metabolism. The Wnt/ $\beta$ -catenin pathway might be associated with the protection of osteogenesis by PEMFs antagonizing GCs. For example, GCs disturb the BMSC differentiation balance by upregulating adipogenesis-related genes and downregulating osteogenesis-associated genes by suppressing the Wnt/ $\beta$ -catenin pathway (Li et al., 2013). The mRNA and protein expression levels associated with the Wnt/ $\beta$ -catenin pathway were significantly upregulated in GIOP rats after PEMF stimulation

for 12 weeks, indicating that the canonical Wnt signaling pathway was activated during PEMF stimulation (Ding et al., 2011; Jing et al., 2013; Jiang et al., 2016). Meanwhile, high levels of GCs also promote the expression of Wnt inhibitors such as SOST and DKK1 to suppress osteogenesis (Mak et al., 2009). PEMFs not only increase the expression of genes involved in the Wnt signaling pathway, such as Lrp5, Lrp6, Wnt1a, and Wnt3a but also downregulate SOST and DKK1 (Zhou et al., 2015; Cai et al., 2020). Moreover, dying osteocytes are the main sources of SOST and DKK1, indicating that PEMFs could also alleviate osteocyte apoptosis induced by GCs (Ramli and Chin, 2020). With regard to the ECM, chronic GC treatment suppresses mineralization (Canalis, 1983; Wang et al., 2005), which can be reversed by PEMFs (Sollazzo et al., 2010).

In addition to osteogenesis, GCs increase osteoclast survival indirectly by inhibiting OPG production by osteoblastic cells, thereby upregulating available RANKL and inhibiting osteoclast apoptosis. Jiang et al. (2016) found that the OPG/RANKL ratio, which decreased in the GIOP group, improved after PEMF treatment, indicating that the OPG/RANKL signaling pathway might participate in this process. PEMFs inhibit RANKL expression and enhance OPG expression, leading to an upregulation in the ratio of OPG/RANKL (Jiang et al., 2016). Another osteoclast population, termed POCs, positively regulate osteogenesis by regulating angiogenesis. Chronic GC treatment has been demonstrated to lead to reduced POC numbers and thus inhibition of type H vessel formation, ultimately resulting in osteoporosis, bone growth retardation, and osteonecrosis (Peng et al., 2020b). In addition, exposure to GCs inhibits the angiogenic molecule VEGF (Pufe, 2003; Athanasopoulos et al., 2007; Rae et al., 2009), causing a decrease in bone water volume and skeletal blood flow (Goans et al., 1995; Drescher et al., 2000). PEMFs exert angiogenic–osteogenic effects on bone marrow during GC treatment by maintaining this change (Wang et al., 2021; Wang et al., 2022a).

Recently, cellular senescence was demonstrated to play a fundamental role in GIOP (Liu et al., 2021; Wang et al., 2021; Wang et al., 2022c). Nestin<sup>+</sup> MSCs in young mice and LepR<sup>+</sup> MSCs of adult mice undergo senescence in response to GCs (Li et al., 2017; Su et al., 2020; Wang et al., 2021). Clearance of senescent cells by PEF treatment (8 Hz, 3.8 mT, 1 h per day) for 4 weeks rescued GC-induced bone loss (Wang et al., 2021) through the EZH2–H3K27me3 axis.

Overall, GCs cause osteoporosis by inhibiting bone formation and enhancing bone resorption, which is prevented by PEFs through different mechanisms. Thus, PEFs should be considered a promising method for treating GIOP. Moreover, it seems that PEFs with different parameters including frequency, intensity, and duration can still influence GIOP (Cai et al., 2020; Wang et al., 2022b). However, studies have focused on the physiological effects of PEFs on bone cells or on other types of osteoporosis; thus, the effects of PEFs on GIOP are still questionable. The positive effects of PEFs on osteoporosis are still unclear due to the use of different parameters including the PEF waveform, daily exposure time, treatment starting point and duration, and other subject-related factors. Moreover, there are great differences between clinical experiments and animal experiments. To verify these findings, more high-quality, reliable, randomized controlled trials with large sample sizes and long-term follow-up are needed in the future. In addition, the contraindications of long-term PEFs should be considered in further studies.

## 6 Conclusion

Current studies of PEFs and their potential roles in regulating bone metabolism in GIOP are summarized in this review (Figures 1, 2). PEFs should be recommended based on more reliable evidence from high-quality, randomized controlled trials, which require clinical studies with large sample sizes and long-term follow-up. Moreover, gene-knockout mice should be used to determine the specific target for treating GIOP by PEFs. After that, the usage of PEFs can be considered a safe treatment for GIOP.

## References

- Adami, G., and Saag, K. G. (2019). Glucocorticoid-induced osteoporosis: 2019 concise clinical review. *Osteoporos. Int.* 30 (6), 1145–1156. doi:10.1007/s00198-019-04906-x
- Athanasopoulos, A. N., Schneider, D., Keiper, T., Alt, V., Pendurthi, U. R., Liegibel, U. M., et al. (2007). Vascular endothelial growth factor (VEGF)-induced up-regulation of CCN1 in osteoblasts mediates proangiogenic activities in endothelial cells and promotes fracture healing. *J. Biol. Chem.* 282 (37), 26746–26753. doi:10.1074/jbc.m705200200
- Bedwell, J. P., Yang, J., and Robling, A. G. (2008). Is *HMGB1* an osteocyte alarmin? *J. cell biochem. J. Cell. Biochem.* 103 (6), 1671–1680. doi:10.1002/jcb.21572
- Bonyadi, M., Waldman, S. D., Liu, D., Aubin, J. E., Grynpas, M. D., and Stanford, W. L. (2003). Mesenchymal progenitor self-renewal deficiency leads to age-dependent osteoporosis in Sca-1/Ly-6A null mice. *Proc. Natl. Acad. Sci. U. S. A.* 100 (10), 5840–5845. doi:10.1073/pnas.1036475100
- Borsje, M. A., Ren, Y., de Haan-Visser, H. W., and Kuijter, R. (2010). Comparison of low-intensity pulsed ultrasound and pulsed electromagnetic field treatments on OPG and RANKL expression in human osteoblast-like cells. *Angle Orthod.* 80 (3), 498–503. doi:10.2319/060809-318.1
- Boyle, W. J., Simonet, W. S., and Lacey, D. L. (2003). Osteoclast differentiation and activation. *Nature* 423 (6937), 337–342. doi:10.1038/nature01658
- Buck, D. W., and Dumanian, G. A. (2012). Bone biology and physiology: Part I. *Fundam.* 129 (6), 1314–1320. doi:10.1097/prs.0b013e31824eca94
- Bujalska, I. J., Kumar, S., Hewison, M., and Stewart, P. M. (1999). Differentiation of adipose stromal cells: The roles of glucocorticoids and 11 $\beta$ -hydroxysteroid dehydrogenase\*. *Endocrinology* 140 (7), 3188–3196. doi:10.1210/endo.140.7.6868
- Cai, J., Shao, X., Yang, Q., Yang, Y., Yan, Z., Luo, E., et al. (2020). Pulsed electromagnetic fields modify the adverse effects of glucocorticoids on bone architecture, bone strength and porous implant osseointegration by rescuing bone-anabolic actions. *Bone* 133, 115266. doi:10.1016/j.bone.2020.115266
- Canalis, E. (1983). Effect of glucocorticoids on type I collagen synthesis, alkaline phosphatase activity, and deoxyribonucleic acid content in cultured rat calvariae. *Endocrinology* 112 (3), 931–939. doi:10.1210/endo-112-3-931
- Canalis, E., Bilezikian, J. P., Angeli, A., and Giustina, A. (2004). Perspectives on glucocorticoid-induced osteoporosis. *Bone* 34 (4), 593–598. doi:10.1016/j.bone.2003.11.026
- Canalis, E., Mazziotti, G., Giustina, A., and Bilezikian, J. P. (2007). Glucocorticoid-induced osteoporosis: Pathophysiology and therapy. *Osteoporos. Int.* 18 (10), 1319–1328. doi:10.1007/s00198-007-0394-0
- Chamberlain, G., Fox, J., Ashton, B., and Middleton, J. (2007). Concise review: Mesenchymal stem cells: Their phenotype, differentiation capacity, immunological features, and potential for homing. *Stem Cells* 25 (11), 2739–2749. doi:10.1634/stemcells.2007-0197
- Chang, K., and Chang, W. H. (2003). Pulsed electromagnetic fields prevent osteoporosis in an ovariectomized female rat model: A prostaglandin E2-associated process. *Bioelectromagnetics* 24 (3), 189–198. doi:10.1002/bem.10078
- Chang, K., Hong-Shong Chang, W., Yu, Y. H., and Shih, C. (2004). Pulsed electromagnetic field stimulation of bone marrow cells derived from ovariectomized rats affects osteoclast formation and local factor production. *Bioelectromagnetics* 25 (2), 134–141. doi:10.1002/bem.10168

## Author contributions

TW conceived and designed the study. TW, TZ, and ZZ wrote the manuscript. All authors were involved in revising the article and approved the final version.

## Funding

Supported by the National Natural Science Foundation (82102656); China Postdoctoral Science Foundation (2022T150452, 2021M692299); PostDoctor Research Project, West China Hospital, Sichuan University (2021HXBH021). Natural Science Foundation of Sichuan Province (2022NSFSC1392).

## Acknowledgments

We thank AJE for editing this manuscript.

## Conflict of interest

The authors declare that the research was conducted in the absence of any commercial or financial relationships that could be construed as a potential conflict of interest.

## Publisher's note

All claims expressed in this article are solely those of the authors and do not necessarily represent those of their affiliated organizations, or those of the publisher, the editors and the reviewers. Any product that may be evaluated in this article, or claim that may be made by its manufacturer, is not guaranteed or endorsed by the publisher.

- Chen, J., He, H. C., Xia, Q. J., Huang, L. Q., and Hu, Y. J. (2010). Effects of pulsed electromagnetic fields on the mRNA expression of RANK and CAII in ovariectomized rat osteoclast-like cell. *Connect. Tissue Res.* 51 (1), 1–7. doi:10.3109/03008200902855917
- Chen, Q., Shou, P., Zheng, C., Jiang, M., Cao, G., Yang, Q., et al. (2016). Fate decision of mesenchymal stem cells: Adipocytes or osteoblasts? *Cell Death Differ.* 23 (7), 1128–1139. doi:10.1038/cdd.2015.168
- Crawford, B. A., Liu, P. Y., Kean, M. T., Bleasel, J. F., and Handelsman, D. J. (2003). Randomized placebo-controlled trial of androgen effects on muscle and bone in men requiring long-term systemic glucocorticoid treatment. *J. Clin. Endocrinol. Metab.* 88 (7), 3167–3176. doi:10.1210/jc.2002-021827
- Ding, S., Peng, H., Fang, H. S., Zhou, J. L., and Wang, Z. (2011). Pulsed electromagnetic fields stimulation prevents steroid-induced osteonecrosis in rats. *BMC Musculoskelet. Disord.* 12, 215. doi:10.1186/1471-2474-12-215
- Diniz, P., Shomura, K., Soejima, K., and Ito, G. (2002). Effects of pulsed electromagnetic field (PEMF) stimulation on bone tissue like formation are dependent on the maturation stages of the osteoblasts. *Bioelectromagnetics* 23 (5), 398–405. doi:10.1002/bem.10032
- Diomedea, F., Marconi, G. D., Fonticoli, L., Pizzicarella, J., Merciaro, I., Bramanti, P., et al. (2020). Functional relationship between osteogenesis and angiogenesis in tissue regeneration. *Int. J. Mol. Sci.* 21, 3242. doi:10.3390/ijms21093242
- Dovio, A., Perazzolo, L., Osella, G., Ventura, M., Termine, A., Milano, E., et al. (2004). Immediate fall of bone formation and transient increase of bone resorption in the course of high-dose, short-term glucocorticoid therapy in young patients with multiple sclerosis. *J. Clin. Endocrinol. Metab.* 89 (10), 4923–4928. doi:10.1210/jc.2004-0164
- Drescher, W., Li, H., Qvesel, D., Jensen, S. D., Flo, C., Hansen, E. S., et al. (2000). Vertebral blood flow and bone mineral density during long-term corticosteroid treatment: An experimental study in immature pigs. *Spine (Phila Pa 1976)* 25 (23), 3021–3025. doi:10.1097/00007632-200012010-00009
- Esmail, M. Y., Sun, L., Yu, L., Xu, H., Shi, L., and Zhang, J. (2012). Effects of PEMF and glucocorticoids on proliferation and differentiation of osteoblasts. *Electromagn. Biol. Med.* 31 (4), 375–381. doi:10.3109/15368378.2012.662196
- Ferroni, L., Gardin, C., Dolkart, O., Salai, M., Barak, S., Piattelli, A., et al. (2018). Pulsed electromagnetic fields increase osteogenic commitment of MSCs via the mTOR pathway in TNF- $\alpha$  mediated inflammatory conditions: An *in-vitro* study. *Sci. Rep.* 8 (1), 5108. doi:10.1038/s41598-018-23499-9
- Ganesan, K., Gengadharan, A. C., Balachandran, C., Manohar, B. M., and Puvanakrishnan, R. (2009). Low frequency pulsed electromagnetic field—a viable alternative therapy for arthritis. *Indian J. Exp. Biol.* 47 (12), 939–948.
- Ge, X., and Zhou, G. (2021). Protective effects of naringin on glucocorticoid-induced osteoporosis through regulating the PI3K/Akt/mTOR signaling pathway. *Am. J. Transl. Res.* 13 (6), 6330–6341.
- Goans, R. E., Weiss, G. H., Abrams, S. A., Perez, M. D., and Yergey, A. L. (1995). Calcium tracer kinetics show decreased irreversible flow to bone in glucocorticoid treated patients. *Calcif. Tissue Int.* 56 (6), 533–535. doi:10.1007/bf00298584
- Goldring, S. R. (2015). The osteocyte: Key player in regulating bone turnover. *RMD Open* 1, e000049. doi:10.1136/rmdopen-2015-000049
- Harris, C., Roohk, D. J., Fitch, M., Boudignon, B. M., Halloran, B. P., and Hellerstein, M. K. (2013). Large increases in adipose triacylglycerol flux in Cushingoid CRH-Tg mice are explained by futile cycling. *Am. J. Physiol. Endocrinol. Metab.* 304, E282–E293. doi:10.1152/ajpendo.00154.2012
- Hayashi, K., Yamaguchi, T., Yano, S., Kanazawa, I., Yamauchi, M., Yamamoto, M., et al. (2009). BMP/Wnt antagonists are upregulated by dexamethasone in osteoblasts and reversed by alendronate and PTH: Potential therapeutic targets for glucocorticoid-induced osteoporosis. *Biochem. Biophys. Res. Commun.* 379 (2), 261–266. doi:10.1016/j.bbrc.2008.12.035
- He, J., Zhang, Y., Chen, J., Zheng, S., Huang, H., and Dong, X. (2015). Effects of pulsed electromagnetic fields on the expression of NFATc1 and CAII in mouse osteoclast-like cells. *Aging Clin. Exp. Res.* 27 (1), 13–19. doi:10.1007/s40520-014-0239-6
- Jansen, J. H., van der Jagt, O. P., Punt, B. J., Verhaar, J. A., van Leeuwen, J. P., Weinans, H., et al. (2010). Stimulation of osteogenic differentiation in human osteoprogenitor cells by pulsed electromagnetic fields: An *in vitro* study. *BMC Musculoskelet. Disord.* 11, 188. doi:10.1186/1471-2474-11-188
- Jiang, Y., Gou, H., Wang, S., Zhu, J., Tian, S., and Yu, L. (2016). Effect of pulsed electromagnetic field on bone formation and lipid metabolism of glucocorticoid-induced osteoporosis rats through canonical Wnt signaling pathway. *Evid. Based. Complement. Altern. Med.* 2016, 4927035. doi:10.1155/2016/4927035
- Jing, D., Li, F., Jiang, M., Cai, J., Wu, Y., Xie, K., et al. (2013). Pulsed electromagnetic fields improve bone microstructure and strength in ovariectomized rats through a Wnt/Lrp5/ $\beta$ -catenin signaling-associated mechanism. *PLoS One* 8, e79377. doi:10.1371/journal.pone.0079377
- Kfoury, Y., and Scadden, D. T. (2015). Mesenchymal cell contributions to the stem cell niche. *Cell Stem Cell* 16 (3), 239–253. doi:10.1016/j.stem.2015.02.019
- Kusumbe, A. P., Ramasamy, S. K., and Adams, R. H. (2014). Coupling of angiogenesis and osteogenesis by a specific vessel subtype in bone. *Nature* 507 (7492), 323–328. doi:10.1038/nature13145
- Kylmaja, E., Nakamura, M., and Tuukkanen, J. (2016). Osteoclasts and remodeling based bone formation. *Curr. Stem Cell Res. Ther.* 11 (8), 626–633. doi:10.2174/1574888x10666151019115724
- Lacey, D. L., Timms, E., Tan, H. L., Kelley, M., Dunstan, C., Burgess, T., et al. (1998). Osteoprotegerin ligand is a cytokine that regulates osteoclast differentiation and activation. *Cell* 93 (2), 165–176. doi:10.1016/s0092-8674(00)81569-x
- Lee, J. H., and McLeod, K. J. (2000). Morphologic responses of osteoblast-like cells in monolayer culture to ELF electromagnetic fields. *Bioelectromagnetics* 21 (2), 129–136. doi:10.1002/(sici)1521-186x(200002)21:2<129::aid-bem8>3.0.co;2-q
- Lee, N. K., Sowa, H., Hinoi, E., Ferron, M., Ahn, J. D., Confavreux, C., et al. (2007). Endocrine regulation of energy metabolism by the skeleton. *Cell* 130 (3), 456–469. doi:10.1016/j.cell.2007.05.047
- Li, C., Chai, Y., Wang, L., Gao, B., Chen, H., Gao, P., et al. (2017). Programmed cell senescence in skeleton during late puberty. *Nat. Commun.* 8 (1), 1312. doi:10.1038/s41467-017-01509-0
- Li, J. K., Lin, J. C. A., Liu, H. C., and Chang, W. H. S. (2007). Cytokine release from osteoblasts in response to different intensities of pulsed electromagnetic field stimulation. *Electromagn. Biol. Med.* 26 (3), 153–165. doi:10.1080/15368370701572837
- Li, J., Zhang, N., Huang, X., Xu, J., Fernandes, J. C., Dai, K., et al. (2013). Dexamethasone shifts bone marrow stromal cells from osteoblasts to adipocytes by C/EBP $\alpha$  promoter methylation. *Cell Death Dis.* 4, e832. doi:10.1038/cddis.2013.348
- Li, X., Jin, L., Cui, Q., Wang, G. J., and Balian, G. (2005). Steroid effects on osteogenesis through mesenchymal cell gene expression. *Osteoporos. Int.* 16 (1), 101–108. doi:10.1007/s00198-004-1649-7
- Lin, N. Y., Chen, C. W., Kagwiria, R., Liang, R., Beyer, C., Distler, A., et al. (2016). Inactivation of autophagy ameliorates glucocorticoid-induced and ovariectomy-induced bone loss. *Ann. Rheum. Dis.* 75 (6), 1203–1210. doi:10.1136/annrheumdis-2015-207240
- Liu, H. F., Yang, L., He, H. C., Zhou, J., Liu, Y., Wang, C. Y., et al. (2013). Pulsed electromagnetic fields on postmenopausal osteoporosis in southwest China: A randomized, active-controlled clinical trial. *Bioelectromagnetics* 34 (4), 323–332. doi:10.1002/bem.21770
- Liu, H., Zhou, J., Gu, L., and Zuo, Y. (2017). The change of HCN1/HCN2 mRNA expression in peripheral nerve after chronic constriction injury induced neuropathy followed by pulsed electromagnetic field therapy. *Oncotarget* 8 (1), 1110–1116. doi:10.18632/oncotarget.13584
- Liu, X., Chai, Y., Liu, G., Su, W., Guo, Q., Lv, X., et al. (2021). Osteoclasts protect bone blood vessels against senescence through the angiogenin/plexin-B2 axis. *Nat. Commun.* 12 (1), 1832. doi:10.1038/s41467-021-22131-1
- Lohmann, C. H., Schwartz, Z., Liu, Y., Li, Z., Simon, B. J., Sylvia, V. L., et al. (2003). Pulsed electromagnetic fields affect phenotype and connexin 43 protein expression in MLO-Y4 osteocyte-like cells and ROS 17/2.8 osteoblast-like cells. *J. Orthop. Res.* 21 (2), 326–334. doi:10.1016/s0736-0266(02)00137-7
- Loiselle, A. E., Jiang, J. X., and Donahue, H. J. (2013). Gap junction and hemichannel functions in osteocytes. *Bone* 54 (2), 205–212. doi:10.1016/j.bone.2012.08.132
- Lu, T., Huang, Y., Zhang, C., Chai, M., and Zhang, J. (2015). Effect of pulsed electromagnetic field therapy on the osteogenic and adipogenic differentiation of bone marrow mesenchymal stem cells. *Genet. Mol. Res.* 14 (3), 11535–11542. doi:10.4238/2015.september.28.5
- Mak, W., Shao, X., Dunstan, C. R., Seibel, M. J., and Zhou, H. (2009). Biphasic glucocorticoid-dependent regulation of Wnt expression and its inhibitors in mature osteoblastic cells. *Calcif. Tissue Int.* 85 (6), 538–545. doi:10.1007/s00223-009-9303-1
- Martin, S. K., Fitter, S., Dutta, A. K., Matthews, M. P., Walkley, C. R., Hall, M. N., et al. (2015). Brief report: The differential roles of mTORC1 and mTORC2 in mesenchymal stem cell differentiation. *Stem Cells* 33 (4), 1359–1365. doi:10.1002/stem.1931
- Matsunaga, S., Sakou, T., and Ijiri, K. (1996). Osteogenesis by pulsing electromagnetic fields (PEMFs): Optimum stimulation setting. *Vivo* 10 (3), 351–356.
- O'Brien, C. A., Jia, D., Plotkin, L. I., Bellido, T., Powers, C. C., Stewart, S. A., et al. (2004). Glucocorticoids act directly on osteoblasts and osteocytes to induce their apoptosis and reduce bone formation and strength. *Endocrinology* 145 (4), 1835–1841. doi:10.1210/en.2003-0990
- Ongaro, A., Pellati, A., Bagheri, L., Fortini, C., Setti, S., and De Mattei, M. (2014). Pulsed electromagnetic fields stimulate osteogenic differentiation in human bone marrow and adipose tissue derived mesenchymal stem cells. *Bioelectromagnetics* 35 (6), 426–436. doi:10.1002/bem.21862
- Ono, N., Ono, W., Mizoguchi, T., Nagasawa, T., Frenette, P., and Kronenberg, H. (2014). Vasculature-associated cells expressing nestin in developing bones encompass early cells in the osteoblast and endothelial lineage. *Dev. Cell* 29 (3), 330–339. doi:10.1016/j.devcel.2014.03.014
- Peng, Y., Lv, S., Li, Y., Zhu, J., Chen, S., Zhen, G., et al. (2020). Glucocorticoids disrupt skeletal angiogenesis through transrepression of NF- $\kappa$ B-Mediated preosteoclast pdgfr transcription in young mice. *J. Bone Min. Res.* 35 (6), 1188–1202. doi:10.1002/jbmr.3987
- Peng, Y., Lv, S., Li, Y., Zhu, J., Chen, S., Zhen, G., et al. (2020). Glucocorticoids disrupt skeletal angiogenesis through transrepression of NF- $\kappa$ B-Mediated preosteoclast pdgfr



- transcription in young mice. *Official J. Am. Soc. Bone Mineral Res.* 35 (6), 1188–1202. doi:10.1002/jbmr.3987
- Pereira, R. C., Delany, A. M., and Canalis, E. (2002). Effects of cortisol and bone morphogenetic protein-2 on stromal cell differentiation: Correlation with CCAAT-enhancer binding protein expression. *Bone* 30 (5), 685–691. doi:10.1016/s8756-3282(02)00687-7
- Pereira, R. M. R., Perez, M. O., Paula, A. P., Moreira, C., Castro, C. H. M., Zerbini, C. A. F., et al. (2020). 2020 *Arch. Osteoporos.* 16(1): 49. doi:10.1007/s11657-021-00902-z
- Piemontese, M., Onal, M., Xiong, J., Wang, Y., Almeida, M., Thostenson, J. D., et al. (2015). Suppression of autophagy in osteocytes does not modify the adverse effects of glucocorticoids on cortical bone. *Bone* 75, 18–26. doi:10.1016/j.bone.2015.02.005
- Pufe, T. (2003). The role of vascular endothelial growth factor in glucocorticoid-induced bone loss: Evaluation in a minipig model. *Bone* 33 (6), 869–876. doi:10.1016/j.bone.2003.08.002
- Qian, G., Wang, M., Dong, Y., Hong, Y., Yu, Y., and Mei, J. (2021). Effect of combined treatment with pulsed electromagnetic field stimulation and sclerostin monoclonal antibody on changes in bone metabolism and pedicle screw augmentation in rabbits with ovariectomy-induced osteoporosis. *Ann. Palliat. Med.* 10 (2), 1070–1078. doi:10.21037/apm-20-473
- Rae, M., Mohamad, A., Price, D., Hadoke, P. W. F., Walker, B. R., Mason, J. I., et al. (2009). Cortisol inactivation by 11 $\beta$ -hydroxysteroid dehydrogenase-2 may enhance endometrial angiogenesis via reduced thrombospondin-1 in heavy menstruation. *J. Clin. Endocrinol. Metab.* 94 (4), 1443–1450. doi:10.1210/jc.2008-1879
- Raggatt, L. J., and Partridge, N. C. (2010). Cellular and molecular mechanisms of bone remodeling. *J. Biol. Chem.* 285 (33), 25103–25108. doi:10.1074/jbc.r109.041087
- Ramli, F. F., and Chin, K.-Y. (2020). A review of the potential application of osteocyte-related biomarkers, fibroblast growth factor-23, sclerostin, and dickkopf-1 in predicting osteoporosis and fractures. *Diagn. (Basel)* 10, 145. doi:10.3390/diagnostics10030145
- Reeve, J., Arlot, M., Wootton, R., Edouard, C., Tellez, M., Hesp, R., et al. (1988). Skeletal blood flow, iliac histomorphometry, and strontium kinetics in osteoporosis: A relationship between blood flow and corrected apposition rate. *J. Clin. Endocrinol. Metab.* 66 (6), 1124–1131. doi:10.1210/jcem-66-6-1124
- Roosbeh, N., and Abdi, F. (2018). Influence of radiofrequency electromagnetic fields on the fertility system: Protocol for a systematic review and meta-analysis. *JMIR Res. Protoc.* 7, e33. doi:10.2196/resprot.9102
- Ross, C. L., Ang, D. C., and Almeida-Porada, G. (2019). Targeting mesenchymal stromal cells/pericytes with pulsed electromagnetic field (PEMF) has the potential to treat rheumatoid arthritis. *Front. Immunol.* 10, 266. doi:10.3389/fimmu.2019.00266
- Sarbassov, D. D., Ali, S. M., Sengupta, S., Sheen, J. H., Hsu, P. P., Bagley, A. F., et al. (2006). Prolonged rapamycin treatment inhibits mTORC2 assembly and Akt/PKB. *Mol. Cell* 22 (2), 159–168. doi:10.1016/j.molcel.2006.03.029
- Schorlemmer, S., Ignatius, A., Claes, L., and Augat, P. (2005). Inhibition of cortical and cancellous bone formation in glucocorticoid-treated OVX sheep. *Bone* 37 (4), 491–496. doi:10.1016/j.bone.2005.05.002
- Schwartz, Z., Simon, B. J., Duran, M. A., Barabino, G., Chaudhri, R., and Boyan, B. D. (2008). Pulsed electromagnetic fields enhance BMP-2 dependent osteoblastic differentiation of human mesenchymal stem cells. *J. Orthop. Res.* 26 (9), 1250–1255. doi:10.1002/jor.20591
- Shen, G., Ren, H., Shang, Q., Qiu, T., Yu, X., Zhang, Z., et al. (2018). Autophagy as a target for glucocorticoid-induced osteoporosis therapy. *Cell Mol. Life Sci.* 75 (15), 2683–2693. doi:10.1007/s00018-018-2776-1
- Siddiqui, J. A., and Partridge, N. C. (2016). Physiological bone remodeling: Systemic regulation and growth factor involvement. *Physiology* 31 (3), 233–245. doi:10.1152/physiol.00061.2014
- Sivagurunathan, S., Muir, M. M., Brennan, T. C., Seale, J. P., and Mason, R. S. (2005). Influence of glucocorticoids on human osteoclast generation and activity. *J. Bone Min. Res.* 20 (3), 390–398. doi:10.1359/jbmr.041233
- Sivaraj, K. K., and Adams, R. H. (2016). Blood vessel formation and function in bone. *Development* 143 (15), 2706–2715. doi:10.1242/dev.136861
- Smith, T. L., Wong-Gibbons, D., and Maultsby, J. (2004). Microcirculatory effects of pulsed electromagnetic fields. *J. Orthop. Res.* 22 (1), 80–84. doi:10.1016/s0736-0266(03)00157-8
- Sollazzo, V., Palmieri, A., Pezzetti, F., Massari, L., and Carinci, F. (2010). Effects of pulsed electromagnetic fields on human osteoblastlike cells (MG-63): A pilot study. *Clin. Orthop. Relat. Res.* 468 (8), 2260–2277. doi:10.1007/s11999-010-1341-5
- Song, L., Cao, L., Liu, R., Ma, H., Li, Y., Shang, Q., et al. (2020). The critical role of T cells in glucocorticoid-induced osteoporosis. *Cell Death Dis.* 12 (1), 45. doi:10.1038/s41419-020-03249-4
- Su, J., Chai, Y., Ji, Z., Xie, Y., Yu, B., and Zhang, X. (2020). Cellular senescence mediates the detrimental effect of prenatal dexamethasone exposure on postnatal long bone growth in mouse offspring. *Stem Cell Res. Ther.* 11 (1), 270. doi:10.1186/s13287-020-01790-9
- Takano-Murakami, R., Tokunaga, K., Kondo, N., Ito, T., Kitahara, H., Ito, M., et al. (2009). Glucocorticoid inhibits bone regeneration after osteonecrosis of the femoral head in aged female rats. *Tohoku J. Exp. Med.* 217 (1), 51–58. doi:10.1620/tjem.217.51
- Tschon, M., Veronesi, F., Contartese, D., Sartori, M., Martini, L., Vincenzi, F., et al. (2018). Effects of pulsed electromagnetic fields and platelet rich plasma in preventing osteoclastogenesis in an *in vitro* model of osteolysis. *J. Cell Physiol.* 233 (3), 2645–2656. doi:10.1002/jcp.26143
- Waldorff, E. I., Zhang, N., and Ryaby, J. T. (2017). Pulsed electromagnetic field applications: A corporate perspective. *J. Orthop. Transl.* 9, 60–68. doi:10.1016/j.jot.2017.02.006
- Wang, F. S., Ko, J. Y., Weng, L. H., Yeh, D. W., Ke, H. J., and Wu, S. L. (2009). Inhibition of glycogen synthase kinase-3 $\beta$  attenuates glucocorticoid-induced bone loss. *Life Sci.* 85 (19–20), 685–692. doi:10.1016/j.lfs.2009.09.009
- Wang, F. S., Lin, C. L., Chen, Y. J., Wang, C. J., Yang, K. D., Huang, Y. T., et al. (2005). Secreted frizzled-related protein 1 modulates glucocorticoid attenuation of osteogenic activities and bone mass. *Endocrinology* 146 (5), 2415–2423. doi:10.1210/en.2004-1050
- Wang, Q., Zhou, J., Wang, X., Xu, Y., Liang, Z., Gu, X., et al. (2022). Coupling induction of osteogenesis and type H vessels by pulsed electromagnetic fields in ovariectomy-induced osteoporosis in mice. *Bone* 154, 116211. doi:10.1016/j.bone.2021.116211
- Wang, T., Huang, S., and He, C. (2022). Senescent cells: A therapeutic target for osteoporosis. *Cell Prolif.* 55, e13323. doi:10.1111/cpr.13323
- Wang, T., Xie, W., and Ye, W. (2019). Effects of electromagnetic fields on osteoarthritis. *Biomed. Pharmacother.* 118, 109282. doi:10.1016/j.biopha.2019.109282
- Wang, T., Yang, L., Jiang, J., Liu, Y., Fan, Z., Zhong, C., et al. (2019). Pulsed electromagnetic fields: Promising treatment for osteoporosis. *Osteoporos. Int.* 30 (2), 267–276. doi:10.1007/s00198-018-04822-6
- Wang, T., Yang, L., Liang, Z., Bai, L., Pei, H., Zhang, T., et al. (2022). Pulsed electromagnetic fields attenuate glucocorticoid-induced bone loss by targeting senescent LepR(+) bone marrow mesenchymal stromal cells. *Biomater. Adv.* 133, 112635. doi:10.1016/j.msec.2021.112635
- Wang, T., Yang, L., Liang, Z., Wang, L., Su, F., Wang, X., et al. (2021). Targeting cellular senescence prevents glucocorticoid-induced bone loss through modulation of the DPP4-GLP-1 axis. *Signal Transduct. Target Ther.* 6 (1), 143. doi:10.1038/s41392-021-00528-0
- Wang, T., Yu, X., and He, C. (2018). Pro-inflammatory cytokines: Cellular and molecular drug targets for glucocorticoid-induced-osteoporosis via osteocyte. *Curr. Drug Targets* 20, 1. doi:10.2174/1389450119666180405094046
- Wang, T., Yu, X., and He, C. (2019). Pro-inflammatory cytokines: Cellular and molecular drug targets for glucocorticoid-induced-osteoporosis via osteocyte. *Curr. Drug Targets* 20 (1), 1–15. doi:10.2174/1389450119666180405094046
- Wang, X. Y., Gong, L. J., Huang, J. M., Jiang, C., and Yan, Z. Q. (2020). Pinocembrin alleviates glucocorticoid-induced apoptosis by activating autophagy via suppressing the PI3K/Akt/mTOR pathway in osteocytes. *Eur. J. Pharmacol.* 880, 173212. doi:10.1016/j.ejphar.2020.173212
- Weinstein, R. S. (2007). Is long-term glucocorticoid therapy associated with a high prevalence of asymptomatic vertebral fractures? *Nat. Clin. Pract. Endocrinol. Metab.* 3 (2), 86–87. doi:10.1038/ncpendmet0372
- Weinstein, R. S., Chen, J. R., Powers, C. C., Stewart, S. A., Landes, R. D., Bellido, T., et al. (2002). Promotion of osteoclast survival and antagonism of bisphosphonate-induced osteoclast apoptosis by glucocorticoids. *J. Clin. Invest.* 109 (8), 1041–1048. doi:10.1172/jci0214538
- Weinstein, R. S., and Manolagas, S. C. (2000). Apoptosis and osteoporosis. *Am. J. Med.* 108 (2), 153–164. doi:10.1016/s0002-9343(99)00420-9
- Xia, X., Kar, R., Gluhak-Heinrich, J., Yao, W., Lane, N. E., Bonewald, L. F., et al. (2010). Glucocorticoid-induced autophagy in osteocytes. *J. Bone Min. Res.* 25 (11), 2479–2488. doi:10.1002/jbmr.160
- Xie, H., Cui, Z., Wang, L., Xia, Z., Hu, Y., Xian, L., et al. (2014). PDGF-BB secreted by preosteoclasts induces angiogenesis during coupling with osteogenesis. *Nat. Med.* 20 (11), 1270–1278. doi:10.1038/nm.3668
- Xu, F., and Teitelbaum, S. L. (2013). Osteoclasts: New insights. *Bone Res.* 1 (1), 11–26. doi:10.4248/br201301003
- Yao, W., Cheng, Z., Busse, C., Pham, A., Nakamura, M. C., and Lane, N. E. (2008). Glucocorticoid excess in mice results in early activation of osteoclastogenesis and adipogenesis and prolonged suppression of osteogenesis: A longitudinal study of gene expression in bone tissue from glucocorticoid-treated mice. *Arthritis Rheum.* 58 (6), 1674–1686. doi:10.1002/art.23454
- Yin, L., Li, Y. B., and Wang, Y. S. (2006). Dexamethasone-induced adipogenesis in primary marrow stromal cell cultures: Mechanism of steroid-induced osteonecrosis. *Chin. Med. J. Engl.* 119 (7), 581–588. doi:10.1097/00029330-200604010-00012
- Zhen, G., Dan, Y., Wang, R., Dou, C., Guo, Q., Zarr, M., et al. (2021). An antibody against Siglec-15 promotes bone formation and fracture healing by increasing TRAP+ mononuclear cells and PDGF-BB secretion. *Bone Res.* 9 (1), 47. doi:10.1038/s41413-021-00161-1
- Zhou, J., Li, X., Liao, Y., Feng, W., Fu, C., and Guo, X. (2015). Pulsed electromagnetic fields inhibit bone loss in streptozotocin-induced diabetic rats. *Endocrine* 49 (1), 258–266. doi:10.1007/s12020-014-0439-z
- Zhu, S., He, H., Zhang, C., Wang, H., Gao, C., Yu, X., et al. (2017). Effects of pulsed electromagnetic fields on postmenopausal osteoporosis. *Bioelectromagnetics* 38 (6), 406–424. doi:10.1002/bem.22065





## OPEN ACCESS

## EDITED BY

Nora Bloise,  
University of Pavia, Italy

## REVIEWED BY

Gabriele Ceccarelli,  
University of Pavia, Italy  
Livia Visai,  
University of Pavia, Italy

## \*CORRESPONDENCE

Heng Liu,  
✉ liuxiaoheng2018@gmail.com  
Roland M. Klar,  
✉ rkyh7@umkc.edu

## SPECIALTY SECTION

This article was submitted  
to Biomaterials,  
a section of the journal  
Frontiers in Bioengineering  
and Biotechnology

RECEIVED 08 January 2023

ACCEPTED 06 March 2023

PUBLISHED 16 March 2023

## CITATION

Liu H, Müller PE, Aszódi A and Klar RM  
(2023), Osteochondrogenesis by TGF- $\beta$ 3,  
BMP-2 and noggin growth factor  
combinations in an *ex vivo* muscle tissue  
model: Temporal function changes  
affecting tissue morphogenesis.  
*Front. Bioeng. Biotechnol.* 11:1140118.  
doi: 10.3389/fbioe.2023.1140118

## COPYRIGHT

© 2023 Liu, Müller, Aszódi and Klar. This is  
an open-access article distributed under  
the terms of the [Creative Commons  
Attribution License \(CC BY\)](#). The use,  
distribution or reproduction in other  
forums is permitted, provided the original  
author(s) and the copyright owner(s) are  
credited and that the original publication  
in this journal is cited, in accordance with  
accepted academic practice. No use,  
distribution or reproduction is permitted  
which does not comply with these terms.

# Osteochondrogenesis by TGF- $\beta$ 3, BMP-2 and noggin growth factor combinations in an *ex vivo* muscle tissue model: Temporal function changes affecting tissue morphogenesis

Heng Liu<sup>1,2\*</sup>, Peter E. Müller<sup>1</sup>, Attila Aszódi<sup>1</sup> and Roland M. Klar<sup>1,3\*</sup>

<sup>1</sup>Department of Orthopaedics and Trauma Surgery, Musculoskeletal University Center Munich (MUM), University Hospital, LMU Munich, Munich, Germany, <sup>2</sup>Department of Orthopaedics and Traumatology, Beijing Jishuitan Hospital, The Fourth Medical College of Peking University, Beijing, China, <sup>3</sup>Department of Oral and Craniofacial Sciences, University of Missouri-Kansas City, Kansas City, MO, United States

In the absence of clear molecular insight, the biological mechanism behind the use of growth factors applied in osteochondral regeneration is still unresolved. The present study aimed to resolve whether multiple growth factors applied to muscle tissue *in vitro*, such as TGF- $\beta$ 3, BMP-2 and Noggin, can lead to appropriate tissue morphogenesis with a specific osteochondrogenic nature, thereby revealing the underlying molecular interaction mechanisms during the differentiation process. Interestingly, although the results showed the typical modulatory effect of BMP-2 and TGF- $\beta$ 3 on the osteochondral process, and Noggin seemingly downregulated specific signals such as BMP-2 activity, we also discovered a synergistic effect between TGF- $\beta$ 3 and Noggin that positively influenced tissue morphogenesis. Noggin was observed to upregulate BMP-2 and OCN at specific time windows of culture in the presence of TGF- $\beta$ 3, suggesting a temporal time switch causing functional changes in the signaling protein. This implies that signals change their functions throughout the process of new tissue formation, which may depend on the presence or absence of specific singular or multiple signaling cues. If this is the case, the signaling cascade is far more intricate and complex than originally believed, warranting intensive future investigations so that regenerative therapies of a critical clinical nature can function properly.

## KEYWORDS

tissue engineering, TGF- $\beta$ 3, BMP-2, noggin, temporal modulation, muscle tissue

## 1 Introduction

Successful regeneration of cartilage and bone remains an unresolved enigma to be solved clinically (Pittenger et al., 2019; Xiong et al., 2021). Due to intrinsic limitations in the ability of articular cartilage to self-renew and repair, cartilage-related injuries often result in osteoarthritic degeneration and long-term pain (Huang et al., 2019; Huynh et al., 2019). Among numerous restoration techniques, osteochondral grafts hold a more favorable prognosis than cartilage grafts alone because the bone-to-bone interface is more likely to integrate than the cartilage-to-chondral interface (Schaefer et al., 2002; Sheehy et al., 2013).

An engineered osteochondral construct with cartilage and bone phenotypes seems to be a potential strategy for the treatment of chondral and osteochondral defects (Schaefer et al., 2002; Alhadlaq and Mao, 2005). During the past decade, although some great successes have been achieved to engineer ideal biomimetic osteochondral tissue, numerous challenges still need to be cleared to realize its final clinical application (Chen et al., 2011; Rodrigues et al., 2012; Zhang et al., 2019). Therefore, alternative models and improved osteochondral tissue engineering (TE) technologies should be explored.

According to previous studies, the growth factors-loaded, muscle tissue-based, biomaterial induction system is a promising novel technology for TE (Betz et al., 2015; Betz et al., 2018; Ren et al., 2018; Xiong et al., 2020). Muscle is a relatively easily obtained tissue with a firm and durable self-repair capability; thus, harvesting muscle tissue does not cause severe morbidity in the donor area (Betz et al., 2009). It is well known that muscle tissue is an attractive cell source for TE since it contains abundant stem cells, which possess the potential to differentiate into an osteogenic lineage (Bosch et al., 2000; Ren et al., 2019). Compared to traditional cell culture-based TE approaches, the tissue culture system does not require the extraction and proliferation of autologous-derived osteoprogenitor cells, thus making it easier to operate and much cheaper (Betz et al., 2008; Virk et al., 2011). Additionally, the muscle tissue fragment is a one hundred percent biocompatible scaffold with a complex three-dimensional (3D) structure (Betz et al., 2008; Ren et al., 2019). Its intrinsic extracellular matrix (ECM) contains the necessary amino acids and the essential signaling molecules, providing an in vivo-like culturing milieu that supports cell growth and activity (Brand, 1997; Albert, 2005; Blair et al., 2017). Moreover, as a natural soft tissue scaffold, its easy deformability facilitates its matching to osteochondral defect sites. Furthermore, muscle tissue typically contains tiny blood vessels and numerous capillaries critical for nutrient flow and anabolic activities (Betz et al., 2013; Perniconi and Coletti, 2014; He et al., 2020).

Members of the transforming growth factor-beta (TGF- $\beta$ ) superfamily perform various pleiotropic functions during both antenatal and postnatal development (Alliston et al., 2008). Among them, TGF- $\beta$ 3 and bone morphogenetic protein-2 (BMP-2) play crucial roles in processes of skeletogenesis, including the regulation of mesenchymal stem cell condensation, chondrocyte and osteoblast differentiation, and growth plate expansion (Ripamonti et al., 2016; Wu et al., 2016). TGF- $\beta$ 3 has a bi-functional impact on the maintenance of cartilage metabolic homeostasis, as it favors early-stage chondrocyte proliferation but arrests downstream chondrocyte hypertrophy, which is crucial to preserving hyaline cartilage integrity (Kato et al., 1988; Wu et al., 2016). However, TGF- $\beta$  signaling is also known to induce osteogenesis and accelerate osteoarthritis through a Smad2/3 independent pathway (van der Kraan et al., 2012; van der Kraan, 2014). The osteogenic potential of TGF- $\beta$ 3 has been demonstrated in many different models. For instance, Ripamonti et al. (2015) identified in vivo experiments that TGF- $\beta$ 3 functions as the crucial signaling in regulating osteogenic relative gene expression and thus inducing ectopic bone formation in baboons. BMP-2 is a prerogative molecule during bone formation, as it plays a role in nearly the entire endochondral bone formation process (Gazzerro and Canalis, 2006; Ripamonti, 2006). Evidence has shown that BMP-2 is one

of the most potent inducers for osteogenic differentiation (Huang et al., 2010), in which Noel et al. (2004) certified that even a short duration of BMP-2 expression is sufficient to induce irreversible endochondral bone. Moreover, amongst its other tissue-inductive capabilities, BMP-2 can also promote chondrogenesis (Keller et al., 2011; Chen et al., 2020). The first evidence of this ability was given by Urist (1965), who discovered that BMP-2 could induce both ectopic cartilage and bone formation within the rectus abdominis muscle of adult rabbits.

As a classical extracellular antagonist of BMP-2, Noggin performs pleiotropic roles in various physiological and pathological developmental processes, such as the induction of neural and skeletal muscle tissue in early embryogenesis (Smith and Harland, 1992), and it is also crucial for chondrogenic and osteogenic differentiation (Bayramov et al., 2011; Krause et al., 2011). In mice overexpressing Noggin in the skeleton, osteoblast differentiation and bone formation were impaired, resulting in decreased bone mineral density and weakened osteoblastic function (Devlin et al., 2003; Wu et al., 2003). Nevertheless, the downregulation of Noggin in cells in the bone environment increases the expression of osteogenic differentiation markers and thus enhances the regeneration of bone defects (Gazzerro et al., 2003; Wan et al., 2007). Furthermore, proximal symphalangism and multiple synostoses syndrome in humans can also be attributed to Noggin mutations (Gong et al., 1999).

Previous experimental studies have reported that a combination of morphogens acting synergistically or in modulatory roles could result in superior morphogenesis (Cicione et al., 2015; Huang et al., 2020). For example, Xiong et al. (2020) demonstrated that the combined treatment of TGF- $\beta$ 3, BMP-2, and BMP-7 could promote chondrogenesis in muscle tissue more efficiently than either morphogen applied on its own or in various duplicate combinations. Similar synergistic effects have also been investigated by other scientists, in which co-administration of BMP-2 and TGF- $\beta$ 3 resulted in an improved bone formation response (Haschtmann et al., 2012; Wang et al., 2016; He et al., 2019). However, the antagonistic effect between different TGF- $\beta$ s and BMPs has also been discussed by other researchers (Mehlhorn et al., 2007; Wakefield and Hill, 2013; Xiong, 2020). In addition, the mutual impact between BMPs and Noggin has been intensively explored in the last decades (Re'em-Kalma et al., 1995; Zakin and De Robertis, 2010; Wang et al., 2013). Recent studies have also shown the association between TGF- $\beta$ 3 and Noggin during the process of endochondral bone formation within muscle tissue (Klar et al., 2014; Ripamonti et al., 2015). Nevertheless, the detailed complex interaction mechanisms among these three growth factors and their temporal and spatial behavior have yet to be thoroughly explained.

Therefore, the present study attempted to detect what the osteochondrogenic effects, if any, would be under a temporal signaling cascade of these three growth factors, which are applied to this specialized muscle tissue model platform in seven different patterns. The differentiated cultured muscle tissue was analyzed at 7, 14, and 30 days using three methods (Pittenger et al., 2019): quantitative reverse transcription-polymerase chain reaction (RT-qPCR) (Xiong et al., 2021), immunohistochemistry (IHC), and (Huang et al., 2019) histology. The objectives of this study were (Pittenger et al., 2019): to assess the osteochondrogenic induction

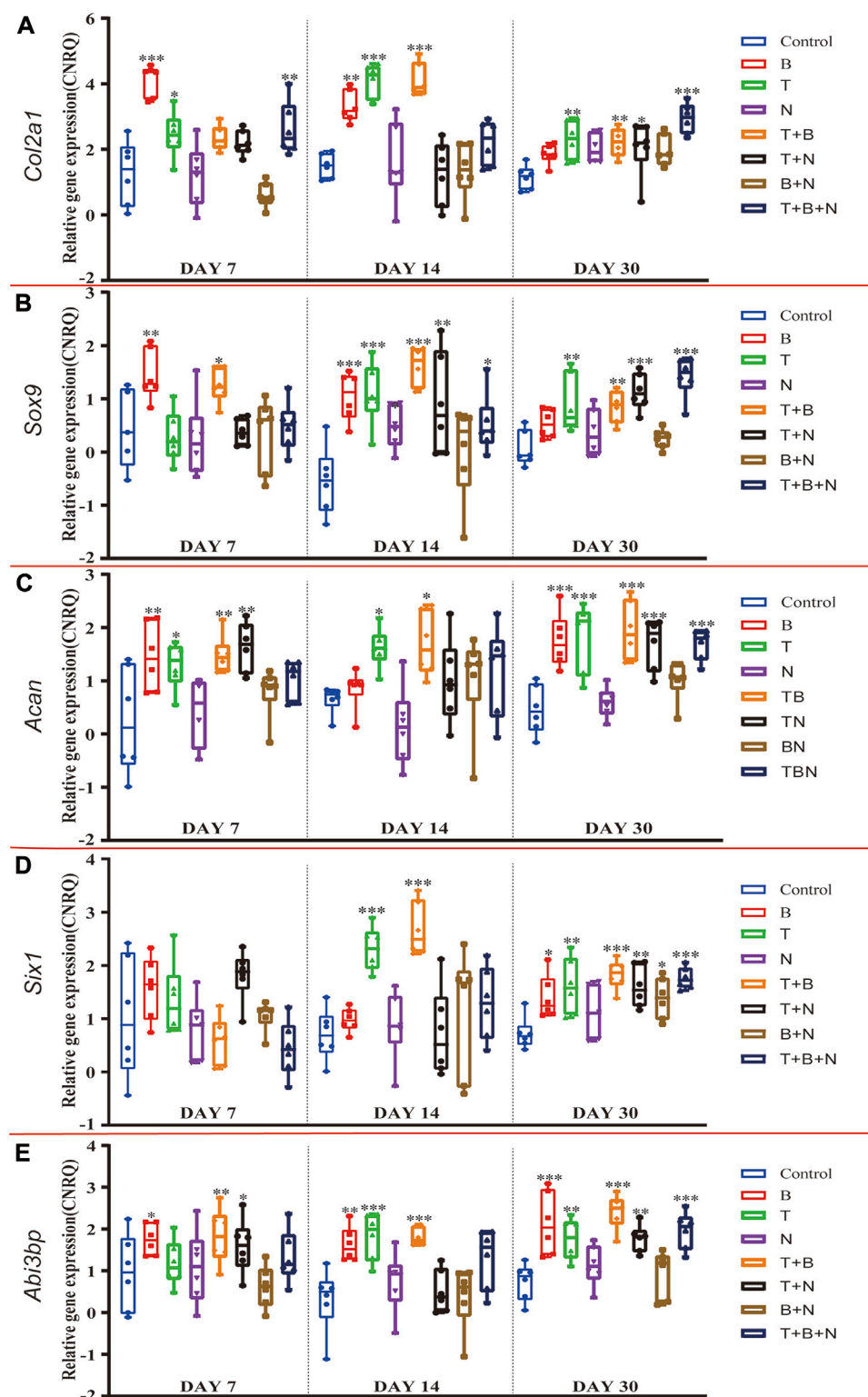


FIGURE 1

The relative gene expression of (A) *Col2a1*, (B) *Sox9*, (C) *Acan*, (D) *Six1* and (E) *Abi3bp* at 7, 14, and 30 days, which were shown as CNRQ. The asterisks indicate that the stimulated group is statistically significant compared to the control group. The baseline number 0 indicates non-cultured fresh tissue was used as the normalization parameter. (n = 6; \* $p < 0.05$ ; \*\* $p < 0.01$ ; \*\*\* $p < 0.001$ ).

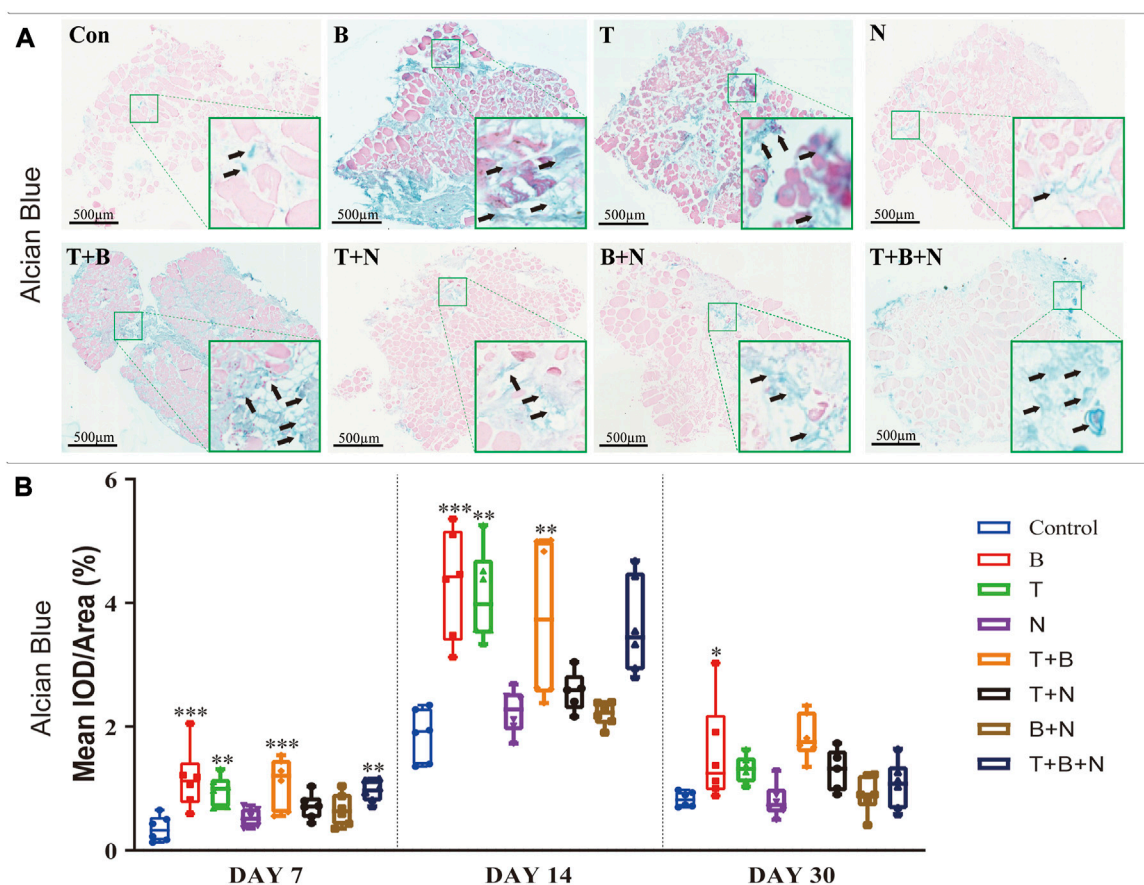


FIGURE 2

The staining results of Alcian Blue in each group. (A) Staining results on day 30; the positive staining color was blue (marked by black arrows). (B) Histomorphometrical assessment; the result was shown as Mean IOD/Area. Control group vs. stimulated groups at 7, 14, and 30 days; the asterisks indicate that the stimulated group is statistically significant compared to the control group. (Magnification:  $\times 40$ ;  $n = 6$ ; \* $p < 0.05$ ; \*\* $p < 0.01$ ; \*\*\* $p < 0.001$ ).

potential of the muscle tissue after 1 month of continuous application of BMP-2 and/or TGF- $\beta 3$  and/or Noggin and (Xiong et al., 2021) to investigate the so far unclear interaction mechanisms between the three growth factors during the endochondral bone induction process and if there are unique interactions in respect to tissue morphogenesis between the various growth factor combinations.

## 2 Results

### 2.1 Chondrogenesis

The chondrogenesis was evaluated at the following levels: gene expression (Figure 1), Alcian Blue (Figure 2) and IHC-ACAN staining (Figure 3, Table 1).

In order to evaluate chondrogenic gene expression in response to single or combined exposure of the modulating factors TGF- $\beta 3$  (T), BMP-2 (B) and Noggin (N) in the muscle tissue model, temporal gene expression of cartilage-specific marker genes were analyzed by RT-qPCR. For the fibrillar collagen marker gene *Col2a1*, the control group showed similar, moderately upregulated

expression on each day compared to the non-cultured, fresh muscle tissue (Figure 1A). The B group had the highest relative *Col2a1* expression on day 7, which was significantly upregulated compared to the control, similar to T and T + B + N groups. The combination of T + B increased *Col2a1* expression significantly only on days 14 and 30. The T + B and T + B + N groups showed the highest relative gene expression on days 14 and 30, respectively. Except for day 30 of the T + N and T + B + N groups and day 7 of the T + B + N group, *Col2a1* gene expression did not change significantly in all other N-treated groups compared to the control (Figure 1A, Supplementary Table S1).

The expression of the chondrogenic master transcription factor *Sox9* peaked in groups B, T + B, and T + B + N on days 7, 14, and 30, respectively, and all three groups showed significant differences compared to the control. The T group exhibited the highest *Sox9* expression on day 14 and showed significant upregulation on days 14 and 30. Among N-treated groups, significant *Sox9* upregulation was observed in the N group on day 14 and in the T + N and T + B + N groups on days 14 and 30, respectively (Figure 1B, Supplementary Table S1). For the major proteoglycan marker *Acan*, significantly upregulated gene expression was found in the B-, T-, T + B-, and T + N-stimulated groups on day 7 compared to the control. On day 14,



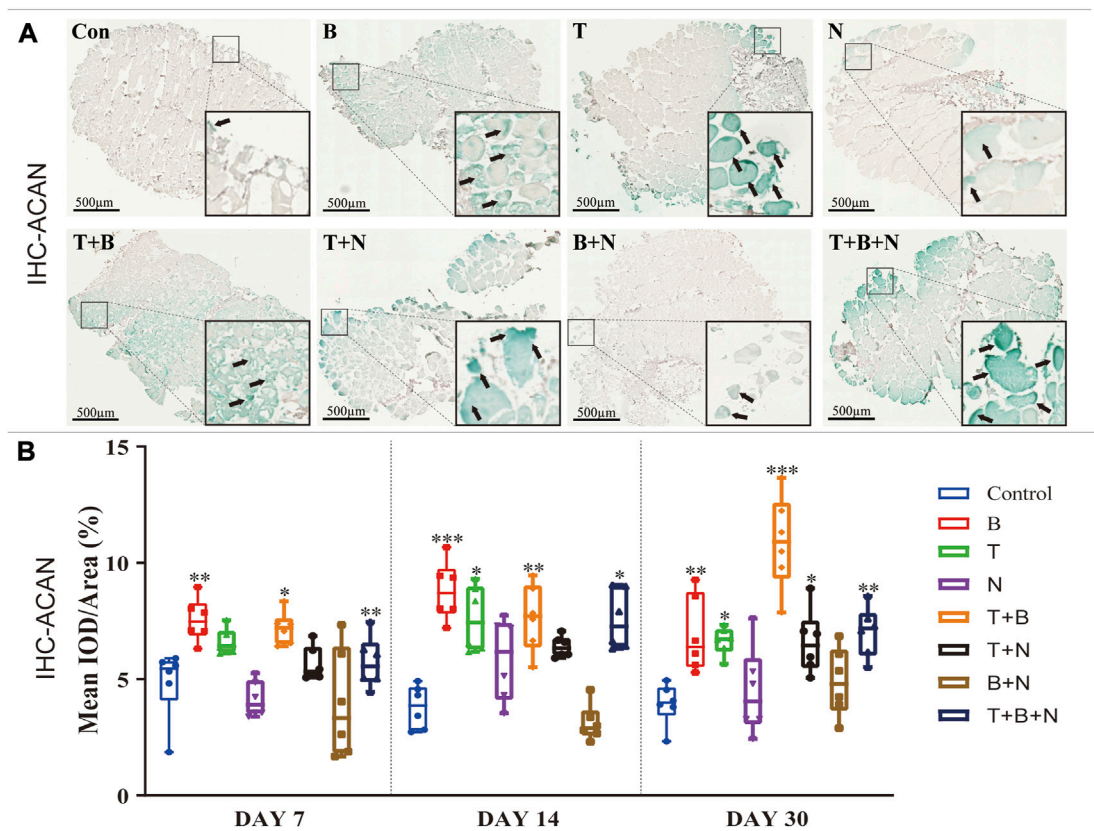


**FIGURE 3**  
The staining results of ACAN antigen in IHC in each group. **(A)** Staining results on day 30; the positive staining color was green (marked by black arrows). **(B)** Histomorphometrical assessment; the result was shown as Mean IOD/Area. Control group vs. stimulated groups at 7, 14, and 30 days; the asterisks indicate that the stimulated group is statistically significant compared to the control group. (Magnification:  $\times 40$ ;  $n = 6$ ;  $*p < 0.05$ ;  $**p < 0.01$ ;  $***p < 0.001$ ).

**TABLE 1** The summarized results of/between these three growth factors.

Growth factor application	Effect/Result (culture period vs reaction intensity chondrogenesis)			Effect/Result (culture period vs reaction intensity for osteogenesis)			Interpretation
	Day 7	Day 14	Day 30	Day 7	Day 14	Day 30	
BMP-2	+++	++	+	+++	++	++	BMP-2 may function as an initiator only with a short effect period
TGF- $\beta$ 3	+	+++	+++	+	+++	+++	TGF- $\beta$ 3 affects tissue morphogenesis mid-late term
Noggin	–	–	–	–	–	–	Noggin inhibits tissue morphogenesis
TGF- $\beta$ 3+BMP-2	–/+	+++	+++	–	++	++	Early stage antagonism that inverts to synergism at later stages
TGF- $\beta$ 3+Noggin	++	–	+++	+	–	++	Synergistic stimulatory effect at early and late culturing stages with periods of inhibition in between (modulation of tissue morphogenesis?)
BMP-2+Noggin	–	–	–	–	–	–	Noggin inhibits BMP-2 function, prevents tissue differentiation
TGF- $\beta$ 3+BMP-2 +Noggin	–	++	+++	–	–	+++	Noggin synergizes with BMP-2 only at specific periods and when in the presence of TGF- $\beta$ 3

Remarks: little to no reaction; –/+ a weakish reaction; + low reacting; ++ mid reaction; +++ high reaction.

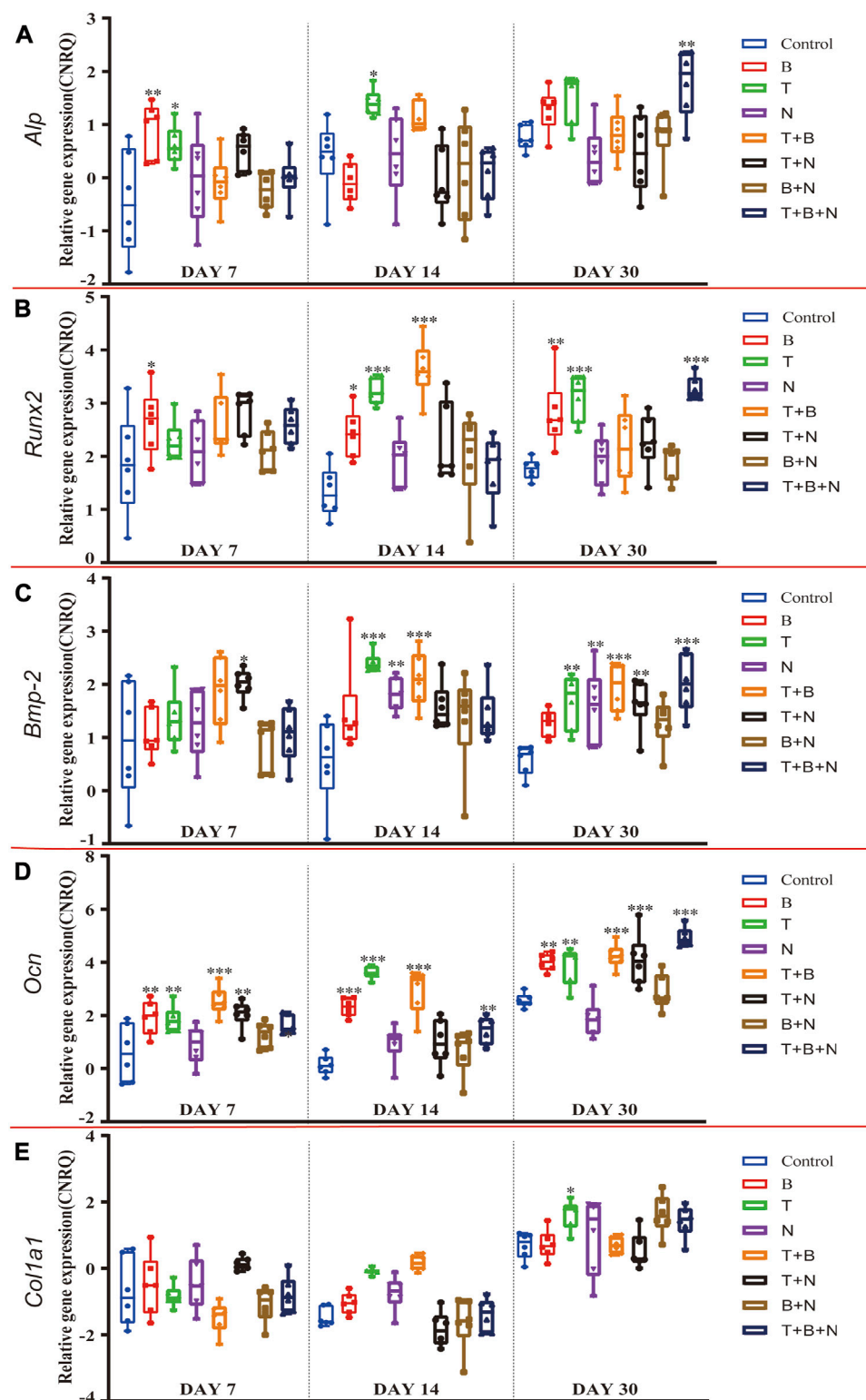


FIGURE 4

The relative gene expression of (A) *Alp*, (B) *Runx2*, (C) *Bmp-2*, (D) *Ocn*, and (E) *Col1a1* at 7, 14, and 30 days, which were shown as CNRQ. The asterisks indicate that the stimulated group is statistically significant compared to the control group. The baseline number 0 indicates non-cultured fresh tissue was used as the normalization parameter. (n = 6; \* $p < 0.05$ ; \*\* $p < 0.01$ ; \*\*\* $p < 0.001$ ).

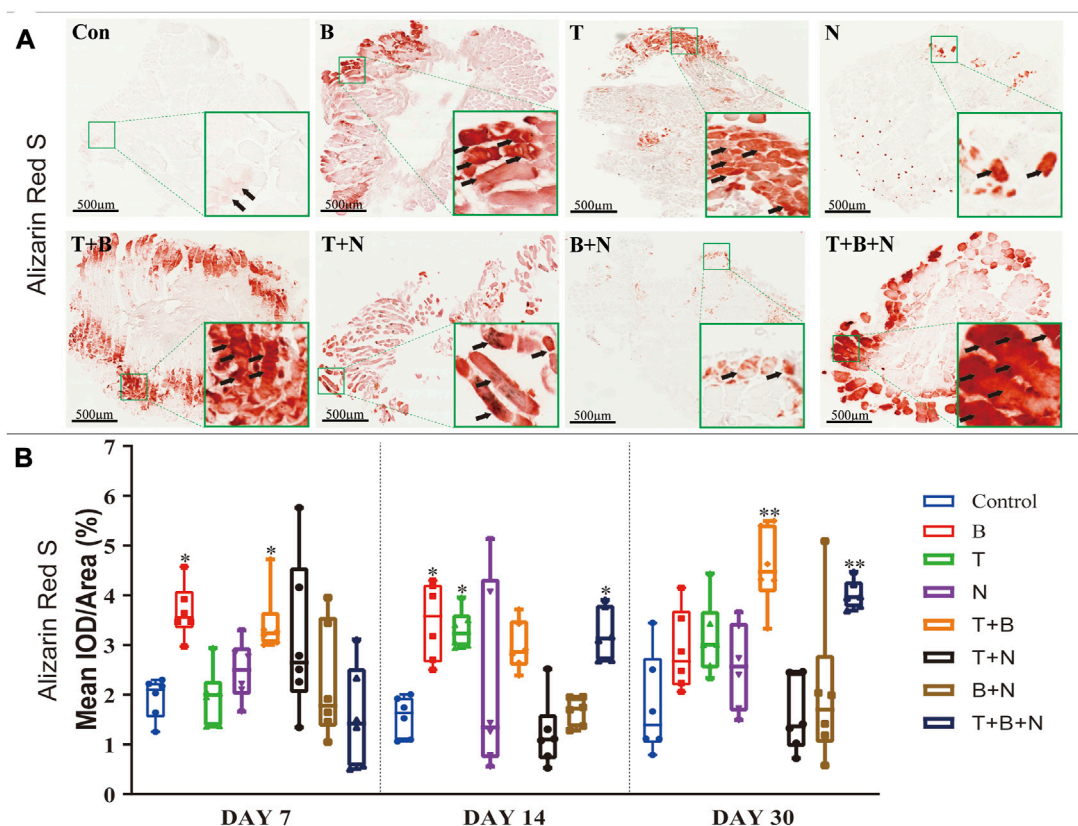


FIGURE 5

The staining results of Alizarin Red S in each group. (A) Staining results on day 30; the positive staining color was red (marked by black arrows). (B) Histomorphometrical assessment; the result was shown as Mean IOD/Area. Control group vs. stimulated groups at 7, 14, and 30 days; the asterisks indicate that the stimulated group is statistically significant compared to the control group. (Magnification:  $\times 40$ ;  $n = 6$ ; \* $p < 0.05$ ; \*\* $p < 0.01$ ; \*\*\* $p < 0.001$ ).

only the T and T + B groups showed significant upregulation. On day 30, all groups except N and B + N presented significant *Acan* upregulation compared to the control (Figure 1C, Supplementary Table S1).

It has been previously shown that transcripts of *Six1* and *Abi3bp* are enriched in articular chondrocytes compared to growth plate chondrocytes; therefore, these genes have been proposed as markers for articular cartilage (Lee et al., 2021). In our muscle tissue model, we found that on day 30, *Six1* gene expression was upregulated in all treated groups compared to the control, except N (Figure 1, Supplementary Table S1), and *Abi3bp* was upregulated in all treated groups, except N and N + B (Figure 1, Supplementary Table S2). In the case of *Six1*, there was no significant difference in gene expression relative to control in either group on day 7, while on day 14, only the T and T + B groups displayed significant *Six1* upregulation (Figure 1D, Supplementary Table S1). Significantly upregulated expression of *Abi3bp* was found in the B, B + T, and T + N groups on day 7 and in the B, B + T, T + N, and T + B + N groups on day 14. Moreover, *Abi3bp* gene expression in the N and B + N groups showed no significant difference compared with control at all three time points (Figure 1E, Supplementary Table S2).

Alcian Blue staining was used to assess chondrogenesis in the cultured muscle tissue samples. Increased staining areas in blue were observed near the fascia or in the intercellular region of the muscle when stimulated by T, B, T + B, and T + B + N at all detection time points compared to the control (Figure 2A). Histomorphometric comparisons with the control showed that the B and T + B groups presented a significantly increased positive reaction area at all three-time points, while the T- and T + B + N-stimulated groups displayed significant positive reactions on days 7 and 14. On the other hand, all groups showed the strongest positive Alcian Blue staining results at 14 days, while the N and B + N groups consistently showed no significant differences compared with the control (Figure 2B, Supplementary Table S4).

IHC-ACAN staining was carried out to show the presence of ACAN antigens. A positive antigen-antibody interaction would be stained in a green color, which could be observed in close proximity to the fascia or in the intercellular region of the muscle when stimulated by B, T, T + B, T + N, and T + B + N at all detection time points (Figure 3A). The histomorphometrical assessments of IHC-ACAN staining showed that the B and T + B groups presented a positive reaction during all three-time points, while the T and T + B + N groups displayed a positive reaction on days 14 and 30. In addition, the T + N group also exhibited a significant difference on

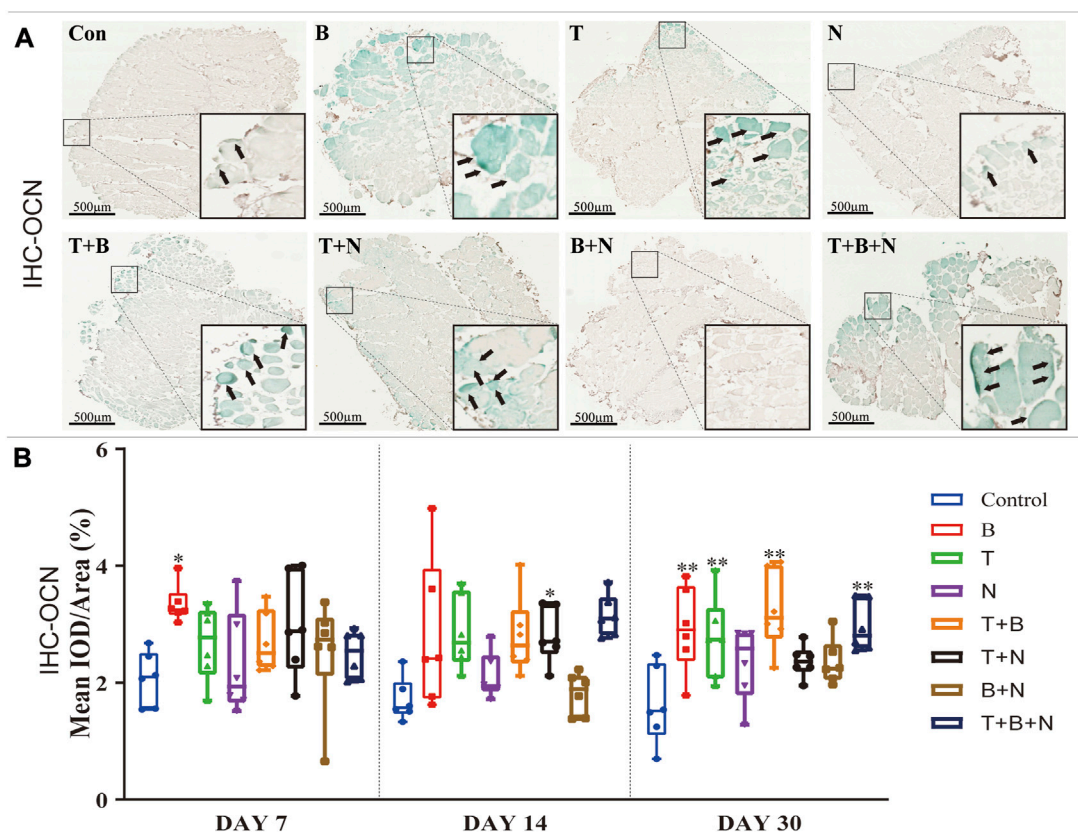


FIGURE 6

The staining results of the OCN antigen in the IHC in each group. (A) Staining results on day 30; the positive staining color was green (marked by black arrows). (B) Histomorphometrical assessment; the result was shown as Mean IOD/Area. Control group vs. stimulated groups at 7, 14, and 30 days; the asterisks indicate that the stimulated group is statistically significant compared to the control group. (Magnification:  $\times 40$ ;  $n = 6$ ;  $*p < 0.05$ ;  $**p < 0.01$ ;  $***p < 0.001$ ).

day 30. Additionally, no B + N group showed a significant difference (Figure 3B, Supplementary Table S4).

## 2.2 Osteogenesis

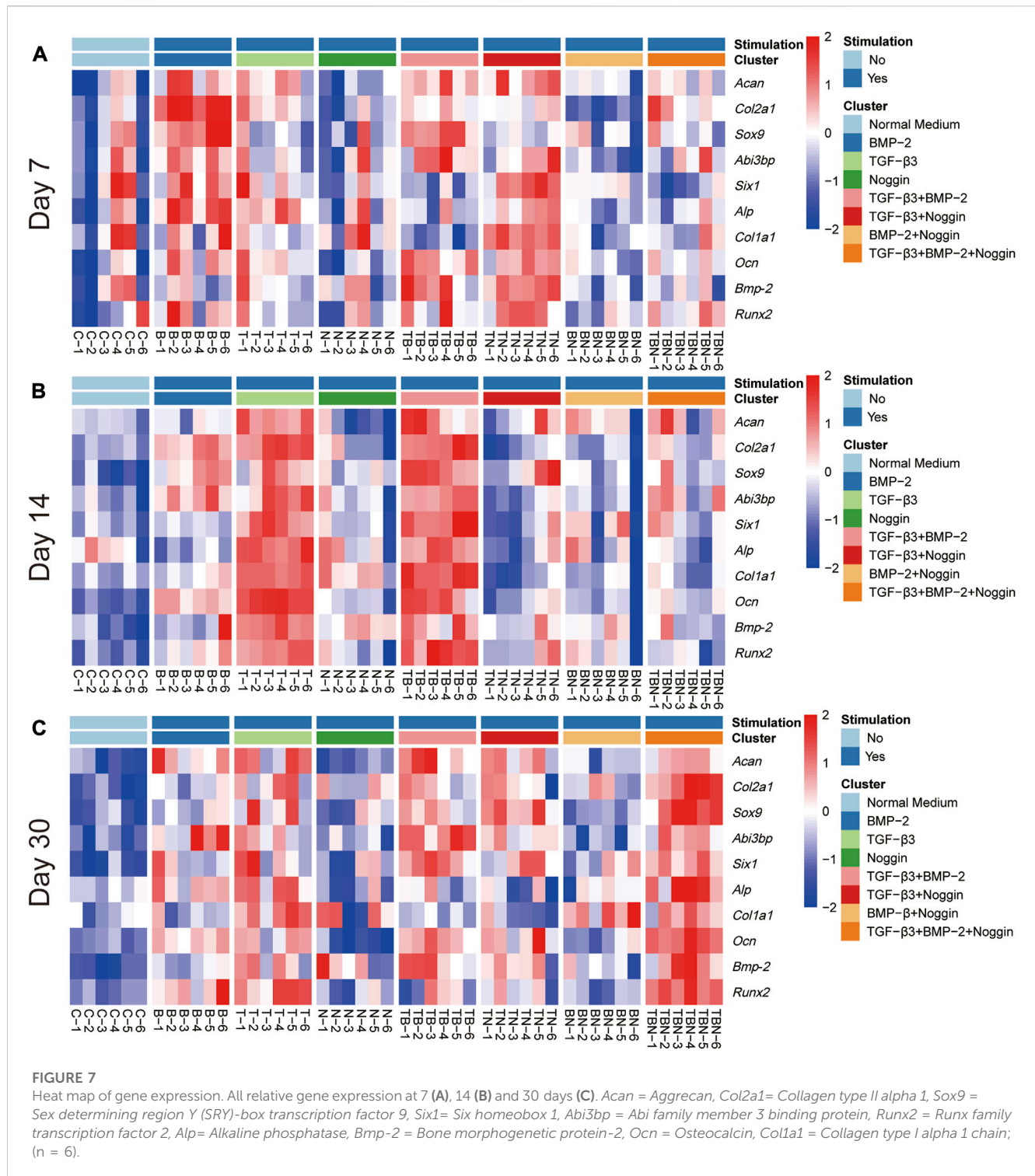
The osteogenesis was evaluated at the following levels: gene expression (Figure 4), Alizarin Red S (Figure 5) and IHC-OCN staining (Figure 6).

For *Alp*, the B group showed the highest relative gene expression on day 7, which was significantly upregulated, along with the T and T + B + N groups. Additionally, the T-induced group was the only one that presented a significant *Alp* expression on day 14, and only the T + N and T + B + N groups demonstrated a significant upregulation of *Alp* expression. On the other hand, *Alp* expression in all N-involved groups showed no significant difference (Figure 4A, Supplementary Table S2). For the relative *Runx2* gene expression, the T + N group became the only group that showed a significant difference at 7 days, while at 14 days, the significantly upregulated *Runx2* gene expression was found in B, T, and T + B groups. By 30 days, the B, T, and T + B + N groups showed high and significant gene expression. In addition, except for the 7-day T + N and 30-day T + B + N groups, *Runx2* gene expression in

all other Noggin-involved groups was not significant (Figure 4B, Supplementary Table S2). For the relative *Bmp-2* gene expression, the T + N group showed a significant difference across all three-time points; in addition, T, N, and T + B groups presented significantly upregulated *Bmp-2* gene expression at both day 14 and 30. Moreover, the T + B + N group showed the highest and most significant gene expression on day 30. In addition, all B + N groups showed non-significant *Bmp-2* gene expression (Figure 4C; Supplementary Table S3). For the relative *Ocn* gene expression, the B, T, T + B, and T + B + N groups all presented significant upregulation among the three-time points. Additionally, the T + N group also showed significant *Ocn* gene expression on days 7 and 30, but a non-significant difference was found on day 14. Furthermore, the N and B + N groups exhibited non-significant *Ocn* gene expression all the time (Figure 4D, Supplementary Table S3). For *Colla1*, no treatment group showed upregulated relative gene expression at 7 days, while the T and T + B groups were significantly upregulated at 14 days. By 30 days, although most stimulated groups showed upregulation of *Colla1* gene expression, only the T group exhibited a significant difference (Figure 4E, Supplementary Table S3).

Alizarin Red S staining was applied to show the depositions of calcium ions in tissues as a measure of osteogenesis. Under B,

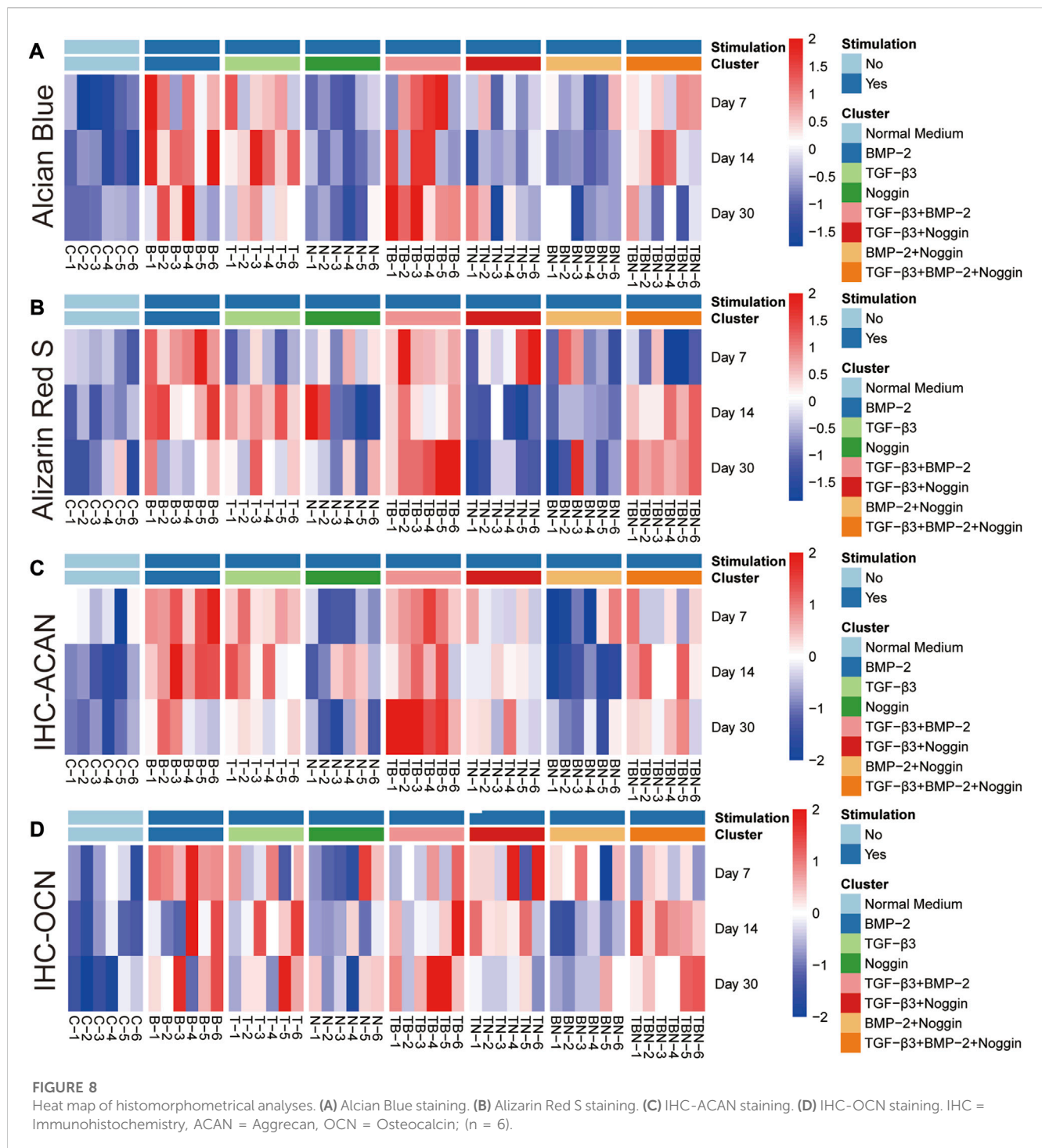




T, T + B, T + N, and T + B + N stimulation, areas of positive staining in red were observed in close proximity to the fascia or intercellular regions of the muscle at all detection time points (Figure 5A). Histomorphometric evaluation of Alizarin Red S staining showed that the B group presented a significant positive reaction on days 7 and 14, while the T group only displayed a significant positive reaction on day 14 compared to the control. In addition, the T + B group displayed a positive

reaction on days 7 and 30. Moreover, the T + B + N group showed significant stimulation of osteogenesis from day 14 until day 30. The N and B + N groups consistently showed no significant difference compared to the control (Figure 5B, Supplementary Table S4).

IHC-OCN staining was carried out to show the presence of the OCN antigen. Under the stimulation of B, T, T + B, T + N, and T + B + N, areas of positive staining were observed in close proximity to



the fascia or intercellular regions of the muscle with green color at all detection time points (Figure 6A). The histomorphometrical assessment of IHC-OCN staining showed that, although there was a generally high positive reaction on day 7, the B group was the only one that had a significant difference. In addition, the T + B + N group became the only significant positive stimulation group at 14 days, while the B, T, T + B, and T + B + N groups all showed significant differences by day 30. Additionally, no B + N group showed a significant difference (Figure 6B, Supplementary Table S4).

## 2.3 Heat map analysis

The heat map analysis of gene expression and histomorphometrical data are represented in Figure 7 and Figure 8, respectively. The heat map is a summary of the results (Table 1) indicating where significant differences exist in the gene expression and tissue development.

The heat map of gene expression showed that the B- and T + N-stimulated groups promoted relatively high gene expression at 7 days (Figure 7A); the T- and T + B-stimulated groups displayed

relatively high gene expression at 14 days (Figure 7B); while the stimulation of T, T + B, T + N, and T + B + N exhibited high gene expression at 30 days (Figure 7C). Compared to 7 and 30 days, stimulation by T + N resulted in less gene expression at 14 days. Additionally, the N and B + N groups did not show high gene expression at all time periods (Figure 7).

As seen in all the histomorphometrical analyses of the heat map, the B and T + B groups presented the most robust positive response results compared to the other participating groups. However, the single B group performed better in the early phase (7 and 14 days), while the combined T + B group was more dominant in the late phase (30 days). In addition, stimulation by T alone also displayed positive results, although slightly weaker than the T + B combination. Furthermore, the T + B + N group resulted in relatively higher positive reactions in all staining at late stages (at 14 and 30 days), except for the 30-day Alcian Blue staining (Figure 8). All results were summarized in Table 1.

### 3 Discussion

The TGF- $\beta$ /BMP signaling pathway is an important thread essential for osteochondrogenic tissue formation (Zhou et al., 2005; Bami et al., 2016; Izadpanahi et al., 2018). Endochondral bone development and articular chondrogenesis are closely regulated by diverse growth factors (Chung et al., 2001; Liao et al., 2014). Generally, the results of this study showed that both chondrogenic and osteogenic-related genes underwent significant changes over the 30 days of *in vitro* culturing with TGF- $\beta$ 3 and/or BMP-2 groups and the TGF- $\beta$ 3+BMP-2+Noggin sets. Combined with the histomorphometrical results, the findings suggest that our muscle tissue may be undergoing an osteochondrogenic process, favoring an articular to endochondral bone transdifferentiation activity. The positive IHC-ACAN and the strong Alcian Blue staining in conjunction with the significant upregulation of *Sox9*, *Acan*, and *Col2a1* genes, in addition to the upregulation of articular cartilage genes *Abi3bp* and *Six1*, suggest that a form of articular chondrogenesis was being induced (Xiong et al., 2020). Whilst it remains unclear if this is proper articular cartilage or a specialized undiscovered form of the process, its detection corroborates the principle that the process of endochondral bone formation is always accompanied by the appearance of hyaline cartilage (Blumer et al., 2005; Grässel and Aszódi, 2016). On the other hand, the positive results of IHC-OCN and Alizarin Red S staining showed the abundant presence of OCN and calcium deposition, inferring that a bone-related ECM was either also being formed or a transition was underway from the chondrogenic tissue to that of a bone-like tissue (McLeod, 1980; Ding et al., 2019). We believed this to be the case, as the increases in *Runx2*, *Alp*, *Ocn*, *Bmp-2*, and *Col1a1* gene expressions over the culturing periods were indicative of a trend towards osteogenic morphogenesis (Karsenty et al., 2009; Scott et al., 2012).

Though this seemed to be a general trend among the various growth factor groups analyzed, marked differences were also recorded. The present research experiment verified that both TGF- $\beta$ 3 and BMP-2 alone could initiate osteochondrogenesis. Especially *Sox9* and *Runx2*, master transcription factors for chondrogenesis and osteogenesis, respectively (Eames et al., 2004; Zhang et al., 2013), showed overlapping and significantly increased

expressional regulation. On day 7, *Sox9* was positively expressed in the single BMP-2 group, while no significant result was detected for *Runx2* gene expression. This result was consistent with many previous studies that *Sox9* and *Runx2* play a reciprocal inhibitory role during osteo-chondrogenesis to influence mesenchymal cell fate (Yamashita et al., 2009; Cheng and Genever, 2010). During the early chondrogenic differentiation stage, BMP-2-induced *Runx2* expression was suppressed by *Sox9* to inhibit the subsequent endochondral ossification process and maintain the hyaline cartilage phenotype (Zhou et al., 2006; Liao et al., 2014). However, *Sox9* also contributed to BMP-2-induced osteogenic differentiation since *Sox9* silencing causes reduced osteogenesis in bone-marrow-derived mesenchymal stem cells (BMSCs) (Zhao, 2008; Fang et al., 2019). Alternatively, the groups treated with TGF- $\beta$ 3 only showed the positive upregulation of *Bmp-2* and *Runx2* gene expressions on days 14 and 30, confirming previous claims by Klar et al. (2014) and other studies that TGF- $\beta$ 3 seems to be able to regulate osteogenesis by modulating endogenous *Bmp-2* levels, followed by increased *Runx2* expression (Wang et al., 2016).

For the TGF- $\beta$ 3+BMP-2 groups, both synergistic and antagonistic activities were discovered that occurred at specific temporal culturing stages of our *in vitro* model. From day 0 to day 7 and 14, the addition of TGF- $\beta$ 3 blocked most of the BMP-2 gene and protein upregulation that normally would occur if TGF- $\beta$ 3 were absent. In relation to the inhibitory effects, it is known that both TGF- $\beta$ 3 and BMP-2 have similar receptor binding mechanisms, inferring that competitive inhibition of the TGF- $\beta$ s and BMPs receptors is possible (Keller et al., 2011). Alternatively, TGF- $\beta$ s could be blocking BMP signaling transduction by forming mix-linked Smad1/5-Smad3 inhibitory complexes (Daly et al., 2008; van der Kraan et al., 2012), or it could be that TGF- $\beta$ 3-induced inhibitory Smad6 or Smad7 are also interfering with the BMP signaling pathway (Keller et al., 2011). This has been well-described by various scientists. For instance, Ehnert et al. (2010); Ehnert et al. (2012) showed that Smad1/5/8-mediated BMP-2 and -7 signaling could be blocked entirely by adding recombinant human TGF- $\beta$  in primary human osteoblasts. Similarly, Mehlhorn et al. (2007) presented that BMP-2 induced chondrogenesis and osteogenesis in adipocyte-derived stem cells could be prevented by simultaneously applying any of the three TGF- $\beta$  isoforms.

However, the synergistic activities between TGF- $\beta$  and BMP signaling were also found in the same tissue model system, but only during the later 30-day stages of culture. From 14 to 30 days, most detected genes and proteins were significantly higher upregulated in the TGF- $\beta$ 3+BMP-2 group than either the TGF- $\beta$ 3 or BMP-2 groups (Figure 7B). The possible underlying mechanisms of the synergistic effect, and those at specific time points, could be that TGF- $\beta$ s switch function over time. This would suggest that TGF- $\beta$ 3 can alternate between being a competitive inhibitor of the BMPs pathways to being an activator of cellular stimulation, at specific time points, either due to changes in concentration or intrinsic cellular alteration. Apart from binding ALK5 to stimulate the canonical Smad2/3 signaling pathway, TGF- $\beta$ s can also exert functions *via* activating the BMP signaling pathway by associating with ALK1 and ALK2 directly and then triggering Smad1/5/8 for signal transmission (Wrighton et al., 2009; Keller et al., 2011). The synergistic effect between TGF- $\beta$ s and BMPs is well known (Wu et al., 2016). However, if growth factors change function with time, switching roles based on cellular activity or differentiation/transformation changes, this needs to be further

analyzed in future studies. This is especially critical given that our Noggin results showed a similar function switching from inhibitor to stimulator.

The ectopic application of Noggin in our experiment confirms that one of the roles of Noggin is to antagonize BMP-2-induced osteochondrogenic differentiation. Nearly all applications of Noggin alone and BMP-2+Noggin combined presented insignificant expressional changes, both at the gene and protein levels and at all culturing time points. As a key natural BMPs antagonist, Noggin can specifically bind BMP-2, -4, -5, -6, and -7 with several degrees of affinity, including GDF-5/-6, yet provides little to no binding affinity to the other TGF family members (Smith and Harland, 1992; Song et al., 2010). However, our experiment counteracts this assumption as Noggin seemed to actively inhibit exogenously applied TGF- $\beta$ 3 growth factor functioning, since Noggin prevented the upregulation of all genes that TGF- $\beta$ 3 normally activated on day 14 (Figure 7B). Indeed, the inhibitory effect of Noggin on TGF- $\beta$ 3 has been discovered and reported by many scholars. Nakayama et al. (2003) showed that Noggin could block TGF- $\beta$ 3 induced chondrogenesis, suggesting a BMP-associated pathway was involved. In addition, Bayramov et al. (2011) put forward a novel inhibitory function of Noggin by demonstrating that, in addition to BMPs, several non-BMP ligands, such as Activin B, Xnr2, and Xnr4, can also be antagonized by Noggin, albeit less efficiently. Interestingly, these blocked non-BMP ligands regulate specific genes' transcription through cytoplasmic Smad2/3. This point may indicate another link between TGF- $\beta$ 3 and Noggin regarding non-BMP ligands and downstream effectors Smad2/3. From this and in conjunction with our results, we deduce that the application of Noggin can, at specific time points, inhibit the differentiation function of both BMP-2 and TGF- $\beta$ 3 signaling.

However, the inhibition effect of Noggin + TGF- $\beta$ 3 was not observed at day 7 nor day 30. Instead, at these time points, our results showed that most of the gene and protein expression markers increased significantly, promoting the idea that signals, whether they be growth factors or antagonists such as Noggin, possess various roles that are not limited to a single function but are temporally dependent. Indeed, our results suggest a positive function of Noggin in osteo-chondrogenesis at specific temporal stages. Interestingly, a similarly positive result could also be observed with our TGF- $\beta$ 3+BMP-2+Noggin groups at day 30 (Figures 7A, C; Figures 8B–D). While this interpretation does go against the traditional concept that Noggin should inhibit osteo-chondrogenesis, Noggin's positive stimulatory functions have been reported. For instance, Chen et al. (2012) proposed that Noggin can stimulate human MSCs osteogenesis, as the suppression of significantly reduced BMP-2-induced ALP activity. Rifas (2007) made a similar observation showing that Noggin could induce ALP action and upregulate *Bmp-2* and *Ocn* gene expression. Unusually, other than these ordinary osteogenic markers, they also found increased ActRII expression (Rifas, 2007). Furthermore, Hashimi (2019) found that exogenous Noggin treatment could induce osteogenesis by binding to and stimulating the BMP-2 receptor (Hashimi, 2019). Taken together with our discoveries, this would suggest that Noggin may perform a stimulatory role during specific temporal stages of osteo-chondrogenesis development, especially when it is in the presence of TGF- $\beta$ 3. Future research needs to investigate this more clearly, as there is a definitive lack of knowledge regarding the temporal

behavior of growth factors and inhibitors over time and at which time points signals change their function.

Over the course of nearly 3 decades, research into the possible mechanisms for the formation and regenerating of bone or articular cartilage tissue, have yielded few clinically relevant solutions (Wei and Dai, 2021). Whilst a large spectrum of regenerative scientists and tissue engineers are trying to find new alternatives, Klar (2018) possibly provided one of the most prudent solutions to solving this dilemma, being that “all of the relevant signals and their interactions had not been fully established”. This inferred that gaps in the knowledge exist in how ligands are activated and how their effect changes over time when affecting tissue development. Indeed, the current work not only establishes that our knowledge on signals and their behavior over the course of time changes drastically between stimulation, antagonism, and regulation, but that with the correct combination of signals any tissue could be indirectly (*in vitro*) or directly (*in vivo*) transformed into whatever tissue/organ we desire. The clinical implications of such information would be invaluable for future therapies as whole organs or even limbs could be fully grown from excess damaged tissue areas or excess tissue types be biological recycled to form new tissues/organs (Betz et al., 2009; Xiong et al., 2020).

Whilst our results did show some critical new discoveries and possible avenues of research, the study also had certain limitations. A critical limitation was that we did not consider the effect of the dose gradient of the applied growth factors on the experimental results. Whilst we tried to choose a dose that would elicit a response without causing inhibition, some studies have reported that the TGF- $\beta$  superfamily factors serve as a double-edged sword in DNA synthesis (Chen et al., 1991; Harris et al., 1994). For example, a low concentration of TGF- $\beta$  can promote osteogenic differentiation but inhibit it at a high concentration (Karst et al., 2004; Crane et al., 2016). In addition, low doses of active TGF- $\beta$  have also been shown in chondrocytes to preferentially signal through the Smad2/3 pathway, while the Smad1/5 pathway becomes predominant at high doses (Finnson et al., 2008; Blaney Davidson et al., 2009). In addition, that BMP-2 controls bone formation in a concentration-dependent manner has also been demonstrated in bone TE studies (Meinel et al., 2006; Shi et al., 2012; Dang et al., 2016). Thus, an appropriate molecular concentration may play a vital role in a differentiation system as time progresses. Subsequently, another limitation was that we did not apply the growth factors in a truly temporal manner, i.e., first BMP-2 for 2 days then TGF- $\beta$ 3 for 2 days, etc., nor adjust the application order. Iwakura et al. (2013) established that morphogen treatment order could produce varying effects. Applying growth factors, such as BMP-7 followed by TGF- $\beta$ 1, resulted in more effective chondrogenesis than TGF- $\beta$ 1 following BMP-7. On the other hand, although numerous types of cells give the muscle tissue the possibility of multiple differentiation, it also increases the uncertainty of its differentiation direction. It is challenging to match various differentiated phenotypes with corresponding cell types in such a complex 3D cellular assembly. As such, a comparison between the muscle tissue explant and a specific single cell type, such as satellite cells or myoblasts, may be necessary to be conducted, especially in a 3D pellet culture condition, to confirm the superiority of this muscle tissue induction model. Moreover, the increasing trend of gene expression in the control group, although not significantly different compared to the 0-day sample (baseline), might suggest that the



induced phenotypes were not absolutely derived from the exogenous molecules. One of the explanations may be that the FBS in the normal medium provided some supplementary signals for differentiation. The other reason may be attributed to the injury from tissue excision since the trauma-induced various BMPs expression and followed heterotopic ossification have been verified by many investigators (Li, 2020; Strong et al., 2021). Finally, to achieve a more realistic *in vitro* physiological simulation system, mechanical and even electrochemical stimulation, as directed by nerves, should also be considered as a complement to biochemical cues in this muscle-tissue-based model because they can also play essential and unique roles as temporal biophysical signals to participate in cellular activities (Boonen et al., 2010; Maleiner et al., 2018; Urdeix and Doweidar, 2020).

## 4 Materials and methods

### 4.1 Collection of muscle tissue samples

The rectus abdominis muscle tissue was collected from two Fischer-344 adult *Rattus norvegicus* (Charles River Wiga, Sulzbach, Germany). The animals were sacrificed with an excess of isoflurane (Abbot, Chicago, United States) and disinfected with 10% povidone-iodine (Betadine, Bonn, Germany) and 75% alcohol (Apotheke Großhadern, Munich, Germany). Under a sterile environment, the harvested muscle was incubated in graded concentrations of penicillin and streptomycin (2% and 1%) (A2213; P/S, Biochrom GmbH, Berlin, Germany) in Alpha-Medium (Biochrom GmbH, Berlin, Germany) for 20 min, respectively. Then, 288 fragments of the tissue 4 mm in diameter were obtained with a specific biopsy punch (PFM medical, Cologne, Germany). The rules and regulations of the Animal Protection Laboratory Animal Regulations (2013) of the European Directive 2010/63/EU Act were strictly complied with during the above procedures. The experiments were also approved by the Animal ethics research committee of the Ludwig Maximilian University of Munich (LMU), Bavaria, Germany Tierschutzgesetz §1/§4/§17 (<https://www.gesetze-im-internet.de/tierschg/TierSchG.pdf>) with regard to animal usage for pure tissue or organ harvesting only.

### 4.2 Muscle tissue culture

The muscle tissue biopsies (n = 288) were cultured in 96-well plates (Thermo Fisher Scientific, Waltham, MA, United States) in normal culture medium (containing Alpha-Medium, 1% P/S, 0.02 mM/mL L-glutamine (Biochrom GmbH, Berlin, Germany) and 15% fetal bovine serum (FBS; Biochrom GmbH, Berlin, Germany)) for 48 h in a humidified incubator with 5% CO<sub>2</sub> at 37°C to allow for the cells in the tissue to recover. The muscle tissue fragments were then divided into eight independent treatment groups:

(Pittenger et al., 2019) Control (**Con**) group, containing the normal culture medium (Xiong et al., 2021); Rat BMP-2 (**B**) group, containing the normal culture medium and 50 ng/mL BMP-2 (CUSABIO, United States) (Huang et al., 2019); Rat TGF-β3 (**T**)

group, containing the normal culture medium and 50 ng/mL TGF-β3 (Cloud-Clone Corp, United States) (Huynh et al., 2019); Rat Noggin (**N**) group, containing the normal culture medium and 50 ng/mL Noggin (Cloud-Clone Corp, United States) (Sheehy et al., 2013); TGF-β3+BMP-2 (**T + B**) group, containing the normal culture medium and 50 ng/mL TGFβ3+50 ng/mL BMP-2 (Schaefer et al., 2002); TGF-β3+Noggin (**T + N**) group, containing the normal culture medium and 50 ng/mL TGF-β3+50 ng/mL Noggin (Alhadlaq and Mao, 2005); BMP-2+Noggin (**B + N**) group, containing the normal culture medium and 50 ng/mL BMP-2+50 ng/mL Noggin (Zhang et al., 2019); TGF-β3+BMP-2+Noggin (**T + B + N**) group, containing the normal culture medium and 50 ng/mL TGF-β3+50 ng/mL BMP-2+50 ng/mL Noggin.

Each modality had 36 samples that were divided up into quantitative genes (n = 6) as well as histological (n = 6) assessment groups and further into subsequent culture period lengths of 7, 14, and 30 days. In the end, for each treatment modality, there were always 6 muscle fragments for a given culture length and assessment method.

### 4.3 RT-qPCR

The minimum information for publication of quantitative real-time PCR experiments (MIQE) principles was strictly applied to guide the entire RT-qPCR procedure (Bustin and Wittwer, 2017). After flash freezing in liquid nitrogen, the harvested muscle tissue samples were homogenized by a mortar and pestle under an RNase-free work hood. The RNeasy® Fibrous Tissue Mini Kit (Qiagen, Hilden, Germany) was used to extract and purify the total RNA. The obtained RNA samples had an A260/A280 ratio of 1.86–2.07 and a concentration of 76.7–123.7 ng/μL, which were measured by a NanoDrop™ Lite (Thermo Fisher Scientific, Waltham, MA, United States). Finally, a QuantiTect complementary DNA (cDNA) Synthesis Kit (Qiagen, Hilden, Germany) was applied according to their specialized protocol to conduct reverse transcription. The resulting cDNA was deposited at –20°C for subsequent qPCR analysis.

The qPCR process was performed on a LightCycler® 96 Instrument (Roche, Switzerland), utilizing the FastStart Essential DNA Green Master and SYBR Green I Kit (Roche, Switzerland). The thermal cycling parameters were set in 3 min initial denaturation steps at 95°C; 40 cycles, including a denaturation step at 95°C for 10 s, an annealing step at 60°C for 15 s, and an extension step at 72°C for 30 s, respectively; and a final extension at 72°C for 5 min. The final reaction volume was 10 μL, consisting 2 μL cDNA (5 ng/μL), 1.8 μL RNase-free water, 5 μL Green Master, 0.6 μL forward primer, and 0.6 μL reverse primer. The primers of eight reference genes and ten target genes (Table 2) were designed and analyzed on the IDT website (<https://eu.idtdna.com/site>).

The GeNorm (<http://medgen.ugent.be/wjvdesomp/genorm/>) was applied to assess and select Glyceraldehyde-3-phosphate dehydrogenase (*Gapdh*); Succinate dehydrogenase complex flavoprotein subunit A (*Sdha*); Ribosomal protein lateral stalk subunit P0 (*Rplp0*); RNA polymerase II, I and III subunit E (*Polr2e*); and Actin beta (*Actb*) as the final reference genes (Table 1) for the subsequent gene expression calibration process.

TABLE 2 The target and reference genes information.

	Gene name	Accession nr	Fwd. (5'-3')	Rev. (5'-3')
	<i>Actb</i>	NM_031144.3	AGCTATGAGCTGCCTGA	GGCAGTAATCTCCTTCTGC
	<i>Rplp0</i>	BC001834.2	CAACCCAGCTCTGGAGA	CAGCTGGCACCTTATTGG
Reference genes	<i>Gapdh</i>	BC083511.1	CATGGGTGTGAACCATGA	TGTCATGGATGACCTTGG
	<i>Polr2e</i>	BC158787.1	GACCATCAAGGTGTACTGC	CAGCTCCTGCTGTAGAAAC
	<i>Sdha</i>	NM_130428.1	GCGGTATGAGACCAGTTATT	CCTGGCAAGGTAAACACG
	<i>Acan</i>	NM_022190.1	CAAGTGGAGCCGTGTTT	TTTAGGTCTTGGAAGCGAG
	<i>Col2a1</i>	NM_012929.1	ATCCAGGCTCCAATGA	TCCTCTGGAGTGCAGAA
	<i>Sox9</i>	NM_080403.1	CCAGAGAACGCACATCAAG	ATACTGATGTGGCTGGTGG
Target genes	<i>Six1</i>	NM_053759.1	CAGGTTCTTGTGGTCGTT	TTTGGGATGGTTGTGAGG
	<i>Abi3bp</i>	XM_017598145.1	ACGGGACATTCCTCTCATA	GGTGCCTGAGTTGTCTTT
	<i>Runx2</i>	NM_001278484.2	CCCAAGTGGCCACTTAC	CTGAGGCGGTCAGAGA
	<i>Alp</i>	NM_013059.2	CGACAGCAAGCCCAAG	AGACGCCCATACCATCT
	<i>Bmp-2</i>	NM_017178.1	GGAAGTGGCCCACTTAGA	TCACTAGCAGTGGTCTTACC
	<i>Ocn</i>	NM_013414.2	GCGACTCTGAGTCTGACA	GGCAACACATGCCCTAAA
	<i>Col1a1</i>	NM_053304.1	GGTGACAGAGGCATAAAGG	AGACCGTTGAGTCCATCT

*Actb* = Actin beta, *Rplp0* = Ribosomal protein lateral stalk subunit p0, *Gapdh* = Glyceraldehyde-3-phosphate dehydrogenase, *Polr2e* = RNA, polymerase II, subunit e, *Sdha* = Succinate dehydrogenase complex flavoprotein subunit a; *Acan* = Aggrecan, *Col2a1* = Collagen type II, alpha 1, *Sox9* = Sex determining region Y (SRY)-box transcription factor 9, *Six1* = Six homeobox 1, *Abi3bp* = Abi family member 3 binding protein, *Runx2* = Runx family transcription factor 2, *Alp* = Alkaline phosphatase, *Bmp-2*, Bone morphogenetic protein-2, *Ocn* = Osteocalcin, *Col1a1* = Collagen type I alpha 1 chain.

Targets included the chondrogenesis-associated genes collagen type II (*Col2a1*), SRY-box transcription factor 9 (*Sox9*), aggrecan (*Acan*), SIX homeobox 1 (*Six1*) and ABI family member 3 binding protein (*Abi3bp*), and the osteogenesis-associated genes Alkaline phosphatase (*Alp*), RUNX family transcription factor 2 (*Runx2*), Bone morphogenetic protein 2 (*Bmp-2*), osteocalcin (*Ocn*) and Collagen type I alpha 1 chain (*Col1a1*). The relative gene expression levels were characterized in calibrated normalized relative quantities (CNRQs), which were obtained by normalization with the pre-determined reference genes in the qBase + software (<https://www.qbaseplus.com/>), including the relevant endogenous control (fresh muscle tissue 0-day).

#### 4.4 Histological and immunohistochemical (IHC) staining

Harvested samples for histological analysis were first placed in 4% paraformaldehyde (Microcos GmbH, Garching, Germany) for overnight fixation, followed by dehydration in Spin Tissue Processor-120 (Especialidades Médicas Myr, S.L., Tarragona, Spain), then embedded in paraffin blocks. Afterwards, 3 µm-thick sections were cut for subsequent staining.

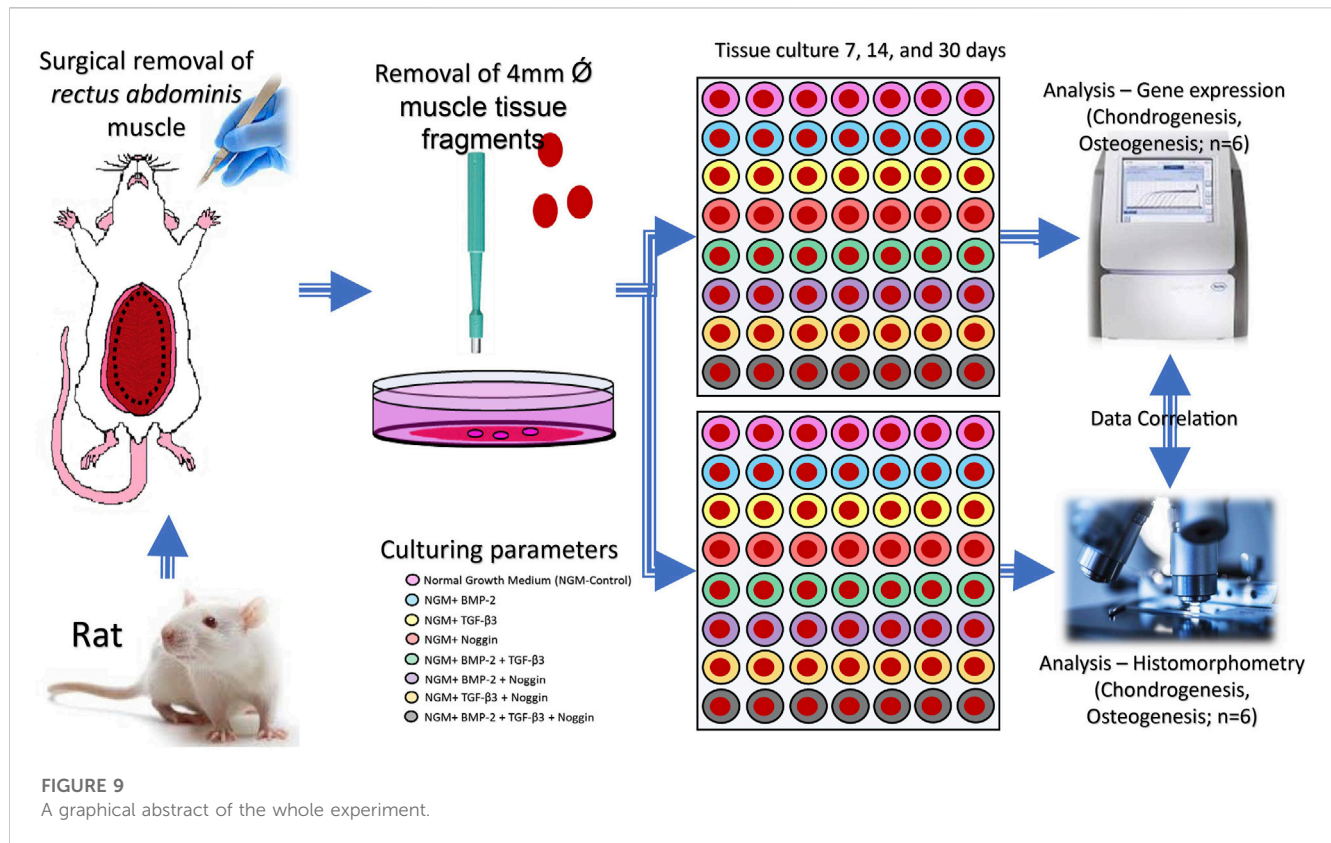
Alcian Blue staining was used to evaluate the effectiveness of chondrogenesis in this study. Deparaffinized and hydrated sections were stained in 1% Alcian Blue solution (pH 2.5, Morphisto, Frankfurt, Germany) and counterstained in 0.1% Nuclear Fast Red solution (Morphisto, Frankfurt, Germany)

and were then dehydrated and covered with EUKITT mounting media (O. Kindler GmbH, Bobingen, Germany). Alizarin Red S staining was used to identify the efficiency of osteogenesis in this study. Sections were stained in Alizarin Red S solution (pH 9, Morphisto, Frankfurt, Germany), re-stained in Alizarin Red S solution (pH 7, Morphisto, Frankfurt, Germany), then dehydrated and mounted in synthetic resin (O. Kindler GmbH, Bobingen, Germany).

To observe the chondrogenic or osteogenic response within the muscle tissue samples, Rabbit polyclonal anti-ACAN (1:150, orb213537) and anti-OCN (1:100, orb259644) antibodies (Biorbyt, Eching, Germany) were utilized for IHC staining. Rabbit-on-Rodent HRP-Polymer (ZYTOMED SYS-TEMS GmbH) was applied as a secondary antibody. Negative control was also set up using Antibody Diluent (ZYTOMED SYSTEMS GmbH, Berlin, Germany) instead of the primary antibodies. Finally, a Vina-Green™ chromogenic kit (Biocare-Medical, Concord, CA, United States) was used to show positive interactions between antigen and antibody.

#### 4.5 Histomorphometric analysis

Histological and IHC stainings were captured using the PreciPoint M8 Digital Microscope & Scanner (PreciPoint GmbH, Freising, Germany). The images were histomorphometrically analyzed by the Image-Pro plus 6.0 software (Media Cybernetics, Inc. Silver spring, MD United States). The ratio of the positive-range



optical density value (IOD) to the whole range of the sample was the raw staining result.

## 4.6 Statistical analysis

GraphPad Prism software 8 (La Jolla, CA, United States, <http://www.graphpad.com>) was used for statistical assessment. Quantile-quantile (q-q) plot was used to test the normality of the data distribution (Supplementary Figure S1–S3). The comparison between different experimental and corresponding control groups was performed by one-way analysis of variance (ANOVA) with Dunnett's multiple comparisons test. The comparison between each group at different time periods was performed by one-way ANOVA with Tukey's multiple comparisons test. A significance level of  $p < 0.05$  was considered statistically significant. The results are shown as box plots showing the mean and the upper and lower interquartile range with whiskers encompassing the minimum and the maximum value of each group. Rstudio (R-Studio, Boston, MA, United States; <http://www.rstudio.com>) was utilized to create the final heat maps. Depending on the culture conditions, the heat map was grouped into 8 clusters. The materials and methods were summarized as a graphical abstract in Figure 9.

## 5 Conclusion

Tissue morphogenesis is a tightly modulated temporal and spatial combination of various signaling cues that are improperly

elucidated, causing clinical TE processes to fail. Continuing our systematic studies that attempt to understand how the interactions of multiple growth factors regulate osteo-chondrogenesis of muscle tissue over a specific time frame, we have observed clear differences. The combination of BMP-2+TGF- $\beta$ 3, while able to synergize with each other to stimulate osteo-chondrogenesis, also showed that they could antagonize each other in a time-dependent manner. However, the Noggin results were most intriguing. Not only does Noggin appear to be able to antagonize TGF- $\beta$ 3, albeit only at specific temporal intervals, but Noggin appears to be able to synergize with TGF- $\beta$ 3 to promote osteo-chondrogenesis in a temporal manner. This study thus demonstrated a clear need to reconsider the temporal function of growth factors and their inhibitors during the differentiation process in order to achieve more effective TE approaches in clinical applications.

## Data availability statement

The datasets presented in this study can be found in online repositories. The names of the repository/repositories and accession number(s) can be found in the article/Supplementary Material.

## Ethics statement

The animal study was reviewed and approved by Animal ethics research committee of the Ludwig Maximilian University of

Munich (LMU), Bavaria, Germany Tierschutzgesetz §1/§4/§17 (<https://www.gesetze-im-internet.de/tierschg/TierSchG.pdf>).

## Author contributions

Conceptualization, RK; methodology, RK and HL; software, RK and HL; validation, RK and HL; formal analysis, RK and HL; investigation, HL; resources, RK; data curation, RK, AA, and HL writing—original draft preparation, HL; Writing—review and editing, RK, PM, and AA; visualization, HL; supervision, RK and PM; project administration, RK and AA; funding acquisition, PM and RK. All authors have read and agreed to the published version of the manuscript.

## Funding

This research was funded by the China Scholarship Council/LMU program (#201906170069), and the Friedrich Baur Foundation (Grant Acronym: CaMuTe).

## Acknowledgments

We would like to thank Prof. V. Jansson for having supported part of the project funding through his Friedrich Baur Grant and allowing part of the project to be conducted in the Laboratory research premises of the University Hospital of

Munich, of the Ludwig-Maximilians University. We would also like to thank all our friends, families and colleagues for their help and support during the challenging periods of this project.

## Conflict of interest

The authors declare that the research was conducted in the absence of any commercial or financial relationships that could be construed as a potential conflict of interest.

## Publisher's note

All claims expressed in this article are solely those of the authors and do not necessarily represent those of their affiliated organizations, or those of the publisher, the editors and the reviewers. Any product that may be evaluated in this article, or claim that may be made by its manufacturer, is not guaranteed or endorsed by the publisher.

## Supplementary material

The Supplementary Material for this article can be found online at: <https://www.frontiersin.org/articles/10.3389/fbioe.2023.1140118/full#supplementary-material>

## References

- Albert, R. (2005). Scale-free networks in cell biology. *J. Cell Sci.* 118 (21), 4947–4957. doi:10.1242/jcs.02714
- Alhadlaq, A., and Mao, J. J. (2005). Tissue-engineered osteochondral constructs in the shape of an articular condyle. *J. bone Jt. Surg. Am. volume* 87 (5), 936–944. doi:10.2106/jbjs.d.02104
- Alliston, T., Piek, E., Derynck, R., Miyazono, K., and Derynck, R. (2008). TGF-Beta family signaling in skeletal development, maintenance, and disease. 667
- Bami, M., Mavrogenis, A. F., Angelini, A., Milonaki, M., Mitsiokapa, E., Stamoulis, D., et al. (2016). Bone morphogenetic protein signaling in musculoskeletal cancer. *J. Cancer Res. Clin. Oncol.* 142 (10), 2061–2072. doi:10.1007/s00432-016-2149-9
- Bayramov, A. V., Eroshkin, F. M., Martynova, N. Y., Ermakova, G. V., Solovieva, E. A., and Zaraisky, A. G. (2011). Novel functions of noggin proteins: Inhibition of activin/nodal and wnt signaling. *Development* 138 (24), 5345–5356. doi:10.1242/dev.068908
- Betz, O. B., Betz, V. M., Abdulazim, A., Penzkofer, R., Schmitt, B., Schroder, C., et al. (2009). Healing of large segmental bone defects induced by expedited bone morphogenetic protein-2 gene-activated, syngeneic muscle grafts. *Hum. Gene Ther.* 20 (12), 1589–1596. doi:10.1089/hum.2009.037
- Betz, O. B., Betz, V. M., Schroder, C., Penzkofer, R., Gottlinger, M., Mayer-Wagner, S., et al. (2013). Repair of large segmental bone defects: BMP-2 gene activated muscle grafts vs. autologous bone grafting. *BMC Biotechnol.* 13 (1), 65. doi:10.1186/1472-6750-13-65
- Betz, V. M., Betz, O. B., Harris, M. B., Vrahas, M. S., and Evans, C. H. (2008). Bone tissue engineering and repair by gene therapy. *Front. Biosci.* 13 (13), 833–841. doi:10.2741/2724
- Betz, V. M., Betz, O. B., Rosin, T., Keller, A., Thirion, C., Salomon, M., et al. (2015). The effect of BMP-7 gene activated muscle tissue implants on the repair of large segmental bone defects. *Injury* 46 (12), 2351–2358. doi:10.1016/j.injury.2015.09.016
- Betz, V. M., Ren, B., Messmer, C., Jansson, V., Betz, O. B., and Muller, P. E. (2018). Bone morphogenetic protein-2 is a stronger inducer of osteogenesis within muscle tissue than heterodimeric bone morphogenetic protein-2/6 and -2/7: Implications for expedited gene-enhanced bone repair. *J. Gene Med.* 20 (9), e3042. doi:10.1002/jgm.3042
- Blair, H. C., Larrouture, Q. C., Li, Y., Lin, H., Beer-Stoltz, D., Liu, L., et al. (2017). Osteoblast differentiation and bone matrix formation *in vivo* and *in vitro*. *Tissue Eng. Part B Rev.* 23 (3), 268–280. doi:10.1089/ten.teb.2016.0454
- Blaney Davidson, E. N., Remst, D. F., Vitters, E. L., van Beuningen, H. M., Blom, A. B., Goumans, M. J., et al. (2009). Increase in ALK1/ALK5 ratio as a cause for elevated MMP-13 expression in osteoarthritis in humans and mice. *J. Immunol. Baltim. Md : 1950* 182 (12), 7937–7945. doi:10.4049/jimmunol.0803991
- Blumer, M. J., Longato, S., Richter, E., Perez, M. T., Konakci, K. Z., and Fritsch, H. (2005). The role of cartilage canals in endochondral and perichondral bone formation: Are there similarities between these two processes? *J. Anat.* 206 (4), 359–372. doi:10.1111/j.1469-7580.2005.00404.x
- Boonen, K. J., Langelaan, M. L., Polak, R. B., van der Schaft, D. W., Baaijens, F. P., and Post, M. J. (2010). Effects of a combined mechanical stimulation protocol: Value for skeletal muscle tissue engineering. *J. Biomech.* 43 (8), 1514–1521. doi:10.1016/j.jbiomech.2010.01.039
- Bosch, P., Musgrave, D. S., Lee, J. Y., Cummins, J., Shuler, T., Ghivizzani, T. C., et al. (2000). Osteoprogenitor cells within skeletal muscle. *J. Orthop. Res.* 18 (6), 933–944. doi:10.1002/jor.1100180613
- Brand, M. D. (1997). Regulation analysis of energy metabolism. *J. Exp. Biol.* 200 (2), 193–202. doi:10.1242/jeb.200.2.193
- Bustin, S. A., and Wittwer, C. T. (2017). Miqe: A step toward more robust and reproducible quantitative PCR. *Clin. Chem.* 63 (9), 1537–1538. doi:10.1373/clinchem.2016.268953
- Chen, C., Uludag, H., Wang, Z., and Jiang, H. (2012). Noggin suppression decreases BMP-2-induced osteogenesis of human bone marrow-derived mesenchymal stem cells *in vitro*. *J. Cell Biochem* 113 (12), 3672–3680. doi:10.1002/jcb.24240
- Chen, J., Chen, H., Li, P., Diao, H., Zhu, S., Dong, L., et al. (2011). Simultaneous regeneration of articular cartilage and subchondral bone *in vivo* using MSCs induced by a spatially controlled gene delivery system in bilayered integrated scaffolds. *Biomaterials* 32 (21), 4793–4805. doi:10.1016/j.biomaterials.2011.03.041
- Chen, L., Liu, J., Guan, M., Zhou, T., Duan, X., and Xiang, Z. (2020). <p>Growth factor and its polymer scaffold-based delivery system for cartilage tissue engineering</p>. *Int. J. Nanomedicine* 15, 6097–6111. doi:10.2147/ijn.s249829
- Chen, T. L., Bates, R. L., Dudley, A., Hammonds, R. G., Jr., and Amento, E. P. (1991). Bone morphogenetic protein-2b stimulation of growth and osteogenic phenotypes in rat osteoblast-like cells: Comparison with TGF-beta 1. *J. Bone Min. Res.* 6 (12), 1387–1393. doi:10.1002/jbmr.5650061216



- Cheng, A., and Genever, P. G. (2010). SOX9 determines RUNX2 transactivity by directing intracellular degradation. *J. Bone Min. Res.* 25 (12), 2680–2689. doi:10.1002/jbmr.174
- Chung, U. I., Schipani, E., McMahon, A. P., and Kronenberg, H. M. (2001). Indian hedgehog couples chondrogenesis to osteogenesis in endochondral bone development. *J. Clin. Invest.* 107 (3), 295–304. doi:10.1172/jci11706
- Cicione, C., Muinos-Lopez, E., Hermida-Gomez, T., Fuentes-Boquete, I., Diaz-Prado, S., and Blanco, F. J. (2015). Alternative protocols to induce chondrogenic differentiation: Transforming growth factor-beta superfamily. *Cell Tissue Bank.* 16 (2), 195–207. doi:10.1007/s10561-014-9472-7
- Crane, J. L., Xian, L., and Cao, X. (2016). Role of TGF- $\beta$  signaling in coupling bone remodeling. *Methods Mol. Biol.* 1344, 287–300. TGF- $\beta$  Signaling: Springer. doi:10.1007/978-1-4939-2966-5\_18
- Daly, A. C., Randall, R. A., and Hill, C. S. (2008). Transforming growth factor beta-induced Smad1/5 phosphorylation in epithelial cells is mediated by novel receptor complexes and is essential for anchorage-independent growth. *Mol. Cell Biol.* 28 (22), 6889–6902. doi:10.1128/mcb.01192-08
- Dang, P. N., Dwivedi, N., Yu, X., Phillips, L., Bowerman, C., Murphy, W. L., et al. (2016). Guiding chondrogenesis and osteogenesis with mineral-coated hydroxyapatite and BMP-2 incorporated within high-density hMSC aggregates for bone regeneration. *ACS Biomater. Sci. Eng.* 2 (1), 30–42. doi:10.1021/acsbomaterials.5b00277
- Devlin, R. D., Du, Z., Pereira, R. C., Kimble, R. B., Economides, A. N., Jorgetti, V., et al. (2003). Skeletal overexpression of noggin results in osteopenia and reduced bone formation. *Endocrinology* 144 (5), 1972–1978. doi:10.1210/en.2002-220918
- Ding, Y., Jiang, H., Meng, B., Zhu, B., Yu, X., and Xiang, G. (2019). Sweroside-mediated mTORC1 hyperactivation in bone marrow mesenchymal stem cells promotes osteogenic differentiation. *J. Cell Biochem* 120 (9), 16025–16036. doi:10.1002/jcb.28882
- Eames, B. F., Sharpe, P. T., and Helms, J. A. (2004). Hierarchy revealed in the specification of three skeletal fates by Sox9 and Runx2. *Dev. Biol.* 274 (1), 188–200. doi:10.1016/j.ydbio.2004.07.006
- Ehnhert, S., Baur, J., Schmitt, A., Neumaier, M., Lucke, M., Dooley, S., et al. (2010). TGF- $\beta$ 1 as possible link between loss of bone mineral density and chronic inflammation. *PLoS One* 5 (11), e14073. doi:10.1371/journal.pone.0014073
- Ehnhert, S., Zhao, J., Pscherer, S., Freude, T., Dooley, S., Kolk, A., et al. (2012). Transforming growth factor beta1 inhibits bone morphogenic protein (BMP)-2 and BMP-7 signaling via upregulation of ski-related novel protein N (SnoN): Possible mechanism for the failure of BMP therapy? *BMC Med.* 10 (1), 101. doi:10.1186/1741-7015-10-101
- Fang, S., Li, Y., and Chen, P. (2019). Osteogenic effect of bone marrow mesenchymal stem cell-derived exosomes on steroid-induced osteonecrosis of the femoral head. *Drug Des. Devel. Ther.* 13, 45–55. doi:10.2147/dddt.s178698
- Finsson, K. W., Parker, W. L., ten Dijke, P., Thorikay, M., and Philip, A. (2008). ALK1 opposes ALK5/Smad3 signaling and expression of extracellular matrix components in human chondrocytes. *J. Bone Min. Res.* 23 (6), 896–906. doi:10.1359/jbmr.080209
- Gazzerro, E., and Canalis, E. (2006). Bone morphogenetic proteins and their antagonists. *Rev. Endocr. Metab. Disord.* 7 (1–2), 51–65. doi:10.1007/s1154-006-9000-6
- Gazzerro, E., Du, Z., Devlin, R. D., Rydziel, S., Priest, L., Economides, A. N., et al. (2003). Noggin arrests stromal cell differentiation *in vitro*☆☆This work was supported by grant AR21707 from the national institute of arthritis and musculoskeletal and skin diseases, and grant DK45227 from the national institute of diabetes, digestive and kidney diseases. *Bone* 32 (2), 111–119. doi:10.1016/s8756-3282(02)00948-1
- Gong, Y., Krakow, D., Marcelino, J., Wilkin, D., Chitayat, D., Babul-Hirji, R., et al. (1999). Heterozygous mutations in the gene encoding noggin affect human joint morphogenesis. *Nat. Genet.* 21 (3), 302–304. doi:10.1038/6821
- Grässel, S., and Aszodi, A. (2016). *Cartilage*. Springer.
- Harris, S. E., Bonewald, L. F., Harris, M. A., Sabatini, M., Dallas, S., Feng, J. Q., et al. (1994). Effects of transforming growth factor beta on bone nodule formation and expression of bone morphogenetic protein 2, osteocalcin, osteopontin, alkaline phosphatase, and type I collagen mRNA in long-term cultures of fetal rat calvarial osteoblasts. *J. Bone Min. Res.* 9 (6), 855–863. doi:10.1002/jbmr.5650090611
- Haschtmann, D., Ferguson, S. J., and Stoyanov, J. V. (2012). BMP-2 and TGF- $\beta$ 3 do not prevent spontaneous degeneration in rabbit disc explants but induce ossification of the annulus fibrosus. *Eur. Spine J.* 21 (9), 1724–1733. doi:10.1007/s00586-012-2371-3
- Hashimi, S. M. (2019). Exogenous noggin binds the BMP-2 receptor and induces alkaline phosphatase activity in osteoblasts. *J. Cell Biochem* 120 (8), 13237–13242. doi:10.1002/jcb.28597
- He, T., Hausdorf, J., Chevalier, Y., and Klar, R. M. (2020). Trauma induced tissue survival *in vitro* with a muscle-biomaterial based osteogenic organoid system: A proof of concept study. *BMC Biotechnol.* 20 (1), 8. doi:10.1186/s12896-020-0602-y
- He, W., Chen, L., Huang, Y., Xu, Z., Xu, W., Ding, N., et al. (2019). Synergistic effects of recombinant Lentiviral-mediated BMP2 and TGF-beta3 on the osteogenic differentiation of rat bone marrow mesenchymal stem cells *in vitro*. *Cytokine* 120, 1–8. doi:10.1016/j.cyto.2019.03.020
- Huang, Y., Seitz, D., Chevalier, Y., Muller, P. E., Jansson, V., and Klar, R. M. (2020). Synergistic interaction of hTGF- $\beta$ 3 with hBMP-6 promotes articular cartilage formation in chitosan scaffolds with hADSCs: Implications for regenerative medicine. *BMC Biotechnol.* 20 (1), 48. doi:10.1186/s12896-020-00641-y
- Huang, Y., Seitz, D., Konig, F., Muller, P. E., Jansson, V., and Klar, R. M. (2019). Induction of articular chondrogenesis by chitosan/hyaluronic-acid-based biomimetic matrices using human adipose-derived stem cells. *Int. J. Mol. Sci.* 20 (18), 4487. doi:10.3390/ijms20184487
- Huang, Z., Ren, P. G., Ma, T., Smith, R. L., and Goodman, S. B. (2010). Modulating osteogenesis of mesenchymal stem cells by modifying growth factor availability. *Cytokine* 51 (3), 305–310. doi:10.1016/j.cyto.2010.06.002
- Huynh, N. P. T., Zhang, B., and Guilak, F. (2019). High-depth transcriptomic profiling reveals the temporal gene signature of human mesenchymal stem cells during chondrogenesis. *FASEB J.* 33 (1), 358–372. doi:10.1096/fj.201800534r
- Iwakura, T., Sakata, R., and Reddi, A. H. (2013). Induction of chondrogenesis and expression of superficial zone protein in synovial explants with TGF- $\beta$ 1 and BMP-7. *Tissue Eng. Part A* 19 (23–24), 2638–2644. doi:10.1089/ten.tea.2013.0047
- Izadpanahi, M., Seyedjafari, E., Arefian, E., Hamta, A., Hosseinzadeh, S., Kehtari, M., et al. (2018). Nanotopographical cues of electrospun PLLA efficiently modulate non-coding RNA network to osteogenic differentiation of mesenchymal stem cells during BMP signaling pathway. *Mater. Sci. Eng. C Mater. Biol. Appl.* 93, 686–703. doi:10.1016/j.msec.2018.08.023
- Karsenty, G., Kronenberg, H. M., and Settembre, C. (2009). Genetic control of bone formation. *Annu. Rev. Cell Dev. Biol.* 25, 629–648. doi:10.1146/annurev.cellbio.042308.113308
- Karst, M., Gorny, G., Galvin, R. J., and Oursler, M. J. (2004). Roles of stromal cell RANKL, OPG, and M-CSF expression in biphasic TGF-beta regulation of osteoclast differentiation. *J. Cell Physiol.* 200 (1), 99–106. doi:10.1002/jcp.20036
- Kato, Y., Iwamoto, M., Koike, T., Suzuki, F., and Takano, Y. (1988). Terminal differentiation and calcification in rabbit chondrocyte cultures grown in centrifuge tubes: Regulation by transforming growth factor beta and serum factors. *Proc. Natl. Acad. Sci. U S A* 85 (24), 9552–9556. doi:10.1073/pnas.85.24.9552
- Keller, B., Yang, T., Chen, Y., Munivez, E., Bertin, T., Zabel, B., et al. (2011). Interaction of TGF $\beta$  and BMP signaling pathways during chondrogenesis. *PLoS One* 6 (1), e16421. doi:10.1371/journal.pone.0016421
- Klar, R. M., Duarte, R., Dix-Peek, T., and Ripamonti, U. (2014). The induction of bone formation by the recombinant human transforming growth factor- $\beta$ 3. *Biomaterials* 35 (9), 2773–2788. doi:10.1016/j.biomaterials.2013.12.062
- Klar, R. M. (2018). The induction of bone formation: The translation enigma. *Front. Bioeng. Biotechnol.* 6, 74. doi:10.3389/fbioe.2018.00074
- Krause, C., Guzman, A., and Knaus, P. (2011). *Noggin*. *Int. J. Biochem Cell Biol.* 43 (4), 478–481. doi:10.1016/j.biocel.2011.01.007
- Lee, M. S., Stebbins, M. J., Jiao, H., Huang, H. C., Leiferman, E. M., Walczak, B. E., et al. (2021). Comparative evaluation of isogenic mesodermal and ectomesodermal chondrocytes from human iPSCs for cartilage regeneration. *Sci. Adv.* 7 (21), eabf0907. doi:10.1126/sciadv.abf0907
- Li, Tuan R. S. (2020). Mechanism of traumatic heterotopic ossification: In search of injury-induced osteogenic factors. *J. Cell Mol. Med.* 24 (19), 11046–11055. doi:10.1111/jcmm.15735
- Liao, J., Hu, N., Zhou, N., Lin, L., Zhao, C., Yi, S., et al. (2014). Sox9 potentiates BMP2-induced chondrogenic differentiation and inhibits BMP2-induced osteogenic differentiation. *PLoS One* 9 (2), e89025. doi:10.1371/journal.pone.0089025
- Maleiner, B., Tomasch, J., Heher, P., Spadiut, O., Runzler, D., and Fuchs, C. (2018). The importance of biophysical and biochemical stimuli in dynamic skeletal muscle models. *Front. Physiol.* 9, 1130. doi:10.3389/fphys.2018.01130
- McLeod, M. J. (1980). Differential staining of cartilage and bone in whole mouse fetuses by alcian blue and alizarin red S. *Teratology* 22 (3), 299–301. doi:10.1002/tera.1420220306
- Mehlhorn, A. T., Niemeyer, P., Kaschte, K., Muller, L., Finkenzeller, G., Hartl, D., et al. (2007). Differential effects of BMP-2 and TGF- $\beta$ 1 on chondrogenic differentiation of adipose derived stem cells. *Cell Prolif.* 40 (6), 809–823. doi:10.1111/j.1365-2184.2007.00473.x
- Meinel, L., Hofmann, S., Betz, O., Fajardo, R., Merkle, H. P., Langer, R., et al. (2006). Osteogenesis by human mesenchymal stem cells cultured on silk biomaterials: Comparison of adenovirus mediated gene transfer and protein delivery of BMP-2. *Biomaterials* 27 (28), 4993–5002. doi:10.1016/j.biomaterials.2006.05.021
- Nakayama, N., Duryea, D., Manoukian, R., Chow, G., and Han, C. Y. (2003). Macroscopic cartilage formation with embryonic stem-cell-derived mesodermal progenitor cells. *J. Cell Sci.* 116 (10), 2015–2028. doi:10.1242/jcs.00417
- Noel, D., Gazit, D., Bouquet, C., Apparailly, F., Bony, C., Ponce, P., et al. (2004). Short-term BMP-2 expression is sufficient for *in vivo* osteochondral differentiation of mesenchymal stem cells. *Stem Cells* 22 (1), 74–85. doi:10.1634/stemcells.22-1-74
- Perniconi, B., and Coletti, D. (2014). Skeletal muscle tissue engineering: Best bet or black beast? *Front. Physiol.* 5, 255. doi:10.3389/fphys.2014.00255
- Pittenger, M. F., Discher, D. E., Péault, B. M., Phinney, D. G., Hare, J. M., and Caplan, A. I. (2019). Mesenchymal stem cell perspective: Cell biology to clinical progress. *NPJ Regen. Med.* 4, 22. doi:10.1038/s41536-019-0083-6

- Re'em-Kalma, Y., Lamb, T., and Frank, D. (1995). Competition between noggin and bone morphogenetic protein 4 activities may regulate dorsalization during *Xenopus* development. *Proc. Natl. Acad. Sci. U S A* 92 (26), 12141–12145. doi:10.1073/pnas.92.26.12141
- Ren, B., Betz, V. M., Thirion, C., Salomon, M., Jansson, V., Muller, P. E., et al. (2018). Gene-activated tissue grafts for sustained bone morphogenetic protein-2 delivery and bone engineering: Is muscle with fascia superior to muscle and fat? *J. Tissue Eng. Regen. Med.* 12 (4), 1002–1011. doi:10.1002/term.2575
- Ren, B., Betz, V. M., Thirion, C., Salomon, M., Jansson, V., Muller, P. E., et al. (2019). Osteoinduction within BMP-2 transduced muscle tissue fragments with and without a fascia layer: Implications for bone tissue engineering. *Gene Ther.* 26 (1–2), 16–28. doi:10.1038/s41434-018-0047-2
- Rifas, L. (2007). The role of noggin in human mesenchymal stem cell differentiation. *J. Cell Biochem* 100 (4), 824–834. doi:10.1002/jcb.21132
- Ripamonti, U., Dix-Peek, T., Parak, R. M., Milner, B., and Duarte, R. (2015). Profiling bone morphogenetic proteins and transforming growth factor- $\beta$ s by hTGF- $\beta$ 3 pretreated coral-derived macroporous bioreactors: The power of one. *Biomaterials* 49, 90–102. doi:10.1016/j.biomaterials.2015.01.058
- Ripamonti, U., Parak, R., Klar, R. M., Dickens, C., Dix-Peek, T., and Duarte, R. (2016). The synergistic induction of bone formation by the osteogenic proteins of the TGF-beta supergene family. *Biomaterials* 104, 279–296. doi:10.1016/j.biomaterials.2016.07.018
- Ripamonti, U. (2006). Soluble osteogenic molecular signals and the induction of bone formation. *Biomaterials* 27 (6), 807–822. doi:10.1016/j.biomaterials.2005.09.021
- Rodrigues, M. T., Lee, S. J., Gomes, M. E., Reis, R. L., Atala, A., and Yoo, J. J. (2012). Bilayered constructs aimed at osteochondral strategies: The influence of medium supplements in the osteogenic and chondrogenic differentiation of amniotic fluid-derived stem cells. *Acta Biomater.* 8 (7), 2795–2806. doi:10.1016/j.actbio.2012.04.013
- Schaefer, D., Martin, I., Jundt, G., Seidel, J., Heberer, M., Grodzinsky, A., et al. (2002). Tissue-engineered composites for the repair of large osteochondral defects. *Arthritis Rheum.* 46 (9), 2524–2534. doi:10.1002/art.10493
- Scott, M. A., Levi, B., Askarim, A., Nguyen, A., Rackohn, T., Ting, K., et al. (2012). Brief review of models of ectopic bone formation. *Stem Cells Dev.* 21 (5), 655–667. doi:10.1089/scd.2011.0517
- Sheehy, E. J., Vinardell, T., Buckley, C. T., and Kelly, D. J. (2013). Engineering osteochondral constructs through spatial regulation of endochondral ossification. *Acta Biomater.* 9 (3), 5484–5492. doi:10.1016/j.actbio.2012.11.008
- Shi, Q., Li, Y., Sun, J., Zhang, H., Chen, L., Chen, B., et al. (2012). The osteogenesis of bacterial cellulose scaffold loaded with bone morphogenetic protein-2. *Biomaterials* 33 (28), 6644–6649. doi:10.1016/j.biomaterials.2012.05.071
- Smith, W. C., and Harland, R. M. (1992). Expression cloning of noggin, a new dorsalizing factor localized to the Spemann organizer in *Xenopus* embryos. *Cell* 70 (5), 829–840. doi:10.1016/0092-8674(92)90316-5
- Song, K., Krause, C., Shi, S., Patterson, M., Suto, R., Grgurevic, L., et al. (2010). Identification of a key residue mediating bone morphogenetic protein (BMP)-6 resistance to noggin inhibition allows for engineered BMPs with superior agonist activity. *J. Biol. Chem.* 285 (16), 12169–12180. doi:10.1074/jbc.M109.087197
- Strong, A. L., Spreadborough, P. J., Dey, D., Yang, P., Li, S., Lee, A., et al. (2021). BMP ligand trap ALK3-fc attenuates osteogenesis and heterotopic ossification in blast-related lower extremity trauma. *Stem Cells Dev.* 30 (2), 91–105. doi:10.1089/scd.2020.0162
- Urdeix, P., and Doweidar, M. H. (2020). Mechanical stimulation of cell microenvironment for cardiac muscle tissue regeneration: A 3D *in-silico* model. *Comput. Mech.* 66 (4), 1003–1023. doi:10.1007/s00466-020-01882-6
- Urist, M. R. (1965). Bone: Formation by autoinduction. *Science* 150 (3698), 893–899. doi:10.1126/science.150.3698.893
- van der Kraan, P. M. (2014). Age-related alterations in TGF beta signaling as a causal factor of cartilage degeneration in osteoarthritis. *Bio-medical Mater. Eng.* 24 (1), 75–80. doi:10.3233/bme-140976
- van der Kraan, P. M., Goumans, M. J., Blaney Davidson, E., and ten Dijke, P. (2012). Age-dependent alteration of TGF-beta signalling in osteoarthritis. *Cell Tissue Res.* 347 (1), 257–265. doi:10.1007/s00441-011-1194-6
- Virk, M. S., Sugiyama, O., Park, S. H., Gambhir, S. S., Adams, D. J., Drissi, H., et al. (2011). Same day" *ex-vivo* regional gene therapy: A novel strategy to enhance bone repair. *Mol. Ther. : J. Am. Soc. Gene Ther.* 19 (5), 960–968. doi:10.1038/mt.2011.2
- Wakefield, L. M., and Hill, C. S. (2013). Beyond TGF $\beta$ : Roles of other TGF $\beta$  superfamily members in cancer. *Nat. Rev. Cancer* 13 (5), 328–341. doi:10.1038/nrc3500
- Wan, D. C., Pomerantz, J. H., Brunet, L. J., Kim, J. B., Chou, Y. F., Wu, B. M., et al. (2007). Noggin suppression enhances *in vitro* osteogenesis and accelerates *in vivo* bone formation. *J. Biol. Chem.* 282 (36), 26450–26459. doi:10.1074/jbc.M703282200
- Wang, Y., He, T., Liu, J., Liu, H., Zhou, L., Hao, W., et al. (2016). Synergistic effects of overexpression of BMP-2 and TGF- $\beta$ 3 on osteogenic differentiation of bone marrow mesenchymal stem cells. *Mol. Med. Rep.* 14 (6), 5514–5520. doi:10.3892/mmr.2016.5961
- Wang, Y., Hong, S., Li, M., Zhang, J., Bi, Y., He, Y., et al. (2013). Noggin resistance contributes to the potent osteogenic capability of BMP9 in mesenchymal stem cells. *J. Orthop. Res.* 31 (11), 1796–1803. doi:10.1002/jor.22427
- Wei, W., and Dai, H. (2021). Articular cartilage and osteochondral tissue engineering techniques: Recent advances and challenges. *Bioact. Mater* 6 (12), 4830–4855. doi:10.1016/j.bioactmat.2021.05.011
- Wrighton, K. H., Lin, X., Yu, P. B., and Feng, X. H. (2009). Transforming growth factor  $\beta$  can stimulate Smad1 phosphorylation independently of bone morphogenetic protein receptors. *J. Biol. Chem.* 284 (15), 9755–9763. doi:10.1074/jbc.M809223200
- Wu, M., Chen, G., and Li, Y. P. (2016). TGF-beta and BMP signaling in osteoblast, skeletal development, and bone formation, homeostasis and disease. *Bone Res.* 4, 16009. doi:10.1038/boneres.2016.9
- Wu, X. B., Li, Y., Schneider, A., Yu, W., Rajendren, G., Iqbal, J., et al. (2003). Impaired osteoblastic differentiation, reduced bone formation, and severe osteoporosis in noggin-overexpressing mice. *J. Clin. Invest* 112 (6), 924–934. doi:10.1172/jci15543
- Xiong, F., Cheng, X., Zhang, C., Klar, R. M., and He, T. (2021). Optimizations for identifying reference genes in bone and cartilage bioengineering. *BMC Biotechnol.* 21 (1), 25. doi:10.1186/s12896-021-00685-8
- Xiong, F., Hausdorf, J., Niethammer, T. R., Jansson, V. A., and Klar, R. M. (2020). Temporal TGF-beta supergene family signalling cues modulating tissue morphogenesis: Chondrogenesis within a muscle tissue model? *Int. J. Mol. Sci.* 21 (14), 4863. doi:10.3390/ijms21144863
- Xiong, F. (2020). *Induction of chondrogenic morphogenesis in tissue culture using different combinations of transforming growth factor-beta superfamily proteins in vitro*. Imu.
- Yamashita, S., Andoh, M., Ueno-Kudoh, H., Sato, T., Miyaki, S., and Asahara, H. (2009). Sox9 directly promotes Bapx1 gene expression to repress Runx2 in chondrocytes. *Exp. Cell Res.* 315 (13), 2231–2240. doi:10.1016/j.yexcr.2009.03.008
- Zakin, L., and De Robertis, E. M. (2010). Extracellular regulation of BMP signaling. *Curr. Biol.* 20 (3), R89–R92. doi:10.1016/j.cub.2009.11.021
- Zhang, H., Zhao, X., Zhang, Z., Chen, W., and Zhang, X. (2013). An immunohistochemistry study of Sox9, Runx2, and Osterix expression in the mandibular cartilages of newborn mouse. *Biomed. Res. Int.* 2013, 1–11. doi:10.1155/2013/265380
- Zhang, Y., Liu, X., Zeng, L., Zhang, J., Zuo, J., Zou, J., et al. (2019). Tissue engineering: Polymer fiber scaffolds for bone and cartilage tissue engineering (adv. Funct. Mater. 36/2019). *Adv. Funct. Mater.* 29 (36), 1970246. doi:10.1002/adfm.201970246
- Zhao, L. (2008). *The role of Sox9 in osteogenesis*. Queen's University Belfast.
- Zhou, G., Zheng, Q., Engin, F., Munivez, E., Chen, Y., Sebald, E., et al. (2006). Dominance of SOX9 function over RUNX2 during skeletogenesis. *Proc. Natl. Acad. Sci. U S A* 103 (50), 19004–19009. doi:10.1073/pnas.0605170103
- Zhou, S., Yates, K. E., Eid, K., and Glowacki, J. (2005). Demineralized bone promotes chondrocyte or osteoblast differentiation of human marrow stromal cells cultured in collagen sponges. *Cell Tissue Bank.* 6 (1), 33–44. doi:10.1007/s10561-005-4253-y

## Glossary

**3D** 3-dimension

**Abi3bp** ABI family member 3 binding protein

**ACAN** Aggrecan

**Actb** Actin beta

**Alp** Alkaline phosphatase

**ANOVA** Analysis of variance

**BMP-2** Bone morphogenetic protein-2

**BMSCs** Bone marrow derived mesenchymal stem cells

**Col2a1** Collagen type II alpha 1

**Col1a1** Collagen type I alpha 1

**CNRQs** Calibrated normalized relative quantities

**ECM** Extracellular matrix

**FBS** Fetal bovine Serum

**Gapdh** Glyceraldehyde-3-phosphate dehydrogenase

**IOD** Optical density value

**IHC** Immunohistochemistry

**LMU** Ludwig Maximilian University of Munich

**MIQE** Minimum information for publication of quantitative real-time PCR experiments

**OCN** Osteocalcin

**Polr2e** RNA polymerase II subunit e

**P/S** Penicillin and streptomycin

**Runx2** Runx family transcription factor 2

**Rplp0** Ribosomal protein lateral stalk subunit p0

**SEM** Standard error of mean

**SdhA** Succinate dehydrogenase complex flavoprotein subunit A

**Six1** Sineoculis homeobox homolog 1

**Sox9** Sex determining region Y (SRY)-box transcription factor 9

**TGF- $\beta$ 3** Transforming growth factor-beta 3

**TE** Tissue engineering

**RT-qPCR** Quantitative reverse transcription polymerase chain reaction

# Frontiers in Bioengineering and Biotechnology

Accelerates the development of therapies,  
devices, and technologies to improve our lives

A multidisciplinary journal that accelerates the  
development of biological therapies, devices,  
processes and technologies to improve our lives  
by bridging the gap between discoveries and their  
application.

## Discover the latest Research Topics

See more →

### Frontiers

Avenue du Tribunal-Fédéral 34  
1005 Lausanne, Switzerland  
[frontiersin.org](https://frontiersin.org)

### Contact us

+41 (0)21 510 17 00  
[frontiersin.org/about/contact](https://frontiersin.org/about/contact)



Frontiers in  
Bioengineering  
and Biotechnology

